Lappeenranta
University of Technology

Almasi S. Maguya

USE OF AIRBORNE LASER SCANNER DATA IN DEMANDING FOREST CONDITIONS

Thesis for the degree of Doctor of Science (Technology) to be presented with due permission for public examination and criticism in Auditorium 1382 at Lappeenranta University of Technology, Lappeenranta, Finland on the 21st of December, 2015, at 12:00 p.m.

Acta Universitatis
Lappeenrantaensis 683

Supervisor Docent, PhD Tuomo Kauranne
Faculty of Technology
Department of Mathematics and Physics
Lappeenranta University of Technology
Finland

PhD Virpi Junttila
Faculty of Technology
Department of Mathematics and Physics
Lappeenranta University of Technology
Finland

Reviewers Professor Timo Tokola
Faculty of Science and Forestry
School of Forest Sciences
University of Eastern Finland
Finland

Docent, PhD Jari Vauhkonen
Faculty of Science and Forestry
School of Forest Sciences
University of Eastern Finland
Finland

Opponent Professor Timo Tokola
Faculty of Science and Forestry
School of Forest Sciences
University of Eastern Finland
Finland

ISBN 978-952-265-902-6
ISBN 978-952-265-903-3 (PDF)
ISSN 1456-4491
ISSN-L 1456-4491

Lappeenrannan teknillinen yliopisto
Yliopistopaino 2015

Abstract

Almasi S. Maguya
USE OF AIRBORNE LASER SCANNER DATA IN DEMANDING FOREST CONDITIONS
Lappeenranta, 2015
90 p.
Acta Universitatis Lappeenrantaensis 683
Diss. Lappeenranta University of Technology
ISBN 978-952-265-902-6, ISBN 978-952-265-903-3 (PDF), ISSN 1456-4491, ISSN-L 1456-4491

Most of the applications of airborne laser scanner data to forestry require that the point cloud be normalized, i.e., each point represents height from the ground instead of elevation. To normalize the point cloud, a digital terrain model (DTM), which is derived from the ground returns in the point cloud, is employed. Unfortunately, extracting accurate DTMs from airborne laser scanner data is a challenging task, especially in tropical forests where the canopy is normally very thick (partially closed), leading to a situation in which only a limited number of laser pulses reach the ground. Therefore, robust algorithms for extracting accurate DTMs in low-ground-point-density situations are needed in order to realize the full potential of airborne laser scanner data to forestry.

The objective of this thesis is to develop algorithms for processing airborne laser scanner data in order to: (1) extract DTMs in demanding forest conditions (complex terrain and low number of ground points) for applications in forestry; (2) estimate canopy base height (CBH) for forest fire behavior modeling; and (3) assess the robustness of LiDAR-based high-resolution biomass estimation models against different field plot designs. Here, the aim is to find out if field plot data gathered by professional foresters can be combined with field plot data gathered by professionally trained community foresters and used in LiDAR-based high-resolution biomass estimation modeling without affecting prediction performance. The question of interest in this case is whether or not the local forest communities can achieve the level technical proficiency required for accurate forest monitoring.

The algorithms for extracting DTMs from LiDAR point clouds presented in this thesis address the challenges of extracting DTMs in low-ground-point situations and in complex terrain while the algorithm for CBH estimation addresses the challenge of variations in the distribution of points in the LiDAR point cloud caused by things like variations in tree species and season of data acquisition. These algorithms are adaptive (with respect to point cloud characteristics) and exhibit a high degree of tolerance to variations in the density and distribution of points in the LiDAR point cloud.

Results of comparison with existing DTM extraction algorithms showed that DTM extraction algorithms proposed in this thesis performed better with respect to accuracy of estimating tree heights from airborne laser scanner data. On the other hand, the proposed DTM extraction algorithms, being mostly based on trend surface interpolation, can not retain small artifacts in the terrain (e.g., bumps, small hills and depressions). Therefore, the DTMs generated by these algorithms are only suitable for forestry applications where the primary objective is to estimate tree heights from normalized airborne laser scanner data.

On the other hand, the algorithm for estimating CBH proposed in this thesis is based on the idea of *moving voxel* in which gaps (openings in the canopy) which act as fuel breaks are located and

their height is estimated. Test results showed a slight improvement in CBH estimation accuracy over existing CBH estimation methods which are based on height percentiles in the airborne laser scanner data. However, being based on the idea of moving voxel, this algorithm has one main advantage over existing CBH estimation methods in the context of forest fire modeling: it has great potential in providing information about vertical fuel continuity. This information can be used to create vertical fuel continuity maps which can provide more realistic information on the risk of crown fires compared to CBH.

Keywords: Digital terrain model, LiDAR, forest inventory, remote sensing, forest fire, canopy base height, ground filtering, airborne laser scanning

Preface

I began my PhD research in November, 2011. My research has been carried out in the Centre of Computational Engineering and Integrated Design (CEID) at Lappeenranta University of Technology. Although I have been the main player throughout the course of my research, I would not have been able to get this far without the contribution, guidance, and cooperation of many other individuals in different capacities. Therefore, I would like to take this opportunity to thank and acknowledge all those who helped me in one way or another.

First and foremost, I would like to thank my supervisors, Tuomo Kauranne and Virpi Junttila for their continued support and guidance since day one of my research. The four years of my research under your supervision have been really exciting ones and I am glad to have been able to tap the knowledge which you have accumulated over many years of practicing in both academia and industry; working with you, gave me the opportunity to learn how things work in the real world.

Special thanks go to my reviewers Docent Jari Vauhkonen and Prof. Timo Tokola of the University of Eastern Finland for their valuable comments and recommendations. Your good comments and recommendations helped me greatly in improving and restructuring my thesis. I also thank Docent Ilkka Korpela of the University of Helsinki for his detailed and insightful comments and criticism about my work. I really appreciate your time and effort.

Next, I would also like to express my sincere gratitude to the research and development (R & D) team at Arbonaut Ltd. for their support and cooperation. In particular, I thank Anna Eivazi, Basanta Gautam, Blanca Sanz, Janice Burns, Katja Gunia, Katri Tegel, Markus Korhonen, Risto Rautianen, and Vesa Leppanen. I would not be able to complete this work on time without your help. I appreciate the quick responses I got from you whenever I had a query or problem and the valuable comments you gave regarding the publications which appear as part of this thesis.

I also thank CEID and Mzumbe University (MU) too for providing me with financial support during the entire course of my research, the money is well-spent. This work would not have been completed on time without this support. I thank Arbonaut Ltd. too for for handling logistics (particularly data acquisition and documentation) and financing my trips to Arbonaut head quarters in Joensuu to attend various workshops and discuss research matters with the R & D team at Arbonaut.

The four years of my stay in Finland would really seem longer and more difficult and lonely without the company of my fellow Tanzanian PhD researchers and master's students: Amani Metta, Daniel Osima, Felix John, Frank Seth, Gasper Mwanga, Idrissa Said, Isambi Mbalawata, Pendo Kivyiro, and Zubeda Mussa. The friendship and togetherness we have been enjoying has been one of the driving forces behind my motivation and the drive to keep going during difficult (academic) times– the political and comic discussions in WhatsApp were really refreshing. By the same token, I thank other colleagues of mine at CEID: Ashvinkumar Chaudhari, Ivan Martynov, Miika Tolonen, Ville Maninen, Saku Kukkonen, and Zeinab Zeleti, among others, for their help and cooperation ranging from academics to social topics like the meaning of the text on various Finnish traffic signs (like "huoltoajo salittu" and "pelastustie") and how not to get stranded in freezing winter mornings because of "frozen" car doors.

Last, but not least, I extend my deepest gratitude to my lovely and caring wife Zainab© and our

cute and energetic children Mustafa (Mu), Abdulrahim (Im), and Helmi. Your never-ending encouragement and support are much appreciated and duly noted, I understand the four years of partial separation have not been easy ones. Thank you for taking care of things at home, especially making sure that our kids go to school and do their homework. By the same token, many thanks too go to my inspiring and hard-working mother–Halima (Bibi Mu). Thank you for sending me to school and inspiring me to be a hard-working person.

Lappeenranta, December 2015

Almasi S. Maguya

CONTENTS

LIST OF THE ORIGINAL ARTICLES AND THE AUTHOR'S CONTRIBUTION

This thesis consists of two parts, namely the introduction and publications parts. The introduction part gives background information on the main topic of the thesis while the publications part presents four, refereed journal articles featured in the thesis. Below is a list of the featured articles and a summary of the author's contribution in each article.

I **Maguya, A. S., Junttila, V. and T. Kauranne**, Adaptive Algorithm for Large Scale DTM Interpolation From LiDAR Data For Forestry Applications in Steep Forested Terrain, *ISPRS Journal of Photogrammetry and Remote Sensing*, 85(2013), 74–83, 2013.

II **Maguya, A. S., Junttila, V. and Kauranne, T.**, Algorithm For Extracting Digital Terrain Models under Forest Canopy from Airborne LiDAR Data, *Remote Sensing*, 6(7), 6524–6548, 2014.

III **Maguya, A. S., Tegel, K., Junttila, V., Kauranne, T., Korhonen, M., Burns, J., Leppanen, V. and Sanz, B.**, Moving Voxel Method For Estimating Canopy Base Height From Airborne LiDAR Data, *Remote Sensing*, 7(7), 8950–8972, 2015

IV **Junttila, V., Gautam, B., Karky, B. S., Maguya, A. S., Tegel, K., Kauranne, T., Gunia, K., Hämäläinen, J., Latva-Käyrä, P., Nikolaeva, E., and Peuhkurinen, J.**, Robustness of model-based high-resolution prediction of forest biomass against different field plot designs, *Carbon Balance and Management*, 10(29), 2015

In publications **I** and **II** the author designed, implemented and tested the algorithms and also wrote the articles. In publication **III** the author designed, implemented and tested the algorithm and wrote most of the article. In publication **IV** the author participated in writing and editing the article. The author also handled the publication process for all the four articles, including submission, revision, and re-submission and all the correspondence with the editorial offices of the respective journals.

3-D	Three-Dimensional
AGB	Above Ground Biomass
AGL	Above Ground Level
ALS	Airborne Laser Scanning
ASTER	Advanced Spaceborne Thermal Emission and Reflection Radiometer
BIC	Bayesian Information Criteria
BLUE	Best Linear Unbiased Estimate
CBD	Canopy Bulk Density
CBH	Canopy Base Height
CH	Canopy Height
CHM	Canopy Height Model
CO_2	Carbon Dioxide
CPU	Central Processing Unit
CSM	Canopy Surface Model
CV	Coefficient of Variation
DEM	Digital Elevation Model
DTM	Digital Terrain Model
S	Error Standard Deviation
GB	Gigabyte
GDEM	Global Digital Elevation Model
GHG	Green House Gas
GPS	Global Positioning System
GPU	Graphics Processing Unit
IDW	Inverse Distance Weighting
IMU	Inertial Measurement Unit
INS	Inertial Navigation System
kHz	kiloHertz
LAI	Leaf Area Index

LiDAR	Light Detection and Ranging
LOOCV	Leave One Out Cross Validation
ME	Mean Error
NFI	National Forest Inventory
OK	Ordinary Kriging
PC	Personal Computer
PRISM	Panchromatic Remote Sensing Instrument for Stereo Mapping
R^2	Coefficient of Determination
RAM	Random Access Memory
REDD+	Reducing Emissions from Deforestation and Forest Degradation Plus
RMSE	Root Mean Square Error
$RMSE_{cv}$	Root Mean Square Error of Cross Validation
SRTM	Shuttle Radar Topography Mission
TIFF	Tagged Image File Format
TIN	Triangulated Irregular Network
TLS	Terrestrial Laser Scanning
UNFCCC	United Nations Framework Convention on Climate Change
UTM	Universal Transverse Mercator
WGS84	World Geodetic System 1984

PART I: OVERVIEW OF THE THESIS

CHAPTER I

Introduction

Forests are one of earth's natural resources that serve humans in multiple ways. For example, for many years forests have been used for their economic value—construction, as a source of energy, and as material for making furniture. In the wake of the underlying consequences of the global warming problem, mainly climate change, forests are seen to play yet another key role as one of the most important carbon sinks (van Minnen et al., 2008). In this role, forests help to counter the problems caused by accumulation of green house gases (GHGs) in the earth's atmosphere by sequestering carbon from the atmosphere through the process of photosynthesis (see e.g., Liu, 2013); a prominent example of these problems is global warming. Following this fact, it is therefore of great interest to put in place proper, accurate, and reliable forest management procedures.

These procedures will equip forest managers with the information they need to make timely and informed decisions pertaining to different aspects of the management and well-being of forests. For example, to estimate how much carbon has been sequestered by a forest, the amount of biomass in that forest needs to be estimated. Also, in order to prevent forest fires, for example, fire managers need to know which areas contain high fuel loads that need immediate attention—thinning or prescribed fires—to minimize the risk of fire or reduce the intensity of the fire if it breaks. All these tasks require timely and reliable information if they are to be effective, especially when the operation in question is large scale, for example operations at the regional and national levels).

Traditionally, forest mensuration had been largely manual whereby people would go physically to the forest and take measurements of interest. This approach has the advantage that it can be relatively accurate if done with care. However, the approach suffers from two major limitations. First, it is prohibitively time consuming especially when large areas of forest need to be measured, and second, it is very expensive—it involves a large number of people. Because of these reasons, nowadays this method is limited to small forests and is of no practical use to large scale forest management.

Today, forest management is done at levels as high as the national or even the global level at unprecedented levels of accuracy and flexibility. This has been possible thanks to the application of remote sensing technologies (Næsset, 2004b,a, 2007). Remote sensing technologies such as aerial and satellite imagery, Light Detection and Ranging (LiDAR), and photogrammetry provide a wealthy source of data about forests that can be used to monitor forests in many different ways, from estimating biomass (e.g., Hauglin et al., 2013); detecting changes due to growth and disturbances such as deforestation (e.g., Reutebuch et al., 2005; Herold et al., 2011); and modeling forest fire behavior

(e.g., Wulder et al., 2009).

What makes remote sensing technologies attractive as a source of data for forest mensuration is their ability to cover large areas with relatively low cost and the high accuracy of the data they offer, which is a result of advances in sensor technology in the last decade (Lemmens, 2011a). Moreover, it is possible to combine several remote sensing data sources (data fusion) to achieve even higher estimation accuracy when needed (e.g., Zhang, 2010; Erdody and Moskal, 2010).

LiDAR has received a lot of attention among the forestry community over the last decade. This is mainly due to the advantages LiDAR offers over other remote sensing technologies such as passive optical remote sensing and passive imaging. The most important advantage of LiDAR over other remote sensing technologies is its ability to penetrate the forest canopy and measure the vertical structure of the forest. This ability provides crucial information which other remote sensing technologies do not—height. It is this capability that has made LiDAR a tool of choice for foresters when it comes to estimating various parameters pertaining forests. Moreover, being an active remote sensing technology LiDAR is only slightly affected by weather and visibility conditions therefore data can be acquired both in the day and at night throughout the year (Lemmens, 2011a). Currently, LiDAR is being extensively used in forest fire modeling, biomass estimation, and growth monitoring.

Over the last decade, LiDAR technology has developed into a mature and reliable technology. LiDAR is now considered mainstream by foresters and natural resources researchers in general due to the cost-efficiency of LiDAR data collection and the added value of LiDAR products. Availability of standard algorithms for processing LiDAR data (see e.g., Axelsson, 1999; Hyyppä et al., 2004) and open (as opposed to proprietary) data exchange formats such as the LAS file format (see American Society for Photogrammetry and Remote Sensing (ASPRS) , 2014) used for exchanging 3-D LiDAR data are additional reasons contributing to the widespread adoption of LiDAR technology in the forestry community .

This thesis contributes to LiDAR processing in three areas: (1) Digital terrain model (DTM) extraction in challenging environments; (2) forest fire behavior modeling; and (3) LiDAR-based biomass estimation using different sources of field data (sampling designs) for model training. In (1) and (2) novel methods are proposed while in (3) model-based comparison results of biomass estimation are presented and analyzed.

DTMs play a key role when it comes to the application of LiDAR to forestry, for instance biomass estimation and forest fire behavior modeling, as it is normally necessary to estimate the height of the trees/canopy as a prerequisite step for subsequent processing of the LiDAR data. Unfortunately, DTM extraction from LiDAR data is a challenging task, especially when the number of ground points is limited due to, e.g., canopy cover, high-altitude acquisition of LiDAR data, or when the terrain is complex (steep, rough, or both) (Sithole and Vosselman, 2004).

Forest fires are becoming increasingly difficult to control and they cause a lot of damage when they break out due to large quantities of fuels that has been accumulating in the forests over the years (see e.g., Schoennagel et al., 2004). Furthermore, countries such as Greece, Portugal, and Spain spend a lot of money and considerable time every year for fighting forest fires (San-Miguel-Ayanz et al., 2013). Thus, the ability to model the behavior of forest fires is crucial as it enhances our ability to understand the behavior of forest fires and puts us in a better position to prevent and control forest fires.

The remainder of the thesis is organized as follows. Chapter 2 gives a background on LiDAR tech-

nology, followed by the application of LiDAR technology in forestry in Chapter 3. Chapter 4 covers methods for DTM extraction from LiDAR data while Chapter 5 covers methods for CBH estimation from LiDAR data. Chapter 6 discusses some common challenges faced when applying LiDAR technology to forestry while Chapter 7 concludes the thesis.

CHAPTER II

Overview of LiDAR Technology

This chapter gives a background in LiDAR technology and how the technology is being used in forestry today. The chapter begins by giving an overview of the technology (Section 2.1), followed by a discussion of how LiDAR data is acquired (Section 2.2).

2.1 How LiDAR Technology Works

LiDAR is an active remote sensing technology which uses opto-mechanical sensors to send laser beams to the targets (Wehr and Lohr, 1999). LiDAR technology is used for ranging purposes that measures the distance between the laser sensor and the targets—trees in case of forestry applications—by measuring accurately the 2-way travel time the laser beams use to travel from the sensor to the targets and back (Andersen et al., 2006). The range is estimated by multiplying the speed of light by the time it takes for the laser beam to travel from the sensor to the targets, i.e.,

$$R = c * \left(\frac{t}{2}\right) \tag{2.1}$$

where R is the range, c is the speed of light, and t is the time of travel of the laser beams from the sensor to the targets and back. A typical LiDAR system consists of three main parts (Wehr and Lohr, 1999; Lemmens, 2011a): (1) laser scanner (sensor); (2) Global Positioning System (GPS); and (3) Inertial Navigation System (INS) (also known as Inertial Navigation Unit (INU)).

The laser scanner (sensor) is responsible for ranging, scanning, control, and processing (Wehr and Lohr, 1999). Each of these functions is built in a separate unit. The sensor emits laser pulses at a very high frequency (typically 100000–250000 pulses per second). Reflected pulses are picked up by the receiver part of the sensor. Range calculation is done using the speed of light and the time (measured by a clock) of travel of the laser pulses. The GPS is responsible for measuring the position of the sensor in space (X-, Y-, and Z-coordinates) while the INS measures the orientation of the sensor (roll, pitch, and yaw). Section 2.2 explains the process of LiDAR acquisition.

Most of today's LiDAR systems can be classified into several classes based on different criteria. The most prominent classification is based on the platform used to host the LiDAR system. In the first type, known as airborne LiDAR or airborne laser scanning (ALS), the LiDAR system is mounted on aircraft and flown over the area of interest (Wehr and Lohr, 1999; Lemmens, 2011a). Depending

on circumstances, e.g., nature of terrain and the desired flying altitude, either a helicopter or fixed wing aircraft can be used as an aerial platform. The second type of LiDAR system is known as terrestrial LiDAR or terrestrial laser scanning (TLS). This type of LiDAR system is land-based and is normally mounted on a moving platform such as a motor vehicle or sometimes is mounted on a tripod (Lemmens, 2011b). Figure 2.1 shows typical examples of LiDAR systems.

(a) (b)

Figure 2.1: Examples of LiDAR systems: (a) Optech Pegasus ALTM airborne LiDAR system; (b) Leica Geosystems terrestrial LiDAR system mounted on a tripod. Image sources: (a) Optech (2014); (b) Leica Geosystems UK (2014). Reprinted with permission.

Terrestrial LiDAR systems have received a lot of attention in recent years (Dassot et al., 2011). The main reason for this attention is the range of attractive features and the potential terrestrial LiDAR systems have for forestry applications. The ability to produce rich point clouds with very high precision (in order of millimeters) make terrestrial LiDAR systems suitable for applications aiming at studying forest structures at a very detailed level (Slob and Hack, 2004; Dassot et al., 2011; Listopad et al., 2011), e.g., reconstruction of individual trees (van Leeuwen and Nieuwenhuis, 2010; Dassot et al., 2011) and estimating timber quality (Kankare et al., 2014a). Moreover, a study comparing airborne and terrestrial laser scanning for timber assortments and stem distribution estimation conducted by Kankare et al. (2014b) showed that more accurate results are obtained when the two methods are combined.

However, terrestrial LiDAR is a relatively new technology and therefore it still suffers from some important limitations which airborne LiDAR doesn't (Wulder et al., 2008). The first limitation is the high cost of data acquisition and processing per unit area. The second limitation is restricted operational range inherent with terrestrial LiDAR sensors (typically 50 m) (van Leeuwen and Nieuwenhuis, 2010). In addition, the technology is more susceptible to occlusions—such as branches and leaves—which diminishes its ability to map vegetation. The discussion in this thesis will be restricted to airborne LiDAR and from this point on, unless otherwise stated, the term LiDAR is going to refer to airborne LiDAR. Moreover, the term LiDAR is going to refer to airborne LiDAR technology or LiDAR data.

Another classification of LiDAR is discrete return versus full-waveform LiDAR. Majority of LiDAR sensors in use today can record from one to five returns for each emitted laser pulse; these sensors operate by emitting short laser pulses in the visible and/or infrared part of the electromagnetic

spectrum (Evans et al., 2009; Ussyshkin and Theriault, 2011). As the pulse continue to travel down the canopy it hits tree branches and part of it is reflected back to the sensor. The first return corresponds to the first reflection of the pulse while the last return corresponds to the last reflection of the pulse (Lemmens, 2011a). When scanning forests the first return is normally from the top of the top of canopy while the last return is normally from the ground. In contrast, full-waveform LiDAR sensors sample and record sequences of the returning pulse power at fixed time intervals (typically 1 ns). Because of this high sampling rate, full-waveform LiDAR provides a rich representation of the vertical structure of the canopy (Wagner et al., 2004, 2008). This characteristic makes full-waveform LiDAR more suitable for some kinds of applications, such as vegetation classification and for describing canopy geometry, over discrete return LiDAR (see e.g., Hovi and Korpela, 2014). Moreover, due to its high sampling rate, full-waveform LiDAR is good at positioning scatters and attributing them with echo widths and pick amplitude. This quality is suitable for detecting solid scatters such as the ground and makes full-waveform LiDAR potentially useful for DTM extraction. Figure 2.2 illustrates the difference between discrete return and full-waveform LiDAR.

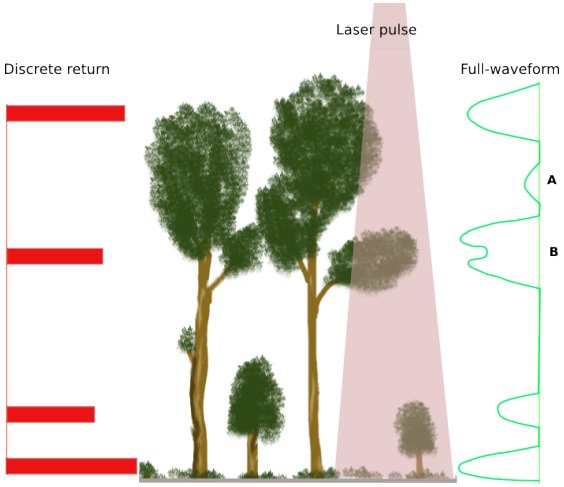

Figure 2.2: Illustration of the difference between full-waveform and discrete return LiDAR. This figure also demonstrates the inability of discrete return LiDAR to separate echoes with two adjacent peaks, indicated by **B**. Also note note that in this example the system can record up to four echoes and it misses the echo labelled with an **A**.

LiDAR can also be classified based on the size of the laser pulse footprint. Pulse footprint refers to the diameter of a laser pulse's circle of illumination on the ground (Wulder et al., 2008). LiDAR may be considered small footprint (0.1–0.2 m in radius) or large footprint (10–100 m in radius). Strictly speaking, footprint size is not a characteristic of a particular LiDAR sensor, rather it is a function of beam divergence and flying altitude (see Section 2.2) (Lemmens, 2011a). For a fixed beam divergence angle, increasing the flying altitude will also lead to an increase in footprint size and vice versa. Also, for a fixed flight altitude, increasing the beam divergence will lead to an increase in footprint size and vice versa. However, since the within-footprint illumination (W/m^2) is important when acquiring ground echoes through gaps of varying size, increasing beam divergence should be accompanied by an increase in beam power per unit area or this increase in beam divergence will

have a detrimental effect on the underlying signal to noise ratio (SNR). Large footprint LiDAR is currently acquired from space (satellites) and its main purpose it not forestry applications; therefore, most forestry applications of LiDAR make use of small footprint LiDAR (van Leeuwen and Nieuwenhuis, 2010).

2.2 Airborne LiDAR Acquisition

Figure 2.3 demonstrates how LiDAR is acquired—an aircraft with the LiDAR system on board flies over the target area in a pre-determined pattern known as flight lines while the LiDAR system scans the area in strips of terrain below the sensor, and along the flight line known as swath widths. As it can be seen in Figure 2.3, this process is affected by several parameters. The most important ones are described next.

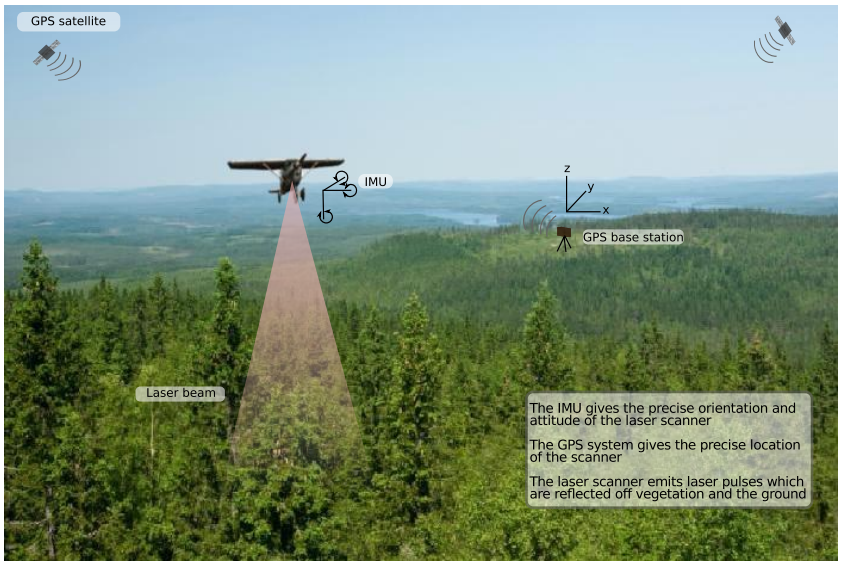

Figure 2.3: Demonstration of airborne laser scanning/LiDAR acquisition showing how the three main parts of LiDAR work together. In this example positioning is based on the global positioning system but any global navigation satellite system (GNSS) system can be used.

2.2.1 Important LiDAR Acquisition Parameters

LiDAR acquisition parameters have a direct effect on the characteristics of the resulting LiDAR data, i.e., the point cloud, particularly point density—total number of returns per square meter. These parameters are of two kinds. The first kind is LiDAR system parameters and the second is flight specification parameters. Table 2.1 presents examples of these parameters and their typical values.

In addition to the parameters which have been mentioned before, other parameters include (Wulder et al., 2008; Evans et al., 2009): projection and datum, which are used for georefencing purposes; pulse density, which refers to the horizontal horizontal spacing of the laser footprints; sensor type,

Table 2.1: Examples of common LiDAR acquisition parameters and their values (see Maguya et al., 2014).

Parameter	Value
Projection	UTM
Datum	WGS84
Aerial platform	Helicopter
Flying altitude	2200 m AGL
Flying speed	80 knots
Sensor type	Leica ALS-50 II
Scan angle	20 degrees
Sensor pulse rate	52.9 kHz
Sensor scan speed	20.4 lines/s
Pulse density	0.8 points/m^2
Swath width	1601.47 m
Beam footprint	50 cm

which refers to the actual LiDAR system, i.e., hardware; scan angle, which is the angular breadth of a scan line (determined by the sensor's scan mechanism); and sensor scan speed, which is the the rate at which laser pulses are directed across the flight line each second. In Table 2.1, the first five parameter are flight specification parameters while the rest are system parameters.

2.2.2 LiDAR Deliverables

McGaughey et al. (2006) recommends a minimum of the following deliverables for a LiDAR acquisition mission: (1) coordinate system; (2) datum; (3) ellipsoid information; (4) the geoid used to compute return elevations; and (5) a description of file formats and file naming conventions. In addition to these deliverables, metadata describing the flight and instrument specifications during LiDAR acquisition, and processing should also be given. The LiDAR point cloud is the fundamental product of any LiDAR acquisition project on which most of the applications of LiDAR in forestry are based (see Figure 2.4).

2.2.3 LiDAR Pre-processing

Pre-processing of the raw LiDAR point cloud is normally done by the vendor before the data is handled over to the client (Evans et al., 2009). Pre-processing includes, among other things, geometrical correction and transformation to a specified geographical projection system and vertical datum; sensor correction to correct for pitch, yaw, and roll of aircraft; and tiling which refers to the division of the data into manageable blocks.

The pre-processed LiDAR point cloud is normally delivered in LAS file format (American Society for Photogrammetry and Remote Sensing (ASPRS) , 2014). The LAS file format is an open binary file format commonly used for exchanging LiDAR. The format is supported by many LiDAR processing utilities, both open source and proprietary.

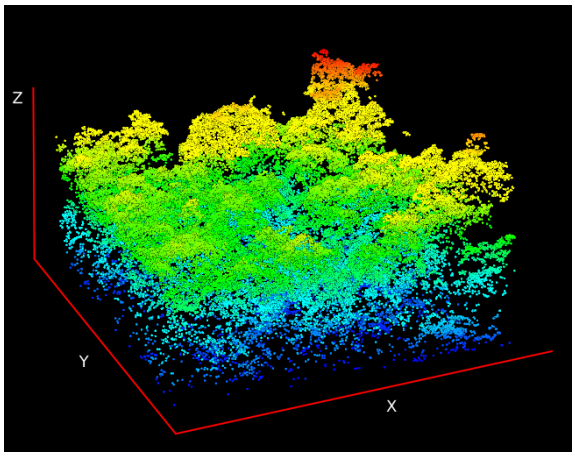

Figure 2.4: An example of a LiDAR point cloud.

CHAPTER III

Applications of Airborne LiDAR in Forestry

The ability of LiDAR to penetrate the forest canopy and give 3-D measurements of the canopy increases its potential for estimating various forest structural parameters with high accuracy. Many forest structural parameters correlate well with metrics derived from LiDAR. This chapter reviews the most common applications of LiDAR in forestry, i.e., forest structural parameter estimation from LiDAR. For the purpose of this discussion, the parameters in question are going to be grouped into L*i*DAR-*observed* and *derived* parameters. First, LiDAR metrics, which are the basis for estimating most of the forest structural parameters from LiDAR are introduced in Section 3.1, followed by an overview of LiDAR-observed forest parameters in Section 3.2. Next, derived forest parameters are discussed in Section 3.3. Section 4.1 gives some examples of high level forestry applications of the aforementioned parameters. Section 3.5 presents a case study on the application of LiDAR in biomass estimation using different field plot designs.

3.1 LiDAR Metrics

LiDAR does not give direct measurements of the forest structural parameters, such as height, canopy cover, etc., instead, it gives rich 3-D data about the general structure of the forest canopy—the point cloud. Thus, in order to use LiDAR for estimating/predicting forest structural parameters, special variables are normally created from the point cloud that exhibit good correlation with forest structural parameters to be estimated/predicted. These variables are referred to as LiDAR metrics.

Common practice has been to use LiDAR metrics as predictor (independent) variables in regression models and to use field-measured variables as response (dependent) for calibrating these models. Commonly used LiDAR metrics are based on LiDAR height percentiles; they include the 25th (h_{25}), 50th (h_{50}), 75th (h_{75}), and the 90th (h_{90}) height percentiles (see e.g., Andersen et al., 2005; Skowronski et al., 2011). These metrics are normally computed from the point cloud at the plot level. Since the metrics are based on LiDAR heights—the Z-coordinate of the points in the point cloud—the point cloud must first be normalized by subtracting the elevation of each point from the elevation of the corresponding XY-coordinate on the DTM so that the points represent height above ground instead of elevation. Other LiDAR metrics include the maximum height (h_{max}), average height (h_{mean}), canopy cover (CC), and coefficient of variation (CV). Figure 3.1 shows an example of a plot extracted from a point cloud which can be used to compute LiDAR metrics at the plot level.

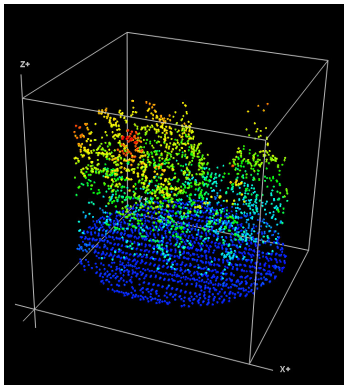

Figure 3.1: An example of a circular plot extracted from LiDAR. LiDAR metrics used for estimating various forest parameters are normally computed from plots similar to this with varying radii. In this example the plot has a radius of 12 m.

3.2 LiDAR-Observed Forest Parameter Estimation

In the following discussion, LiDAR-observed forest parameters refer to those parameters that describe either trees (individual or at the stand/plot level) or the canopy in general. These parameters include: (1) tree height; (2) canopy height; (3) canopy cover; (4) canopy base height; (5) canopy height; and (6) canopy bulk density.

3.2.1 Tree Height

Tree height is a fundamental attribute which may refer to either individual trees or a group of trees in a plot/stand (mean tree height). Tree height is used as an input in many allometric models used to predict derived forest parameters such as biomass (e.g., Asner et al., 2012; Asner and Mascaro, 2014). Many studies have proposed methods for estimating tree height from LiDAR. Majority of these studies use image segmentation approaches (or local maxima filtering) to detect individual tree-top locations in aerial images and consequently locate and extract the corresponding trees from LiDAR (e.g., Leckie et al., 2003; Wang et al., 2004; Takahashi et al., 2005). Other studies (e.g., Maltamo et al., 2004) use a similar approach but they use canopy height models (CHMs) (see Section 3.2.2) instead of aerial imagery for local maxima filtering. Although these studies demonstrated that individual tree height can accurately be estimated from LiDAR, the density of the LiDAR used needs to be relatively high to obtain good results.

Regarding mean tree height, the general approach has been to employ regression analysis to estimate average tree height at the stand level. In the regression models, field-measured individual tree heights are used to calibrate the models while LiDAR metrics are used as predictors (e.g., Næsset and Økland, 2002; Næsset et al., 2005; Yamamoto et al., 2011). This approach takes advantage of the high correlation present between LiDAR metrics and mean tree height (Holmgren, 2004).

3.2.2 Canopy Height

Canopy height (CH) refers to the height of the canopy as a whole and is normally represented as a 3-D surface or raster known as the canopy height model (CHM) (Wulder et al., 2008; van Leeuwen and Nieuwenhuis, 2010). As described in the previous section, CHM is the basis for estimating the height of individual trees (see Figure 3.2) as well as estimating many derived forest parameters (see Section 3.3). LiDAR has proven to be very successful for generating CHMs. To generate a CHM from LiDAR, first LiDAR returns are identified and used for interpolating a 3-D surface known as the canopy surface model (CSM). CHM is then computed as the difference between the canopy surface model and the digital terrain model (DTM), i.e., $\text{CHM} = \text{CSM} - \text{DTM}$ (Næsset, 1997; Magnusen and Boudewyn, 1998). Figure 3.2 illustrates this process.

Estimating CH directly from first returns, however, has proven to be underestimating canopy height (Gaveau and Hill, 2003; Yu et al., 2004; Ronnholm et al., 2004). The reason for the underestimation has to do with the *smearing effect* of the peaks (e.g., tree apexes) due to the lack of enough sample points to required to generate an accurate CSM. Moreover, small canopy elements do not trigger an echo. As a result, indirect methods (e.g., statistical methods) for CH estimation have been proposed (e.g., Wang and Glenn, 2008).

3.2.3 Canopy Cover

Canopy cover refers to the fraction/percentage of the ground area covered by vegetation when viewed vertically from above (projection of tree crowns onto the ground) (van Leeuwen and Nieuwenhuis, 2010). Canopy cover plays an important role in many forest monitoring applications, e.g., growth modeling and fire risk assessment (Jupp et al., 2009). Leaf area index (LAI) is another *cover parameter* which expresses the ratio of total leaf area to unit ground surface area (Zheng and Moskal, 2009). LAI plays an important role in ecological research focusing on understanding of gas-vegetation exchange phenomenon (Zheng and Moskal, 2009).

LiDAR has been used extensively in estimating canopy cover and LAI (e.g., Riaño et al., 2004; Morsdorf et al., 2006; Korhonen et al., 2011). Using LiDAR, canopy cover can be estimated for any vertical layer of the forest (e.g., overstorey, midstorey, and understorey); the general idea is to compare the number of laser pulses (per unit area) of pulses that are uninterrupted by a given forest layer to the total number of points per unit area (Wulder et al., 2008). Figure 3.3 illustrates the general idea behind estimating canopy cover from LiDAR.

3.2.4 Canopy Base Height

Canopy base height (CBH) refers to the lowest height at which the canopy fuel density exceeds a critical threshold (normally $0.011\,\text{kg/m}^3$) (Andersen et al., 2005). CBH plays a critical role in forest fire behavior modeling. LiDAR has been widely used in estimating CBH with high levels of accuracy being reported (e.g., Popescu and Zhao, 2008; Korhonen, 2012; González-Olabarria et al., 2012). This increase in accuracy in CBH estimation means improved accuracy in forest fire behavior modeling, particularly crown fires which depend on CBH for their initiation. Fire behavior simulation tools such as FARSITE (Finney, 2004) take CBH as one of their inputs therefore accurate CBH is crucial for them to give reliable results. Chapter 5 discusses methods of estimating CBH from LiDAR in detail.

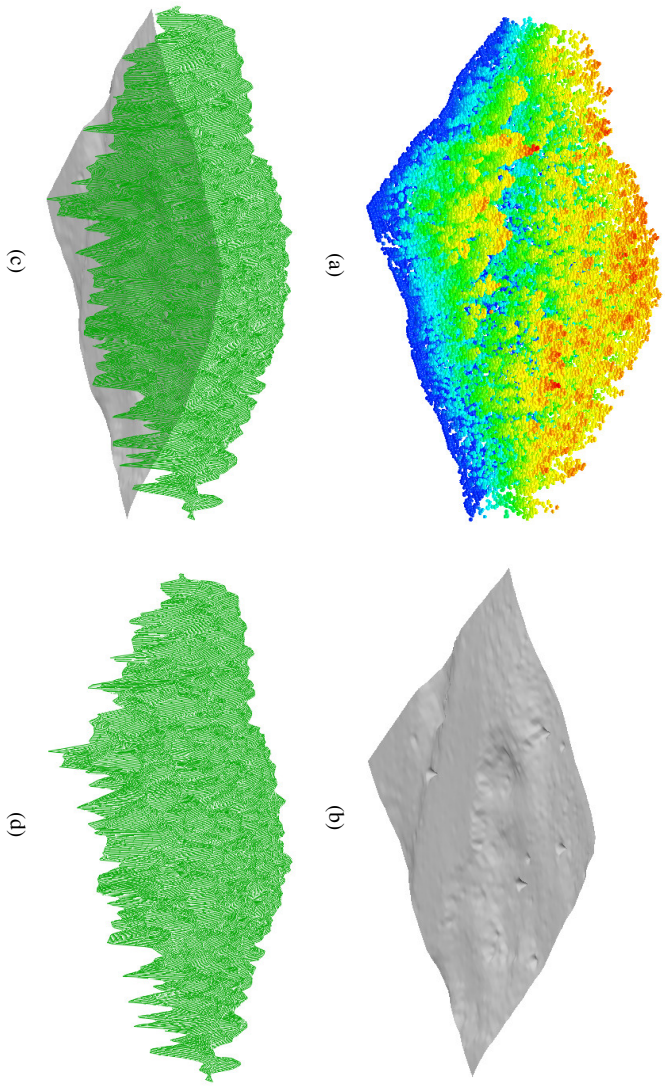

Figure 3.2: Illustration of canopy height estimation from LiDAR: (a) original point cloud; (b) DTM extracted fro the point cloud in (a); (c) DTM overlaid with a CSM generated from the point cloud in (a); (c) a CHM obtained by subtracting the DTM in (b) from the CSM in (c).

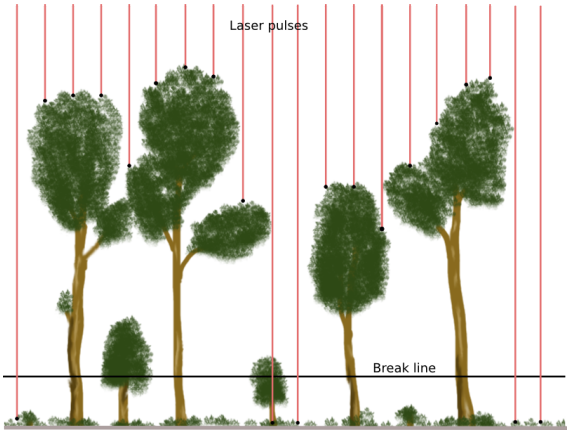

Figure 3.3: Estimating canopy cover from LiDAR. Canopy cover is computed as the percentage of LiDAR pulses that cross a pre-determined cut-off height or break line (shown as a black horizontal line).

3.2.5 Canopy Bulk Density

Canopy bulk density (CBD) is another forest parameter used in forest fire behavior modeling. It refers to the amount of fuel contained per unit of canopy volume (Hall and Burke, 2006). As it has been with CBH, many studies have reported improved accuracy in estimating CBD using LiDAR (e.g., Riaño et al., 2003; Andersen et al., 2005; Erdody and Moskal, 2010; Skowronski et al., 2011). Like CBH, CBD is a direct input to some forest fire simulation models and accurate CBD is crucial for these tools to give reliable results.

3.2.6 Canopy & Crown Volumes

Canopy volume and crown volume (volume metrics) are important parameters that can be used as input for many forestry applications including single-tree branch biomass estimation (Hauglin et al., 2013) and forest fire behavior modeling (particularly CBD estimation) (e.g., Agca et al., 2011). Unfortunately, measuring/estimating volume metrics is very difficult. Because of this challenge, most studies estimate individual tree crown using simple geometric shapes such as cones and cylinders which do not give accurate results, leading to propagation of errors to other parameters computed from these estimates.

Recently, more robust methods for estimating volume metrics from LiDAR have been proposed (Korhonen et al., 2013; Vauhkonen et al., 2014). These methods are based on computational geometry (e.g., topological connectivity, alpha shapes, and 3-D convex hulls) and give more accurate results compared to traditional methods, which means other forest parameters depending on volume metrics can also be estimated with improved accuracy.

3.3 Derived Forest Parameter Estimation

In the following discussion, derived forest parameters refer to those parameters that use one or more LiDAR-observed forest parameters for their estimation. Examples of derived forest parameters include parameters that have to do with, for example, biomass, and forest fire behavior parameters.

3.3.1 Biomass Estimation

Based on the volume of literature on biomass estimation from LiDAR, biomass estimation, particularly above ground biomass (AGB), is perhaps one of the most investigated areas related to the application of LiDAR in forestry. Because of this fact, a great deal of methods and techniques on the application of LiDAR for biomass estimation have been proposed.

Following problems associated with accumulation of green house gases (GHGs), i.e., global warming and climate change, caused mainly by burning of fossil fuels (see e.g., de Figueiredo et al., 2010), a lot of attention has been directed to sustainable forestry as a means to mitigate these problems. Forests play a key role as carbon sinks in mitigating the problems of global warming and climate change (Pan et al., 2011). During the process of photosynthesis, trees sequester carbon from the atmosphere in the form of CO_2 to produce energy for growth and store the rest as carbon (Nowak and Crane, 2002; van Minnen et al., 2008; Willcock et al., 2014). This process is reversible, i.e., the stored carbon can be returned back to the atmosphere through natural decomposition of plant matter and burning of biomass through, for example, forest fires and wood for generating energy. This is the essence of renewable energy sources which do not contribute to accumulation of GHGs in the atmosphere.

To curb the problems of global warming and climate change, it is necessary for nations, particularly developed ones, to reduce their annual GHG emissions while at the same time promoting carbon sinks, mostly forests, to offset their GHG emissions. The Kyoto protocol and the Reducing Emissions From Deforestation and Forest Degradation plus (REDD+) are two important schemes designed to accomplish these goals (Missfeldt and Haites, 2001; Noble and Scholes, 2001). REDD+ is designed to encourage developing nations to put into practice proper and sustainable forest management practices that will minimize forest degradation and deforestation. Both schemes are under the United Nations Framework Convention on Climate Change (UNFCCC).

Currently, developing nations can benefit financially by trading what are known as *carbon credits*, which refer to the amount of carbon stored in the forests of a particular country. This practice is known as *carbon trading*. Under REDD+, for a nation to be eligible for financial benefits its carbon credits needs to be scientifically verifiable (Corbera and Schroeder, 2011). This requirement has been a driving factor for the development of biomass estimation methods from remote sensing technologies, particularly LiDAR (see e.g., Goetz and Dubayah, 2011; Avtar et al., 2013). A few examples of these methods follow.

Estornell et al. (2011) studied the effect of LiDAR point density on the accuracy of shrub biomass estimation in a Mediterranean ecosystem, which is characterized by evergreen or drought deciduous shrublands. LiDAR densities ranging from 2 to 16 points/m^2 were tested. It was found that good estimates of shrub biomass ($R^2 = 0.73$) were obtained with LiDAR densities of upwards of 8 pulses/m^2. The good estimate of shrub biomass found was due to a small DTM error thanks to the high LiDAR density used in the (see Section 4.1).

In another study, Clark et al. (2011) used small-footprint LiDAR and hyperspectral sensors to estimate AGB in a tropical rain forest in Costa Rica. The study used single- and two-variable linear regression analyses to relate LiDAR and hyperspectral metrics to the AGB of plantation, managed parkland and old-growth forest plots. Results of the study showed that using all biomass sample plots (83) and two LiDAR metrics (plot level mean height and maximum height) the best model obtained had: $R^2 = 0.90$ and RMSE $= 38.3$ Mg/ha. When the analysis was constrained to plantation plots, which had the most accurate data, R^2 increased to 0.96 and RMSE dropped to 10.8 Mg/ha. Furthermore, the findings of this study showed that LiDAR metrics are superior in estimating biomass compared to hyperspectral metrics.

In other studies LiDAR has been used together with other remote sensing data for different purposes. Pflugmacher et al. (2014) used both LiDAR and Landsat time series data to map forest biomass dynamics in a mixed-conifer region. In this study, LiDAR was used to create high-resolution AGB maps of the area and the LiDAR-derived AGB was used for training Landsat-based models and for error assessment. Saarela et al. (2015) studied the use of LiDAR and Landsat data as auxiliary data in field-based model-assisted forest inventories in a middle-aged Scots pine boreal forest. Results of this study showed that the use of wall-to-wall Landsat data and LiDAR strip samples as auxiliary data gave very precise results were obtained in estimating growing stock volume compared to the use of LiDAR auxiliary data alone.

3.3.2 Forest Fire Behavior Modeling

Understanding the behavior of forest fires is critical for fire managers in order for them to be in a better position to make informed decisions concerning e.g., resource allocation, fire mitigation plans, and post-fire recovery. There has been an increasing trend in both the frequency and the extent of burned forest area over the past decade (Riebau and Qu, 2005); the main drivers for this trend being extreme drought and accumulation of fuel loads (see e.g., Pausas et al., 2008; Collins et al., 2013; San-Miguel-Ayanz et al., 2013; Montealegre et al., 2014).

For example, the frequency of forest fires in the European area is estimated at 65,000 fires per year and the burned forest area is estimated to be 500,000 ha (San-Miguel-Ayanz et al., 2013). About 85% of these fires take place in the Mediterranean region (Greece, Spain, and Portugal) (European Commission, 2004, 2006; Pausas et al., 2008; San-Miguel-Ayanz et al., 2013; Collins et al., 2013).

Forest fires have a number of consequences. For example, it is not uncommon for forest fires to be associated with human casualties (e.g., loss of life) and loss of property. Forest fires also have financial implications—budget for fire fighting and post-fire recovery. For example, in 2003 21 people lost their lives as a result of large forest fires that took place in the districts of Castelo Branco, Portalegre, and Santerm in Portugal, with damages estimated at 1 billion euros (European Commission, 2004, 2006).

Following the consequences of forest fires, fire managers need accurate and timely information that will enable them to (1) minimize the risks of forest fires happening and; (2) be able to predict the behavior of forest fires when they break out.

To minimize the risk of forest fires, managers rely on fuel management practices (e.g., thinning and prescribed fires) to control the amount of fuel available in forest stands (Agee and Skinner, 2005). If there is less fuel to burn, both the intensity of the fire and its rate of spread will be substantially minimized (Peterson et al., 2003; Graham et al., 2004). In order to organize and conduct fuel management practices, managers need to have information about the spatial distribution of fuels in

a particular area (Arroyo et al., 2008). In addition, fire simulation models such as FARSITE (Finney, 2004), which combine spatial and temporal information on topography, fuels, and weather, and combine existing models for surface fire and crown fire etc., are invaluable to fire managers as they can greatly help to simulate the behavior of fires (e.g., intensity and rate of spread) and help fire managers to plan for fire suppression and mitigation.

Modeling the behavior of forest fires requires a good knowledge of critical fuel metrics, namely canopy base height (CBH), canopy height (CH), and canopy bulk density (CBD) (Riaño et al., 2003; Andersen et al., 2005; Agca et al., 2011). CBD refers to the amount of fuel per unit volume (measured in kg/m^3). CH is the highest height at which the canopy fuel density is greater than a critical threshold (normally 0.011 kg/m^3), and CBH refers to the lowest height at which canopy bulk density exceeds a threshold of 0.011 kg/m^3 (Andersen et al., 2005).

Of the three fuel metrics, CBH is special in that it plays an important role in crown fire initiation (Jain and Graham, 2007; Agca et al., 2011). Crown fires are of special interest because they burn much faster than surface fires; they burn more severely and with larger flames, making them more destructive and difficult to control; and they can occur in a variety of forest types (Rothermel, 1983; Cohen and Butler, 1998). However, depending on the situation, there are other more important parameters that can play part in crown fire initiation. These parameters include ladder fuels (e.g., small trees, lichens, and shrubs) and the fuel strata gap (the distance between the surface and canopy fuels) (Gajardo et al., 2014). The latter, despite being less commonly used in fire modeling, represents a more realistic measure of the risk of crown fires as it represents the physical distance separating the two fuel layers.

Authors have been describing CBH in slightly different ways depending on the situation at hand (Gajardo et al., 2014). When viewed as the distance from the ground to the crown base, an accurate CBH is a good indicator of various stand characteristics including tree growth, forest health, and timber quality (Vauhkonen, 2010; Maltamo et al., 2010).

LiDAR has proven to be robust and accurate in modeling forest fire fuel metrics, particularly CBH (see e.g., Andersen et al., 2005; Hudak et al., 2009; Lemmens, 2011a). Later in this thesis (Chapter 5) a review of methods for CBH estimation from LiDAR will be given and a case study of a method developed in this thesis will be presented.

3.4 Forestry Applications of LiDAR

The LiDAR-derived and derived parameters discussed below are normally used in high level forestry applications. This section discusses two examples of applications namely forest inventory and change detection.

3.4.1 Forest Inventory

Forest inventory refers to the systematic collection and analysis of forest data to obtain valuable information about a forest (Köhl et al., 2006, pp. 1–11). This information includes, for example, number of trees per hectare, species composition, basal area, and stem volume. This information is normally derived by measuring tree variables such as DBH, height, and species of tally and sample trees, which are given varying probabilities of being included in samples that represent the underlying tree population and the dependencies between tree variables.

Forest inventory has been evolving over the years with respect to the type of information and how the information is collected. For example, in the USA the process has evolved from mainly timber-focused inventory in the 50s through the 60s to multiresource inventory covering as diverse areas as non-forest lands, habitats, old growth and primary forests ecosystems, biodiversity, and non-wood goods and services (NWGS) (Lund and Smith, 1997; Köhl et al., 2006, pp. 277).

LiDAR has shown success in forest inventory, especially at large scales involving millions of square kilometers (see e.g., Næsset, 2004a; McRoberts et al., 2010b; Wulder et al., 2012). The use of remote sensing technologies, and LiDAR in particular, has enhanced inventory sampling and estimation over very larger areas; National Forest Inventories (NFIs) are a good example of this. Variables of great interest in NFIs for which population parameters are estimated are forest area and growing stock volume (Tomppo et al., 2010, pp. 19–32). Remote sensing has also facilitated the construction and assessment of forest attribute maps and related spatial products (McRoberts et al., 2010a).

Næsset (2004b), for example, used LiDAR to estimate inventory parameters including basal area, stem number, and timber volume for 116 georeferenced field sample plots in 5000 ha of forest consisting of mainly Norway spruce, Scots pine, and deciduous species using regression analysis. Regression analysis was used to create stratum-specific relationships between field measurements and LiDAR. Inventory variables were regressed against predictor variables derived from LiDAR's distributions of first and last returns (mean values, coefficient of variation, and height deciles).

3.4.2 Detection and Estimation of Forest Dynamics

Forests change over time due to factors such as growth and deforestation/forest degradation. Over time, trees increase in height due to growth while at the same time disturbances such as over-harvesting, forest fires, pests, and climatic events such as drought cause changes in tree height and cover (Riebau and Qu, 2005; Herold et al., 2011).

Several studies have addressed the problem of detecting height changes in forests. What is common in most of these studies is the use of digital elevation models (DEMs) as a means to detect height changes. For example, Avtar and Sawada (2012) used the shuttle radar topography mission digital elevation model (SRTM-DEM) and the advanced space-borne thermal emission and reflection radiometer global digital elevation model (ASTER-GDEM) together with the panchromatic remote sensing instrument for stereo mapping digital surface model (PRISM-DSM) to monitor height changes due to deforestation in Cambodia. This study showed that the method used was cost effective but is not accurate—vertical accuracy of 7–20 m.

With its 3-D accuracy, LiDAR has a great potential for applications in change detection. Elevation models and surface models derived from LiDAR are far more accurate compared to the global digital elevation models such as SRTM and ASTER. When LiDAR is captured with high enough density even the growth of individual tree crowns can be monitored. The study conducted by Reutebuch et al. (2005), for example, illustrates how multitemporal LiDAR can be used to accurately monitor changes of individual trees over time.

However, with new developments in technology, such as the advent of the synthetic aperture radar (SAR)-based TanDEM-X (Huber et al., 2010), the accuracy of global DEMs will continue to improve (see e.g., Rizzoli et al., 2012). Moreover, high-resolution satellite stereo imagery can provide precise DSMs if ground control points are used (see e.g., Aguilar et al., 2013).

3.5 Case study: Use of Different Field Plot Designs For Biomass Estimation

Involving local communities in sustainable forest preservation/monitoring (participatory forest monitoring) has several potential benefits including bringing about a sense of ownership and thus increasing the chance of success of forest monitoring measures. However, skeptics of this approach argue that local-community forest preservation teams can not easily attain the level of technical proficiency required for accurate forest monitoring.

Participatory forest monitoring has a great potential in schemes like REDD+, especially in places where community forests are involved. A good example of this is Nepal. With support from the Norwegian Agency for Development Cooperation (NORAD), the International Center for Integrated Mountain Development (ICIMOD) partnered with the Federation of Community Forestry Users Nepal (FECOFUN) and the Asia Network for Sustainable Agriculture and Bioresources (ANSAB) implemented a project titled

> Design and setting up of a governance and payment system for Nepal's community forest management under reduced emissions from deforestation and forest degradation REDD

The aim of the project was to develop and demonstrate an innovative benefit sharing mechanism for REDD+ incentives using institutionally and socially inclusive approaches to address the drivers of deforestation and forest degradation and improve forest governance in three watersheds in Nepal namely, Kayarkhola, Ludikhola, and Charnawati in Chitwan, Gorkha, and Dolakha districts, respectively. This is one of the first carbon offset demonstration projects in the world that involved local communities in monitoring the carbon in their forests after providing the necessary training to do the job.

3.5.1 Motivation

The motivation behind this study (see publication IV) was to assess the robustness of model-based high-resolution prediction of forest biomass against different field plot designs. Two field plot designs, namely the field plot data collected by local community (Comm.) forest teams, and field plot data collected by professional forest teams (Prof.) are compared for use in model-based biomass estimation, the main questions of interest (hypotheses) being if the two sets of field plot data can give similar results (thus supporting the argument that participatory forest monitoring is viable) and whether the two data sets can be combined and used together in model building (thus improving model robustness). Even though the two data sets were collected in the same area, the data sets are expected to have different characteristics because they were collected by two different teams that operated independently and had different levels of expertise.

For the purpose of this study, AGB was estimated using linear models based on the Bayesian truncated Singular Value Decomposition (BtSVD) proposed by Junttila et al. (2015). BtSVD uses the singular value decomposition (SVD) of normalized predictors and allows a bigger deviation from zero to the regression parameters of the orthonormalized predictors, which are known to explain the original predictor variability the most (have the biggest singular values).

3.5.2 Results

AGB prediction results using BtSVD and different combinations of training/validation sets are shown in Figures 3.4 and 3.5. In Figures 3.4 and 3.5: the solid line represents a 1:1 relationship while the dashed line represents model trend; the values of RMSE are based on leave-one-out cross-validation (LOOCV) using validation sets indicated on the title of each sub-figure; and D is the difference in distribution means of field estimates and predicted AGB values.

3.5.3 Conclusion

Results of this study showed that in one of the test sites, Gorkha, the different field sample plot data produced equivalent regression models. In the other site (Chitwan) discrepancies between the models were observed using the different field sample plot data. This discrepancy can be attributed to the complex nature of the terrain and dense forest in Chitwan which makes it difficult to obtain accurate DTMs (see Section 4.6). Overall, this study showed that field plot data gathered by different teams, i.e., professional forest teams and community forest teams can be used together for model-based biomass estimation without affecting prediction performance, provided that there is good correlation between LiDAR and field measurements (see Figure 3.6).

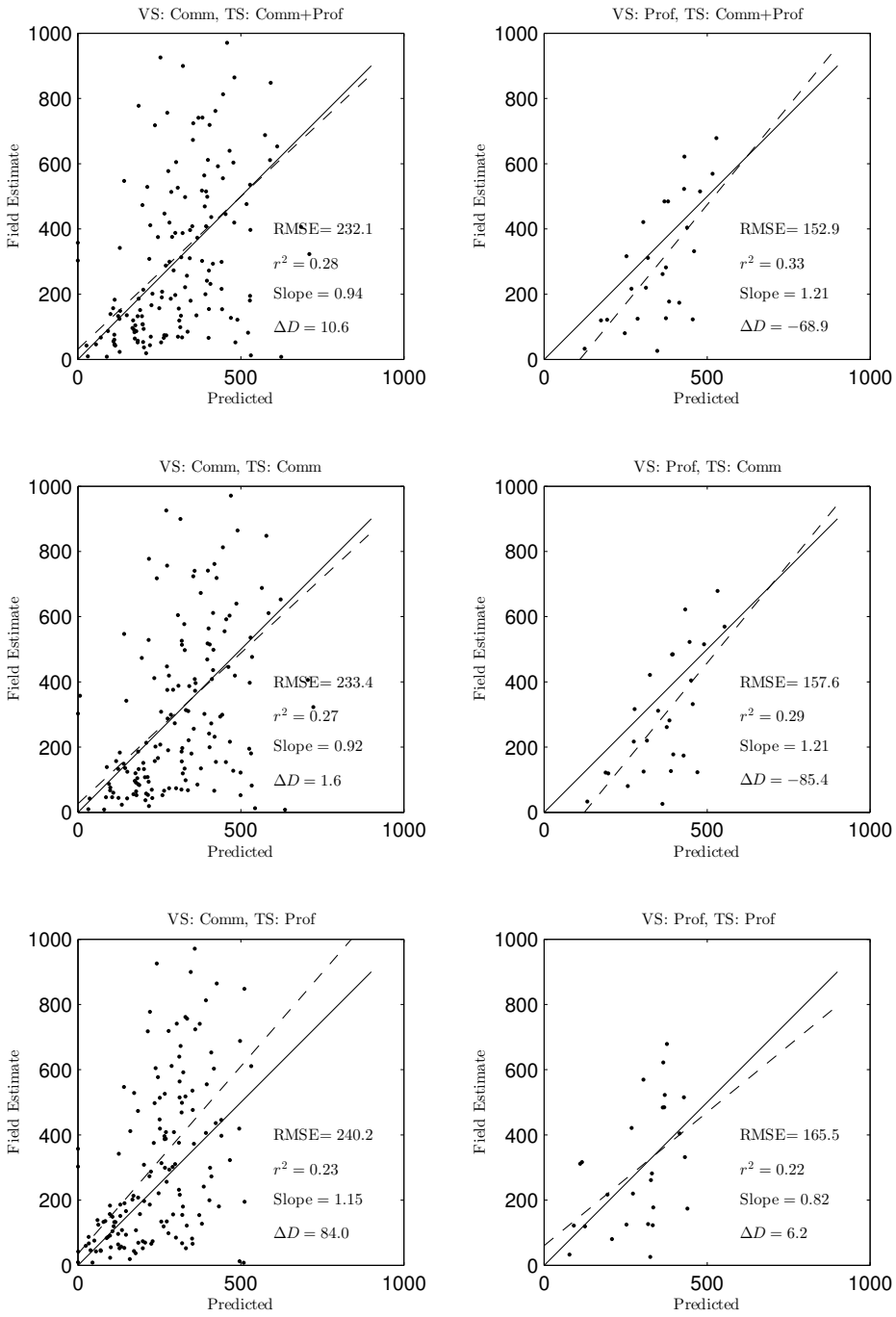

Figure 3.4: Biomass prediction scatterogram and validation results for Chitwan. VS= validation set, TS=training set, and ΔD = mean difference.

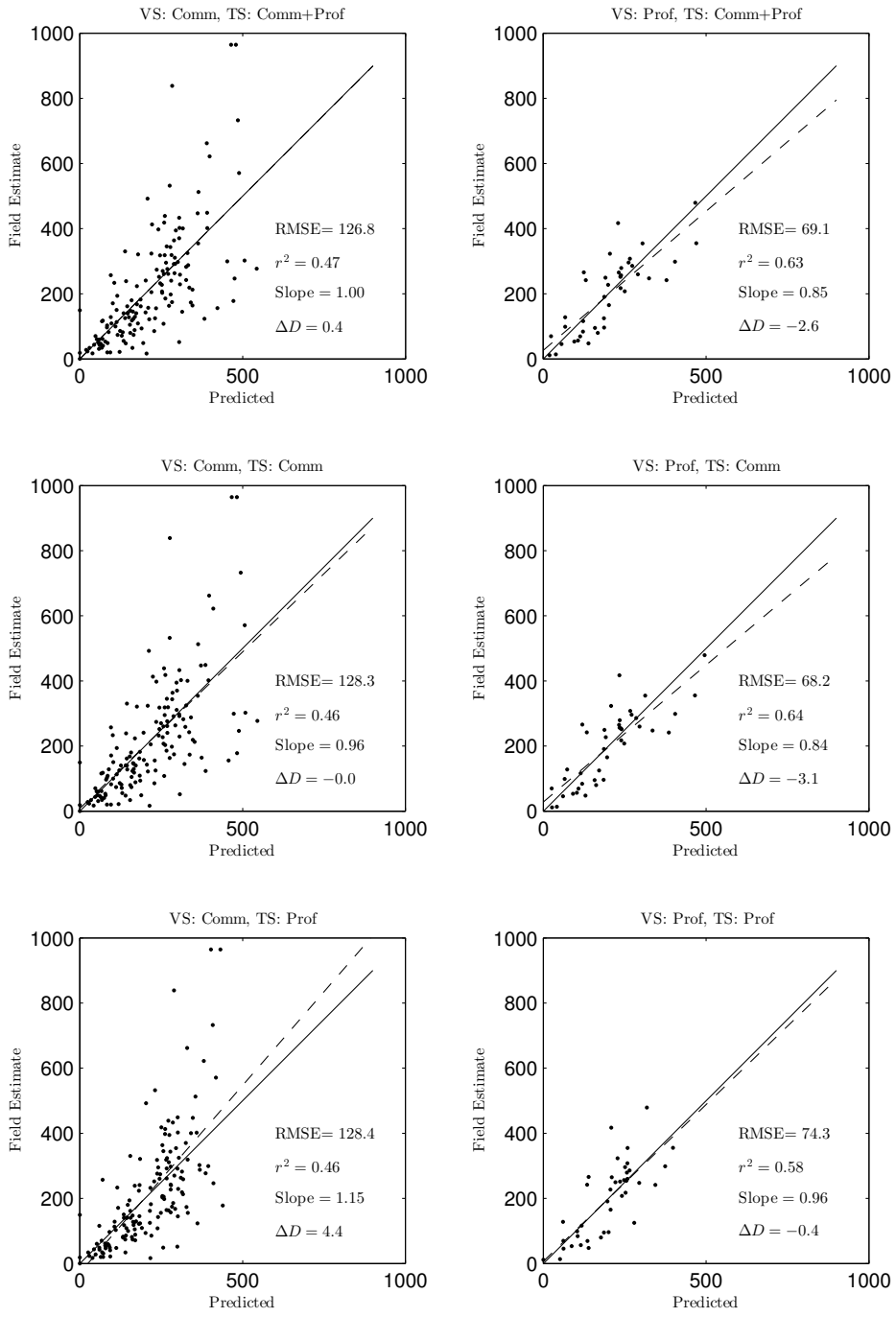

Figure 3.5: Biomass prediction scatterogram and validation results for Gorkha. VS = validation set, TS = training set, and ΔD = mean difference.

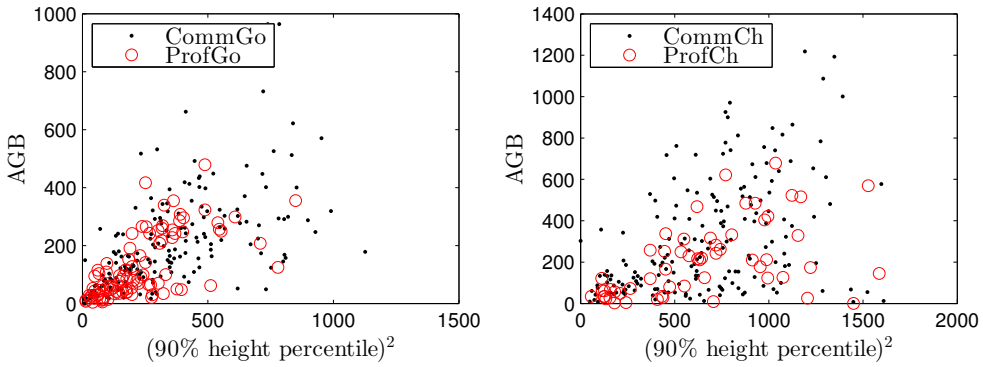

Figure 3.6: Scatterograms of field-estimated AGB against a LiDAR predictor for the two study sites. Notice the poor correlation in the Chitwan case (right). CommGo = Community Gorkha, ProfGo = Professional Gorkha, CommCh = Community Chitwan, and ProfCh = Professional Chiwan.

CHAPTER IV

Methods for DTM Extraction From LiDAR

This chapter begins by discussing the role of the DTM in estimating various structural forest parameters (Section 4.1), followed by a detailed discussion of the process of extracting DTMs from LiDAR. First, an overview of DTM extraction from LiDAR is given in Section 4.2 followed by a discussion of ground filtering and DTM interpolation methods in Section 4.3 and Section 4.4, respectively. Section 4.5 discusses the methods of representing DTMs and their pros and cons. The next two sections (Section 4.6 and Section 4.7) discuss the sources and quantification of errors in DTMs and challenges in DTM extraction from LiDAR, respectively. Section 4.8 summarizes the contents of publication I and publication II.

4.1 The Role of the DTM

In Section 3.1 it was pointed out that estimating structural forest parameters makes use of LiDAR metrics, which are based on LiDAR heights. Since LiDAR point clouds consist of points that represent elevation (the z-coordinates), they must be normalized to represent height from the ground before any metrics are derived from them. To normalize a point cloud, a DTM is used (see e.g., Clark et al., 2004; Estornell et al., 2011). A DTM is a representation of the ground surface which is generated from ground points in the point cloud (see Chapter 4 for details on DTM extraction from LiDAR).

An accurate DTM is therefore critical when estimating structural forest parameters. Errors in the DTM are easily propagated to estimated forest structural parameters. For example, tree height is directly affected by errors in the DTM; as was mentioned in Section 3.2.1, tree height is a fundamental input to many models used to estimate other structural forest parameter, therefore errors in tree height estimation are easily propagated to derived parameters whose estimation depend on tree height. As will be seen in Chapter 5, DTM errors are more pronounced in steep/complex terrain and thick canopy cover. In these conditions, a reliable DTM becomes indispensable to ensure the accuracy of estimated structural forest parameters. Tinkham et al. (2012), for example, investigated the influence of LiDAR-derived DTM errors on derived forest inventories (timber volume) in central Idaho (USA) and found that with steep slopes (>30°) the error in timber volume approached 3% while with gentle slopes the error did not exceed 1%.

4.2 Overview of DTM Extraction

DTM extraction from LiDAR is generally a two-step process. The first step is called *ground filtering* and its purpose is to remove (filter) non-ground points (buildings, boulders, vegetation, etc.) from the LiDAR point cloud, leaving only ground points. The second step is called DTM *interpolation* and its purpose is to estimate the elevations of unsampled locations. Several algorithms have been proposed in the literature for both ground filtering and DTM interpolation; the following sections discuss these algorithms in detail.

4.3 Ground Filtering

A number of ground filtering algorithms (ground filters) have been proposed in the literature. These ground filters can be grouped into four main groups based on criteria used to distinguish between ground and non-ground points: (1) slope-based; (2) interpolation based; (3) mathematical morphology based; and (4) hybrid ground filters.

4.3.1 Slope-based Ground Filters

Slope-based ground filters assume the slope between two ground points is smaller compared to the slope between a ground point and a non-ground point. The idea behind this assumption is that non-ground points are from vegetation and therefore should be located above ground points in the point cloud. These filters operate by comparing the slope between two adjacent candidate points in the point cloud to a pre-determined threshold value; if the slope between the points is less than the threshold slope then the points are assumed to be ground points. If the slope between the points is greater than the threshold slope the point with a higher altitude value is considered a vegetation point.

Vosselman (2000) proposed a slope-based filter which performs filtering by comparing the height difference between two candidate ground points as a function of their distance apart against a given threshold value. For a point to be classified as a ground point, there must be no other point such that the height difference between the point and any other point—computed as a function of their distance apart—is larger than the threshold value.

The major limitation of slope based-filters is their inability to perform well in steep terrain (Sithole and Vosselman, 2004; Liu, 2008; Meng et al., 2010). The main reason for this limitation is the fact that in steep terrain the height difference—and therefore the slope—between two adjacent points can be higher than the height difference between a ground point and a vegetation point, leading to many legitimate ground points being rejected. Sithole (2001) proposed an adaptive slope-based filter in which the threshold varies with respect to terrain slope. With this modification, ground points in steep terrain are not rejected.

4.3.2 Interpolation-based Ground Filters

Unlike slope-based ground filters, which work with two adjacent points at a time, interpolation based ground filters operate on all the points in the point cloud at once. These filters work by iteratively fitting a single large parametric surface to the data and filtering points based on their residuals with respect to the fitted surface. By eliminating points with higher residuals the quality of fit improves

and the surface gets closer and closer to the true ground points. One way of selecting points to eliminate in each iteration is to give each point a weight which is based on its residual relative to the surface; points with negative residuals are below the surface and hence are more likely to be ground points. These points are assigned bigger weights in the following iterations and vice versa.

A good example of an interpolation based ground filter is that proposed by Kraus and Pfeifer (1998)[1]. The algorithm proposed in this study is based on linear prediction with individual accuracy for each measurement (z-value). In the first iteration of the algorithm, an average surface is fitted in the data and all measurements are assigned equal weights. Based on their position relative to the surface, ground points are likely to have negative residuals while vegetation points are likely to have positive or small negative residuals. Residuals for each point are used to compute corresponding weights p_i using the following weight function

$$p_i = \begin{cases} 1 & v_i \leq g \\ \frac{1}{1+(a(v_i-g)^b)} & g < v_i \leq g+w \\ 0 & g+w < v_i \end{cases} \tag{4.1}$$

where v_i are the residuals; a and b are parameters which control the steepness of the weight function (in this study the values of a and b were set to 1 and 4, respectively); g is a shift value (less than zero for LiDAR) whereby all points with residuals less than it are assigned a maximum weight of one; w is an offset from g whereby points with large positive residuals ($p_i > g + w$) are assigned zero weight (see Kraus and Pfeifer, 1998).

Interpolation-based filters, like slope-based filters, do not perform well in steep and complex terrain. However, modifications or additions to the concept of interpolation-based filters show improvements in performance. Mongus and üZalik (2012), for example, proposed an algorithm which is based on thin plate spine interpolation. This algorithm performs better in steep and complex terrain compared to traditional interpolation-based ground filters.

4.3.3 Mathematical-Morphology-based Ground Filters

Unlike slope-based and interpolation-based ground filters, mathematical-morphology-based ground filters are based on the the concept of mathematical morphology commonly used to analyze digital images (see e.g., Haralick et al. (1987)). As a result, these ground filters do not operate on the LiDAR point cloud directly, instead the point cloud has to be transformed into a digital image first. Thereafter, filtering is performed using morphological operations such as *opening* and *closing* (Zhang et al., 2003; Chen et al., 2007).

The main advantage of mathematical-morphology-based ground filters is their simplicity and ease of implementation. These ground filters are suited for filtering surface objects such as buildings. However, mathematical-morphology-based filters perform poorly with low numbers of ground points in the point cloud, especially in steep forested terrain (Sithole and Vosselman, 2004; Liu, 2008; Meng et al., 2010).

[1]This algorithm has been implemented in the FUSION LiDAR processing software which has been used for some of the experiments in this thesis. See `http://forsys.cfr.washington.edu/fusion/fusionlatest.html` for details about this software.

4.3.4 Hybrid Ground Filters

Other ground filters proposed in the literature do not fall perfectly into any of the categories of ground filters discussed above. These ground filters either use a completely different filtering strategy or they combine the functionality of two or more existing ground filters in some way to come up with an improved filtering strategy. Also, some of these ground filters combine ground filtering and DTM interpolation in one algorithm. Maguya et al. (2013), for example, proposed an adaptive, hybrid ground filter which makes use of trend surfaces for ground filtering. Unlike other trend-surface-based ground filters which make use of weights as a basis for rejecting non-ground points, this ground filter rejects non-ground points based on their influence on the goodness of fit (R^2) of the trend surface. Moreover, unlike other trend-surface-based ground filters which fit one trend surface to the entire point cloud, this ground filter fits smaller surfaces (tiles) repeatedly until all of the point cloud is processed. This approach has the advantage that it helps to cope (adapt) with variations in the terrain.

In another example, Kobler et al. (2006) proposed a two-stage ground filter which makes use of existing ground filters (e.g., mathematical-morphology-based and slope-based filters) in the first stage of filtering. In the second stage of the algorithm, DTM interpolation is performed to estimate the elevations of unsampled locations.

4.4 DTM Interpolation

With the exception of mathematical-morphology-based ground filters, ground filters produce points which are randomly distributed. To produce a digital elevation model (DEM) (see Section 4.5) with regularly spaced points, elevations at unsampled locations of the terrain must be estimated using some spatial interpolation algorithm. Examples of common spatial interpolation algorithms (hereafter simply referred to as interpolation algorithm) used for DEM interpolation include inverse distance weighting (IDW), Kriging, and TIN interpolation (Caruso and Quarta, 1998; Mitas and Mitasova, 1999; Li and Heap, 2011).

Interpolation algorithms can be categorized as: (1) exact/inexact; (2) deterministic/schocastic; and (3) local/global (Ali, 2004). Exact interpolation algorithms produce a surface which pass through all the data points while inexact (approximative) interpolation algorithms produce surfaces which do not pass through every original data point but only follow the general trend in the data. Deterministic interpolation algorithms assume every data point has influence when estimating the value of unsampled locations. The influence of each point is inversely proportional to the distance between the point and the point with unsampled value. Stochastic interpolation algorithms, on the other hand, make use of geostatistics to estimate a surface with a certain level of uncertainty. Local interpolation algorithms use only neighboring data points to estimate values at unsampled locations while global interpolation algorithms use all the sampled points to estimate the values at unsampled locations. Table 4.1 lists examples of interpolation algorithms and their classifications.

Following are brief descriptions of the interpolation algorithms commonly used for DEM interpolation (Li and Heap, 2011).

4.4.1 Inverse Distance Weighting (IDW)

Inverse distance weighting estimates the unknown elevation values by using a weighted average of the elevation values of sampled points within a given search radius, or from a given number

Table 4.1: examples of interpolation algorithms and their classifications.

	Classification					
Algorithm	*Exact*	*Inexact*	*Deterministic*	*Schocastic*	*Local*	*Global*
IDW	•		•		•	
Kriging		•		•		•
Splines	•		•		•	
TIN	•		•		•	

of closest points (normally 10–30 points) (Mitas and Mitasova, 1999). Weights used are normally inversely proportional to a power of their distance from the unsampled point. For an unsampled location $\mathbf{r}$ the IDW estimate is given by

$$f(\mathbf{r}) = \sum_{i=1}^{n} w_i f(\mathbf{r}_i) = \frac{\sum_{i=1}^{n} f(\mathbf{r}_i)/|\mathbf{r} - \mathbf{r}_i|^p}{\sum_{i=1}^{n} 1/|\mathbf{r} - \mathbf{r}_i|^p} \tag{4.2}$$

where p (typically $p = 2$) is a parameter and n is the number of neighboring points. Although IDW is easy to understand and implement, the method does not reproduce well the local shape inherent in the data points and tends to produce local extrema at the data points (Lu and Wong, 2008). IDW works well with dense and evenly distributed data (Liu and Mason, 2009). Figure 4.2 shows an example of a raster DEM interpolated from a set of irregularly spaced ground points.

4.4.2 Kriging

Kriging is a geostatistical method for interpolation which is based on the concept of random functions (Mitas and Mitasova, 1999). The surface to be estimated is assumed to be one realization of a random function with a certain spatial covariance. The interpolated surface is constructed using statistical conditions of unbiasedness and minimum variance, hence the Kriging estimate is the best linear unbiased estimate (BLUE). All forms of Kriging are based on the following relationship

$$f(\mathbf{r}) = \mu(\mathbf{r}) + \varepsilon(\mathbf{r}) \tag{4.3}$$

where f represents the predicted surface, μ is the deterministic mean or trend of the data, and ε is the spatially autocorrelated error associated with the prediction (Liu and Mason, 2009).

Kriging exists in many forms that are suited for different applications, the most common form is known as ordinary Kriging (OK). OK assumes there is no trend in the data, i.e., a constant unknown mean at all locations and that the data values are spatially autocorrelated about the mean (Liu and Mason, 2009). Unlike IDW, Kriging is not easy to understand but it offers attractive features such as error estimates and confidence intervals for the estimated points (Lam, 1983).

4.5 DTM Representation

After ground filtering and DTM interpolation the resulting points have to be represented in a special form (structure) such that the spatial proximity and spatial relationship between the points can be determined either implicitly or explicitly. When this happens the resulting structure is referred to

as a DEM. DEMs are normally represented using three main forms, namely triangular irregular networks (TINs), raster (grid) form[2], and mathematically.

4.5.1 Triangular Irregular Networks

A TIN is a structure used to represent a surface in which sample points are connected by line segments to form a network of triangles. These triangles are represented by planes to form a continuous representation of a surface (Ali and Mehrabian, 2009). Many algorithms exist for creating TINs from a sample of points (e.g., LiDAR ground points) but the most commonly used one is the Delaunay (see e.g., Guibas et al., 1992) triangulation which has some favorable geometric properties (e.g., geometrical constraints that tend to avoid skinny triangles) (Fowler and Little, 1979). Figure 4.1 shows an example of a TIN model formed from a set of irregularly spaced ground points.

Since no comprehensive analysis framework for analyzing TINs exists, not much information can be derived from TINs. As a result, TIN models are mostly used for visualization purposes only (Ali and Mehrabian, 2009).

4.5.2 Raster Models

Unlike TIN models, raster models represent DTMs in a regular grid and are therefore not continuous in nature (Ali and Mehrabian, 2009). A raster represents only a selected number of locations sampled at regular intervals, forming a grid of cells in which both, the spatial proximity and the spatial relationship between the cells of the grid can easily be determined. The raster format is a common form of representing terrain data due to its simplicity and suitability for a variety of analyses that may need to be performed on the data (see e.g., Guan and Clarke, 2010). Figure 4.2 shows an example of a raster model formed from a set of irregularly spaced ground points. Rasters are commonly stored using the tagged image file format (TIFF) with georeferencing information embedded into the file (the GeoTIFF file format) (see `http://trac.osgeo.org/geotiff`). The TIFF format has several interesting features, including support for data compression and tiling.

For a given dataset and DEM interpolation method, the accuracy and suitability of rasters for different applications depend on their spatial resolution (cell size); the smaller the cell size the more accurate the raster is and vice versa. The resolution of a raster DEM can vary from a few meters (e.g., DEMs derived from LiDAR) to several tens of meters (e.g., DEMs covering very large geographical areas such as the GDEM).

4.5.3 Mathematical DTM Representation

To represent a DTM mathematically, a function (surface) is constructed from the known sample points and the elevations of unsampled points are interpolated by evaluating the function at those locations (Li et al., 2005). Representation can be achieved by using a single function which covers the entire area and is constructed from all the data points (global), or it can be done locally by using functions that cover smaller areas that are constructed using a subset of the data points. The global approach is used when the terrain is simple while the local approach is used when the terrain

[2]There is no clear distinction between the abbreviations DTM and DEM in the literature; sometimes the terms are used as synonyms while in other occasions they have distinct meanings. See e.g., `http://www.usgs.gov/faq/node/5071` for more information.

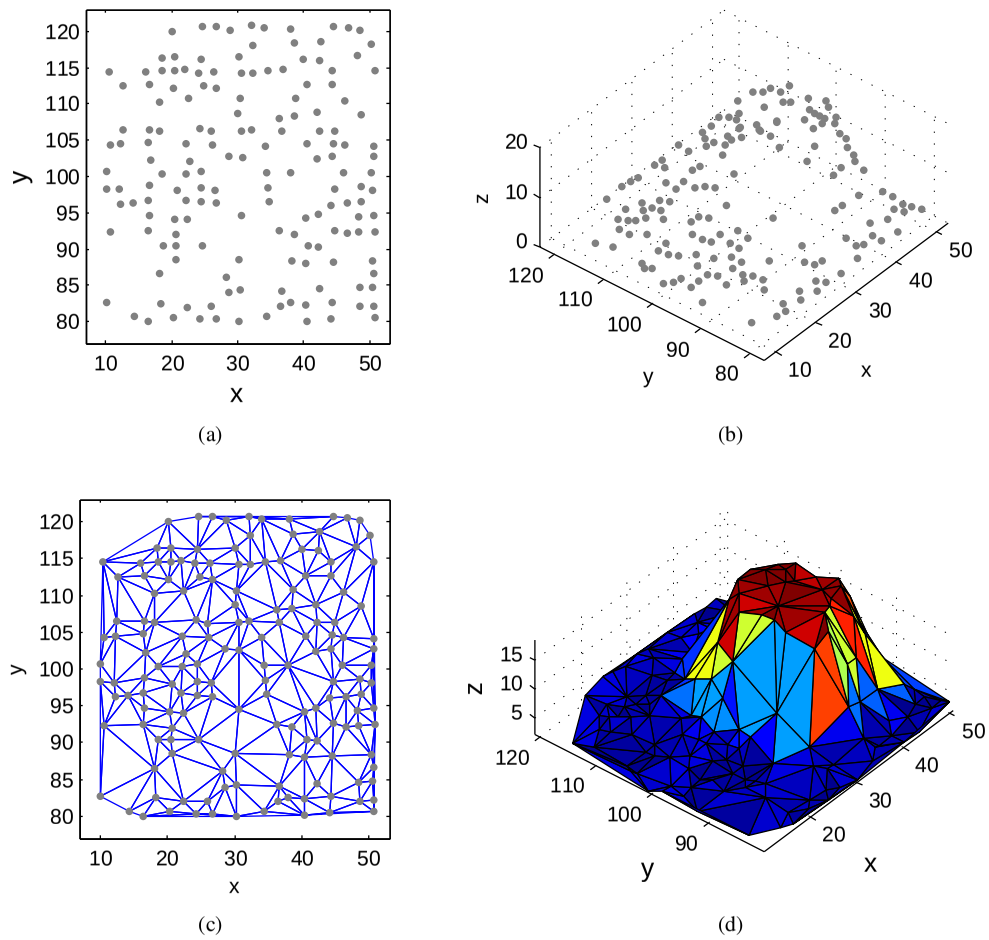

Figure 4.1: Creating a TIN from ground points: (a) Plan view of the original, randomly distributed ground points; (b) 3-D view of the points in (a); (c) Plan view of a TIN created from the points in (a); (d) 3-D view of the TIN in (c).

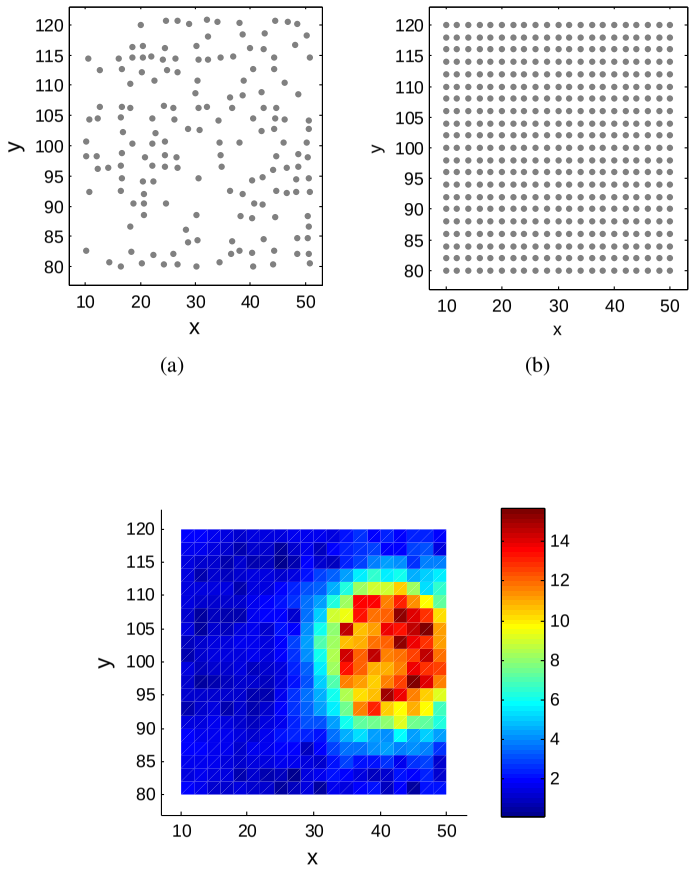

Figure 4.2: Creating a raster DEM from randomly distributed ground points: (a) Plan view of the original, randomly distributed ground points; (b) Plan view of points obtained using IDW interpolation on a regular grid with the points in (a); (c) A raster DEM with a resolution of 2 m created using the points in (b).

is complex. Examples of functions which can be used for the former include Fourier series and polynomials while examples of functions which can be used for the former include regular and irregular patchwise functions (Li et al., 2005).

The choice of a mathematical function to use depends on the complexity of the terrain and the required smoothness of the resulting surface. If the terrain is simple and smoothness is not a requirement, exact bilinear interpolation can be used which takes the form

$$f(x, y) = a_0 + a_1 x + a_2 y + a_3 xy \tag{4.4}$$

where a_0, a_1, a_2, and a_3 are unknown coefficients which have to be determined from a system of four linear equations using four reference points using the following equation

$$\begin{bmatrix} a_0 \\ a_1 \\ a_2 \\ a_3 \end{bmatrix} = \begin{bmatrix} 1 & x_1 & y_1 & x_1 y_1 \\ 1 & x_2 & y_2 & x_2 y_2 \\ 1 & x_3 & y_3 & x_3 y_3 \\ 1 & x_4 & y_4 & x_4 y_4 \end{bmatrix}^{-1} \begin{bmatrix} f(x_1, y_1) \\ f(x_2, y_2) \\ f(x_3, y_3) \\ f(x_4, y_4) \end{bmatrix}. \tag{4.5}$$

After the unknown coefficients have been determined the elevation of any location (x_i, y_i) is obtained by substituting (x_i, y_i) into Equation 4.6.

On the other hand, if the terrain is relatively complex or a smooth surface is required, bicubic exact interpolation can be used, which takes the form

$$\begin{aligned} f(x, y) &= \sum_{j=0}^{3} \sum_{i=0}^{3} a_{ij} x^i y^j \\ &= a_{00} + a_{10} x + a_{20} x^2 + a_{30} x^3 \\ &\quad + a_{01} y + a_{11} xy + a_{21} x^2 y + a_{31} x^3 y \\ &\quad + a_{02} y^2 + a_{12} xy^2 + a_{22} x^2 y^2 + a_{32} x^3 y^2 \\ &\quad + a_{03} y^3 + a_{13} xy^3 + a_{23} x^2 y^3 + a_{33} x^3 y^3 \end{aligned} \tag{4.6}$$

where a_{00}, a_{10}, $a_{20} \ldots a_{33}$ are sixteen coefficients to be determined. To determine these coefficients sixteen equations are needed—four equations formed from four sampled data points and twelve equations formed from conditions of connection between patches.

In the technique described above the function passes through all the data points (exact interpolation). If the terrain is very complicated or the data points contain errors it might not be possible to find a function that can pass through all the data points. In this case a function which best fits the data can be used to approximate the terrain surface. This can be done by using least squares fitting of local surfaces whereby a second order polynomial of the following form is used

$$f(x, y) = a_0 + a_1 x + a_2 y + a_3 xy + a_4 x^2 + a_5 y^2 \tag{4.7}$$

where a_0, $a_1 \ldots a_5$ are six coefficients which need to be determined from n sample points ($n > 6$) using the following system of linear equations

$$\begin{bmatrix} f(x_1, y_1) \\ f(x_2, y_2) \\ \vdots \\ f(x_n, y_n) \end{bmatrix} = \begin{bmatrix} 1 & x_1 & y_1 & x_1 y_1 & x_1^2 & y_1^2 \\ 1 & x_2 & y_2 & x_2 y_2 & x_2^2 & y_2^2 \\ \vdots & \vdots & \vdots & \vdots & \vdots & \vdots \\ 1 & x_n & y_n & x_n y_n & x_n^2 & y_n^2 \end{bmatrix} \begin{bmatrix} a_0 \\ a_1 \\ \vdots \\ a_5 \end{bmatrix}. \tag{4.8}$$

4.6 Sources and Quantification of Errors in DTMs

Although LiDAR has proven to be very accurate for DTM extraction, particularly for forestry applications, there are several factors that can cause errors in DTMs extracted from LiDAR. In this discussion, DTM errors refer to elevation errors, i.e., discrepancies between the elevation of points in the DTM and the elevation of actual ground points (ground truth)—vertical accuracy. Unlike errors present in traditional DTM generation methods such as ground surveys, which are mostly human-centered (Fisher and Tate, 2006), errors in DTMs extracted from LiDAR (and other remote sensing technologies) depend on three main factors (Gong et al., 2000): (1) the nature of data used for DTM interpolation; (2) the nature of the terrain in question; and (3) the nature of the DTM interpolation algorithm employed. These factors together with the quantification of error in DTMs are discussed next.

4.6.1 Nature of LiDAR Data

The nature of the data (accuracy, density, and distribution) used in generating a DTM has a direct impact on the accuracy of the resulting DTM. The accuracy of the LiDAR data is affected by two types of errors, namely systematic and random errors (Wei and Bartels, 2012). Systematic errors are due to the LiDAR equipment and its settings and are therefore reproducible. Random errors are due to gross errors, blunders, and random perturbations such as birds and low flying aircraft (Sithole and Vosselman, 2004).

The density and distribution of the LiDAR data also depend on equipment settings (scan parameters) as well as the nature of the vegetation covering the scanned area (see Section 4.7). Scan parameters such as point spacing, flying speed, and beam footprint size affect the density of the resulting data while the nature of the vegetation in the area under study affects the distribution of points.

Vertical DTM error can also be caused by planimetric errors (shifts) in the LiDAR point cloud (Liu and Mason, 2009; Höhle and Pedersen, 2010). If the LiDAR point cloud is affected by planimetric shifts, the resulting DTM is also going to be shifted by the same amount, resulting in vertical DTM errors. The effect of this shift on vertical DTM accuracy more evident in steep terrain. The main causes of planimetric errors include drifts in the INS, mechanical vibrations and oscillations on the scanning mirror, nature of terrain, and post processing of the data. In addition, scan zenith angle influences the ability of the laser beams to penetrate the canopy and reach the ground and its effect is coupled with vegetation geometry.

4.6.2 Nature of Terrain

The nature of the terrain (complexity) in the area under study has great influence on the accuracy of the resulting DTM (see Section 4.7). Errors in DTMs caused by the complexity of the terrain are the result of the inability of many ground filtering algorithms to perform well in complex terrain (steep and undulating) (see e.g., Hodgson and Bresnahan, 2004).

Terrain complexity can be deduced from the degree of similarity between terrain points in a given horizontal interval d (Li et al., 2005). Generally, the higher the degree of similarity between the points the simpler the terrain and vice versa. The degree of similarity in a DTM is normally expressed using either an auto-correlation function or the semivariogram. An auto-correlation function is given

by the following equation:

$$R(d) = \frac{Cov(d)}{V} \tag{4.9}$$

where $R(d)$ represents the correlation coefficient of all the terrain points falling in a horizontal distance d, $Cov(d)$ is the covariance of all the points in the same horizontal interval, and V represents the variance calculated from all the points in the interval. $Cov(d)$ and V are given by the following equations

$$Cov(d) = \frac{\sum_{i=1}^{N}(Z_i - M)(Z_{i+d} - M)}{N-1} \tag{4.10}$$

$$V = \frac{\sum_{i=1}^{N}(Z_i - M)^2}{N-1} \tag{4.11}$$

where Z_i represents the elevation of point i, Z_{i+d} is the elevation of the point at an interval d from point i, M is the average elevation of all the points, and N is the number of points in the interval.

The autocorrelation curve is normally represented by the exponential function as

$$Cov(d) = Ve^{-2d/c} \tag{4.12}$$

and the Gaussian model as

$$Cov(d) = Ve^{-2d^2/c^2} \tag{4.13}$$

where c is a parameter that represents the distance at which the value of the covariance approaches zero, i.e., the smaller the value of c the less similar are the terrain points (complex terrain) and vice versa (Li et al., 2005).

The simivariogram is given by

$$\gamma(d) = \frac{\sum_{i=1}^{N}(Z_i - Z_{i+d})^2}{2N} \tag{4.14}$$

where Z_i is the elevation of point i, Z_{i+d} is the elevation of the point at an interval d from point i, and N is the number of points in the interval. Like in the case of $R(d)$, values of $\gamma(d)$ can be plotted against d. The resulting curve can be approximated by the exponential function

$$\gamma(d) = Ad^b \tag{4.15}$$

where A and b are parameters describing terrain roughness with a large value of b indicating smooth terrain. This behavior can be explained by the fact that, unlike the auto-correlation function whose values tend to decrease with increasing values of d, the values of $\gamma(d)$ tend to increase with increasing values of d.

4.6.3 Nature of DTM Interpolation Algorithm

Interpolation algorithms differ in terms of how accurately they estimate the elevation of unsampled points as well as how well they preserve topographical features (see e.g., Smith et al., 2004; Chu et al., 2014). This is particularly true when the data used for interpolation is sparsely distributed; previous studies (e.g., Desmet, 1997; Chaplot et al., 2006) have shown that when the density of the data is high most interpolation algorithms give similar results (insignificant differences). For lower data densities, however, DTM accuracy is significantly influenced by the choice of an interpolation algorithm.

4.6.4 Quantification of Errors in DTMs

The role of the DTM in accurately estimating forest structural parameters was discussed in Chapter 3. It follows that the suitability of a DTM for this purpose should be based on how accurate the DTM is. The accuracy of a DTM is judged by the magnitude of error present in a given DTM, i.e., the discrepancies between the elevations reported by the DTM and the actual elevations (ground truth) of a set of control points whose elevations are known. The most common way of quantifying this error is the root mean square error (RMSE) (Fisher and Tate, 2006), which is given by

$$RMSE = \sqrt{\frac{\sum (Z_{DTM} - Z_{Ref})^2}{n}} \tag{4.16}$$

where Z_{DTM} is the DTM elevation value, Z_{Ref} is the reference elevation value (ground truth), and n is the number of control points. Different approaches exist for producing reference elevation values. Examples include ground surveying (Reutebuch et al., 2003; Stereńczak and Kozak, 2011); data partitioning, i.e., dividing the LiDAR ground points into prediction and validation sets (Bater and Coops, 2009); and using terrestrial laser scanning to generate a reference DTM (Heritage et al., 2009).

Since RMSE is calculated for an entire DTM based on a limited number of control points, it does not give a good picture of the statistical distribution of error in a DTM (Fisher and Tate, 2006). As a result, some authors have proposed alternative metrics to quantify errors in DTMs which give a good overall picture of the statistical distribution of errors (e.g., Fisher, 1998). These metrics are the mean error (ME) and the standard deviation of error (S) which are respectively given by

$$ME = \frac{\sum (Z_{DTM} - Z_{Ref})}{n} \tag{4.17}$$

and

$$S = \sqrt{\frac{\sum [(Z_{DTM} - Z_{Ref}) - ME]^2}{n-1}}. \tag{4.18}$$

ME can assume either negative or positive values and represents the under- or over-estimation of elevations in the DTM, i.e., bias. Thus, RMSE can be expressed as

$$RMSE = \sqrt{ME^2 + S^2} = \sqrt{bias^2 + S^2}. \tag{4.19}$$

It should be noted, however, in addition to the number of reference, the layout (pattern) of the reference points is also important in quantifying DTM errors. To assess DTM accuracy with higher sampling density stratification based on, for example, canopy height/closure or landform type can be used.

4.7 Challenges in DTM Extraction

Although LiDAR has proven to be an accurate and reliable technology for DTM extraction (especially in large forested areas) compared to other remote sensing technologies, several challenges face the process of extracting DTMs from LiDAR in forested areas. The major challenges, however, are canopy cover and terrain complexity.

To address these challenges, several algorithms have been developed specifically for extracting DTMs form LiDAR in forested terrain. These algorithms use different approaches to for ground filtering. The algorithm by Mongus and üZalik (2012) is based on thin plate spline surface interpolation. Thin plate spline interpolation is used in order to overcome the challenges posed by complex terrain and discontinuities in the data caused by presence of objects such as buildings and vegetation. The advantage of this algorithm is that it is parameter-free, i.e., no tuning of parameters to suit a specific area is required. Despite this fact test results showed that the algorithms works well in forested terrain and complex terrain. Kraus and Pfeifer (1998) proposed a similar algorithm that uses linear prediction. The algorithm starts by fitting an averaging surface to the data which is improved (approaches the true ground) iteratively. In each iteration vegetation points are removed based on their residuals from the surface (see Section 4.3.2). This algorithm works well in forested terrain but its performance tends to deteriorate with increasing canopy cover and terrain complexity.

In another example, Kobler et al. (2006) propose an algorithm for ground filtering in steep forested terrain. This algorithm is designed to perform well in heterogeneous forests where there is more variation in the number of ground returns per unit area. The algorithm filters LiDAR in two stages. In the first stage, the LiDAR is filtered using existing methods in order to remove outliers and non-ground points. The points obtained in the first stage are then used in the second stage to repetitively interpolate elevation samples at each DTM location to form a distribution of elevation estimates at each DTM location. The final elevation values for each DTM location are finally derived from these distributions. Test results showed that this algorithm performs well in steep and forested terrain with an RMSE value ranging between 0.16 and 0.37 m.

Finally, Axelsson (2000) proposed an algorithm for ground filtering based on TINs. Like most ground filters, this algorithm works in an iterative manner whereby initially a sparse TIN-based surface constructed from a set of seed points is fitted to the data from below. Next, the TIN surface is iteratively densified by adding more points that meet data-derived threshold parameters. This algorithm is capable of generating high resolution DEMs with mean elevation errors of as low as 0.05 m (on well defined surfaces).

These algorithms perform well with relatively high number of ground points which are obtained when flying heights are relatively low (typically 200–300 m AGL) due to improved penetration rate of LiDAR pulses (Takahashi et al., 2008). However, in large scale forestry applications (e.g., REDD+) flying at such low heights would be prohibitively expensive and therefore in such projects the flying height is normally higher (typically 1–2 km AGL) so as to cover as large areas as possible for the given budget without compromising the utility of the data for DTM extraction (particularly point

density) and estimation of various forest parameters (see e.g., Jakubowski et al. (2013) for the effect of LiDAR point density on estimation accuracy of various forest parameters). The following sections discuss the effect of canopy cover and terrain complexity in DTM extraction from LiDAR.

4.7.1 Effect of Canopy Cover

Extracting accurate DTMs relies on the availability of an adequate number of ground points; however, in forested terrain the number of ground points is often limited due to most of the laser pulses being blocked by the forest canopy. This is particularly true in tropical rain forests where the canopy is normally very thick and the understorey is more pronounced. These factors make it very difficult for laser pulses to penetrate the canopy and reach the ground, as a result very few pulses reach the ground. Moreover, this problem also affects the spatial distribution of ground points, i.e., in some places where the canopy is completely closed no ground hits will be recorded while in places where the canopy is partially open some ground hits will be recorded. This phenomenon adds complexity to DTM interpolation; under extreme conditions ground filters are fooled into classifying points from low-lying branches as ground points, leading to large DTM errors.

Takahashi et al. (2006) studied the penetration rate of small footprint laser pulses in closed canopy forest stands of middle-aged pure sugi and hinoki cypress in Japan. In this study it was found that in the middle-aged pure sugi only 1.1% of the transmitted pulses reached the ground while in the hinoki cypress only 8.1% of the transmitted pulses reached the ground. The effect of canopy cover is also seen in the study sites of publication II whereby the percentage of ground points diminishes with increasing canopy cover: Nepal (29.3%), Ghana (4.54%), and Brazil (2.2%).

In certain kinds of forests (e.g., managed forests), however, the canopy normally contains openings due to human activity through which laser pulses can pass and reach the ground. In these forests, DTMs of reasonable accuracy can be extracted using small footprint LiDAR and the DTM error is normally low (see e.g., Reutebuch et al., 2003; Hyyppä et al., 2005). Furthermore, the rate of penetration of laser pulses can be improved by adjusting some of the LiDAR acquisition parameters, e.g., flight altitude and scan angle (Hyyppä et al., 2005; Takahashi et al., 2008).

4.7.2 Effect of Terrain Complexity

Several studies (e.g., Gong et al., 2000; Hyyppä et al., 2005) have shown that terrain complexity has a significant impact on DTM extraction from LiDAR. Steep slopes, discontinuities, and undulating terrain are among the most difficult terrain features for both ground filters and DTM interpolation algorithms (Sithole and Vosselman, 2004; Maguya et al., 2014). Slope-based filters are the most vulnerable to terrain complexity; based on the way they operate, these filters tend to reject legitimate ground points on steep slopes. On the other hand, steep slopes also affect DTM interpolation—most DTM interpolation algorithms are based on the assumption that points closer to the point to be estimated (unknown elevation value) posses more information about the unknown point and are thus given more weight. However, on steep slopes even neighboring points can have big elevation differences.

Complex terrain, combined with canopy cover, has proven to be a very challenging combination for ground filters and DTM interpolation algorithms (Sithole and Vosselman, 2004). In publication II, the performance of three ground filtering algorithms is compared in three sites (Nepal, Ghana, and Brazil) which differ greatly in terms of canopy closure and terrain complexity. Results of the

publication show that the biggest DTM errors are observed in Nepal which has the highest percentage of ground points (more open canopy) but has the most complex terrain.

4.8 Case study: Novel Methods For DTM Extraction

This section summarizes the contents of publication I and publication II. It covers the motivation behind the proposed algorithm (Section 4.8.1), algorithm design (Section 4.8.2), algorithm design challenges (Section 4.8.3), and proposed solutions to address these algorithm design challenges (Section 4.8.4).

4.8.1 Motivation

The cost of LiDAR for large scale acquisition continues to fall; at the same time the rate at which LiDAR is being adopted as the tool of choice for estimating forest structural parameters is unprecedented (see Chapter 3). Despite these developments, the area of LiDAR processing is still facing many challenges (see Chapter 6), particularly DTM extraction in forested and complex terrain is one of these challenges and an important one.

Although many algorithms for DTM extraction from LiDAR have been proposed in the literature, they tend to be limited in scope, i.e., they can only be applied to certain types of terrain or LiDAR data with certain characteristics. For example, the flying altitude reported in most of the LiDAR-studies varies in the 200–500 m range. Flying altitudes in this range lead to good pulse penetration rates, and hence a good number of ground hits needed by many DTM interpolation algorithms is obtained. However, in large scale LiDAR applications (e.g., REDD+) flying at such low altitudes would be prohibitively expensive, this is why in such LiDAR applications flying altitudes of up to 2 km AGL are sometimes necessary to cover large areas and minimize cost (see e.g., publication I).

Flying at high altitudes helps to minimize cost but the data collected tends to contain limited ground hits because the rate of penetration of LiDAR pulses decreases with increasing flying altitude. Since many DTM interpolation algorithms were not designed to perform well with a limited number of ground points, they tend to perform poorly when applied to data collected in this way. Furthermore, covering large areas also increases the chances of encountering different kinds of terrain: from flat terrain which do not pose any challenges to ground filters to steep and undulating terrain which pose serious challenges to ground filters.

This study aimed at addressing these challenges by proposing an algorithm which can cope with a low number of ground hits and cope with variations in terrain (adaptability). The algorithm would be able to filter the point cloud for ground points and use the ground points to interpolate a DEM of reasonable which can be used for forestry applications.

4.8.2 Algorithm Design

The design of the algorithm for ground filtering and DTM interpolation had to address the two main issues mentioned above, i.e. complex terrain and limited number of ground points in LiDAR data, and produce an algorithm that will accomplish two goals, i.e., the algorithm should

(i) be able to perform well in different kinds of terrain as well as coping with terrain variations within the same site by adapting itself to accommodate those changes; and

(ii) perform reasonably well with a low number of ground points in LiDAR point clouds typical of high-altitude LiDAR acquisition missions.

To achieve the first goal, two design decisions were made. The first design decision was to view the terrain as being made up (consisting) of patches (tiles) of the same size which lie adjacent to one another. Using this approach even complex terrain can be broken down to relatively simpler sub-terrains which can easily be modeled individually.

To model the individual tiles, two types of approximation strategies were employed, namely trend surface and cubic spline interpolation. In the first stage, a sample of candidate ground points are taken (sampled at regular intervals) from the points with the lowest elevations and used for modeling the current tile. The type of approximation strategy to use (trend surface or cubic splines) is decided based on the result of fitting a surface (starting with a linear trend surface) using the sample points and examining the the goodness of fit (R^2 value) (see publication I). After fitting the surface to the candidate points, points with positive residuals are removed in turn and the value of R^2 is examined: if the value of R^2 decreases the point is considered a vegetation point and discarded, otherwise the point is retained. When all the points with positive residuals have been tested the final value of R^2 is compared to a pre-determined threshold value R^2. If the final R^2 value is greater than or equal to the threshold value of R^2 the current surface is accepted, otherwise the surface is rejected and a quadratic trend surface is fitted to the original sample points and the process of examining points with positive residuals is repeated. If both the linear and quadratic trend surfaces fail to attain the required R^2 value, cubic splines are used instead (the tile is too complex to be modeled with a trend surface). Figure 4.3 shows examples of tiles which are suitable for different approximation strategies.

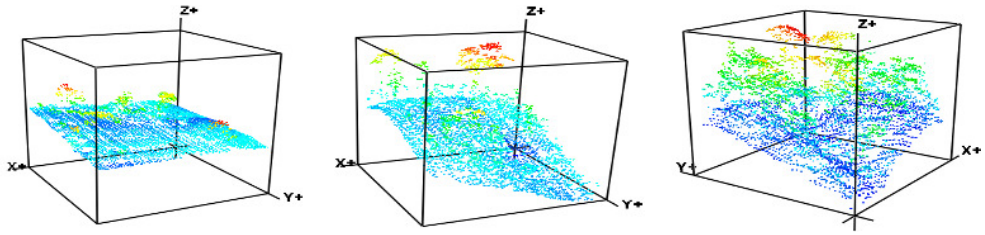

(a) (b) (c)

Figure 4.3: Examples of tiles suitable for different approximation strategies: (a) linear (planar) trend surface; (b) quadratic trend surface; (c) cubic splines. The z-axis represents elevation while the x- and y-axes represent easting and northing values, respectively.

The steps described above constitute the ground filtering part of the algorithm. If cubic splines are used, ground filtering is done by examining the points in a cubic spline for abrupt changes in slope. Points at which there is an abrupt change in slope on both sides of the point are considered vegetation points and discarded. Abrupt changes in slope are considered to indicate discontinuities in terrain–indicating the presence of a non-ground point.

In the second stage—DTM interpolation—elevations at selected unknown locations are estimated. This step is done by evaluating the respective function (trend surface) obtained in the previous stage

(ground filtering stage).

Using the approach described above enables the algorithm to adapt to variations in the terrain. Also, by splitting the terrain into tiles even complex terrain can be reduced to smaller, manageable tiles which can be modeled using the strategies described above. Dealing with a low number of ground points is achieved by making use of the trend in the trend surfaces or cubic splines. The assumption made here is that within a tile ground points lie close to the surface/cubic splines, i.e., they follow the trend of the surface. Therefore, following this assumption, if there are a few ground points that can be used to fit a trend surface with reasonable accuracy then the fitted surface can be used to approximate the elevations of the missing points.

4.8.3 Design Challenges

The design challenges associated with the design decisions made above include the following questions:

(i) how to choose the threshold value for R^2?,

(ii) what is the appropriate tile size to use?,

(iii) how to minimize the misalignment of adjacent tiles?, and

(iv) how to deal with insufficient number of ground points?

Figure 4.4 presents an illustration of the third challenge.

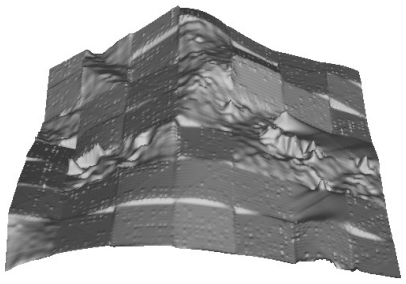

Figure 4.4: The problem of misalignment between adjacent tiles (border effect). Notice the lack of proper alignment between some of the adjacent tiles.

Proposed solutions for addressing these challenges are outlined in the following section.

4.8.4 Proposed Solutions

Choosing the appropriate threshold value for R^2 has to be done by experimenting with different values of R^2 and picking a value which works well for the entire area under study. The effect of choosing a small threshold value for R^2 is that most of the tiles will be approximated with a linear

trend surface (thus leading to a considerable loss of terrain artifacts) while the effect of using a large (more strict) value is that most of the tiles will be approximated with cubic splines (thus introducing unnecessary computational overhead). To avoid this behavior a suitable value for R^2 that works well in the entire study area should be chosen experimentally.

The approach used for choosing a suitable threshold value for R^2, i.e., experimenting with different values and picking the best one, was also used for choosing an appropriate tile size to use. This approach is necessary because these values are highly dependent on the characteristics of the LiDAR point cloud, particularly the distribution of points. Figure 4.5 shows how the value of tile (patch) size affects the accuracy of modeling results.

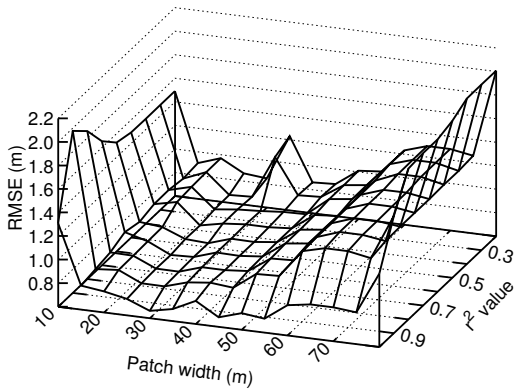

Figure 4.5: Plot showing how the choice of a combination of tile size and threshold value for R^2 affects the accuracy of approximating tiles using trend surfaces for the test data used in publication I. Accuracy is assessed based on the value of RMSE in the DTM.

To deal with the third challenge, i.e., the border effect, an iterative DTM interpolation scheme has been proposed in publication II. In this scheme, several coarse DTMs are generated using varying tile sizes and these DTMs are then combined to generate the final DTM. The reason behind this technique is to induce an overlapping effect between the tiles thus minimizing the border effect. Figure 4.6 illustrates how this technique works and helps to minimize the border effect.

The last challenge is about insufficient ground points to fit neither a trend surface nor cubic splines. This happens, for example, when most of the laser beam is blocked by vegetation, leading to gaps in the LiDAR point cloud. To overcome this problem, an interpolation technique was introduced to estimate the elevations at these gaps. The technique uses linear interpolation in $\mathbb{R}^3$ and makes use of the elevation values of neighboring points. This technique is illustrated in Figures 4.7 and 4.8.

As it can be seen in Figures 4.7 and 4.8, the interpolation technique performs well when the terrain is relatively flat. With undulating terrain, however, the technique performs poorly. This behavior is expected as there is no way to recover/estimate the lost elevation information from neighboring points in undulating terrain.

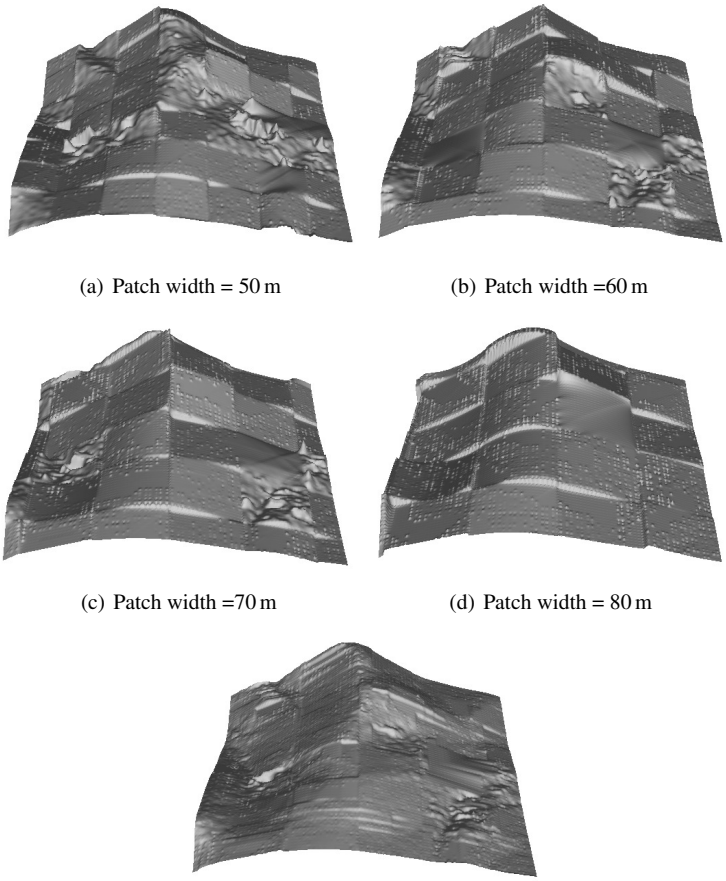

(a) Patch width = 50 m

(b) Patch width =60 m

(c) Patch width =70 m

(d) Patch width = 80 m

(e) Final DTM after combining sample DTMs above by taking the median elevation value at each DTM location.

Figure 4.6: Minimizing the border effect by combining several coarse DTMs generated using varying tile sizes. The different tile sizes used to generate the sample DTMs help to induce an overlapping effect between adjacent tiles. Notice how spikes in the sample DTMs are also suppressed.

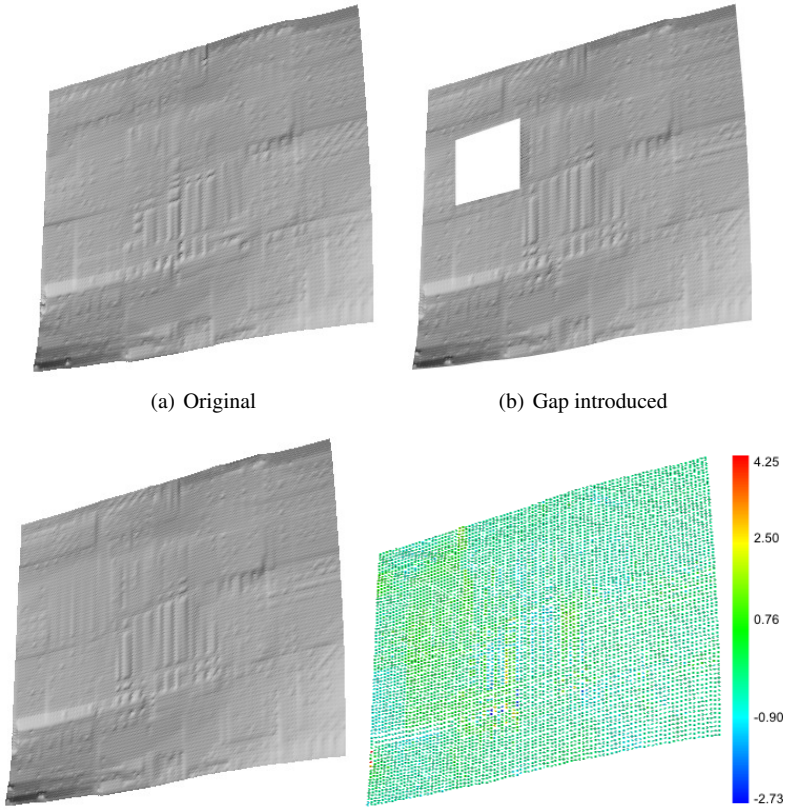

(a) Original (b) Gap introduced

(c) Gap repaired (d) Difference model

Figure 4.7: Filling gaps in a DTM on a level surface on a steep slope: (a) original terrain before a gap is introduced; (b) after a 40 m by 40 m gap has been introduced; (c) after the gap has been repaired; (d) a difference model showing the error in estimation between the original and estimated elevation values. Slope at this location is approximately 37%.

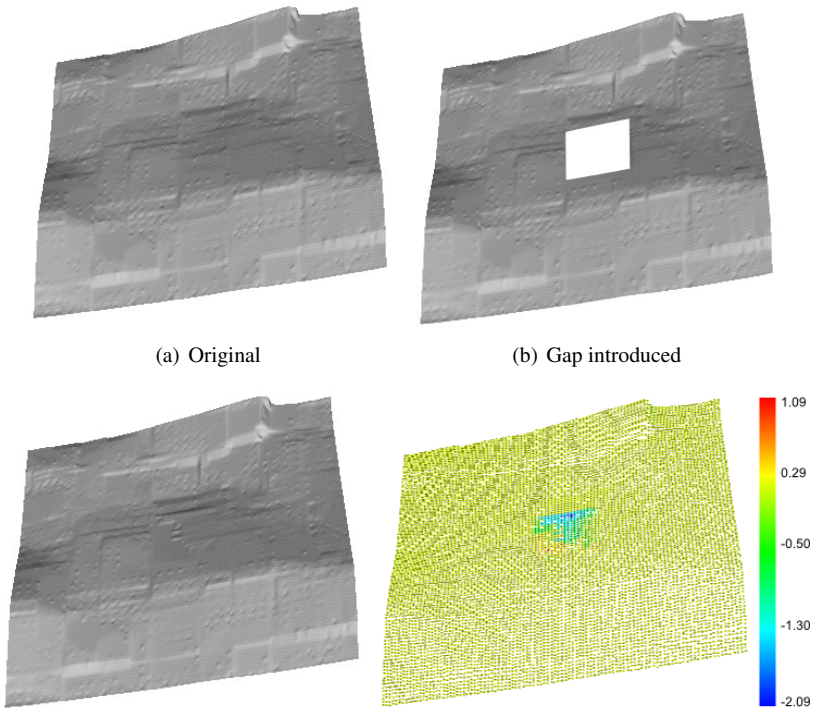

(a) Original (b) Gap introduced

(c) Gap repaired (d) Difference model

Figure 4.8: Filling gaps in a DTM on a curved surface on a steep slope: (a) original terrain before a gap is introduced; (b) after a 40 m by 40 m gap has been introduced; (c) after the gap has been repaired; (d) a difference model showing the error in estimation between the original and estimated elevation values. Slope at this location is approximately 33%.

CHAPTER V

Methods for CBH Estimation From LiDAR

CBH is a critical parameter used in modeling and analysis of forest fire behavior and it plays a key role in crown fire initiation (see Chapter 3). Spatial CBH maps are valuable resources to fire managers as they help the managers easily identify high-risk areas (prone to crown fires) so that they can take appropriate measures.

Like modeling (estimating) of other forest structural parameters, CBH estimation has been greatly enhanced by the use of LiDAR (see Chapter 3). However, estimating CBH is a challenging task. One reason which makes CBH estimation a challenging task is the fact that to accurately model the behavior of forest fires, e.g., its intensity and rate of spread, a good knowledge of the physical characteristics of fuels in a particular area is needed. Since it is very difficult to describe all the physical characteristics for all the fuels in an area, a generalized description, known as a *fuel model*, is normally used (Keane et al., 2001). However, these fuel models have several limitations (Arroyo et al., 2008). In particular, they are

(i) *site-specific*: created for a given geographical area and forest type hence can't easily be applied elsewhere;

(ii) *application-specific*: they are created for a specific purpose, e.g., modeling the rate of fire spread and therefore can't be used for other purposes, such as fire intensity modeling;

(iii) *confusing*: there are many classification systems in existence making it challenging to pick the right model for a given task.

Another factor which makes estimating CBH difficult is that measuring CBH in the field (at the plot and individual tree levels) is a challenging task. The challenge arises partly due to the way CBH is defined (see Chapter 3) which makes it difficult to measure in practice. Consequently, there is no standard metric which is used to represent CBH at the plot and individual tree levels (Gajardo et al., 2014), making authors to resort to simple metrics such as the arithmetic and Lorey's means (see e.g., Agca et al., 2011) for estimating CBH at the plot level, and the distance between the ground and the lowest live branch in the crown (crown base) as the estimate of tree-level CBH. The latter has been widely used because it is easy to measure on the field (see e.g., Mutlu et al., 2008; Erdody and Moskal, 2010; Agca et al., 2011; González-Olabarria et al., 2012).

These complications are perhaps one of the reasons why different authors have tackled the problem of estimating CBH from LiDAR in many different and problem-specific ways. This chapter summarizes some of the methods for CBH estimation from LiDAR (Section 5.1) and summarizes the findings of publication III (Section 5.2).

5.1 State-of-the-Art in CBH Estimation

The following is a summary of selected works on CBH estimation from LiDAR (for details see: Riaño et al., 2003; Andersen et al., 2005; Popescu and Zhao, 2008; Erdody and Moskal, 2010). In the following discussion these works are going to be referred to as *Erdody and Moscal*, *Popescu and Zhao*, *Andersen and others*, and *Riaño and others*, respectively.

5.1.1 Erdody and Moscal

This study aimed at determining which data source among LiDAR, imagery, and the fusion of the two is the best in estimating canopy fuel metrics. The study was carried out in the Ahtanum State Forest in Washington. The forest is dominated by ponderosa pine (*P*. ponderosa) and associated mixed mesic confers such as Douglas-fir (*P*. menziesii), grand fir (*A*bies grandis), lodgepole pine (*P*inus contorta), Engelmann spruce (*P*icea engalmanii), and western larch (*L*arix occidentalis). Elevations in the area range from 960 to 1530 m.

For estimating CBH, regression models were built using field-measured CBH as the dependent variable and LiDAR and imagery metrics as independent variables. On the field crown base height was used to estimate CBH. LiDAR metrics used are similar to those used by Andersen et al. (2005), i.e., maximum and mean heights (h_{max} and h_{mean}), coefficient of variation (CV), density metric (D), and various percentile values (10th, 25th, 50th, 75th, and 90th).

Three predictive models for CBH were built using derived variables from LiDAR, imagery, and a combination of the two (fusion of LiDAR and imagery). The best models were selected based on the Bayesian Information Criteria (BIC), the coefficient of determination (R^2), and the fit of residuals. To check for collinearity between independent variables, variance of inflation tests were conducted for each model and if collinearity were found another model was selected. Best models were selected as those having a good balance between a high R^2 value, a low RMSE, no collinearity, and parsimony.

Results of this study showed that fusion of LiDAR and imagery gave CBH models with the highest R^2 values and lowest RMSE for cross validation ($RMSE_{cv}$). On the other hand, models based on LiDAR alone had the least discrepancy between RMSE and $RMSE_{cv}$, i.e., the most parsimonious models. Therefore, models based on fusion of LiDAR and imagery should be chosen if the goal is to get lower $RMSE_{cv}$ while models based on LiDAR alone should be chosen if simple, parsimonious models are preferred.

5.1.2 Popescu and Zhao

This study aimed at estimating crown base height from LiDAR using a voxel-based approach. The study was carried out in eastern Texas in a forest consisting of pine plantantions in various developmental stages, old growth pine stands, and hardwoods. The topography in the area consists of gentle slopes with average, minimum, and maximum elevations of 85, 62, and 105 m, respectively.

This study used both the frequency and intensity values of the LiDAR to create vertical intensity and height bins (voxels) which are later used to derive the height to the crown base. The crown base is detected by detecting the height where intensity or the frequency of laser hits drop abruptly on the vertical profile. The height where the intensity of laser hits drops abruptly was detected by fitting a fourth-degree polynomial curve to the vertical profile and analyzing the shape of the fitted polynomial to determine where the drop occurs (using Fourier and wavelet analysis).

Two kinds of linear regression models for CBH were built: (1) models using the LiDAR-derived crown base height as the only independent variable; and (2) models using all LiDAR-derived measurements (total tree height, crown width, and crown base height) as independent variables.

Results of this study showed a high correlation between LiDAR and field-measured CBH estimates for pines compared to deciduous trees. R^2 values obtained for the models ranged between 0.73 and 0.80, which agree well with similar previous studies. Moreover, the study showed that LiDAR-derived crown base height overestimates (RMSE =2.03 m, $R^2 = 0.8$) crown base height, which is consistent with similar previous studies (e.g., Riaño et al., 2003; Andersen et al., 2005; Erdody and Moskal, 2010).

5.1.3 Andersen and Others

This study aimed at estimating canopy fuel parameters, including CBH, using LiDAR. The study was carried out in the Capitol State Forest, Washington. The forest in the area is dominated by coniferous Douglas-fir (*P*seudotsuga menziesii), and western hemlock (*T*suga heterophylla).

As independent variables, the study used standard LiDAR predictor variables, namely the coefficient of variation (CV), canopy density metric (D), and several percentile-based metrics (25th, 50th, 75th, and 90th), together with the maximum and mean LiDAR heights. Plot level CBH values (dependent variables) were estimated at the plot level using the method proposed by Beukema et al. (1997).

To estimate CBH, stepwise regression was used to identify the best model whereby models with a limited number of variables that are parsimonious were preferred. The predictive value of the chosen model was determined using leave-one-out cross validation (LOOCV). The best model for estimating CBH identified in this study had an R^2 value of 0.77 and an RMSE of 3.9 m.

5.1.4 Riaño and Others

This study aimed at estimating crown base height in a forest consisting of green meadows, conifer, and deciduous forests in southwestern Germany. The area consists of mainly gentle slopes with elevations ranging from 572.16 to 603.02 m.

Unlike the studies discussed above, this study is parameter-free, i.e., no model was fitted in order to estimate crown base height. The study uses a decision-tree-like mechanism to estimate crown base height from LiDAR. The method operates on small units of the point cloud called cells. Given a normalized point cloud, the method starts by separating ground points from vegetation points in a cell. The criterion for this step is that all points with height greater than 0.6 m are considered vegetation points while points with height less than or equal to 0.6 m are considered ground points.

After removing ground points, the next step is to determine whether the current cell is a forest cell or it is a shrub, young forest, grass, or bare cell. To determine the type of cell the 99th percentile of the LiDAR heights is computed. If the computed 99th LiDAR height percentile is greater than 4 m the

cell is considered a forest cell. For forest cells, the next step is to cluster the points into overstorey and understorey points. After clustering the points, crown base height (which approximates crown base height) is estimated as the first percentile of the overstorey points.

5.2 Case Study: Innovation in CBH Estimation

This section summarizes the contents of publication III. It covers the motivation behind the proposed algorithm (Section 5.2.1), algorithm design (Section 5.2.2), and limitations of the proposed algorithm (Section 5.2.3).

5.2.1 Motivation

The importance of CBH in modeling the behavior forest fires was described in Chapter 3. Also, Chapter 5 pointed out the different challenges faced when estimating CBH from LiDAR. Traditionally, CBH estimation from LiDAR has been mostly done using LiDAR metrics based on height percentiles. These metrics work well but are prone to LiDAR point cloud variations due to, for example, species and the date/season the data were collected. Because of these variations, it is very challenging to model CBH in an area consisting multiple species using metrics based on height percentiles because the point cloud will have different characteristics that reflect the respective characteristics of the species. The aim of this study was to develop a new LiDAR metric for estimating CBH that will minimize the effects of variability caused by presence of different species and season of LiDAR data collection.

5.2.2 Algorithm Design

The main idea behind the design of the proposed algorithm is to estimate the heights of the partial gaps that exist in the LiDAR point cloud that are formed by the absence of reflecting objects between the tree crowns and the ground (see Figure 5.1).

The height of the partial gap shown in Figure 5.1 from the ground is a close approximation of the height of the lower live branches of the trees from the ground. Since most field-measured CBH values are based on this idea it follows that this quantity can form the basis for a robust metric for estimating CBH from LiDAR.

A moving voxel was used to estimate the heights of the partial gaps in a normalized LiDAR point cloud (search space) from which ground points have been discarded (all points with a height of 0.5 m and less). The search space can be thought of as a large cuboid with its origin at one of the lower corners. To locate gaps, the voxel starts to move horizontally from the origin in predetermined steps until a gap is located. A gap is said to have been located when the number of points contained in the voxel is less than or equal to given threshold value. When a gap is located, its height is estimated by moving the voxel vertically in steps equal to its height, while counting the number of points contained in the voxel at each step, until the number of points contained in the voxel exceeds the point threshold value. The height of the gap is estimated to be $\mathrm{N} * \mathrm{H}_v$, where N is the number of times the voxel moved up and H_v is the height of the voxel.

Since the voxel moves in fixed steps along rows in the search space, a completed search in the search space results in a raster (grid) of gap height values. Each cell of the raster represents the height of

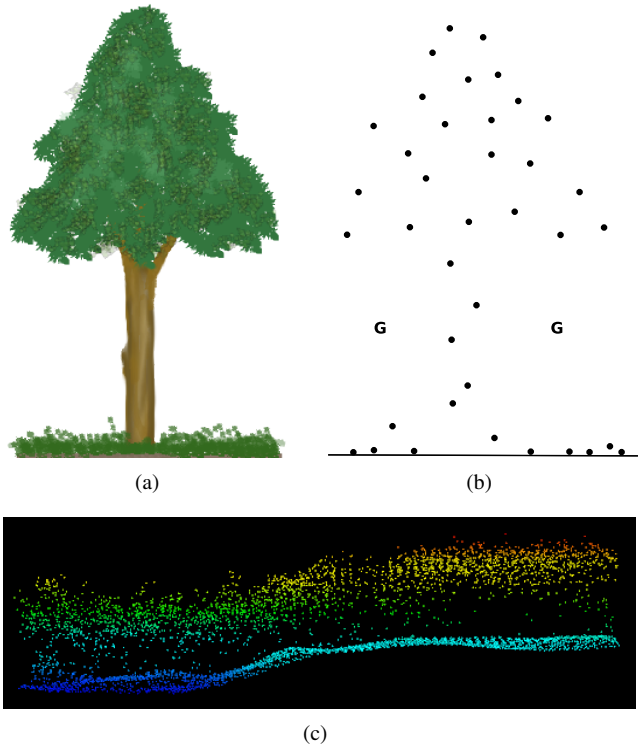

Figure 5.1: Formation of a partial gap below the canopy due to the absence of reflecting objects between the tree crowns and the ground: (a) & (b) show a tree crown and the effect of lack of reflecting objects between the crown and the ground, respectively; (c) a cross section of a real LiDAR point cloud showing a partial gap between the canopy and the ground.

the gap (or zero) found at that location. The resolution of the raster is equal to the step size the voxel moves in the horizontal direction.

The next step is to generate metrics from the raster produced in the previous step. To do this, circular plots are extracted from the raster that correspond to field plots (in this study the field plots had a radius of 9 m approximately). Depending on the step size used to move the voxel in previous step, the gap height values extracted from the plots may contain many duplicates especially if the step size used to move the voxel is relatively small (in this study the step size was 0.5 m and it led to many duplicates in each plot); therefore the next step is to remove the duplicates form the gap height values for each plot. The remaining values after removing duplicates are then used to extract the metrics used to model CBH as independent variables. The metrics used are the percentile values (25th, 50th, 75th, and 90th) of remaining gap height values. These metrics correlate strongly with the field-measured CBH values as shown in Figure 5.2.

The values in Figure 5.2 were generated for each plot by removing duplicates from gap height values, sorting the values in descending order and taking the largest values corresponding to the number of measured trees in respective plots; for example, if a plot had 10 measured trees then after sorting the gap height values in descending order only the first 10 values were taken.

The generated metrics are used as independent variables (predictors) when estimating CBH using linear regression while field-measured CBH values are used as dependent variables (responses). For comparison purposes different derived dependent variables were used, including Lorey's mean (LOR), arithmetic mean (AVG), and the 40th (P40) and 50th (P50) percentile values of measured CBH values for individual trees in each plot.

Tables 5.1 and 5.2 and Figures 5.3 and 5.4 show a comparison of regression models obtained using the metrics proposed in this study (indicated by g_is) against traditional height percentile metrics (indicated by h_is). As seen in these figures and tables, the metrics proposed in this study perform better when compared to traditional height percentile metrics (see publication III).

Table 5.1: Regression models obtained using different dependent variables against the proposed LiDAR metrics as predictor variables.

Variable	Model	RMSE (m)	RMSE$_{cv}$ (m)	R^2	p-value
LOR	$CBH = (0.60)g_{75} + 0.79$	2.40	2.69	0.46	0.0003
AVG	$CBH = (1.05)g_{25} - (1.47)g_{50} + (1.06)g_{75} + 0.40$	2.04	3.66	0.61	0.0003
P40	$CBH = (1.28)g_{25} - (1.97)g_{50} + (1.98)g_{75} - (0.69)g_{90} + 1.20$	1.74	3.36	0.75	0.00002
P50	$CBH = (1.16)g_{25} - (1.82)g_{50} + (2.09)g_{75} - (0.75)g_{90} + 1.16$	2.01	3.90	0.71	0.00006

5.2.3 Limitations of the Algorithm

The main limitation of the proposed algorithm for CBH estimation is its inability to distinguish between legitimate gaps formed due to the absence of reflecting objects underneath the tree crowns and the gaps formed when laser pulses are completely blocked by the canopy. In both cases the algorithm will report a gap.

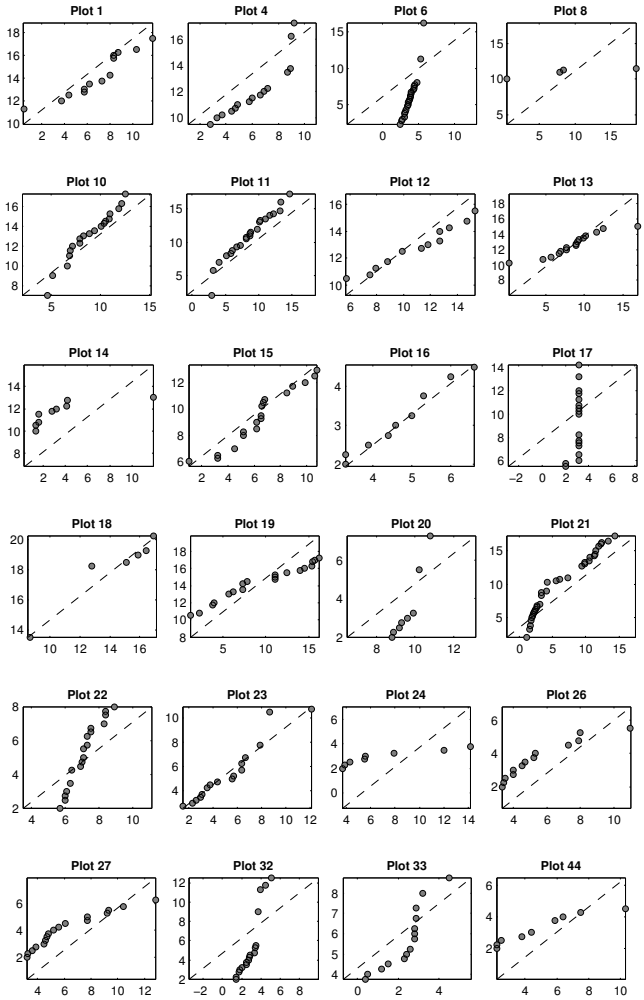

Figure 5.2: Correlation between calculated gap heights (in meters) (y-axis) and field-measured CBH values (x-axis) for the 24 sample plots used in this study. The strong linear relationship evident in the figures suggests that metrics based on gap height values can serve as good predictors of CBH. There was no immediate explanation for the deviation seen in plot no. 17.

Table 5.2: Regression models obtained using different dependent variables against traditional percentile LiDAR metrics.

Variable	Model	RMSE (m)	RMSE$_{cv}$ (m)	R^2	p-value
LOR	$CBH = (0.56)h_{50} - 0.31$	1.92	3.34	0.65	0.002
AVG	$CBH = (0.44)h_{50} - 0.07$	2.31	3.51	0.44	0.0004
P40	$CBH = (1.62)h_{50} - (1.19)h_{75} + 2.56$	2.48	5.15	0.44	0.002
P50	$CBH = (1.80)h_{50} - (1.26)h_{75} + 2.29$	2.38	4.98	0.55	0.0002

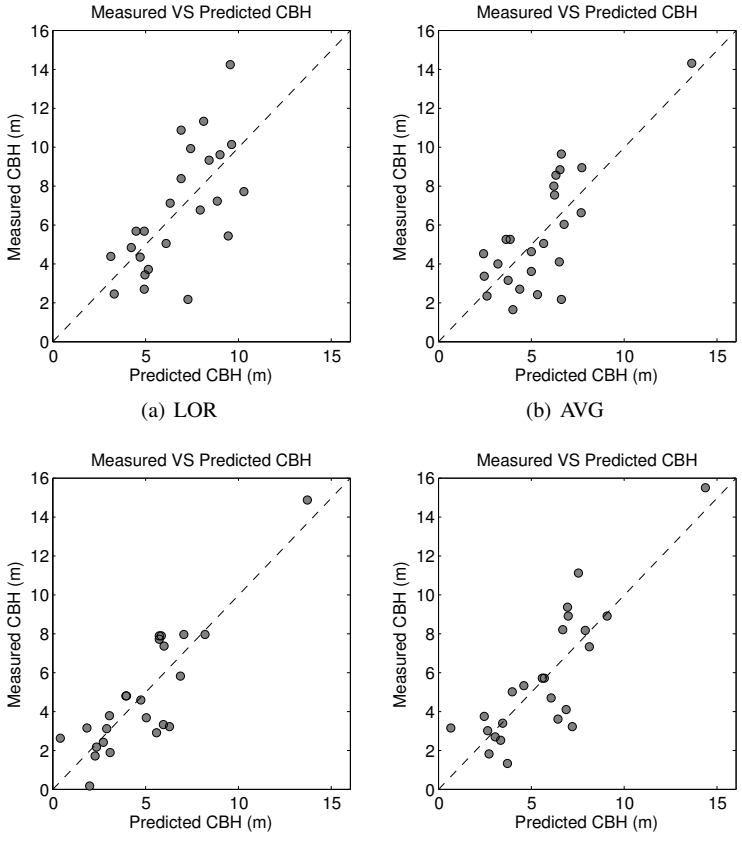

(a) LOR (b) AVG

(c) P40 (d) P50

Figure 5.3: Plots showing comparison between measured and estimated CBH for the proposed LiDAR metrics. The diagonal line shows a 1:1 relationship.

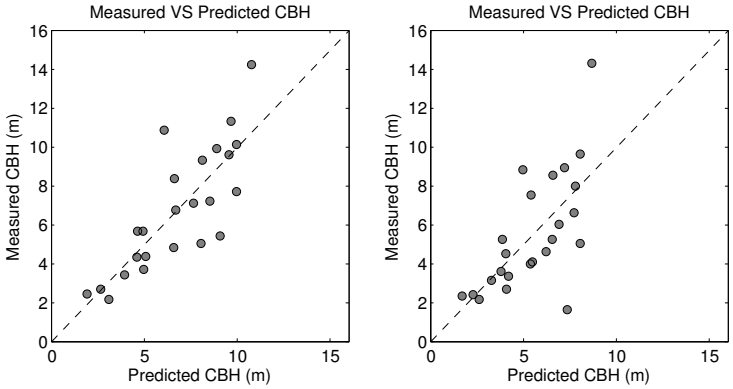

(a) LOR

(b) AVG

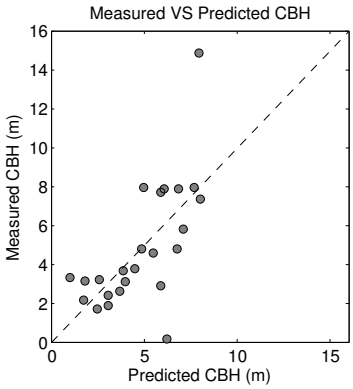

(c) P40

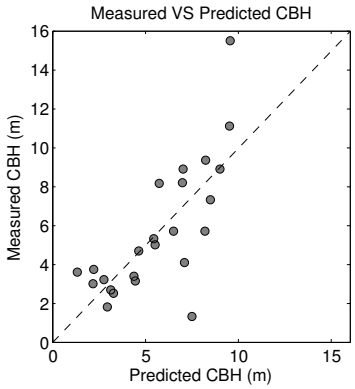

(d) P50

Figure 5.4: Plots showing comparison between measured and estimated CBH traditional percentile LiDAR metrics metrics. The diagonal line shows a 1:1 relationship.

CHAPTER VI

Implementational Challenges in Forestry Applications of LiDAR

The success of LiDAR in forestry applications has been discussed in previous chapters. This chapter discusses the challenges in the application of LiDAR in forestry applications. These challenges are going to be categorized into six groups: (1) field measurement challenges (2) data acquisition costs; (3) computing power limitations; (4) algorithm development; (5) processing software problems; and (6) operational challenges. Sections 6.1–6.6 discuss these challenges.

6.1 Field Measurement Challenges

While LiDAR has a high potential for estimating various forest parameters, the estimation accuracy of these parameters relies on the quality of the field measurements used to calibrate LiDAR models. Obtaining accurate field measurements, however, is a challenging task especially when the canopy is dense and the terrain is complex taking into consideration that a large number of sample field plots is normally required (see e.g., Maltamo et al., 2011).

Dense canopy causes two main problems pertaining to taking field measurements. First, it is difficult for field measurement teams to navigate to the identified sample plot locations under dense canopy. Hence, presence of a dense canopy in a study area does not only hamper the process of taking field measurements, but it also makes the process expensive and time consuming. Second, dense canopy makes the process of measuring tree attributes, especially height, error prone. Most tree height measuring devices require the top of the tree to be visible, when the canopy is dense it becomes difficulty to distinguish tree tops. To address this challenge, different techniques for minimizing the number of sample field plots have been proposed (e.g., Junttila et al., 2013).

Complex terrain, on the other hand, causes two main problems. First, like in the case of dense canopy, complex terrain makes it difficult for measurement teams to navigate the plots. Second, measuring tree height on steep slopes is difficult and error prone. Although the error due to slope can be corrected, the chance of making errors while measuring tree height in complex terrain remains high.

In addition to the above challenges, an interesting phenomenon arises when measuring the height of leaning trees. The common method of measuring tree height in the field is based on simple trigonometry whereby a simple device is used to measure the angle of elevation relative to the top of the tree. This information together with the horizontal distance between the operator and the tree

trunk is then used to derive the height of the tree using simple trigonometry. With leaning trees the height can be significantly underestimated or overestimated depending on the position from which the measurement is taken relative to the tree (see Figure 6.1).

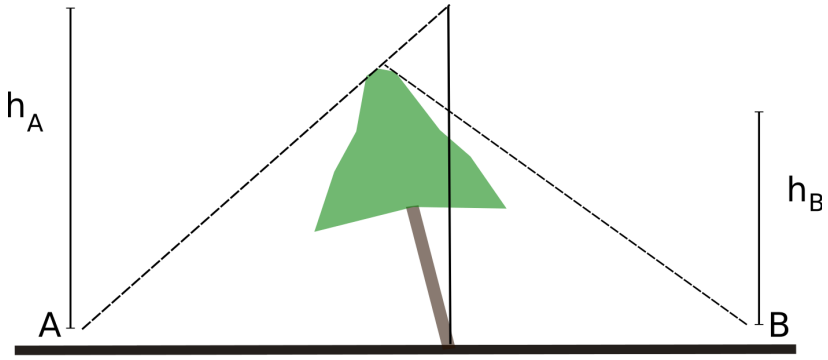

Figure 6.1: Measurement errors when estimating the height of leaning trees using trigonometric techniques. When measured from position *A* the perceived height is h_A (overestimation). When measured from position *B* the perceived height is h_B (underestimation).

Leaning trees also cause problems when calculating LiDAR heights. When normalizing LiDAR points to obtain their heights, the elevation of each point is subtracted from the elevation of the DEM cell vertically below it. With leaning trees the heights can either be underestimated (if the terrain is flat) or overestimated (if the terrain is steep). This phenomenon is illustrated in Figure 6.2.

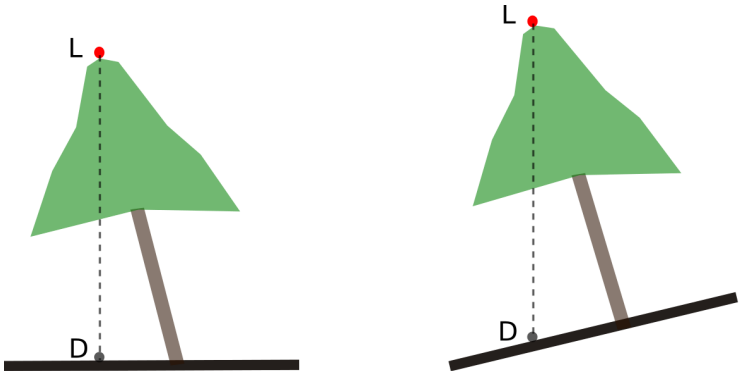

Figure 6.2: Problems arising when calculating LiDAR height from leaning tree point clouds. Left: leaning tree on flat terrain (underestimation); right: leaning tree on steep terrain (overestimation). The points marked with an *L* represent LiDAR points while the points marked with a *D* represent DEM elevations. The broken line represents the perceived height of the LiDAR points.

6.2 Data Acquisition Costs

While the cost of LiDAR acquisition is considered relatively low, especially for acquisitions covering large areas, in some cases the cost of data pre-processing can be considerably high. Hummel et al. (2011), for example, reports a price of $1.35/acre for data acquisition over an area of 31,614 acres and an additional $33,424 for processing the data to get various raster layers required for further analysis. Therefore, while the cost of data acquisition might have dropped over the years, there are additional costs which need to be considered as part of data acquisition and these have to do with data handling and pre-processing.

Furthermore, the cost of acquiring LiDAR normally quoted in many studies considers what can be considered the *ideal case*, i.e., moderate terrain and normal flight parameters (pulse frequency, flying height, footprint size, etc.). However, as was pointed out in Chapter 3 that the accuracy of various forest structural parameters estimated from LiDAR highly depend on the availability of an accurate DTM, and later in Chapter 4 that extracting DTMs in forested and complex terrain is a challenging task. Following this fact, flight parameters mentioned above may have to be adapted (e.g., lowering the flying height and flying speed; and increasing pulse frequency) in order to facilitate the process of creating accurate DTMs. Adapting flight parameters in order to overcome complex terrain and increase pulse penetration rate can add significantly to the cost of data acquisition. In some forests, e.g., tropical forests, this adaptation may be necessary in order to obtain data of required density (see e.g., publication II).

Another factor which can contribute to the cost of LiDAR is the fact that many forestry applications have an element of monitoring; for example, monitoring growth over time (height changes), monitoring carbon stocks, etc. This means to monitor these variables over time several LiDAR mission have to be flown in order to detect the changes. Again, this requirement translates to additional costs.

6.3 Computing Power Limitations

Processing LiDAR point clouds requires a considerable amount of computing power. This power requirement is due to the fact that a typical LiDAR point cloud tends to contain an enormous number of points. For example, the LiDAR data used in publication I consisted of 300 tiles with the number of points in each return type in all the tiles as follows: first return (511,192,368 points), second return (130,878,981 points), third return (18,425,728 points), and fourth return (1,028,612) for a total of 661,525,689 points. This is a considerable amount of data to process even for a fast personal computer (PC)[1].

The computing power challenges have to do with both processing power (CPU speed) and memory (RAM) requirements. A fast CPU is needed to process the point cloud in a reasonable period of time while a good amount of RAM, apart from facilitating the processing speed, helps to ensure that large data tiles can be loaded into memory for processing thus avoiding the need to fragment the data into small tiles (thus avoiding file handling overhead).

Several approaches have been proposed for dealing with the challenge of computing power. The first approach is based on data reduction. Previous studies which have investigated the relationship

[1] It used to take up to one week to process this data for DTM extraction in Matlab running under Ubuntu GNU/Linux and in a PC with Intel Core i5 processor and 8GB of RAM running at 3.1 GHz.

between LiDAR data/pulse density and the accuracy of prediction of common forest structural parameters such as tree height, DBH, and basal area showed that reducing the density of the data does not have a significant impact on the accuracy of the estimated forest parameters; for example, in the study by Jakubowski et al. (2013) it was found that correlations between LiDAR and forest parameters such as tree height, DBH, and basal area are not relatively affected until when the pulse density is dropped below 1 pulse/m^2. The results of this study mean that not only can the data processing times be significantly reduced, but also the cost of data acquisition can be reduced (see Section 6.2).

Data reduction is also possible with DTM extraction in areas with high pulse penetration rates (Liu et al., 2007; Liu and Zhang, 2008). In the study by Liu et al. (2007), for example, it was found that data can be reduced to 50% of the original point cloud without a significant difference in DEM accuracy. Furthermore, reducing the data to 50% of the original point cloud also led to halving the processing time for DEM generation.

The second approach for dealing with computing power challenges is to make use of high-performance distributed computing facilities such as cloud computing environments (see e.g., Hegeman et al., 2014). High-performance computing environments such as cloud computing environments are still confined to a select group of research institutions and therefore this approach is currently mainly for research purposes only. However, the emergence of graphics processing unit (GPU) parallel programming technology, which offer a low-cost and readily available parallel computing platform is opening new possibilities (see e.g., Barlas, 2015; Allombert et al., 2014).

6.4 Challenges in Algorithm Development

Although LiDAR technology has matured and is in widespread use, there are still challenges in the area of point cloud processing algorithms (Wulder et al., 2013). Although many algorithms have been proposed in the literature, these algorithms tend to be narrow in scope and therefore perform poorly outside their scope. For example, many general purpose ground filters will not perform well in forested terrain because these ground filters were not designed to cope with such low numbers of ground points. Even ground filters designed specifically to operate in forested terrain tend to be specific to or designed to work in specific settings (point cloud characteristics and terrain type) hence they tend to perform poorly when applied to other kinds of terrain or point clouds with different characteristics (see e.g., publication II).

Complex terrain and vegetation cover continue to be the major challenges for ground filters (Sithole and Vosselman, 2004; Meng et al., 2010). Therefore, to keep up with the developments in LiDAR technology and take full advantage of the same, a new generation of ground filters need to be developed or existing ones improved. Because of these challenges some authors have decided to take a *hybrid* approach, i.e., combining several ground filters in order to take advantage of the good features of the different ground filters. One particular case where this approach is necessary is in wetland environments (see e.g., Rose et al., 2013). In these environments, there is no clear division between ground, peat, and vegetation and therefore ground filters tend to miss many ground points.

6.5 Processing Software Problems

When it comes to point cloud processing software several challenges can be identified. First, the availability of point cloud processing software for research purposes (open source or free software)

is limited. Several free software tools exist (see e.g., Evans et al., 2009) but they are either not well maintained, limited in functionality, or they are offered in library form and therefore require programming skills in order to use them. The second challenge with the available point cloud processing software is that they tend to be outdated in terms of the algorithms they support. A good example of this is the FUSION LiDAR processing and visualization software (McGaughey and Carson, 2003). Although several new and improved ground filters for forested terrain (e.g., Kobler et al., 2006) have been proposed, this software still uses an old algorithm proposed by Kraus and Pfeifer (1998). This algorithm works well with moderate forest cover but its performance deteriorates in thick canopy cover and complex terrain (see publication II).

6.6 Operational Challenges

Many LiDAR missions are flown today, ranging from small scale missions geared for research purposes to large scale missions conducted by government agencies and large corporations. Despite this large number of LiDAR missions and the widespread use of LiDAR in the forestry community, there is still a lack of standards governing LiDAR acquisition missions (Reutebuch et al., 2005; Evans et al., 2009). As described in the previous chapters, LiDAR acquisition encompasses a number of parameters which affect the characteristics of the resulting data. Therefore, standards in project planning are essential to ensure the suitability of the data for a particular purpose. Evans et al. (2009) identifies three specific areas for which standards are needed: project planning, data processing, and deliverables. In project planning things to consider for standardization include sensor type (terrestrial versus airborne, discrete return versus full waveform), acquisition parameters, equipment used (aircraft, laser scanner, GPS equipment etc.), and processing software. Data processing should consider what level/type of processing should be done by the vendor (e.g., ground filtering) while deliverables should standardize the number and types of deliverables the vendor should provide (e.g., metadata, DEM, and DSM).

CHAPTER VII

Conclusion and Discussion

This thesis has investigated the area of LiDAR data processing in three areas, namely ground filtering/ DTM extraction, forest fire behavior modeling, and robust use of different field plot designs for model-based high-resolution biomass estimation. Regarding the area of DTM extraction, the thesis has proposed algorithms for DTM extraction from LiDAR data in demanding environments typical of tropical rainforests, i.e., complex terrain and low LiDAR data density (low number of ground points). The algorithms for DTM extraction from LiDAR data proposed in this thesis differ from most existing algorithms in that they operate on the LiDAR data in a piecemeal fashion, i.e., they view the terrain as being made up of smaller units called patches (tiles) which are processed individually. Using this approach, together with the use of trend surfaces and cubic splines for DTM interpolation, the algorithms can automatically adapt to terrain changes and cope with a low number of ground points in the LiDAR data.

Regarding the area of forest fire behavior modeling, the thesis has proposed a new metric for modeling canopy base height (CBH). This metric is the result of a moving-voxel algorithm which searches for and estimates the height of partial gaps available in the LiDAR point cloud (and therefore the corresponding forest from which the LiDAR data was acquired) between the ground and the canopy formed by the absence of reflecting objects between the ground and the canopy. The height of these gaps exhibit a strong correlation with field-measured individual tree CBH (especially that based on the height of first live branches from the ground) thus they make a good predictor of CBH.

Regarding the use of different field plot designs for model-based high-resolution biomass estimation, the thesis has established that field plot data from different sources (e.g., professional foresters and professionally trained community foresters) can be combined and used together for LiDAR-based high-resolution of forest biomass without affecting prediction performance. However, prediction performance relies on presence of a good correlation between LiDAR predictors and field measurements. Moreover, results of a study conducted in two watersheds in Nepal, namely Chitwan and Gorkha showed that difficult terrain and dense canopy have a big impact on biomass prediction performance. This is because in difficult terrain and dense canopy obtaining a reliable DTM is a challenging task. In addition, obtaining reliable field measurements in difficulty terrain and dense canopy is also difficult. This fact is reflected in the results of the study conducted in Chitwan and Gorkha whereby in Gorkha where the terrain is relatively less complex biomass prediction performance using field plot data form different sources gave good results. In Chitwan, where the terrain is relatively complex, biomass prediction performance was poor.

The algorithms for LiDAR data processing proposed in this thesis can find uses in forestry applications particularly in challenging environments. The algorithms for DTM extraction have been tested in different real tropical forest LiDAR data in Brazil, Ghana, and Nepal, covering a wide variety of terrain complexity/data density combinations with promising results. Similarly, the algorithm for CBH estimation has been tested in the Koli forest, Finland, and compared with conventional methods for CBH estimation based on LiDAR height percentiles and gave better results (low RMSE/RMSE$_{cv}$).

These algorithms , however, have several limitations. Starting with the algorithm for CBH estimation, the main limitation of the algorithm is its inability to distinguish between legitimate gaps in the LiDAR point cloud formed by the absence of reflecting objects and gaps formed by the inability of the laser pulses to penetrate the forest canopy. On the other hand, the main limitation of the algorithms for DTM extraction is their tendency to suppress small terrain artifacts following the use of trend surfaces for DTM interpolation. However, the improvement in performance offered by the DTM extraction algorithms outweighs this limitation especially in estimating tree heights where small terrain artifacts have little or no effect.

Since the main limitations of the proposed algorithms pertain to the inability of LiDAR pulses to penetrate thick canopies, future research should focus on these limitations by looking into the possibility of data fusion, i.e., combining LiDAR data with data from other sensors. Emerging sensor technologies such as terrestrial LiDAR and full-waveform LiDAR are good candidates to consider.

Finally, results on robust use of different field plot designs for model-based high-resolution biomass estimation can find use in global schemes geared towards fighting the global warming and climate change problems through reducing deforestation and forest degradation (e.g., REDD+). Involving local forest communities in these schemes does not only provide employment to the locals but it also brings about a sense of ownership of the project in question thus increasing the chances of success. Nepal is a notable example of involving local forestry communities in forest preservation schemes.

BIBLIOGRAPHY

Agca, M., Popescu, S., Harper, C. W., 2011. Deriving forest canopy fuel parameters for loblolly pine forests in eastern Texas. Canadian Journal of Forest Research 41, 1618–1625.

Agee, J. K., Skinner, C. N., 2005. Basic principles of forest fuel reduction treatments. Forest ecology and management 211 (1), 83–96.

Aguilar, M. A., Saldaãa, M., Aguilar, F. J., 2013. Assessing geometric accuracy of the orthorectification process from GeoEye-1 and WorldView-2 panchromatic images. International Journal of Applied Earth Observation and Geoinformation 21 (0), 427–435.

Ali, T., Mehrabian, A., 2009. A novel computational paradigm for creating a Triangular Irregular Network (TIN) from LiDAR data. Nonlinear Analysis: Theory, Methods & Applications 71 (12), e624–e629.

Ali, T. A., 2004. On the selection of an interpolation method for creating a terrain model (TM) from LIDAR data. In: Proceedings of the American Congress on Surveying and Mapping (ACSM) Conference. Nashville TN, USA.

Allombert, V., Michea, D., Dupros, F., Bellier, C., Bourgine, B., Aochi, H., Jubertie, S., 2014. An Out-of-core GPU Approach for Accelerating Geostatistical Interpolation. Procedia Computer Science 29 (0), 888–896, 2014 International Conference on Computational Science.

American Society for Photogrammetry and Remote Sensing (ASPRS) , 2014. LAS Specification. http://www.asprs.org/Committee-General/LASer-LAS-File-Format-Exchange-Activities.html, accesed on November 29, 2014.

Andersen, H., McGaughey, R. J., Reutebuch, S. E., 2005. Estimating forest canopy fuel parameters using LIDAR data. Remote Sensing of Environment 94 (4), 441–449.

Andersen, H., Reutebuch, S. E., McGaughey, R. J., 2006. Active remote sensing. In: Shao, G., Reynolds, K. (Eds.), Computer Applications in Sustainable Forest Management. Vol. 11. Springer Netherlands, pp. 43–66.

Arroyo, L. A., Pascual, C., Manzanera, J. A., 2008. Fire models and methods to map fuel types: The role of remote sensing. Forest Ecology and Management 256 (6), 1239–1252.

Asner, G. P., Mascaro, J., 2014. Mapping tropical forest carbon: Calibrating plot estimates to a simple LiDAR metric. Remote Sensing of Environment 140 (0), 614–624.

Asner, G. P., Mascaro, J., Muller-Landau, H. C., Vieilledent, G., Vaudry, R., Rasamoelina, M., Hall, J. S., van Breugel, M., 2012. A universal airborne LiDAR approach for tropical forest carbon mapping. Oecologia 168 (4), 1147–1160.

Avtar, R., Sawada, H., 2012. Use of DEM data to monitor height changes due to deforestation. Arabian Journal of Geosciences, 1–13.

Avtar, R., Sawada, H., Kumar, P., 2013. Role of remote sensing and community forestry to manage forests for the effective implementation of REDD+ mechanism: a case study on Cambodia. Environment, Development and Sustainability, 1–11.

Axelsson, P., 1999. Processing of laser scanner data–algorithms and applications. ISPRS Journal of Photogrammetry and Remote Sensing 54, 138–147.

Axelsson, P., 2000. DEM generation from laser scanner data using adaptive tin models. In: International Archives of Photogrammetry and Remote Sensing. Vol. XXXIII. pp. 110–117.

Barlas, G., 2015. Chapter 6 - GPU programming. In: Barlas, G. (Ed.), Multicore and GPU Programming. Morgan Kaufmann, Boston, pp. 391–526.

Bater, C. W., Coops, N. C., 2009. Evaluating error associated with lidar-derived DEM interpolation. Computers & Geosciences 35 (2), 289–300.

Beukema, S. J., Greenough, D. C., Robinson, C. E., Werner, A. K., Elizabeth, D. R., Nicholas, L. C., James, K. B., Colin, C. H., Albert, R. S., 1997. An introduction to the fire and fuels extension to FVS. In: Proceedings of the Forest Vegetation Simulator Conference. pp. 191–195.

Caruso, C., Quarta, F., 1998. Interpolation methods comparison. Computers & Mathematics with Applications 35 (12), 109–126.

Chaplot, V., Darboux, F., Bourennane, H., Leguédois, S., Silvera, N., Phachomphon, K., 2006. Accuracy of interpolation techniques for the derivation of digital elevation models in relation to landform types and data density. Geomorphology 77 (1-2), 126–141.

Chen, Q., Gong, P., Baldocchi, D., Xie, G., 2007. Filtering Airborne Laser Scanning Data with Morphological Methods. Photogrammetric Engineering & Remote Sensing 73 (2), 175–185.

Chu, H., Wang, C., Huang, M., Lee, C., Liu, C., Lin, C., 2014. Effect of point density and interpolation of LiDAR-derived high-resolution DEMs on landscape scarp identification. GIScience & Remote Sensing 51 (6), 731–747.

Clark, M. L., Clark, D. B., Roberts, D. A., 2004. Small-footprint lidar estimation of sub-canopy elevation and tree height in a tropical rain forest landscape. Remote Sensing of Environment 91 (1), 68–89.

Clark, M. L., Roberts, D. A., Ewel, J. J., Clark, D. B., 2011. Estimation of tropical rain forest aboveground biomass with small-footprint lidar and hyperspectral sensors. Remote Sensing of Environment 115 (11), 2931–2942.

Cohen, J. D., Butler, B. W., 1998. Modeling potential structure ignitions from flame radiation exposure with implications for wildland/urban interface fire management. In: Proceedings of the 13th Fire and Forest Meteorology Conference, International Association of Wildland Fire. pp. 81–86.

Collins, R. D., de Neufville, R., Claro, J., Oliveira, T., Pacheco, A. P., 2013. Forest fire management to avoid unintended consequences: A case study of Portugal using system dynamics. Journal of Environmental Management 130 (0), 1–9.

Corbera, E., Schroeder, H., 2011. Governing and implementing REDD+. Environmental sceince & Policy 14, 89–99.

Dassot, M., Constant, T., Fournier, M., 2011. The use of terrestrial LiDAR technology in forest science: application fields, benefits and challenges. Annals of Forest Science 68 (5), 959–974.

de Figueiredo, E., Panosso, A., Romao, R., La Scala, N., 2010. Greenhouse gas emission associated with sugar production in southern Brazil. Carbon Balance and Management 5 (1), 3.

Desmet, P. J. J., 1997. Effects of interpolation errors on the analysis of DEMs. Earth Surface Processes and Landforms 22, 563–580.

Erdody, T. L., Moskal, L. M., 2010. Fusion of LiDAR and imagery for estimating forest canopy fuels. Remote Sensing of Environment 114 (4), 725–737.

Estornell, J., Ruiz, L. A., Velázquez-Martí, B., Fernández-Sarría, A., 2011. Estimation of shrub biomass by airborne LiDAR data in small forest stands. Forest Ecology and Management 262 (9), 1697–1703.

European Commission, 2004. Forest fires in Europe 2003. Tech. Rep. SPI.04.124 EN, Institute for Environment and Sustainability, official Publication of the European Communities.

European Commission, 2006. Forest fires in Europe 2005. Tech. Rep. EUR 22 312 EN, Institute for Environment and Sustainability, official Publication of the European Communities.

Evans, J. S., Hudak, A. T., Faux, R., Smith, A. M. S., 2009. Discrete Return Lidar in Natural Resources: Recommendations for Project Planning, Data Processing, and Deliverables. Remote Sensing 1 (4), 776–794.

Finney, M. A., 2004. FARSITE, Fire Area Simulator–model development and evaluation.

Fisher, P., 1998. Improved Modeling of Elevation Error with Geostatistics. GeoInformatica 2 (3), 215–233.

Fisher, P. F., Tate, N. J., 2006. Causes and consequences of error in digital elevation models. Progress in Physical Geography 30 (4), 467–489.

Fowler, R. J., Little, J. J., 1979. Automatic Extraction of Irregular Network Digital Terrain Models. SIGGRAPH Comput. Graph. 13 (2), 199–207.

Gajardo, J., García, M., Riaño, D., 2014. Applications of Airborne Laser Scanning in Forest Fuel Assessment and Fire Prevention. In: Maltamo, M., Næsset, E., Vauhkonen, J. (Eds.), Forestry Applications of Airborne Laser Scanning. Vol. 27 of Managing Forest Ecosystems. Springer Netherlands, pp. 439–462.

Gaveau, D. L. A., Hill, R. A., 2003. Quantifying canopy height underestimation by laser pulse penetration in small-footprint airborne laser scanning data. Canadian Journal of Remote Sensing 29 (5), 650–657.

Goetz, S., Dubayah, R., 2011. Advances in remote sensing technology and implications for measuring and monitoring forest carbon stocks and change. Carbon Management 2 (3), 231–244.

Gong, J., Li, Z., Q. Zhu, H. S., Zhou, Y., 2000. Effects of various factors on the accuracy of DEMs: an intensive experimental investigation. Photogrammetric Engineering and Remote Sensing 66 (9), 1113–1117.

González-Olabarria, J., Rodríguez, F., Fernández-Landa, A., Mola-Yudego, B., 2012. Mapping fire risk in the Model Forest of Urbión (Spain) based on airborne LiDAR measurements. Forest Ecology and Management 282 (0), 149–156.

Graham, R. T., McCaffrey, S., Jain, T. B., 04 2004. Science basis for changing forest structure to modify wildfire behavior and severity. Tech. rep., USDA Forest Service, Rocky Mountain Research Station.

Guan, Q., Clarke, K. C., 2010. A general-purpose parallel raster processing programming library test application using a geographic cellular automata model. International Journal of Geographical Information Science 24 (5), 695–722.

Guibas, L. J., Knuth, D. E., Sharir, M., 1992. Randomized incremental construction of Delaunay and Voronoi diagrams. Algorithmica 7 (1-6), 381–413.

Hall, S. A., Burke, I. C., 2006. Considerations for characterizing fuels as inputs for fire behavior models. Forest Ecology and Management 227 (1-2), 102–114, perspectives on Site Productivity of Loblolly Pine Plantations in the Southern United States.

Haralick, R., Sternberg, S. R., Zhuang, X., July 1987. Image Analysis Using Mathematical Morphology. Pattern Analysis and Machine Intelligence, IEEE Transactions on PAMI-9 (4), 532–550.

Hauglin, M., Dibdiakova, J., Gobakken, T., Næsset, E., 2013. Estimating single-tree branch biomass of Norway spruce by airborne laser scanning. ISPRS Journal of Photogrammetry and Remote Sensing 79 (0), 147–156.

Hegeman, J. W., Sardeshmukh, V. B., Sugumaran, R., Armstrong, M. P., 2014. Distributed LiDAR data processing in a high-memory cloud-computing environment. Annals of GIS 20 (4), 255–264.

Heritage, G. L., Milan, D. J., Large, A. R., Fuller, I. C., 2009. Influence of survey strategy and interpolation model on DEM quality. Geomorphology 112 (3-4), 334–344.

Herold, M., Román-Cuesta, R., Mollicone, D., Hirata, Y., Van Laake, P., Asner, G., Souza, C., Skutsch, M., Avitabile, V., MacDicken, K., 2011. Options for monitoring and estimating historical carbon emissions from forest degradation in the context of REDD+. Carbon Balance and Management 6 (1), 1–7.

Hodgson, M. E., Bresnahan, P., 2004. Accuracy of Airborne Lidar-Derived Elevation. Photogrammetric Engineering & Remote Sensing 70 (3), 331–339.

Höhle, J., Pedersen, C., 2010. A new method for checking the planimetric accuracy of digital elevation models data derived by airborne laser scanning. In: Proceedings of the 9th International Symposium on Spatial Accuracy Assessment in Natural Resources and Environmental Sciences, University of Leicester, Leicester, UK. pp. 253–256.

Holmgren, J., 2004. Prediction of tree height, basal area and stem volume in forest stands using airborne laser scanning. Scandinavian Journal of Forest Research 19 (6), 543–553.

Hovi, A., Korpela, I., 2014. Real and simulated waveform-recording LiDAR data in juvenile boreal forest vegetation. Remote Sensing of Environment 140 (0), 665–678.

Huber, S., Younis, M., Krieger, G., 2010. The TanDEM-X mission: overview and interferometric performance. International Journal of Microwave and Wireless Technologies 2, 379–389.

Hudak, A. T., Evans, J. S., Stuart Smith, A. M., 2009. LiDAR Utility for Natural Resource Managers. Remote Sensing 1 (4), 934–951.

Hummel, S., Hudak, A. T., Uebler, E. H., Falkowski, M. J., Megown, K. A., 2011. A comparison of accuracy and cost of LiDAR versus stand exam data for landscape management on the Malheur National Forest. Journal of forestry 109 (5), 267–273.

Hyyppä, H., Yu, X., Hyyppä, J., Kaasalainen, H., Honkavaara, E., Rönnholm, P., 2005. Factors affecting the quality of DTM generation in forested areas. International Archives of Photogrammetry Remote Sensing and Spatial Information Sciences 36 (3/W19), 85–90.

Hyyppä, J., Hyyppä, H., Litkey, P., Yu, X., Haggrén, H., Rönnholm, P., Pyysalo, U., Pitkänen, J., Maltamo, M., 2004. Algorithms and methods of airborne laser scanning for forest measurements. International archives of photogrammetry, remote sensing and spatial information sciences XXXVI, 82–89.

Jain, T. B., Graham, R. T., 2007. The relation between tree burn severity and forest structure in the Rocky Mountains. In: Restoring fire-adapted ecosystems: Proceedings of the 2005 National Silviculture Workshop. USDA Forest Service Gen. Tech. Rep PSW-GTR-203. pp. 213–250.

Jakubowski, M. K., Guo, Q., Kelly, M., 2013. Tradeoffs between lidar pulse density and forest measurement accuracy. Remote Sensing of Environment 130 (0), 245–253.

Junttila, V., Finley, A. O., Bradford, J. B., Kauranne, T., 2013. Strategies for minimizing sample size for use in airborne LiDAR-based forest inventory. Forest Ecology and Management 292 (0), 75–85.

Junttila, V., Kauranne, T., Finley, A. O., Bradford, J. B., 2015. Linear Models for Airborne-Laser-Scanning-Based Operational Forest Inventory With Small Field Sample Size and Highly Correlated LiDAR Data. Geoscience and Remote Sensing, IEEE Transactions on 53 (10), 5600–5612.

Jupp, D., Culvenor, D., Lovell, J., Newnham, G., Strahler, A., Woodcock, C., 2009. Estimating forest LAI profiles and structural parameters using a ground-based laser called 'Echidna©'. Tree Physiology 29 (2), 171–181.

Kankare, V., Joensuu, M., Vauhkonen, J., Holopainen, M., Tanhuanpää, T., Vastaranta, M., Hyyppä, J., Hyyppä, H., Alho, P., Rikala, J., Sipi, M., 2014a. Estimation of the Timber Quality of Scots Pine with Terrestrial Laser Scanning. Forests 5 (8), 1879–1895.

Kankare, V., Vauhkonen, J., Tanhuanää, T., Holopainen, M., Vastaranta, M., Joensuu, M., Krooks, A., Hyyppä, J., Hyyppä, H., Alho, P., Viitala, R., 2014b. Accuracy in estimation of timber assortments and stem distribution - A comparison of airborne and terrestrial laser scanning techniques. ISPRS Journal of Photogrammetry and Remote Sensing 97 (0), 89–97.

Keane, R. E., Burgan, R., van Wagtendonk, J., 2001. Mapping wildland fuels for fire management across multiple scales: integrating remote sensing, GIS, and biophysical modeling. International Journal of Wildland Fire 10 (4), 301–319.

Kobler, A., Pfeifer, N., Ogrinc, P., Todorovski, L., Oštir, K., Džeroski, S., 2006. Repetitive interpolation: A robust algorithm for DTM generation from Aerial Laser Scanner Data in forested terrain. Remote Sensing of Environment 108 (2007), 9–23.

Köhl, M., Magnussen, S. S., Marchetti, M., 2006. Sampling Methods, Remote Sensing and GIS Multiresource Forest Inventory. Tropical Forestry. Springer.

Korhonen, L., Korpela, I., Heiskanen, J., Maltamo, M., 2011. Airborne discrete-return LIDAR data in the estimation of vertical canopy cover, angular canopy closure and leaf area index. Remote Sensing of Environment 115 (4), 1065–1080.

Korhonen, L., Vauhkonen, J., Virolainen, A., Hovi, A., Korpela, I., 2013. Estimation of tree crown volume from airborne lidar data using computational geometry. International Journal of Remote Sensing 34 (20), 7236–7248.

Korhonen, M., 2012. Predicting canopy base height (CBH) from sparse airborne LiDAR in a Scots pine dominated forest and enhancing the efficiency of field measurements of CBH (in Finnish). Master's thesis, University of Eastern Finland.

Kraus, K., Pfeifer, N., 1998. Determination of terrain models in wooded areas with airborne laser scanner data. ISPRS Journal of Photogrammetry and Remote Sensing 53, 193–203.

Lam, N. S., 1983. Spatial Interpolation Methods: A Review. The American Cartographer 10 (2), 129–150.

Leckie, D., Gougeon, F., Hill, D., Quinn, R., Armstrong, L., Shreenan, R., 2003. Combined high-density lidar and multispectral imagery for individual tree crown analysis. Int. J. Remote Sens. 29, 633–649.

Leica Geosystems UK, 2014. Leica Geosystems terrestrial laser scanner. http://www.leica-geosystems.co.uk/thumbs/originals/PGQI_1230.jpg, accesed on November 29, 2014.

Lemmens, M., 2011a. Airborne Lidar. In: Gatrell, J. D., Jensen, R. R. (Eds.), Geo-information. Vol. 5 of Geotechnologies and the Environment. Springer Netherlands, pp. 153–170.

Lemmens, M., 2011b. Terrestrial Laser Scanning. In: Gatrell, J. D., Jensen, R. R. (Eds.), Geo-information. Vol. 5 of Geotechnologies and the Environment. Springer Netherlands, pp. 101–121.

Li, J., Heap, A. D., 2011. A review of comparative studies of spatial interpolation methods in environmental sciences: Performance and impact factors. Ecological Informatics 6 (3-4), 228–241.

Li, X., Li, Z., Zhu, Q., Gold, C., 2005. Digital Terrain Modelling. CRC Press.

Listopad, C. M., Drake, J. B., Masters, R. E., Weishampel, J. F., 2011. Portable and Airborne Small Footprint LiDAR: Forest Canopy Structure Estimation of Fire Managed Plots. Remote Sensing 3 (7), 1284–1307.

Liu, J. G., Mason, P. J., 2009. Extracting Information from Point Data: Geostatistics. John Wiley & Sons, Inc., pp. 197–209.

Liu, X., 2008. Airborne LiDAR for DEM generation: some critical issues. Progress in Physical Geography 32 (1), 31–49.

Liu, X., Zhang, Z., 2008. Lidar data reduction for efficient and high quality dem generation. International Archives of the Photogrammetry, Remote Sensing and Spatial Information Sciences 37, 173–178.

Liu, X., Zhang, Z., Peterson, J., Chandra, S., 2007. The effect of LiDAR data density on DEM accuracy. In: Proceedings of the International Congress on Modelling and Simulation (MODSIM07). Modelling and Simulation Society of Australia and New Zealand Inc., pp. 1363–1369.

Liu, Z., 2013. Review on the Role of Terrestrial Aquatic Photosynthesis in the Global Carbon Cycle. Procedia Earth and Planetary Science 7 (0), 513–516.

Lu, G. Y., Wong, D. W., 2008. An adaptive inverse-distance weighting spatial interpolation technique. Computers & Geosciences 34 (9), 1044–1055.

Lund, H. G., Smith, W. B., June 1997. The United States forest inventory program. In: In: Nyysönen, Aarne; Ahti, Anne, Eds. Proceedings, FAO/ECE meeting of experts on Global Forest Resource Assessment. Tropical Forestry. Finnish Forest Research Inst. Research paper 620, pp. 331–333.

Magnusen, S., Boudewyn, P., 1998. Derivations of stand heights from airbone laser scanner data with canopy-based quantile estimators. Canadian Jornal of Forest Research 28, 1016–1031.

Maguya, A., Junttila, V., Kauranne, T., 2013. Adaptive algorithm for large scale dtm interpolation from lidar data for forestry applications in steep forested terrain. ISPRS Journal of Photogrammetry and Remote Sensing 85 (0), 74–83.

Maguya, A. S., Junttila, V., Kauranne, T., 2014. Algorithm for Extracting Digital Terrain Models under Forest Canopy from Airborne LiDAR Data. Remote Sensing 6 (7), 6524–6548.

Maltamo, M., Bollandsås, O. M., Vauhkonen, J., Breidenbach, J., Gobakken, T., Næsset, E., 2010. Comparing different methods for prediction of mean crown height in Norway spruce stands using airborne laser scanner data. Forestry 83 (3), 257–268.

Maltamo, M., Bollandsås, O. M., Næsset, E., Gobakken, T., Packalén, P., 2011. Different plot selection strategies for field training data in ALS-assisted forest inventory. Forestry 84 (1), 23–31.

Maltamo, M., Mustonen, K., Hyyppä, J., Pitkänen, J., Yu, X., 2004. The accuracy of estimating individual tree variables with airborne laser scanning in a boreal nature reserve. Canadian Journal of Forest Research 34 (9), 1791–1801.

McGaughey, R. J., Andersen, H., Reutebuch, S. E., 2006. Consideration for planning, acquiring, and processing LiDAR data for forestry applications. In: Proceedings of the eleventh Biennial USDA Forest Service Remote Sensing Applications Conference. American Society of Photogrammetry and Remote Sensing. Salt Lake City, UT.

McGaughey, R. J., Carson, W. W., 2003. Fusing LIDAR data, photographs, and other data using 2D and 3D visualization techniques. In: Proceedings of Terrain Data: Applications and Visualization - Making the Connection. American Society for Photogrammetry and Remote Sensing, Charleston, South Carolina: Bethesda, pp. 16–24.

McRoberts, R. E., Cohen, W. B., Næsset, E., Stehman, S. V., Tomppo, E. O., 2010a. Using remotely sensed data to construct and assess forest attribute maps and related spatial products. Scandinavian Journal of Forest Research 25 (4), 340–367.

McRoberts, R. E., Tomppo, E. O., Næsset, E., 2010b. Advances and emerging issues in national forest inventories. Scandinavian Journal of Forest Research 25 (4), 368–381.

Meng, X., Currit, N., Zhao, K., 2010. Ground filtering algorithms for airborne LiDAR data: A review of critical issues. Remote Sensing 2, 833–860.

Missfeldt, F., Haites, E., 2001. The potential contribution of sinks to meeting Kyoto Protocol commitments. Environmental Science and Policy 4 (2001), 269–292.

Mitas, L., Mitasova, H., 1999. Spatial interpolation. Vol. 1 of Geographical information systems: principles and technical issues. Wiley, New York, Ch. 34, pp. 481–492.

Mongus, D., üZalik, B., 2012. Parameter-free ground filtering of LiDAR data for automatic DTM generation. ISPRS Journal of Photogrammetry and Remote Sensing 67, 1–12.

Montealegre, A. L., Lamelas, M. T., Tanase, M. A., de la Riva, J., 2014. Forest Fire Severity Assessment Using ALS Data in aÂ Mediterranean Environment. Remote Sensing 6 (5), 4240–4265.

Morsdorf, F., Kötz, B., Meier, E., Itten, K. I., Allgöwer, B., 2006. Estimation of LAI and fractional cover from small footprint airborne laser scanning data based on gap fraction. Remote Sensing of Environment 104 (1), 50–61.

Mutlu, M., Popescu, S. C., Stripling, C., Spencer, T., 2008. Mapping surface fuel models using lidar and multispectral data fusion for fire behavior. Remote Sensing of Environment 112 (1), 274–285.

Næsset, E., 1997. Determination of mean tree height of forest stands using airborne laser scanner data. ISPRS Journal of Photogrammetry and Remote Sensing 52, 49–56.

Næsset, E., 2004a. Accuracy of forest inventory using airborne laser scanning: evaluating the first nordic full-scale operational project. Scandinavian Journal of Forest Research 19 (6), 554–557.

Næsset, E., 2004b. Practical large-scale forest stand inventory using a small-footprint airborne scanning laser. Scandinavian Journal of Forest Research 19 (2), 164–179.

Næsset, E., 2007. Airborne laser scanning as a method in operational forest inventory: Status of accuracy assessments accomplished in Scandinavia. Scandinavian Journal of Forest Research 22 (5), 433–442.

Næsset, E., Bollandsås, O. M., Gobakken, T., 2005. Comparing regression methods in estimation of biophysical properties of forest stands from two different inventories using laser scanner data. Remote Sensing of Environment 94 (4), 541–553.

Næsset, E., Økland, T., 2002. Estimating tree height and tree crown properties using airborne scanning laser in a boreal nature reserve. Remote Sensing of Environment 79 (1), 105–115.

Noble, I., Scholes, R. J., 2001. Sinks and the Kyoto Protocol. Climate Policy 1 (2001), 5–25.

Nowak, D. J., Crane, D. E., 2002. Carbon storage and sequestration by urban trees in the USA. Environmental Pollution 116 (3), 381–389.

Optech, 2014. Optech Pegasus ALTM. http://www.optech.com/index.php/product/pegasus-altm/, accesed on November 29, 2014.

Pan, Y., Birdsey, R. A., Fang, J., Houghton, R., Kauppi, P. E., Kurz, W. A., Phillips, O. L., Shvidenko, A., Lewis, S. L., Canadell, J. G., Ciais, P., Jackson, R. B., Pacala, S. W., McGuire, A. D., Piao, S., Rautiainen, A., Sitch, S., Hayes, D., 2011. A Large and Persistent Carbon Sink in the World's Forests. Science 333 (6045), 988–993.

Pausas, J. G., Llovet, J., Rodrigo, A., Vallejo, R., 2008. Are wildfires a disaster in the erranean basin?–A review. International Journal of Wildland Fire 17, 713–723.

Peterson, D. L., Johnson, M. C., Agee, J. K., Jain, T. B., Mckenzie, D., Reinhardt, E. D., 2003. Fuels planning: managing forest structure to reduce fire hazard. In: Proceedings of the 2nd International Wildland Fire Ecology and Fire Management Congress. Washington DC. Orlando, FL: American Meteorological Society.

Pflugmacher, D., Cohen, W. B., Kennedy, R. E., Yang, Z., 2014. Using Landsat-derived disturbance and recovery history and lidar to map forest biomass dynamics. Remote Sensing of Environment 151 (0), 124–137.

Popescu, S. C., Zhao, K., 2008. A voxel-based lidar method for estimating crown base height for deciduous and pine trees. Remote Sensing of Environment 112 (3), 767–781.

Reutebuch, S. E., Andersen, H., McGaughey, R. J., 2005. Light Detection and Ranging(LIDAR): An emerging tool for multiple resource inventory. Journal of Forestry, 286–292.

Reutebuch, S. E., McGaughey, R. J., Andersen, H.-E., Carson, W. W., 2003. Accuracy of a high-resolution lidar terrain model under conifer forest canopy. Canadian Journal of Remote Sensing 29 (5), 527–535.

Riaño, D., Chuvieco, E., Condés, S., González-Matesanz, J., Ustin, S. L., 2004. Generation of crown bulk density for Pinus sylvestris L. from lidar. Remote Sensing of Environment 92 (3), 345–352.

Riaño, D., Meier, E., Allgöwer, B., Chuvieco, E., Ustin, S. L., 2003. Modeling airborne laser scanning data for the spatial generation of critical forest parameters in fire behavior modeling. Remote Sensing of Environment 86 (2), 177–186.

Riebau, A. R., Qu, J. J., 2005. Application of Remote Sensing and GIS for Analysis of Forest Fire Risk and Assessment of Forest Degradation. In: Sivakumar, M., Motha, R., Das, H. (Eds.), Natural Disasters and Extreme Events in Agriculture. Springer Berlin Heidelberg, pp. 335–350.

Rizzoli, P., Bräutigam, B., Kraus, T., Martone, M., Krieger, G., 2012. Relative height error analysis of TanDEM-X elevation data. ISPRS Journal of Photogrammetry and Remote Sensing 73 (0), 30–38.

Ronnholm, P., Hyypä, H., Haggren, H., Yu, X., Kaartinen, H., 2004. Calibration of laser-derived tree canopy height estimates by means of photogrammetry techniques. Scandinavian Journal of Forest Research 19, 524–528.

Rose, L. S., Seong, J. C., Ogle, J., Beute, E., Indridason, J., Hall, J. D., Nelson, S., Jones, T., Humphrey, J., 2013. Challenges and lessons from a wetland LiDAR project: a case study of the Okefenokee Swamp, Georgia, USA. Geocarto International 28 (3), 210–226.

Rothermel, R. C., 1983. How to predict the spread and intensity of forest and range fires. Tech. Rep. Gen. Tech. Rep. INT-143. Ogden, U.S. Department of Agriculture, Forest Service, Intermountain Forest and Range Experiment Station.

Saarela, S., Grafström, A., Stahl, G., Kangas, A., Holopainen, M., Tuominen, S., Nordkvist, K., Hyyppä, J., 2015. Model-assisted estimation of growing stock volume using different combinations of LiDAR and Landsat data as auxiliary information. Remote Sensing of Environment 158 (0), 431–440.

San-Miguel-Ayanz, J., Moreno, J. M., Camia, A., 2013. Analysis of large fires in European Mediterranean landscapes: Lessons learned and perspectives. Forest Ecology and Management 294 (0), 11–22.

Schoennagel, T., Veblen, T. T., Romme, W. H., 2004. The interaction of fire, fuels, and climate across Rocky Mountain forests. BioScience 54 (7), 661–676.

Sithole, G., 2001. Filtering of laser altimetry data using a slope adaptive filter. International Archives of Photogrammetry and Remote Sensing XXXIV-3/W4, 203–210.

Sithole, G., Vosselman, G., 2004. Experimental comparison of filter algorithms for bare-earth extraction from airborne laser scanning point clouds. ISPRS Journal of Photogrammetry and Remote Sensing 59, 85–101.

Skowronski, N. S., Clark, K. L., Duveneck, M., Hom, J., 2011. Three-dimensional canopy fuel loading predicted using upward and downward sensing LiDAR systems. Remote Sensing of Environment 115 (2), 703–714.

Slob, S., Hack, R., 2004. 3D terrestrial laser scanning as a new field measurement and monitoring technique. In: Engineering Geology for Infrastructure Planning in Europe. Springer, pp. 179–189.

Smith, S. L., Holland, D. A., Longley, P. A., 2004. The importance of understanding error in lidar digital elevation models. International Archives of Photogrammetry Remote Sensing and Spatial Information Sciences 35, 996–1001.

Stereńczak, K., Kozak, J., 2011. Evaluation of digital terrain models generated in forest conditions from airborne laser scanning data acquired in two seasons. Scandinavian Journal of Forest Research 26 (4), 374–384.

Takahashi, T., Awaya, Y., Hirata, Y., Furuya, N., Sakai, T., Sakai, A., 2008. Effects of flight altitude on LiDAR-derived tree heights in mountainous forests with poor laser penetration rates. Photogrammetric Journal of Finland 21 (1), 86–96.

Takahashi, T., Yamamoto, K., Miyachi, Y., Senda, Y., Tsuzuku, M., 2006. The penetration rate of laser pulses transmitted from a small-footprint airborne LiDAR: a case study in closed canopy, middle-aged pure sugi (Cryptomeria japonica D. Don) and hinoki cypress (Chamaecyparis obtusa Sieb. et Zucc.) stands in Japan. Journal of Forest Research 11 (2), 117–123.

Takahashi, T., Yamamoto, K., Senda, Y., Tsuzuku, M., 2005. Estimating individual tree heights of sugi (Cryptomeria japonica D. Don) plantations in mountainous areas using small-footprint airborne LiDAR. Journal of Forest Research 10 (2), 135–142.

Tinkham, W. T., Smith, A. M., Hoffman, C., Hudak, A. T., Falkowski, M. J., Swanson, M. E., Gessler, P. E., 2012. Investigating the influence of LiDAR ground surface errors on the utility of derived forest inventories. Canadian Journal of Forest Research 42 (3).

Tomppo, E., Gschwantner, T., Lawrence, M., McRoberts, R. E., 2010. National Forest Inventories: Pathways For Common Reporting. Springer.

Ussyshkin, V., Theriault, L., 2011. Airborne Lidar: Advances in Discrete Return Technology for 3D Vegetation Mapping. Remote Sensing 3 (3), 416–434.

van Leeuwen, M., Nieuwenhuis, M., 2010. Retrieval of forest structural parameters using LiDAR remote sensing. European Journal of Forest Research 129, 749–770, 10.1007/s10342-010-0381-4.

van Minnen, J., Strengers, B., Eickhout, B., Swart, R., Leemans, R., 2008. Quantifying the effectiveness of climate change mitigation through forest plantations and carbon sequestration with an integrated land-use model. Carbon Balance and Management 3 (1), 3.

Vauhkonen, J., 2010. Estimating crown base height for Scots pine by means of the 3D geometry of airborne laser scanning data. International Journal of Remote Sensing 31 (5), 1213–1226.

Vauhkonen, J., Næsset, E., Gobakken, T., 2014. Deriving airborne laser scanning based computational canopy volume for forest biomass and allometry studies. ISPRS Journal of Photogrammetry and Remote Sensing 96 (0), 57–66.

Vosselman, G., 2000. Slope based filtering of laser altimetry data. International Archives of Photogrammetry, Remote Sensing and Spatial Information Sciences XXXIII, 935–942.

Wagner, W., Hollaus, M., Briese, C., Ducic, V., 2008. 3D vegetation mapping using small-footprint full-waveform airborne laser scanners. International Journal of Remote Sensing 29 (5), 1433–1452.

Wagner, W., Ullrich, A., Melzer, T., Briese, C., Kraus, K., 2004. From single-pulse to full-waveform airborne laser scanners: potential and practical challenge. International Archives of Photogrammetry and Remote Sensing 35 (Part B), 201–206.

Wang, C., Glenn, N. F., 2008. A linear regression method for tree canopy height estimation using airborne lidar data. Canadian Journal of Remote Sensing 34, S217–S227.

Wang, L., Gong, P., S., B. G., 2004. Individual tree-crown delineation and treetop detection in high spatial-resolution aerial imagery. Photogramm. Eng. Remote Sens. 70, 351–357.

Wehr, A., Lohr, U., 1999. Airborne laser scanning–an introduction and overview. ISPRS Journal of Photogrammetry and Remote Sensing 54, 68–82.

Wei, H., Bartels, M., 2012. 3D Digital Elevation Model Generation. In: 3D Imaging, Analysis and Applications. Springer London, pp. 367–415.

Willcock, S., Phillips, O., Platts, P., Balmford, A., Burgess, N., Lovett, J., Ahrends, A., Bayliss, J., Doggart, N., Doody, K., Fanning, E., Green, J., Hall, J., Howell, K., Marchant, R., Marshall, A., Mbilinyi, B., Munishi, P., Owen, N., Swetnam, R., Topp-Jorgensen, E., Lewis, S., 2014. Quantifying and understanding carbon storage and sequestration within the Eastern Arc Mountains of Tanzania, a tropical biodiversity hotspot. Carbon Balance and Management 9 (1), 2.

Wulder, M. A., Bater, C. W., Coops, N. C., Hilker, T., White, J. C., 2008. The role of LiDAR in sustainable forest management. The Forestry Chronicle 84 (6), 807–826.

Wulder, M. A., Coops, N. C., Hudak, A. T., Morsdorf, F., Nelson, R., Newnham, G., Vastaranta, M., 2013. Status and prospects for LiDAR remote sensing of forested ecosystems. Canadian Journal of Remote Sensing 39 (sup1), S1–S5.

Wulder, M. A., White, J. C., Alvarez, F., Rogan, J., Hawkes, B., 2009. Characterizing boreal forest wildfire with multi-temporal Landsat and LIDAR data. Remote Sensing of Environment 113 (0), 1540–1555.

Wulder, M. A., White, J. C., Nelson, R. F., sset, E. N., rka, H. O. O., Coops, N. C., Hilker, T., Bater, C. W., Gobakken, T., 2012. Lidar sampling for large-area forest characterization: A review. Remote Sensing of Environment 121, 196–209.

Yamamoto, K., Takahashi, T., Miyachi, Y., Kondo, N., Morita, S., Nakao, M., Shibayama, T., Takaichi, Y., Tsuzuku, M., Murate, N., 2011. Estimation of mean tree height using small-footprint airborne LiDAR without a digital terrain model. Journal of Forest Research 16, 425–431.

Yu, X., Hyyppä, H., Maltamo, M., 2004. Effects of Flight Altitude on Tree Height Estimation Using Airborne Laser-Scanning. In: Laser-scanners for forest and landscape assessment. Vol. XXXVI. Freiburg, Germany, pp. 96–101.

Zhang, J., 2010. Multi-source remote sensing data fusion: status and trends. International Journal of Image and Data Fusion 1 (1), 5–24.

Zhang, K., Chen, S., Whitman, D., Shyu, M., Yan, J., Zhang, C., 2003. A progressive morphological filter for removing nonground measuments from airborne LIDAR data. IEEE Transactions on Geoscience and Remote Sensing 41 (4), 872–882.

Zheng, G., Moskal, L. M., 2009. Retrieving Leaf Area Index (LAI) Using Remote Sensing: Theories, Methods and Sensors. Sensors 9 (4), 2719–2745.

PART II: PUBLICATIONS

PUBL. I

Maguya, A., S., Junttila, V. and T. Kauranne, Adaptive Algorithm For Large Scale DTM Interpolation From LiDAR Data For Forestry Applications in Steep Forested Terrain, *ISPRS Journal of Photogrammetry and Remote Sensing*, 85(2013), 74–83, 2013.

ISPRS Journal of Photogrammetry and Remote Sensing 85 (2013) 74–83

Contents lists available at ScienceDirect

ISPRS Journal of Photogrammetry and Remote Sensing

journal homepage: www.elsevier.com/locate/isprsjprs

Adaptive algorithm for large scale dtm interpolation from lidar data for forestry applications in steep forested terrain

Almasi S. Maguya [a,b,*], Virpi Junttila [a], Tuomo Kauranne [a]

[a] Lappeenranta University of Technology, Department of Mathematics and Physics, P.O. Box 20, FI-53851 Lappeenranta, Finland
[b] Mzumbe University, Faculty of Science and Technology, P.O. Box 1, Mzumbe, Morogoro, Tanzania

ARTICLE INFO

Article history:
Received 25 March 2013
Received in revised form 14 July 2013
Accepted 19 August 2013
Available online 21 September 2013

Keywords:
LiDAR processing
DTM extraction
Digital surface modeling
Forestry
Point cloud

ABSTRACT

Light Detection and Ranging (LiDAR) has become a valuable tool in forest inventory because it yields accurate measurements of tree heights. However, tree height can be accurate only if the height of the ground, i. e., the Digital Terrain Model (DTM) is first accurately established.

Although great advances have been made in LiDAR technology over the past decade, filtering LiDAR data for Digital Terrain Model (DTM) interpolation is still a challenge, especially in steep and complex terrain with forest cover. Several algorithms proposed in the literature address this challenge but their performance deteriorates with the decreasing point density caused by the presence of forest cover and steep slopes. In this paper, we propose a new adaptive algorithm for DTM interpolation from LiDAR data in steep terrain with forest cover. The algorithm partitions the input data and estimates a section of the DTM by fitting a linear or quadratic trend surface, or uses cubic spline interpolation depending on the complexity of the section of terrain. The performance of the algorithm is tested in three ways: by visual assessment, by comparison of the tree-height estimates produced using the generated DTM with those obtained using field survey, and by use of International Society for Photogrammetry and Remote Sensing (ISPRS) test data. Test results show that the algorithm can cope well with steep slopes and low LiDAR point densities, giving a more accurate estimate of average tree height compared to conventional algorithms. The algorithm can be used for DTM extraction in large scale forest inventory projects in challenging environments–complex terrain and low LiDAR point densities.

1. Introduction

Digital Terrain Models (DTMs) play a key role in modeling of various geographical phenomena, as well as acting as an intermediate step in modeling of natural resources and man-made features on the earth's surface. For example, DTMs have been used to assess damage caused to the earth's surface after natural disasters (e.g., Kasai et al., 2009). In forestry, DTMs are commonly used to estimate canopy height (e.g., Wang and Glenn, 2008). The estimated canopy height is then used to estimate the mean tree height of forest stands, which is a prerequisite step in multi-resource forest inventory (e.g., Næsset, 1997; van Leeuwen and Nieuwenhuis, 2010; Nord-Larsen and Schumacher, 2012).

Today, several techniques exist for generating DTMs. For example, traditional ground survey, photogrammetry, Interferometric Synthetic Aperture Radar (INSAR), and airborne Light Detection and Ranging (LiDAR). Ground surveys offer high accuracy but are time consuming and laborious, making them unsuitable for large scale applications. On the other hand, due to its passive nature, photogrammetry does not perform well in places with forest cover and during unfavorable weather conditions (e.g., clouds and haze) because the aerial photography process and the quality of the resulting photographs are adversely affected (Kraus and Pfeifer, 1998; Kilian et al., 1996). LiDAR and INSAR have been the technologies of choice for large scale applications because of their accuracy and the ability to cover large areas at relatively low cost (Lemmens, 2011; Wilson, 2012; Zhou et al., 2012).

Over the last decade, LiDAR technology has undergone significant development that has increased its potential for generating high quality DTMs, especially for large scale applications such as forestry (Hyyppä et al., 2004; Lemmens, 2011). These advances include enhanced sensor technology (increased pulse rates) and the introduction of full wave form LiDAR systems (Lemmens, 2011).

Many algorithms for generating DTMs from LiDAR data have been developed in tandem with these changes (Liu, 2008; Meng et al., 2010). These include algorithms for removing non-ground points

* Corresponding author at: Lappeenranta University of Technology, Department of Mathematics and Physics, P.O. Box 20, FI-53851 Lappeenranta, Finland. Tel.: +358 465 233232; fax: +358 5 621 2350.
E-mail addresses: almasi.maguya@lut.fi (A.S. Maguya), virpi.junttila@lut.fi (V. Junttila), tuomo.kauranne@lut.fi (T. Kauranne).

0924-2716/$ - see front matter © 2013 International Society for Photogrammetry and Remote Sensing, Inc. (ISPRS) Published by Elsevier B.V. All rights reserved.
http://dx.doi.org/10.1016/j.isprsjprs.2013.08.005

from LiDAR data (ground filtering), as well as algorithms for DTM interpolation from filtered LiDAR data.

However, many of these algorithms do not perform well in steep and forested terrain, and when LiDAR data density is low. The high accuracy and cost effectiveness of LiDAR make extraction of accurate DTMs from LiDAR data for large scale forestry applications (e.g., above ground biomass estimation) a worthwhile area of investigation. In such applications, flight height is normally relatively high (1–2 km above ground) and the LiDAR footprint is relatively large (0.5 m), resulting in low LiDAR point densities. Although some filtering algorithms (e.g., Mongus and Žalik, 2012; Kobler et al., 2006) have shown good performance on steep slopes and in forested terrain, the reported results are based on data with relatively high point densities collected from low flight heights (typically 200–300 m above ground).

In this paper we present a new, hybrid, adaptive algorithm for DTM interpolation from LiDAR in steep forested terrain. The algorithm is adaptive in the sense that it automatically adapts to terrain changes in the heterogeneous terrains typical of large tropical forests in which steep slopes and a limited number of LiDAR pulses reaching the ground makes the task of DTM extraction challenging for most conventional algorithms.

To overcome the challenges posed by heterogeneous terrain and low LiDAR point densities, the algorithm presented in this paper conducts LiDAR ground filtering in two steps: it automatically adapts to variations in the terrain and takes into account a set of candidate ground points in a neighborhood while filtering ground points. The benefit of this approach over most existing filtering methods is that it does not require the user of the algorithm to determine a single threshold value (representative of the terrain slope) since this can prove to be impractical in highly heterogeneous terrains.

Since the algorithm has been designed to cope with low LiDAR point densities, it is suitable for DTM extraction in large scale forestry applications, especially those which require estimation of tree heights.

The paper is organized as follows. A review of existing algorithms for LiDAR data processing is given is Section 2. In Section 3, an overview of the study area and test data is given, followed by a detailed description of the proposed algorithm. Section 4 presents accuracy assessment of the algorithm, followed by discussion and conclusions in Section 5.

2. Background

This section presents a survey of existing methods for LiDAR data processing. The state of the art in both LiDAR ground filtering and DTM interpolation is presented.

2.1. Ground filtering algorithms

Ground filtering algorithms fall into four major classes: (1) slope based, (2) interpolation based, (3) mathematical morphology based, and (4) hybrid ground filters. A brief overview of these algorithms, which from this point on may also be simply referred to as filters, is given below.

2.1.1. Slope-based filters

Slope based filters work by comparing the slope between two adjacent points to a pre-determined threshold value. The assumption they make is that the slope (and hence the height) between two adjacent ground points is smaller than the slope between a ground point and a non-ground point. Hence, if the slope between two points is larger than the threshold value, the point with a higher altitude value is considered to be a non-ground point. An example of a slope based filter is that proposed by Vosselman (2000). The algorithm compares the height difference between two points as a function of their distance apart against the acceptable height difference. A point is regarded as a ground point only if there is no other point such that the height difference between the two points, computed as a function of their distance apart, is larger than the allowed maximum.

Several studies have compared the performance of ground filtering algorithms (e.g., Sithole and Vosselman, 2004; Liu, 2008; Meng et al., 2010). These studies show that slope-based algorithms work well with LiDAR data from relatively flat terrain but perform poorly with data from complex and steep terrain. One reason for the poor performance is the fact that in steep terrain the height or slope between two ground points can be higher than the predetermined threshold value, which causes many ground points to be misclassified as non-ground. Moreover, determining a good slope threshold may prove to be a very difficult task. To overcome these difficulties, several adaptive filters have been proposed. For example, to overcome the problem of determining a threshold, Sithole (2001) proposed a modified slope-based filter in which the threshold varied with the slope of the terrain. Using this approach fewer ground points were misclassified.

2.1.2. Interpolation-based filters

While most slope-based algorithms work with two data points at a time, interpolation-based filters operate on all points in the data set at once. These filters are iterative algorithms which work by fitting a surface on the data and iteratively filtering points based on their residuals from the fitted surface. In the first iteration, an averaging surface is fit into the data and the residuals of the data points relative to the surface are computed. Ground points are more likely to have negative residuals, so they are given more weight in subsequent iterations. Kraus and Pfeifer (1998) were the first to propose this approach. Their algorithm is based on linear prediction, whereby in the first iteration all points are given equal weights. A special function is used to compute weights for each point based on their residuals. In each iteration, points with large negative residuals are given maximum weights and thus they attract the computed surface towards themselves. Points with medium residuals get smaller weights and therefore have little influence on the computed surface.

Like slope-based filters, interpolation-based filters perform poorly in steep terrain. A similar method based on thin plate spline surface interpolation has, however, been found to yield good results in steep terrain. Mongus and Žalik (2012) have recently proposed a ground filtering algorithm in which a thin plate spline interpolated surface is used iteratively to approximate the ground surface. The approach uses residuals of points from the surface in each iteration with a gradually decreasing window size to filter ground points.i While test results showed that the algorithm can cope well with steep terrain, the results also showed that the algorithm did not perform well with the low point densities commonly found in forest data sets.

2.1.3. Mathematical-morphology-based filters

Mathematical-morphology-based filters are based on the concept of mathematical morphology used in digital image analysis. Unlike slope-based and interpolation-based filters, which work on the original LiDAR data, filters based on mathematical morphology transform the LiDAR data into digital images before performing actual filtering. Filtering is done using morphological operations such as *opening* and *closing* (Chen et al., 2007; Zhang et al., 2003).

These filters are simple and easy to implement and perform relatively well in filtering surface objects, such as buildings, provided that the data contain a high density of ground points. However, the filters perform poorly with low point density in the data and steep

terrains (Sithole and Vosselman, 2004; Liu, 2008; Meng et al., 2010).

2.1.4. Hybrid filters

Some filtering algorithms do not directly fall into any of the above classes. They either use a different approach to filtering or make use of a combination of techniques used in other filters. For example, Kobler et al. (2006) proposed a two-stage algorithm whereby in the first stage negative outliers are removed using some existing filtering algorithm (e.g., morphological filter) and most non-ground points are then removed using a slope-based filter. This stage produces partially filtered data which enters the second stage of the algorithm. In the second stage, elevations at unsampled locations are estimated from repeated independent estimates of elevation samples taken from sampled points. By combining different filtering methods, the algorithm performed better than the individual filters.

2.2. DTM interpolation algorithms

With the exception of morphology-based filters, ground filtering algorithms produce irregularly distributed ground points. Interpolation is used with these points to estimate ground elevation at places where measurements are missing. Interpolation algorithms can be categorized based on the following criteria (Ali, 2004): (1) exact or inexact (2) deterministic or stochastic, and (3) local or global.

Exact interpolation algorithms produce DTM surfaces which pass through every original data point, while approximative interpolation methods produce surfaces which do not pass through every original data point but rather follow the general trend in the data. Examples of exact interpolation algorithms are inverse distance weighting (IDW) and spline interpolation. An example of an inexact interpolation algorithm is trend functions (surfaces). Deterministic interpolation algorithms assume that every data point has influence at an unsampled location that is inversely proportional to its distance from the location. Stochastic algorithms, on the other hand, make use of geostatistics to estimate a surface with some level of uncertainty. Local interpolation algorithms use only neighboring data points to estimate a value at an unsampled location, while global algorithms use the entire data set to estimate values at unsampled locations. Examples of commonly used interpolation algorithms in DTM generation include inverse distance weighting (IDW) (exact, deterministic, local), Kriging (approximative, global, stochastic), and cubic splines (exact, local, deterministic) (Ali, 2004; Liu, 2008).

The choice of an interpolation algorithm to be implemented depends on several factors, including the quality of data and required level of accuracy. For example, IDW offers high accuracy but only when data density is high.

3. Material and methods

3.1. Study area

The study area consists of three watersheds in Nepal, namely, Kayarkhola (Chitwan district), Ludikhola (Ghorka district), and Charnawati (Dolakha district). This area was selected for a pilot project called *Design and setting up of a governance and payment system for Nepal's Community Forest Management under Reducing Emissions from Deforestation and Forest Degradation* (REDD) whose aim was to demonstrate the feasibility of the REDD payment mechanism in community forests. The REDD project is funded mainly by the World Bank.

Table 1
Characteristics of the three watersheds in the study area. Key: DF = Dense Forest, SF = Sparse Forest, BS = Bare Soil, OT = Other. Source: Land Cover Analysis Report (2010).

Watershed	Area (ha)	Alt. (m)	Land use (%)			
			DF	SF	BS	OT
Kayarkhola	8002	245–1944	51.48	21.27	0.38	26.88
Charnawati	14,037	835–3549	35.56	17.82	4.48	42.14
Ludikhola	5750	318–1714	67.34	17.31	4.19	11.16

Table 1 presents a summary of the characteristics of the three watersheds. The other land uses (OT) shown in Table 1 include grasslands and degraded forests, natural water bodies, agricultural land, and built-up areas.

The terrain in the area consists predominantly of steep slopes and hills, with the Charnawati watershed having the highest variation in altitude. The dominant tree species in the area are *Hill Shorea Robusta*, *Schima Castanopsis* and *Rhododendron*.

3.2. Test data

LIDAR data used in this study covers an area of 13,750 ha and were collected in four separate flight missions between March and April 2011. The data were collected using a Leica ALS50-II laser scanner mounted on a Eurocopter AS350 helicopter (9N-AIW). Flying altitude and speed were 2200 m (relative to ground level) and 80 knots respectively. Sensor pulse rate and scan speed were 52.9 kHz and 20.4 lines per second respectively.

These flight parameters led to a swath width of 1601.47 m at ground level, a beam footprint of 50 cm, an average point density of 0.8 points per square meter, and a maximum point spacing of 1.88 m across and 2.02 m down.

The data were collected for the Forest Resource Assessment (FRA) and the Ministry of Forests and Soil Conservation of Nepal. The data were provided courtesy of Arbonaut Ltd. (Finland) and the International Center for Integrated Mountain Development (ICIMOD) in Nepal. The data were provided in raw (LAS ver. 1.2) format and, for each point, it contained, among other fields, intensity, scan angle, return number (1–4), easting, northing, and elevation.

3.3. Proposed algorithm

The operation of the algorithm is based on the assumption that when generating a DTM for complex terrain that is made up of a combination of hills, steep slopes and plateau, the terrain can be partitioned into patches of land that can be modeled using a combination of trend surfaces (for relatively less complex patches) and cubic splines (for more complex patches). The partitioning is done by dividing the x-y plane into square patches (tiles) of a given width (W). Data points falling within a given square are then used to interpolate the corresponding section of the DTM. Fig. 1 shows examples of patches of land of varying complexity which require different interpolation strategies.

Once the data has been partitioned, the algorithm proceeds in two steps: (1) filtering of non-ground points, and (2) DTM interpolation. The first step is governed by two parameters: quality of fit (r^2) and search window width (w). r^2 varies between 0 and 1, controls the accuracy of the DTM (the higher the better), and enables the algorithm to adapt to changes in terrain by choosing an appropriate interpolation strategy based on the complexity of the current patch. The value of r^2 was calculated using Eq. (1).

$$R^2 = 1 - \frac{RSS}{TSS} \tag{1}$$

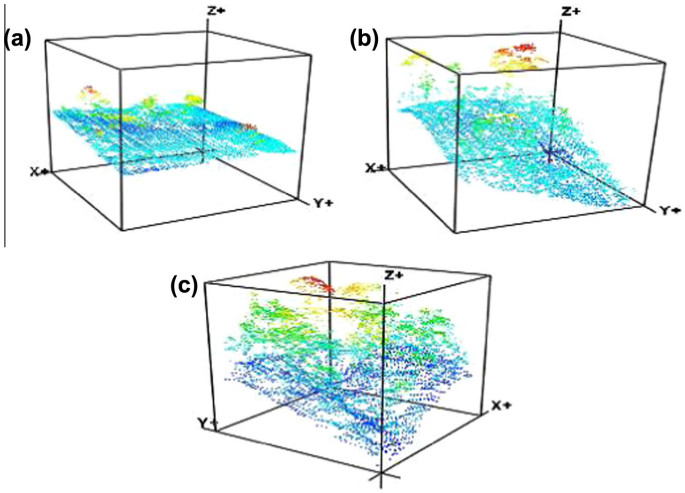

Fig. 1. Examples of square terrain sections of 400 m in width which require different interpolation strategies: (a) planar trend surface, (b) parabolic trend surface, and (c) cubic spline interpolation. The *x*- and *y*-axes represent the easting and northing while the *z*-axis represents elevation.

where *RSS* and *TSS* stand for Residual Sum of Squares and Total Sum of Squares respectively and were calculated using Eqs. (2) and (3)

$$RSS = \sum_{i=1}^{n} (y_i - \hat{y}_i)^2 \tag{2}$$

$$TSS = \sum_{i=1}^{n} (y_i - \bar{y})^2 \tag{3}$$

where the y's are observed minimum elevation values at the current patch, the $\hat{y}$'s are predicted elevation values, $\bar{y}$ is the mean of the y's, and n is the number of observed elevation values.

The value of w determines the area to search for a point with the lowest elevation value (to be used in interpolating the section of DTM). In this study, the values of r^2, w, and W used were 0.95, 5 m, and 40 m respectively. The high value of r^2 used was chosen in order to attain high DTM accuracy. On the other hand, the value of w used was dictated by the data density (points per square meter). In general, the smaller the value of w the better because it helps to minimize interpolation error. With the LiDAR data used in this study, values of w less than 5 m led to search windows that repeatedly contained no points. We determined the optimal value of W by experimenting with a range of values (10–80 m) looking for a value that is robust, minimizes border effects, and works well across the entire study area (terrain) and with the given data.

3.3.1. Ground filtering

To filter non-ground points, a moving window of width w is moved across a patch and, at each location, the window area is searched for a point with the lowest elevation value. The elevation of this point is assigned to the location. If no points are found, the location is left blank. This procedure results in a set of points spaced at least w m apart in the patch. These points are a combination of both first and last returns and all are assumed to be ground points at this stage.

In the second step, two trend surfaces represented by Eqs. (4) and (5) are fit into the grid points obtained previously.

$$Z_1(x,y) = \beta_0^1 + \beta_1^1 x + \beta_2^1 y + \epsilon_1 \tag{4}$$

$$Z_2(x,y) = \beta_0^2 + \beta_1^2 x + \beta_2^2 y + \beta_{12}^2 xy + \beta_{11}^2 x^2 + \beta_{22}^2 y^2 + \epsilon_2 \tag{5}$$

where the β's represent model parameters with the superscript distinguishing the models and the ϵ's are residual terms. x and y represent the easting and northing values respectively at the center of a 5 m grid cell.

For each trend surface, residuals and r^2 values are computed. Points with negative residuals (set A) below the surfaces are assumed to be ground points and are therefore retained. Points with positive residuals (set B) above each surface are considered to consist of a mixture of both ground and non-ground points. At this stage, if either model has a value of r^2 below the threshold value, it is discarded.

Filtering of non-ground points is done on points in set B of the model(s) which pass the goodness-of-fit test as follows. Points in B are sorted in descending order of residuals. Starting with the point with the largest positive residual, each point is left out in turn and the corresponding surface is re-fit using the remaining points in both A and B. The value of r^2 for the new surface is computed and compared to the previous value. If the value of r^2 increases, the point is considered to be a non-ground point and discarded from B; otherwise the point is considered to be a ground point and is therefore retained (see Fig. 2).

In Fig. 2, the value of r^2 for the linear model improved from 0.96 to 0.97 after removing non-ground points, while r^2 for the quadratic model improved from 0.96 to 0.98.

The result of the second stage of filtering is either two sets of ground points corresponding to Eqs. (4) and (5) (if both models passed the r^2 test), one set of points (if only one model passed the r^2 test), or an empty set (if both models failed the r^2 test). If the first case prevails, the set corresponding to a smaller value of r^2 is discarded, while the remaining set (C) is used to interpolate the portion of DTM for the current patch. Failure of both models in the r^2 test means that the patch is too complex to be reasonably

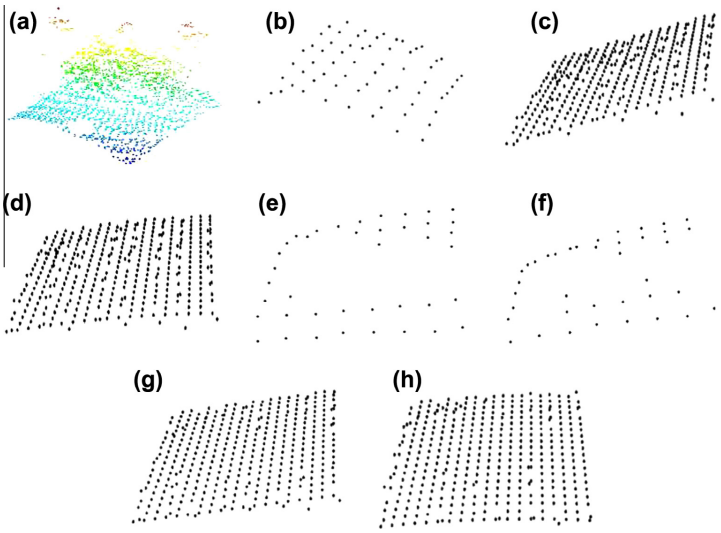

Fig. 2. Ground filtering steps: (a) point cloud for a 160 m^2 patch; (b) points with minimum elevation values obtained from a 5 m search window in the point cloud in (a); (c) and (d) linear and quadratic surfaces (sampled) fitted to points in (b) showing points below the surfaces (set A) and points above the surfaces (set B); (e) and (f) points remaining in the linear and quadratic models after non-ground points have been removed from points in (b); (g) and (h) linear and quadratic models refit after removing non-ground points.

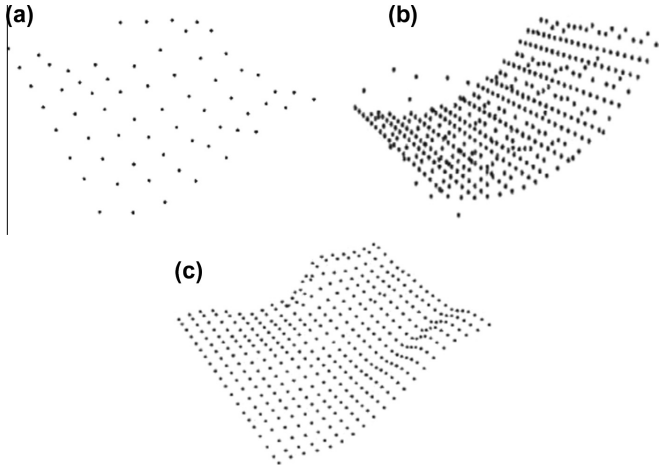

Fig. 3. Illustration of a case when both the linear and quadratic models fail. (a) shows a grid of minimum points extracted from a point cloud while (b) and (c) show a quadratic and cubic splines fit of the data. Note how the quadratic model fails to follow the trend in the data. The r^2 values for the quadratic and linear (not shown) models were 0.39 and 0.65 respectively.

estimated by either of the models. In this case the algorithm resorts to cubic splines (see Section 3.3.3) as illustrated in Fig. 3.

3.3.2. DTM interpolation

Ground points obtained in the filtering step are used to interpolate the section of DTM in the respective patch. Inputs to this stage include the desired DTM resolution (d), model parameters obtained in the filtering step, and ground points in C.

To assign elevation values at unsampled locations, a regular square grid of width W and cell size d is created such that it spans all the data points in C. Each cell of the grid is visited in turn and assigned an elevation value as follows. The cell is searched for

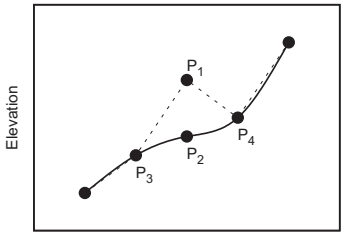

Fig. 4. Detection and replacement of non-ground points during spline interpolation. Due to a change of slope at point P_1, elevation at P_1 is replaced with P_2, whose elevation is the average of elevations at P_3 and P_4.

points (in C) lying within it. If any points are found, the minimum elevation among the points is assigned to the current grid cell, otherwise the elevation at the current cell is obtained by evaluating the trend surface function obtained in the filtering step using the easting and northing values at the cell.

3.3.3. Spline interpolation

Spline interpolation is performed when both linear and quadratic models fail. The input to this stage is points in sets A and B. Before interpolation, non-ground points are identified and discarded. This is achieved by scanning the points in two passes, first along the x-axis, then along the y-axis. Change of slope (positive to negative) is examined (for each point in a line) (see Fig. 4). If there is a change in slope across a point, the point is considered to present a discontinuity in the terrain. All such points are labeled for replacement and their elevations are replaced by the average elevation of their right and left neighbors.

After the second filtering pass, points labeled for replacement are replaced and the remaining points are used for DTM interpolation. First, cubic splines are used to interpolate elevations on each line along the y-axis according to the specified DTM resolution (Fig. 5(a)). Next, interpolation is done along the x-axis as shown in Fig. 5(b). This completes the DTM interpolation step for the current patch. An example of the resulting DTM section is shown in Fig. 5(c).

3.3.4. Degenerate cases

If the area covered by input LIDAR is not rectangular in shape (e.g., if it is triangular), some of the square patches along the diagonal will have very little data. When this happens, neither a linear nor a quadratic trend surface can be fitted to the data as the model matrix in the linear model

$$\mathbf{Y} = \mathbf{X}\boldsymbol{\beta} + \boldsymbol{\epsilon}$$

used in least squares model fitting becomes singular, where $\mathbf{Y}$ is a vector of measured elevations, $\mathbf{X}$ is the model matrix, $\boldsymbol{\beta}$ is a vector of unknown parameters, and $\boldsymbol{\epsilon}$ is a vector of residuals. In such cases, spline interpolation also fails because the data do not form a complete grid of points. This problem can also arise if there are embedded gaps in the data. When this happens the algorithm skips the current patch, leading to gaps in the resulting interpolated DTM. The effect of this problem can be reduced by decreasing the patch width (W), but the feasibility of this solution depends on the data density.

4. Results and discussion

In this section, we present and discuss the results of the accuracy assessment of the proposed algorithm. Accuracy of the algorithm was evaluated in three ways: (1) by visually inspecting the produced DTM; (2) by comparing tree height estimates obtained using the produced DTM with field measurements; and, (3) by testing the algorithm against the International Society for Photogrammetry and Remote Sensing (ISPRS) Commission III/WG3 test data set (See Sithole and Vosselman, 2004).

4.1. Visual inspection of the DTM

The first performance assessment measure entailed visual inspection of the final DTM and intermediate results of the algorithm. In addition, the DTM was compared to a DTM produced by an algorithm for determination of terrain models in wooded areas proposed by Kraus and Pfeifer (1998) and implemented in

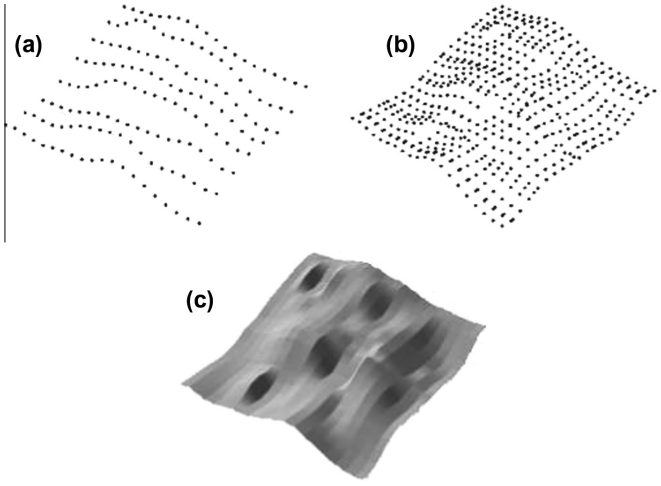

Fig. 5. Spline interpolation stages: (a) interpolation along the y-axis, (b) interpolation along the x-axis using points obtained in (a), and (c) the resulting DTM section.

Fig. 6. Example DTM section generated from a hilly area of approximately 1 km^2. Assessment of how well the DTM follows the variations in the terrain was done by superimposing the original LiDAR point cloud on the DTM.

Fusion software (see McGaughey, 2008). The comparison was based on how well the resulting DTM follows variations in the terrain–slopes,ridges and valleys, and how well the DTM fits the original data. Results are shown in Figs. 6, 7, and 10.

Fig. 6 shows a DTM section for a part of the study area. It can be seen that all the significant terrain features (hills and valleys) are reproduced.

Figs. 7 and 8 show a comparison of DTM sections produced by the proposed algorithm ((a) and (c)) with those produced by the algorithm by Kraus and Pfeifer (1998) ((b) and (d)) using the same data. From Fig. 7, it can be seen that the algorithm proposed in this paper performed better both in terms of smoothness of the DTM and in reproducing the physical features of the terrain. The presence of humps in the DTM in (b), caused by the limited number of ground points in the data, should be noted.

The presence of ridges in the DTM in Fig. 7(c) and the extreme values in the difference model in Fig. 8 should also be noted. The

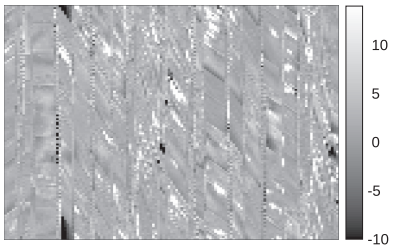

Fig. 8. A difference model obtained by subtracting elevation values of the DTM in Fig. 7(c) from corresponding values in the DTM in Fig. 7(d). Elevation values are in metres.

ridges are due to a lack of overlaps between the patches, which makes DTM interpolation unstable at the borders of the patches. However, due to the way the LiDAR data is normalized using the DTM, the ridges do not make a direct contribution to the error in tree-height estimates computed using the DTM. In normalizing the data, the elevation of each point is subtracted from the elevation of the nearest point on the DTM surface with distance measured in the x–y plane (see Fig. 9). Thus, the error is constrained within individual DTM patches. A possible solution to this problem is to incorporate overlaps in DTM interpolation. On the other hand, the extreme values in Fig. 8 are due to the presence of humps in both Fig. 7(c) and (d). The humps occur at places where there are extremely few ground points caused by closed canopy which leads which makes the algorithms classify points from tree branches as ground points.

The proposed algorithm is designed for use in forestry inventory where a DTM is used to obtain the height of trees. Fig. 10 shows two examples of LiDAR point clouds for complex terrain ((a) and (b)), the resulting DTM sections ((c) and (d)), and the original LiDAR point clouds superimposed on the DTM sections ((e) and (f)). The figure shows that the DTMs fit the data reasonably well ((e) and (f)), leading to accurate tree-height estimates.

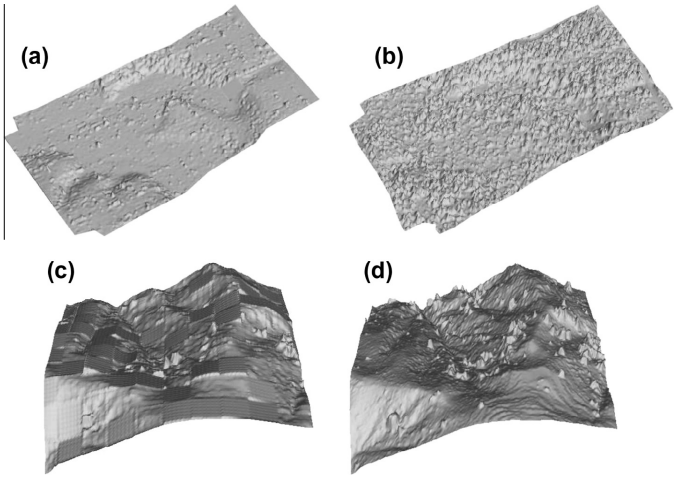

Fig. 7. Comparison of DTM sections produced by the algorithm proposed in this paper ((a) and (c)) with those produced by an algorithm proposed by Kraus and Pfeifer (1998) ((b) and (d)). (a) and (b) are approximately 0.3 km^2 while (c) and (d) are are approximately 0.16 km^2.

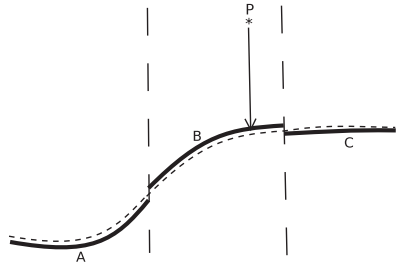

Fig. 9. Illustration of how LIDAR points are normalized. A, B, and C represent misaligned patches (border effects) and the dashed curve represents the true ground surface.

4.2. Comparison with field measurements

In this section, we compare tree heights computed from the DTM obtained using the proposed algorithm and those computed from a DTM obtained from Terrascan software (TS)(Terrascan, 2012) with tree heights obtained from field measurements.

Field measurements used for comparison consisted of tree-height measurements from eighty circular plots with a radius of 12.62 m each. For each plot, the measurements consisted of the heights of all trees in the plot with a diameter at breast height (DBH) greater than or equal to 5 cm. The heights were measured using the Vertex IV and Transponder T3 devices.

The height of the tallest tree in each plot was calculated using both the DTM generated from the algorithm proposed in this paper and the one generated from TS. The height was estimated by taking the average of the heights of the ten highest LIDAR points in each plot. This approach was used because it was not possible to accurately distinguish individual trees within a plot due to low LIDAR point density, hence the assumption that the highest LIDAR points are more likely to belong to the tallest tree in a plot.

Root mean square values of the height estimates found using the proposed algorithm and TS were computed using Eq. (6) and compared.

$$RMSE = \sqrt{\frac{\sum (H_e - H_m)^2}{n}} \tag{6}$$

where H_e is the estimated height, H_m is the measured height and n is the number of plots.

The RMSE for the height estimates found using the proposed algorithm and those found using TS were 1.92 m and 3.04 m respectively. Fig. 11 shows scatter plots of heights computed by

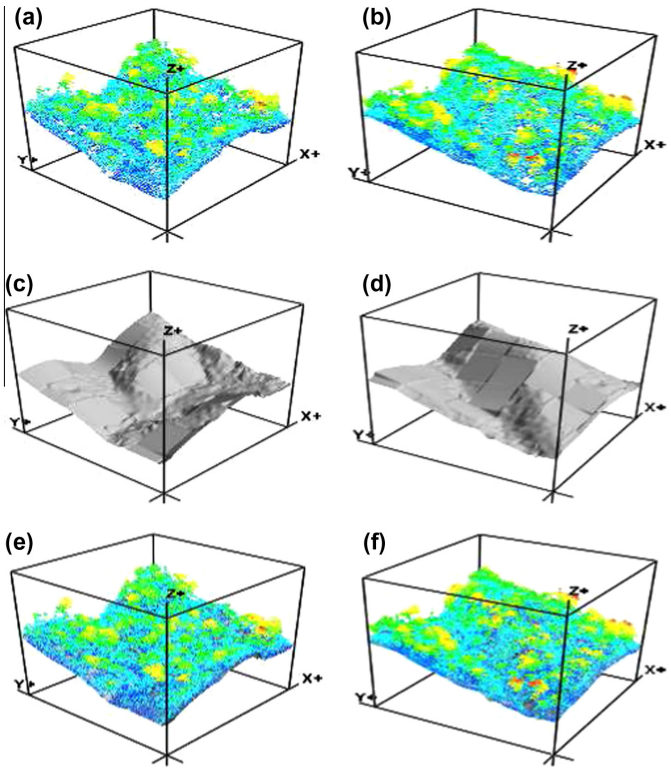

Fig. 10. LIDAR data from square patches of 400 m in width (top row), corresponding DTM sections interpolated from the data (middle row), and original data superimposed on the DTM sections (bottom row). The x- and y-axes represent the easting and northing, while the z-axis represents elevation.

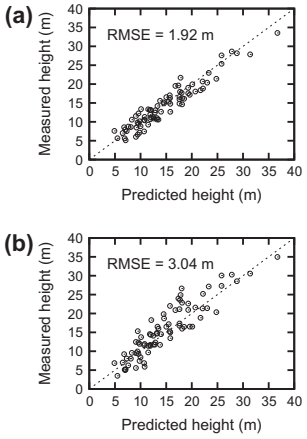

Fig. 11. Scatter plots showing comparison of tree heights computed using the proposed algorithm ((a)) and those computed using TS ((b)) with field-measured tree heights for 80 plots.

the two methods against measured heights.

The RMSE figures reported should, however, be taken as a relative measure of the performance of the two methods only. This is due to the presence of uncertainty in the field measurements (e.g., data entry and instrument errors) and the way the height of the tallest tree in the plots was calculated. For example, branches of tall trees outside the plot but overhanging the plot would be taken as the tallest tree in the plot and contribute to the error.

4.3. ISPRS test data

The ISPRS maintains a set of LIDAR test data used for testing ground filtering algorithms. The data come from different test sites including both city and forest. The data used in this test are from Site 5 (vegetation on a steep slope). The aim of the test was to determine how well the algorithm performs in extreme conditions (e.g., the presence of gaps in the data). ISPRS test data were used because the data set was specifically designed for testing algorithms and comes with reference data.

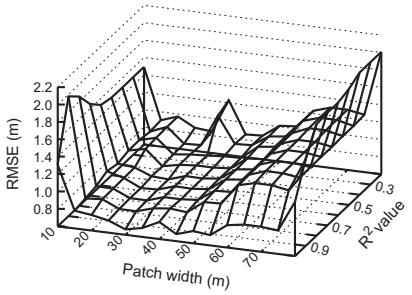

Fig. 12. Plot showing how RMSE varies with patch width (W) and r^2 for the ISPRS test data.

Assessment was done by investigating the effect of the values patch width (W) and r^2 on the resulting DTM root mean square error (RMSE). Fig. 12 shows how RMSE varies with both W and r^2.

With the ISPRS data, the smallest value of RMSE found was about 0.45 m at W = 45 m and $r^2 = 0.9$. RMSE was calculated by normalizing the ground points in the reference data against the DTM using Eq. (7).

$$RMSE = \sqrt{\frac{\sum (Z_{DTM} - Z_{Ref})^2}{n}} \tag{7}$$

where $Z_{DTM} = dtm$ elevation value, Z_{Ref} = reference elevation value, and n = number of sample points. In this case $Z_{Ref} = 0$ (ground points).

The relatively high value of RMSE (0.45 m) is due to the presence of gaps in the test data. As the algorithm cannot cope well with gaps in the data (e.g., those caused by the inability of water to reflect laser pulses), the resulting DTM also contains gaps (as big as the size of the patch used). Gaps in the DTM add significantly to the elevation error of points in the original data falling within the gap, because the height of a point is calculated by subtracting the elevation of the nearest point on the DTM from the elevation of the point. In the presence of gaps in the DTM, the distance between a point in the original data to the nearest point on the DTM can be large, leading to a large elevation error.

5. Conclusions

This paper presented an adaptive algorithm for DTM interpolation in heterogeneous forested terrain consisting of steep slopes, valleys and ridges. The algorithm is based on three kinds of approximation (linear, quadratic and cubic splines) applied iteratively over the terrain using square patches of a given width. Test results showed that the algorithm can cope well with steep slopes and variations in terrain structure. Moreover, since the algorithm uses only a subset of the ground points to interpolate DTM, it can cope well with low point densities in the data. This quality makes the algorithm suitable for large scale LIDAR applications for estimating AGB in large forests where data densities are normally low, due to higher flight heights and the relatively larger LIDAR footprints used in order to reduce data acquisition costs.

Gaps in the input data were found to pose a big challenge to the algorithm. However, the effect of this problem on the accuracy of the heights computed using the DTM can be reduced by reducing the patch width (W) (if the data allows). Moreover, before the algorithm proceeds the original LIDAR data is partitioned (tiled) into manageable blocks that can fit in computer memory. Partitioning the data such that gaps in the data lie in the boundaries of the blocks will also help to minimize the problem. We did not take into account overlaps between patches during DTM interpolation, which led to unstable interpolation along the edges of the patches and contributed to the overall DTM error. Therefore, further work needs to be done to improve the ability of the algorithm to handle gaps in data, and to improve the robustness of the algorithm by incorporating overlaps in the DTM interpolation stage. Additionally, above ground biomass (AGB) estimation tests with LIDAR data from different tropical forests need to be conducted.

Acknowledgements

We would like to express our gratitude to Arbounat Ltd. and ICIMOD for providing the data used in this study. We also thank Risto Rautiainen of Arbonaut Ltd. for his help in answering our queries about the data over the course of this study.

References

Ali, T.A., 2004. On the selection of an interpolation method for creating a terrain model (TM) from LIDAR data. In: Proceedings of the American Congress on Surveying and Mapping (ACSM) Conference. Nashville TN, USA.

Chen, Q., Gong, P., Baldocchi, D., Xie, G., 2007. Filtering airborne laser scanning data with morphological methods. Photogrammetric Engineering & Remote Sensing 73 (2), 175–185.

Hyyppä, J., Hyyppä, H., Litkey, P., Yu, X., Haggrén, H., Rönnholm, P., Pyysalo, U., Pitkänen, J., Maltamo, M., 2004. Algorithms and methods of airborne laser scanning for forest measurements. International Archives of Photogrammetry, Remote Sensing and Spatial Information Sciences XXXVI (8/W2), 82–89.

Kasai, M., Ikeda, M., Asahina, T., Fujisawa, K., 2009. LiDAR-derived DEM evaluation of deep-seated landslides in a steep and rocky region of Japan. Geomorphology 113 (12), 57–69.

Kilian, J., Haala, N., Englich, M., 1996. Capture and evaluation of airborne laser scanner data. International Archives of Photogrammetry, Remote Sensing and Spatial Information Sciences XXXI (B3), 383–388.

Kobler, A., Pfeifer, N., Ogrinc, P., Todorovski, L., Oštir, K., Džeroski, S., 2006. Repetitive interpolation: a robust algorithm for DTM generation from aerial laser scanner data in forested terrain. Remote Sensing of Environment 108 (2007), 9–23.

Kraus, K., Pfeifer, N., 1998. Determination of terrain models in wooded areas with airborne laser scanner data. ISPRS Journal of Photogrammetry and Remote Sensing 53, 193–203.

Lemmens, M., 2011. Airborne lidar. In: Gatrell, J.D., Jensen, R.R. (Eds.), Geo-information, Geotechnologies and the Environment, vol. 5. Springer, Netherlands, pp. 153–170.

Liu, X., 2008. Airborne LiDAR for DEM generation: some critical issues. Progress in Physical Geography 32 (1), 31–49.

McGaughey, R.J., 2008. Fusion software web page. <http://forsys.cfr.washington.edu/fusion/fusionlatest.html> (accessed 22.01.13).

Meng, X., Currit, N., Zhao, K., 2010. Ground filtering algorithms for airborne LiDAR data: a review of critical issues. Remote Sensing 2, 833–860.

Mongus, D., Žalik, B., 2012. Parameter-free ground filtering of LiDAR data for automatic DTM generation. ISPRS Journal of Photogrammetry and Remote Sensing 67, 1–12.

Næsset, E., 1997. Estimating timber volume of forest stands using airborne laser scanner data. Remote Sensing of Environment 61, 246–253.

Nord-Larsen, T., Schumacher, J., 2012. Estimation of forest resources from a country wide laser scanning survey and national forest inventory data. Remote Sensing of Environment 119, 148–157.

Sithole, G., Vosselman, G., 2004. Experimental comparison of filter algorithms for bare-earth extraction from airborne laser scanning point clouds. ISPRS Journal of Photogrammetry and Remote Sensing 59, 85–101.

Sithole, G., 2001. Filtering of laser altimetry data using a slope adaptive filter. International Archives of Photogrammetry, Remote Sensing and Spatial Information Sciences XXXIV (3/W4), 203–210.

Terrascan, 2012. Terrasolid's software for Lidar data processing and 3D vector data creation. <http://www.terrasolid.com/products/terrascanpage.html> (accessed 20.05.13).

van Leeuwen, M., Nieuwenhuis, M., 2010. Retrieval of forest structural parameters using LiDAR remote sensing. European Journal of Forest Research 129, 749–770.

Vosselman, G., 2000. Slope based filtering of laser altimetry data. International Archives of Photogrammetry, Remote Sensing and Spatial Information Sciences XXXIII (B3/2; Part 3), 935–942.

Wang, C., Glenn, N.F., 2008. A linear regression method for tree canopy height estimation using airborne lidar data. Canadian Journal of Remote Sensing 34, S217–S227.

Wilson, J.P., 2012. Digital terrain modeling. Geomorphology 137 (1), 107–121.

Zhang, K., Chen, S., Whitman, D., Shyu, M., Yan, J., Zhang, C., 2003. A progressive morphological filter for removing non ground measurements from airborne LIDAR data. IEEE Transactions on Geoscience and Remote Sensing 41 (4), 872–882.

Zhou, H., Zhang, J., Gong, L., Shang, X., 2012. Comparison and validation of different DEM data derived from InSAR. Procedia Environmental Sciences 12, Part A (0), 590–597.

PUBL. II

Maguya, A. S., Junttila, V. and T. Kauranne, Algorithm For Extracting Digital Terrain Models under Forest Canopy from Airborne LiDAR Data, *Remote Sensing*, 6(7), 6524–6548, 2014.

Remote Sens. **2014**, *6*, 6524-6548; doi:10.3390/rs6076524

OPEN ACCESS

remote sensing

ISSN 2072-4292

www.mdpi.com/journal/remotesensing

Article

Algorithm for Extracting Digital Terrain Models under Forest Canopy from Airborne LiDAR Data

Almasi S. Maguya *, Virpi Junttila and Tuomo Kauranne

Lappeenranta University of Technology, P.O. Box 20, Lappeenranta FI-53851, Finland;
E-Mails: virpi.junttila@lut.fi (V.J.); tuomo.kauranne@lut.fi (T.K.)

* Author to whom correspondence should be addressed; E-Mail: almasi.maguya@lut.fi;
Tel.: +358-465-233-232; Fax: +358-5-621-2350.

Received: 3 April 2014; in revised form: 18 June 2014 / Accepted: 26 June 2014 /
Published: 16 July 2014

Abstract: Extracting digital elevation models (DTMs) from LiDAR data under forest canopy is a challenging task. This is because the forest canopy tends to block a portion of the LiDAR pulses from reaching the ground, hence introducing gaps in the data. This paper presents an algorithm for DTM extraction from LiDAR data under forest canopy. The algorithm copes with the challenge of low data density by generating a series of coarse DTMs by using the few ground points available and using trend surfaces to interpolate missing elevation values in the vicinity of the available points. This process generates a cloud of ground points from which the final DTM is generated. The algorithm has been compared to two other algorithms proposed in the literature in three different test sites with varying degrees of difficulty. Results show that the algorithm presented in this paper is more tolerant to low data density compared to the other two algorithms. The results further show that with decreasing point density, the differences between the three algorithms dramatically increased from about 0.5 m to over 10 m.

Keywords: DTM extraction; airborne LiDAR; biomass estimation; tree height estimation

1. Introduction

Airborne light detection and ranging (LiDAR) is an active remote sensing technology that uses aircraft-mounted laser scanning systems in conjunction with a positioning and orientation system (POS)

for ranging purposes [1]. The system measures the distance between the laser scanner and reflected objects on the ground (or the ground itself) by considering the round-trip time taken by a laser pulse to travel from the sensor to the reflecting surface and back.

The use of airborne LiDAR technology (hereafter, simply referred to as LiDAR) in forestry applications has been increasing constantly in the past decade. This increasing trend in the use of LiDAR technology in forestry applications can be attributed to both promising results obtained in applications of LiDAR technology to forestry (e.g., [2–7]) and the maturity of the LiDAR technology over time; for example, increased pulse rates and the introduction of full-waveform LiDAR [8]. Unlike conventional LiDAR sensors, which can record up to four returns from multiple targets, full-waveform LiDAR sensors can sample and record the entire echo waveform for each laser pulse [9]. This capability makes them able to collect more information about the physical characteristics of the reflecting objects. This feature has been exploited in generating DTMs from LiDAR data with notable improvements in terms of DTM accuracy compared to conventional LiDAR sensors [9,10].

On the other hand, LiDAR data acquisition costs per unit area have gone down significantly, especially for projects covering large areas (large-scale acquisitions) [11]. However, this cost-effectiveness of LiDAR is a trade-off between cost and point density; to cover large areas at minimal costs flying altitude needs to be relatively higher, leading to low point densities. Furthermore, recently, it has been shown [12] that it is possible to minimize the number of field plots required for calibrating regression models used to estimate various forest parameters. This innovation can help to cut the cost of LiDAR campaigns for forest inventory purposes that feature both LiDAR collection and calibration plot measurement by up to one half.

This section presents the state-of-the-art in applications of LiDAR in forestry activities, particularly tree height estimation and DTM extraction. Challenges encountered in extracting DTMs from LiDAR data in forested terrain are also discussed.

1.1. LiDAR-Based Forest Inventory

LiDAR has been used extensively to estimate various forest parameters pertaining to forest inventory [13]. One particular parameter that has received substantial attention is tree height, *i.e.*, mean tree-height, dominant tree height or individual tree heights [14,15]. This is because tree height is an input for estimating other forest parameters, such as biomass and tree volume [16].

A common technique that has been used for tree height estimation involves the estimation of two models from LiDAR data, namely, the digital terrain model (DTM) and the digital surface model (DSM) from which the canopy height model (CHM) is derived as their difference (*i.e.*, $CHM = DSM - DTM$). Using this technique, for example, [15] were able to estimate individual tree heights of sugi plantations in three kinds of terrain: steep slope, gentle slope and gentle, yet rough, terrain. Tree height estimates from this study correlated very well with field-measured tree heights with coefficient of determination (R^2) values of 0.857, 0.923 and 0.955, respectively, for the three terrain types. Similarly, [17] conducted a study to assess the suitability of small-footprint LiDAR technology for estimating ground elevation and tree

heights in tropical landscapes. In this study, individual tree heights were underestimated with a mean absolute error (MAE) of 2.33 m.

Other methods related to tree height estimation, which do not require the use of DTMs, have also been proposed. These are referred to as indirect methods [14].

For example, [18] used a DTM-free method to estimate the mean tree height in a hinoki cypress forest using small footprint LiDAR. The method is based on the assumption that a hypothetical surface passing through predominant tree tops is nearly parallel to the ground (and, hence, the DTM). In this method, the difference in elevation between the hypothetical surface and ground points is assumed to be an estimator of the mean tree height. Although test results showed that tree heights derived using the method correlated well with field measured values ($R^2 = 0.94$), the method was not tested on other forest types and different terrain. Therefore, the suitability of the method to other forest types and different kinds of terrain remains unknown.

In another study, [19] studied the effect of the laser beam footprint and LiDAR data sampling density on tree height estimates in a pine stand. The study used footprints in the range 0.75–3.0 m, and tree heights were underestimated by 2.1–3.7 m due to the lack of calibration using field data.

Forest parameters (e.g., average tree height, basal area, *etc.*,) and associated derivatives (e.g., DTMs and CHMs) from LiDAR data are the inputs used to establish high-level information about forests. This information includes, for example, above-ground biomass and carbon content (e.g., [7,20,21]). On the other hand, LiDAR-derived DTMs and DSMs have been used to monitor forest height and crown diameter changes, due to growth (e.g., [6]) and deforestation [22].

1.2. DTM Extraction in Forested Terrain

Generally, DTM extraction is a two-stage process [4,23,24]. In the first stage, called ground filtering, ground points (points from LiDAR pulses reflected from the ground surface) are separated from vegetation points (points from LiDAR pulses reflected from the canopy and low-lying vegetation). In the second stage, the DTM is generated by estimating ground elevations at places where there are no data through interpolation techniques.

Several general-purpose algorithms for ground filtering and DTM interpolation have been proposed in the literature (e.g., [25–27]). Using a variety of filtering techniques (e.g., mathematical morphology, linear prediction and slope information), some of these algorithms are dedicated to either ground filtering or DTM interpolation, while others combine the two stages into one algorithm. DTM extraction in forested terrain, however, is unique, due to the presence of the canopy (which limits the penetration of LiDAR pulses) and the complex terrain normally present in forests. Most general-purpose DTM interpolation algorithms perform poorly under these conditions. Consequently, specialized algorithms have been developed specifically for this purpose (e.g., [3–5,28–30]).

In the algorithm proposed in [4], for example, filtering of non-ground points for DTM generation is done by creating a surface from below the point cloud base on triangulated irregular network (TIN) structures. This surface is then allowed to fluctuate within certain values based on, for example, active contour models or a constrained spline function, such that ground points are included in the surface.

In another example [3], filtering of non-ground points is done iteratively by fitting a surface to the data points and assigning weights to each point based on the residual the point's elevation residual from the surface. In each iteration, points with large negative residuals (below the surface) receive more weight and attract the surface towards them, while points with large residuals (above the surface) are eliminated.

Despite the development of these specialized algorithms, DTM extraction in forested terrain remains to be a challenging task. This is partly due to the fact that no single algorithm can perform well in all kinds of situations (data and terrain type), on the one hand, and the heterogeneous nature of terrain and LiDAR data typical of forested terrain on the other. For example, an experimental comparison of ground filtering algorithms [31] revealed that while most algorithms perform similarly in less demanding situations (e.g., flat terrain and the absence of discontinuity in the terrain), significant differences were observed in the performance of the algorithms with increasing terrain complexity, the presence of large objects, such as buildings, and the presence of vegetation cover.

1.3. Challenges in DTM Extraction in Forested Terrain

Despite the development of specialized algorithms to solve the problem of DTM extraction in forested terrain, DTM extraction in forested terrain still faces some challenges. For example, [31,32] point out many factors that affect the process of DTM extraction in forested terrain. These factors include, for example, flight altitude above ground level, forest cover (canopy thickness), the date (season) the LiDAR data was collected, terrain slope and scan angle [33–35]. These factors have a direct effect on the penetration rate of LiDAR pulses through the forest canopy and, hence, affect the number of ground hits.

Flight altitude, for example, affects the point density in the data, *i.e.*, the higher the flight altitude above ground level, the lower the point density. For example, in the study carried out by [32], flight altitudes of 400, 800 and 1500 m led to point spacing of 0.80, 1.6 and 3.0 m, respectively.

Similarly, canopy thickness and the season of data collection affect the density of the collected data. Thicker canopies tend to block most of the LiDAR pulses, thus preventing them from reaching the ground. In some extreme cases, the penetration rate of LiDAR pulses can be so low that DTM extraction becomes extremely difficult. For example, in a study by [36], to determine the penetration rate of small-footprint LiDAR in a closed canopy, middle-aged (40–50 years) hinoki cypress, out of the 107,427 points/ha transmitted, only 1% managed to reach the ground. The density of the LiDAR point cloud tends to decrease from the top of the canopy downwards. This decrease is the result of most of the LiDAR pulses being blocked by the thick canopy.

On the other hand, if data is collected during leaf-off season, there will be a higher penetration rate for the LiDAR pulses than if the data were collected during the leaf-on season [32]. This is because in the leaf-off season, there are numerous gaps in the canopy for the LiDAR pulses to penetrate.

Terrain slope also poses a big challenge for most DTM interpolation and ground filtering algorithms. Many studies assessing the effect of terrain slope on DTM accuracy showed that DTM accuracy tends to deteriorate with increasing terrain slope (e.g., [32,37,38]).

The scan angle has also been found to have an impact on the penetration rate of LiDAR pulses through forest canopies. Depending on the thickness of the canopy cover, studies [33,35,36] have shown that a scan angle of 8–15 degrees is required in order to maximize the number of ground hits.

The extent to which LiDAR is being used in forestry activities today suggests that it is the future of forest inventorying. Unfortunately, the area of LiDAR data processing, especially in forested and steep terrain, has not advanced as much as the LiDAR technology itself has. This difference makes the area of LiDAR data processing, particularly ground filtering and DTM extraction in forested terrain, deserving of further investigation. In this paper, we propose an algorithm for DTM extraction in forested terrain from LiDAR data. The algorithm builds on the recent work by [39] and addresses the limitations of the algorithm presented therein, namely, the lack of overlapping between adjacent patches, which leads to ridges in the DTM, and gaps in the DTM caused by a lack of enough points to fit a model and along the edges of non-rectangular patches (tiles).

Therefore, this study had three main objectives. These objectives were to:

(i) overcome the problems of low data density and the lack of overlapping between DTM patches by iteratively generating a series of coarse DTMs (repeated sampling) using patch widths of varying sizes and combining the coarse DTMs to form the final DTM;
(ii) develop an interpolation strategy for estimating elevation values at places where both spline and trend surface interpolation fail (gap-filling); and
(iii) compare the performance of the proposed algorithm with two other algorithms for generating DTMs in forested terrain using data sets from three different tropical test sites, which are characterized by both low point density and varying degrees of terrain roughness.

This approach has the advantage that it helps to deal with low data density by creating a cloud of elevation values using the available data, from which the final DTM is generated. Moreover, in places of extremely low numbers of ground points, approximation is done using a suitable gap-filling algorithm.

2. Material and Methods

2.1. Study Area

This study spans three test sites on three different continents, namely Nepal (Site 1), Brazil (Site 2) and Ghana (Site 3). The three forest types studied in the article were chosen on the principle that they represent typical dense tropical forest types on three different continents. All three LiDAR samples have been collected for a different purpose, as described below.

2.1.1. Site 1

This site consists of three watersheds, namely, Kayarkhola, Charnawati and Ludikhola. The three watersheds cover an area of approximately 27,789 ha. The terrain in the site is predominantly mountainous and complex, consisting of steep slopes and valleys. Altitude in the area varies from 245 m (Kayarkhola) to 3549 m (Charnawati). The average slope in the area is 29.7%, while the maximum slope is 57.3%. The percentage of ground hits in this site is approximately 29.3%.

This site is part of a pilot project for measuring and monitoring carbon stocks in community forests. The aim of the project is to design and set up a governance and payment system for Nepal's community forest management under the Reducing Emissions from Deforestation and Forest Degradation (REDD) payment scheme for developing countries.

The forest tested in the current article lies on mountainous highland and represents steep orographic variation under a dense canopy. The forest itself is looked after by a local community forest program and has grown from a degraded state into a high biomass forest.

2.1.2. Site 2

This site is part of the Brazilian Amazon. The terrain in the area is predominantly flat with thick forest cover. The point density of LiDAR capture is quite high, amounting to some 14 points per m^2. Despite such unusually high point density and the corresponding relatively low flying altitude, the number of ground hits is quite low, thereby making DTM generation a challenge. The percentage of ground hits in this site is approximately 2.2%.

The forest in this site is by far the densest of all three, but like much of the Amazonian Forest, it lies on relatively flat land, with local undulation only. The Brazilian sample is from a natural forest, and it was collected for studying the ability of LiDAR to penetrate a very dense, multi-storied canopy. A very high point density was used in the LiDAR capture in order to make sure that at least some pulses hit the ground.

2.1.3. Site 3

The third site is in southwestern Ghana and represents a West African tropical forest in hilly terrain. The forest is dense, even if the current patch is relatively flat. The percentage of ground hits in this site is approximately 4.54%.

This site is part of a forest and land use inventory scheme for the Ghanaian Forestry Commission (see [40]). It represents a West African closed canopy forest that was inventoried for the sake of land use change analysis. The overall terrain is rugged, but with much less steepness than in the Nepalese case. Forests in the sample are not protected and are used for a variety of purposes by the local population.

2.2. Test Data

Test data used in this study consist of three LiDAR data sets from each of the test sites together with plot-level field measurements of tree heights except for Site 2, where tree height measurement from the ground is not possible.

2.2.1. LiDAR Data

The data were collected to support a LiDAR-assisted Multiresource Programme (LAMP), which is a large-scale method for carbon stock mapping that combines LiDAR sampling and satellite imagery to produce accurate carbon stock maps of areas of interest (see [41]). Table 1 shows a summary of the parameters of interest about the LiDAR data. Flying altitude refers to the vertical distance of the aircraft from the ground level and should be maintained throughout the flight mission. Because of this requirement, a helicopter is the only way to fly in Site 1, since a fixed wing aircraft cannot rise fast enough to maintain a constant flying altitude and follow the quickly undulating terrain. The data was provided courtesy of Arbonaut Ltd. (Joensuu, Finland) in association with the International Center

for Integrated Mountain Development (ICIMOD) (Site 1) of Nepal in raw LASer file format (LAS) (ver. 1.2) format.

Table 1. Parameters of the LiDAR data used in this study.

Parameter	Value		
	Site 1	**Site 2**	**Site 3**
Projection	UTM	UTM	UTM
Datum	WGS84	WGS84	WGS84
Aerial platform	Helicopter	Helicopter	Fixed wing aircraft
Flying altitude	2200 m AGL	850 m AGL	1300 m AGL
Flying speed	80 knots	124 knots	120 knots
Sensor type	Leica ALS-50 II	Leica ALS-50 II	Leica ALS-50 II
Scan angle	20 degrees	Unknown	13.5 degrees
Sensor pulse rate	52.9 Khz	115.8 Khz	81 Khz
Sensor scan speed	20.4 lines/s	Unknown	47.6 lines/s
Average pulse density	0.8 points/m^2	14 points/m^2	2 points/m^2
Swath width at ground level	1601.47 m	350 m	644 m
Beam footprint at ground level	50 cm	Unknown	31 cm
Date collected	March 2011–April 2011	September 2011	December 2011–January 2012

2.2.2. Field Measurements

In addition to the LiDAR data, field measurements consisting of tree height estimates for 80 circular plots (radius = 12.62 m) in Site 1 were used. There were no field measurements for Sites 2 and 3. The height of each tree with a diameter at breast height of 5 cm was measured using Vertex IV and Transponder T3 measuring devices.

2.3. Methods

The proposed method for ground filtering and DTM interpolation can be broken down into five steps: (1) repeated DTM sampling; (2) generating gridded DTM samples; (3) generating initial DTM; (4) filling gaps; and (5) generating final DTM. These steps are detailed below.

2.3.1. Repeated DTM Sampling

The repeated DTM sampling step generates a series of DTMs using varying patch widths. The aim of this step is to generate several elevation samples at each candidate DTM location (cell) from which the best are selected to form the final DTM.

Input to this step is the original LiDAR point cloud (in ASCII xyz format). Using the method for ground filtering and DTM interpolation proposed by [39], a series of DTMs is generated using patch widths of varying sizes (see Figure 1).

Figure 1. Example from Site 1 illustrating repeated sampling of elevation values at DTM locations by repeating DTM interpolation using increasing patch widths ranging from 50 to 80 m at increments of 10 m. (a) Patch width = 50; (b) Patch width = 60; (c) Patch width = 70; (d) Patch width = 80.

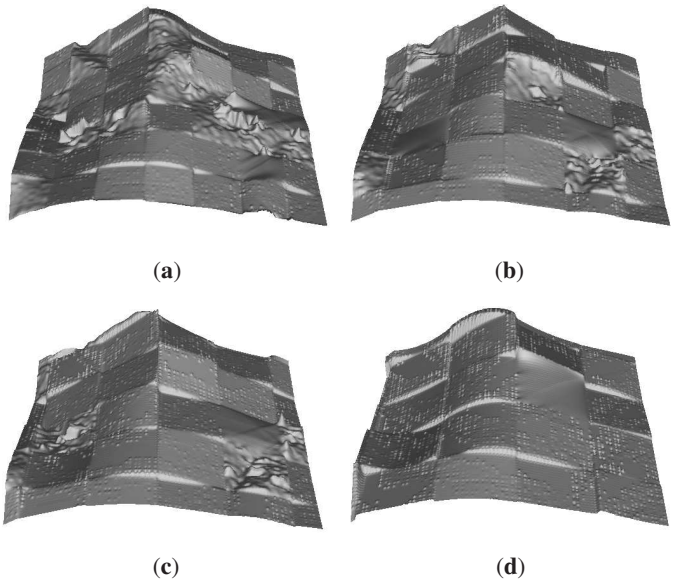

This procedure results in repeated sampling of elevation values at each candidate DTM location (cell), while, at the same time, creating an overlapping effect between the DTM patches of varying widths. The patch widths used in this study were 50, 60, 70 and 80 m. These values were found to work well in all three test sites and were found by experimenting with values between 30 and 100 m using a ten-meter increment.

While generating the individual DTMs in the repeated DTM sampling step, there are times when the algorithm may fail due to a very low number of data points or gaps in the input data (see [39] for details). When this happens during the repeated sampling step, corresponding areas are labeled with a large negative value, so that they can be identified later. We call these bad areas. The magnitude of the value used is roughly twice the average elevation value in the data (see Section 2.3.3 for details).

The output of the repeated DTM sampling step is a series of N DTMs with points created using patch widths of varying widths, where N is the number of sample DTMs created.

2.3.2. Generating Gridded DTM Samples

In this step, a regular grid of desired spatial resolution is generated from each of the sample DTMs generated in the previous step. The purpose of this step is to create candidate DTM locations at the desired resolution, which are common to all the DTM samples and can be aligned easily. Generating gridded DTM samples is done by first creating a grid of regularly spaced points (spaced according to

the desired final DTM resolution) in the *x*-*y* plane. Next, the created grid is superimposed on each of the sampled DTMs from the previous step, and for each point (x, y) in the regular grid, an elevation value is assigned from the elevation of the closest point in the sampled DTM.

This step produces N gridded DTM samples, each with the same number of aligned grid points (DTM locations), but with possibly different elevation values at corresponding grid points.

2.3.3. Generating Initial DTM

The initial DTM is generated by merging the N gridded DTM samples obtained in the previous step. The merging is done by taking the median of the elevation values from corresponding DTM locations in the gridded DTM samples. For example, in this study, four DTM samples were used, therefore the elevation values at DTM locations in the initial DTM were assigned by taking the median of four elevation values from corresponding DTM locations in the four gridded sample DTMs. Figure 2 illustrates how the merging is done.

Figure 2. Generating the initial DTM: DTM samples obtained by repeated sampling (**A**) are converted into gridded DTM samples at the same resolution (**B**) from which the initial DTM (**C**) is obtained by taking the median of corresponding DTM locations. W represents the patch width in meters used to generate each of the sample DTMs.

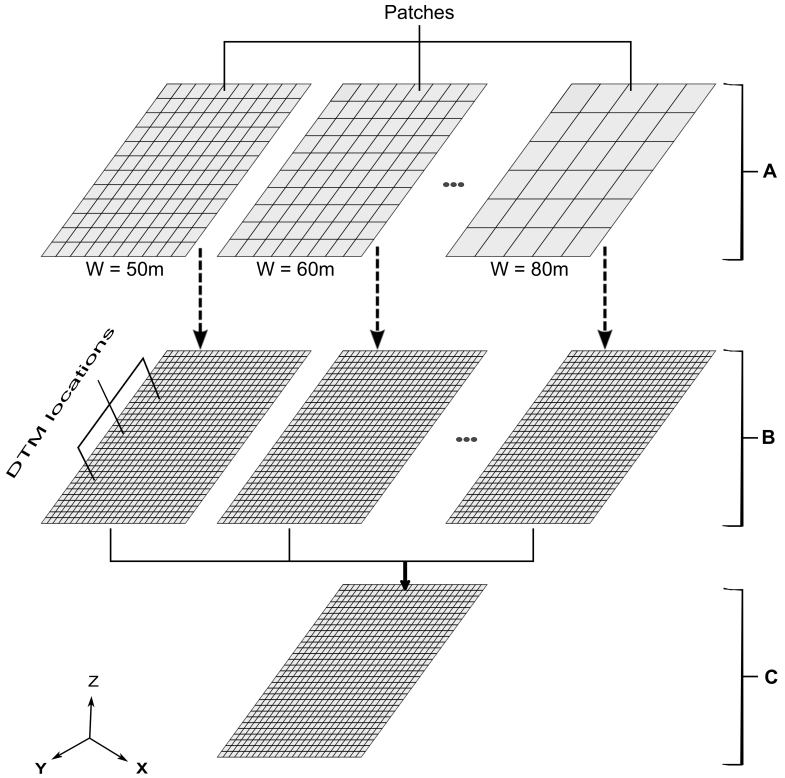

When generating the initial DTM by combining the sample DTMs, there are two possible cases: (1) the number of sample DTMs to be combined is odd; and (2) the number of sample DTMs to be combined is even. If the former case prevails, the median of elevation values at corresponding DTM locations happens to be the middle value. In this case, this value is assigned to the corresponding DTM location in the initial DTM regardless of whether this value is a legitimate elevation value or the large negative value used for labeling bad regions. If the latter case prevails, however, the median value will be the average of the two middle elevation values. In this case, it may happen that one or both of the middle values is the special large negative value used for labeling bad regions. It is important at this point to ensure that the resulting median value calculated is negative in order to preserve the identity of bad regions. To meet this condition, the value used for labeling bad regions is chosen to be a negative number with a magnitude of at least twice the average elevation value in the test data. This ensures that if Case 2 prevails, bad regions retain negative elevation values, so that they can be identified in later steps of the algorithm.

The generating initial DTM step results into an initial gridded DTM. The DTM contains negative elevation values (gaps in the DTM) at places where elevation values could not be estimated in the previous steps due to limited number of data points or gaps in the data. The next step is to estimate the elevation values at those places (hereafter referred to as bad regions).

2.3.4. Filling Gaps

In the gap filling step, bad regions in the DTM are filled (repaired) by interpolation. The bad regions can occur at three places in a DTM: (1) completely embedded in the DTM; (2) on the edge of the DTM; and (3) on the corner of the DTM. Figure 3 shows the three possibilities.

Figure 3. Possible locations for bad regions in a DTM.

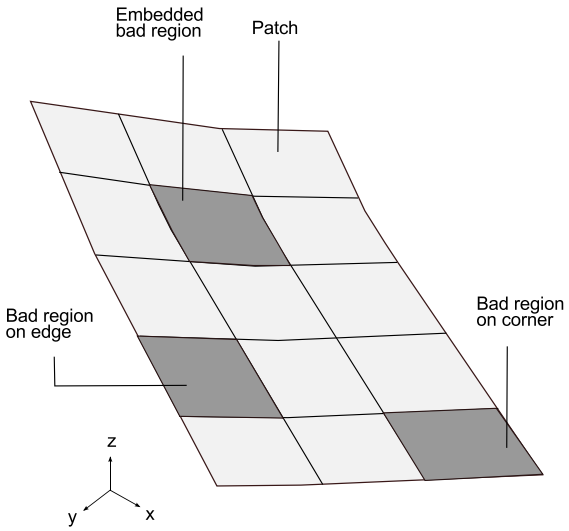

The method described here repairs the bad regions that are completely embedded into the DTM and those occurring on the edges. There is not enough information to reliably repair the bad regions occurring at the corners. To repair the bad regions, the following steps are taken:

(i) locate the next bad DTM location to be repaired;

(ii) locate the coordinates of the first valid DTM location above the current bad point in the current column (see Figure 4); if none exists, take the x and y coordinates of the topmost point and assign a large positive value (L) for the z coordinate (elevation) and form the top point $P_t : (x_t, y_t, z_t)$; Here, we use the terms above and below with respect to the positions of the points in the vertical direction and the terms left and right with respect to the position of the points in the horizontal direction.

(iii) Locate the coordinates of the first valid DTM location below the current bad point in the current column (see Figure 4); if none exists, take the x and y coordinates of the bottom most point and assign a large positive value for the z coordinate and form the bottom point $P_b : (x_b, y_b, z_b)$;

(iv) Locate the coordinates of the first valid DTM location on the left of the current bad point in the current row (see Figure 4); if none exists take the x and y coordinates of the leftmost point and assign a large positive value for the z coordinate and form the left point $P_l : (x_l, y_l, z_l)$;

(v) locate the coordinates of the first valid DTM location on the right of the current bad point in the current row (see Figure 4); if none exists take the x and y coordinates of the rightmost point and assign a large positive value for the z coordinate and form the right point $P_r : (x_r, y_r, z_r)$;

(vi) Determine if the bad DTM location is in a bad region lying on a corner by checking if any of the following conditions are true: $z_t = z_r = L$, or $z_t = z_l = L$, or $z_b = z_l = L$, or $z_b = z_r = L$; if any of these conditions hold, go to Step (i);

(vii) Determine which direction (vertical or horizontal) has a larger slope (steeper) by comparing the magnitudes of the slopes of the lines segments $\overline{P_b P_t}$ and $\overline{P_l P_r}$;

(viii) If the vertical direction is steeper, use the line segment $\overline{P_l P_r}$ to interpolate the elevation value at the current bad point, otherwise use the line segment $\overline{P_b P_t}$.

The value of L is chosen, such that the slope between the current bad DTM location and the topmost DTM location is considerably larger than the slope between the current DTM location and any other valid DTM location in the DTM. In this study, a value of 10,000 was used, and it was about ten times larger than the average elevation in the data.

The reason for using a line segment in the less steeper direction for estimation is to detect bad regions located on the edges and corners of the DTM and to take appropriate action. This is achieved by the use of the large dummy elevation value described above. For example, if a bad region to be filled is located on either the top or bottom edges of the DTM, then the slope in the vertical direction will be larger than that in the horizontal direction (due to a large elevation value assigned), making the algorithm resort to using a horizontal line segment for estimation. On the other hand, if the bad region is located on either the left of right edges of the DTM, vertical line segments are used for estimation.

Figure 4. Locating valid DTM locations when repairing bad regions in a DTM: (a) the case when the bad region is completely embedded into the DTM and all of the required points (P_t, P_r, P_b, and P_l) exist; (b) the case when the bad region lies on the border of the DTM and one of the required points is missing; (c) the case when the bad region lies on the corner of the DTM and either of the pair of the required points $\{P_t, P_r\}$, $\{P_l, P_t\}$, $\{P_l, P_b\}$ or $\{P_b, P_r\}$ is missing. The darkest square at the center represents the DTM location, which is currently being estimated within a bad region (the darker squares); the light squares bordering the bad region represent valid DTM locations used for estimation.

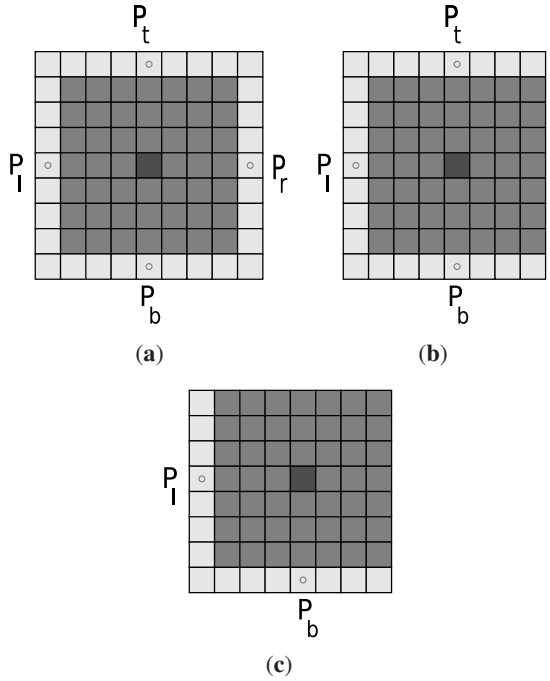

Estimating Unknown Elevation Values

After the four points P_t, P_r, P_b and P_l, as well as the direction of a gentle slope have been determined, estimation of the elevation value at the current bad DTM location is done. First, the direction vector $\mathbf{v}_d$ is computed using either Equation (1) or Equation (2).

$$\mathbf{v}_d = P_r - P_l \tag{1}$$

$$\mathbf{v}_d = P_t - P_b \tag{2}$$

Next, using the equation of a line in 3D,

$$\mathbf{p} = \mathbf{p}_0 + t\mathbf{v}_d \tag{3}$$

where $\mathbf{p}$ is a general point on the line, $\mathbf{p}_0$ is a known point on the line, t is a parameter and $\mathbf{v}$ is a direction vector; the value of the parameter t for line segments $\overline{P_bP_t}$ and $\overline{P_lP_r}$ is determined using Equation (3) above and available information, *i.e.*, the values of the x and y coordinates of the current bad location and either P_l or P_r if a horizontal line segment is used for estimation; and either P_t or P_b if a vertical line segment is used for estimation. Thus, t is calculated using Equation (4).

$$t = \frac{x - x_t}{\mathbf{v}_{d,x}} \tag{4}$$

where x represents the value of the x-coordinate at the current bad location, x_t represents the x-coordinate of the top point, P_t, and $\mathbf{v}_{d,x}$ represents the x-coordinate of the direction vector, $\mathbf{v}_d$. Alternatively, the same result can be obtained by using the y-coordinates of the vectors involved in Equation (3).

After the value of the parameter t for the interpolating line has been determined, it is used to estimate the elevation value at the current bad location. The estimation is done by using the z-coordinates of the vectors in Equation (3) and using Equation (5).

$$z = z_t + t\mathbf{v}_{d,z} \tag{5}$$

where z is the elevation value being estimated, z_t is the z-coordinate of the top point, P_t, and $\mathbf{v}_{d,z}$ represents the z-coordinate of the direction vector, $\mathbf{v}_d$. Here, the vertical line segment $\overline{P_bP_t}$ is being used with P_t as the known point. In a similar fashion, the bottom point P_b can be used or either of the points $\{P_l, P_r\}$ may be used in case a horizontal line is used for estimation.

2.3.5. Generating the Final DTM

The final step in generating the DTM is to detect and remove jumps (spikes) in the DTM. This is a two-step process. In the first step, jumps are detected and marked, and in the second step, the jumps are removed (repaired). To detect jumps, each DTM location's elevation is compared with the elevation of its 8 neighbors (for DTM locations not lying on the border) or 5 neighbors (for DTM locations lying on the border) (see Figure 5).

Figure 5. Two kinds of neighborhoods used to detect jumps in a DTM: (a) 8 neighborhoods; (b) 5 neighborhoods. The asterisk represents the DTM location being tested.

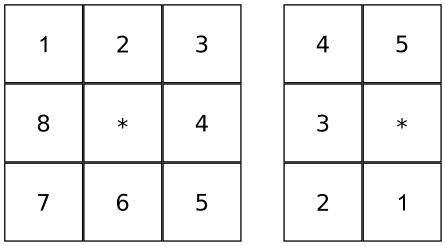

(**a**) (**b**)

A DTM location is marked as a jump if it fails the test:

$$R < T$$

where:

$$R = \sum_{i=1}^{s} |Z_i - Z_c|$$

and Z_i represents the elevation value of the neighboring points, Z_c represents the elevation value of the point being tested, s is the upper limit of the summation (8 for the non-border location and 5 for the border locations) and T is a threshold. The value of R is very sensitive to terrain slope, thus a suitable value for T that works well for a particular area and data has to be determined experimentally. In this study, the value of T roughly equal to $\frac{R}{s}$ was found to be suitable in each test area.

After the jumps have been detected and marked, the next step is to repair them. This is done by treating the jumps as small gaps in the DTM and to repair them using the method for filling gaps described in the previous section. Figure 6 illustrates how jumps are detected and repaired.

Figure 6. Detecting and repairing jumps in the DTM: (a) original DTM section; (b) locations detected as jumps marked (light spots); (c) jumps repaired using the gap-filling approach described in the previous section. The width of each DTM section is approximately 350 m.

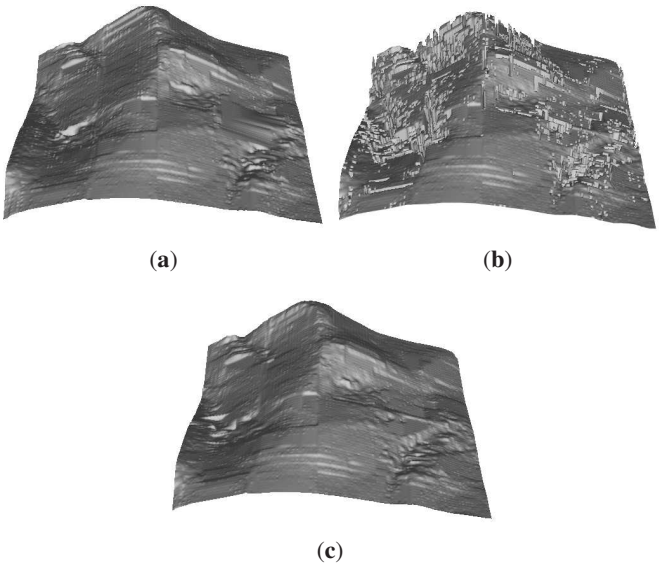

(**a**) (**b**)

(**c**)

3. Results and Discussion

In this section, we present the performance results of the proposed algorithm. First, we show how the proposed iterative approach helps to overcome the shortcomings reported in [39], namely, border effects (poor overlapping between patches) and gaps in the DTM in places of extremely low data or the presence of gaps in the data; second, we present results of the relative performance of the proposed algorithm compared with two existing algorithms for the extraction of DTMs from LiDAR data in forested terrain proposed in the literature in [3,4]. We chose to compare our method with these algorithms, because they are in widespread use by the forestry community, both in research and industry.

3.1. Minimizing Border Effects

Test results showed that by using patch widths of varying sizes, the problem of a lack of overlap between patches is significantly reduced. As opposed to using only one DTM sample, the use of several DTM samples (repeated sampling) results in the creation of several elevation samples at every DTM location. These elevation samples are produced from DTM samples of different patch widths, thus creating an overlapping effect between the patches of the DTM samples. Figure 7 shows how four DTM samples generated using patch widths varying from 50–80 m at a ten-meter increment are combined to produce the final DTM. Note how the border effects appearing in the four DTM samples are significantly reduced after combining the DTM samples.

Figure 7. Combining four DTMs (a) Patch width = 50; (b) Patch width = 60; (c) Patch width = 70; (d) Patch width = 80 generated using different patch widths to produce the final DTM (e) After combining and removing jumps. Each DTM sample measures approximately 350 m in width.

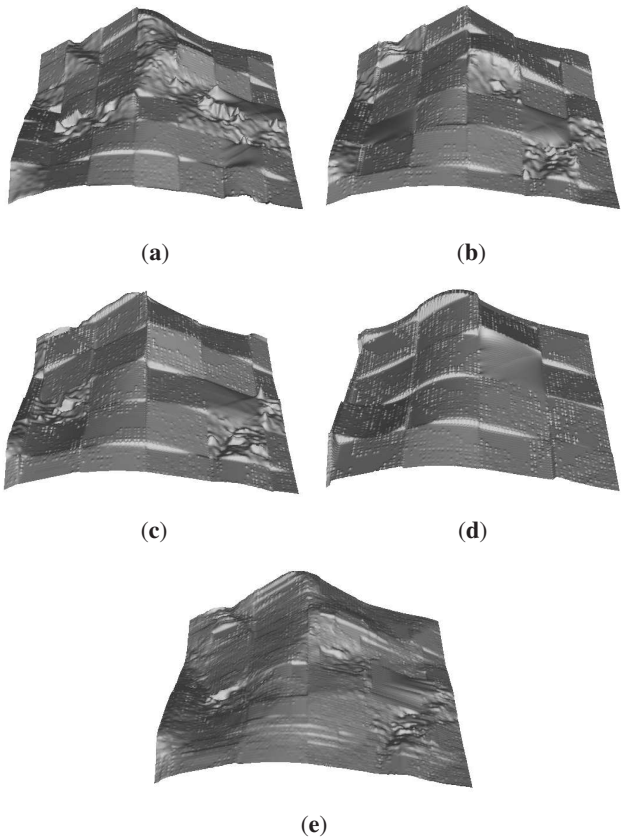

Similarly, repeated sampling of elevation values using DTM samples of increasing patch widths helps to overcome the problem of gaps in the DTM resulting from either gaps in the data or low data densities at certain places (due to closed canopy). This problem can be solved in two ways. First, as the patch size is increased, gaps of a relatively small area compared to the patch width get embedded completely or partially into the much larger patches. This is contrary to using a fixed patch width, where small gaps often emerge. Second, gaps in the data are handled by using the gap-filling procedure described in the previous section. This procedure is used to fill gaps that remain before the final DTM is produced. Figures 8 and 9 show how the gap filling algorithm works.

Figure 8. Filling gaps in a DTM on a level surface on a steep slope: (a) original terrain before a gap is introduced; (b) after a 40 m by 40 m gap has been introduced; (c) after the gap has been repaired; (d) a difference model showing the error in estimation between the original and estimated elevation values. The slope at this location is approximately 37%.

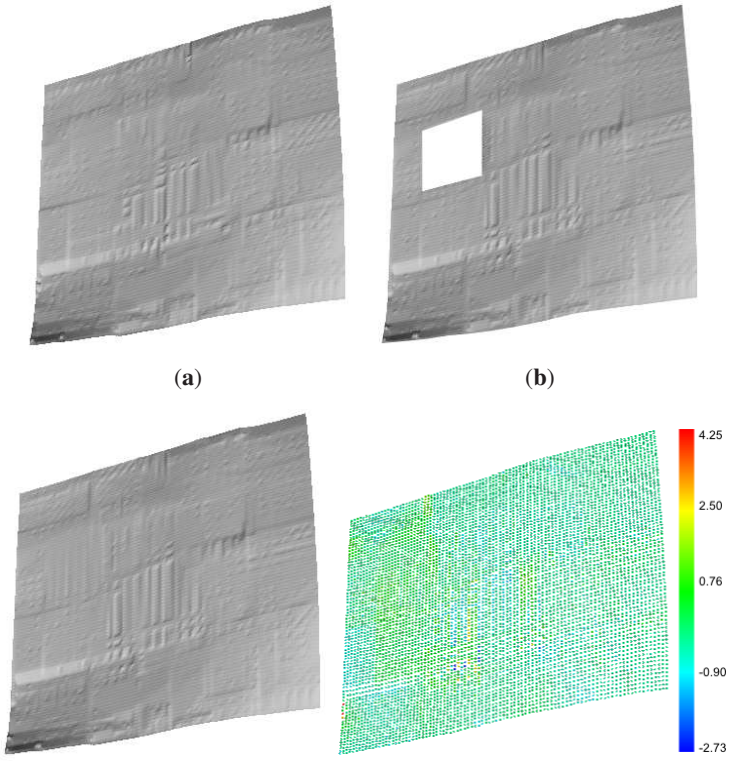

(**a**) (**b**)

(**c**) (**d**)

The difference model in Figure 8 shows that the gap filling algorithm works well on flat surfaces (both on slopes and flat terrain), while the accuracy deteriorates with increasing terrain curvature (Figure 9). This is expected behavior, as a substantial amount of information is lost when a hole is located on curved terrain compared to when a hole of the same size is located on flat terrain.

Figure 9. Filling gaps in a DTM on a curved surface on a steep slope: (a) original terrain before a gap is introduced; (b) after a 40 m by 40 m gap has been introduced; (c) after the gap has been repaired; (d) a difference model showing the error in estimation between the original and estimated elevation values. The slope at this location is approximately 33%.

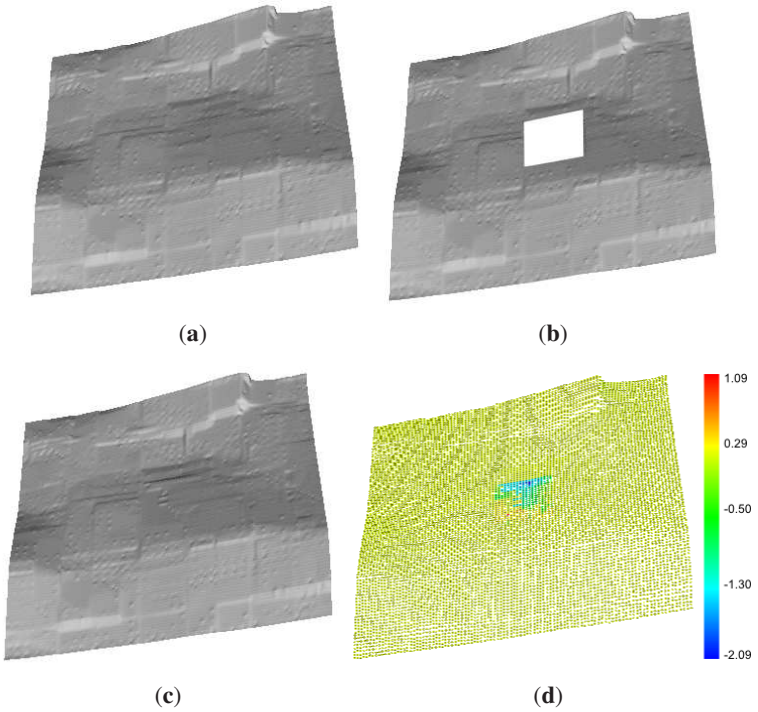

3.2. Comparison with Field Measurements

To assess the accuracy of the algorithm, tree height estimates computed using the algorithm were compared to field-measured tree heights. Computed heights were obtained by first extracting the LiDAR points corresponding to each plot, and the height of the tallest tree in each plot was assumed to correspond to the average of the highest ten LiDAR points.

While comparison of tree heights estimates computed using the algorithm in Site 1 showed a slight improvement against field measurements (RMSE = 1.65 m compared to an RMSE of 1.92 m reported in [39]), the proposed algorithm has shown a significant improvement in dealing with gaps in the data, as well as a low number of ground points. Moreover, the slight improvement in RMSE can be explained by the fact that the field measurements were collected in areas accessible by field measurement crews, *i.e.*, areas with less complex terrain and moderate canopy cover.

3.3. Comparison with Existing Algorithms

We compared the proposed algorithm with algorithms proposed in [3,4]. The comparison was quantitative and was aimed at observing the relative performance of the three algorithms in different kinds of forest cover and terrain type, *i.e.*, the three test sites. This is due to a lack of field ground control data (reference DTMs) in the three test sites. In the following discussion, we are going to refer to the three algorithms as follows. The algorithm proposed by Karl Kraus as KK; the algorithm proposed by Peter Axelsson as PA; and the algorithm proposed in this paper by MA (Maguya Almasi).

In our tests, we used the implementation of KK available in the FUSION software package (see [42]) and that of PA found in the Terrascan software package (see [43]). For details about parameters used to generate the test DTMs from the two software packages; see Appendix A and B. Figures 10–12 show a comparison of the three algorithms. The comparison is based on the differences in elevation between the DTMs and the smoothness of the DTMs, and the area covered measures approximately 0.16 square kilometers.

Figure 10. Comparing DTMs produced by (a) Karl Kraus (KK), (b) Peter Axelsson (PA) and (c) Maguya Almasi (MA) at Site 1. The width of the DTM section is approximately 400 m. (d) Difference model: $KK - MA$; (e) Difference model: $PA - MA$.

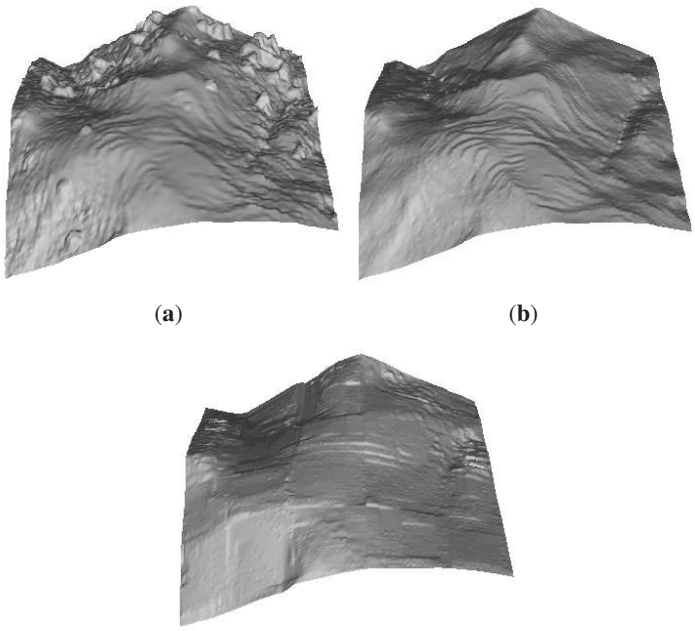

(**a**) (**b**)

(**c**)

Figure 10. *Cont.*

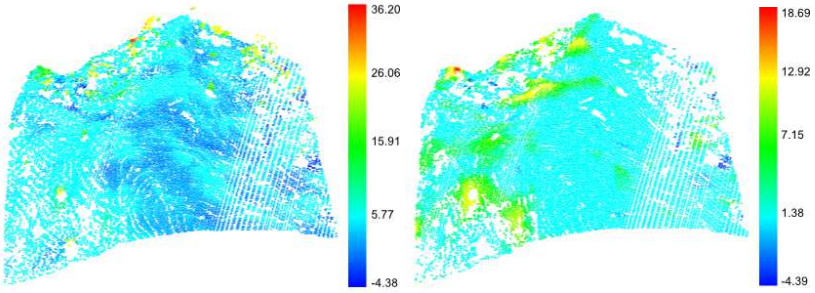

(**d**) (**e**)

Figure 11. Comparing DTMs produced by (a) Karl Kraus (KK), (b) Peter Axelsson (PA) and (c) Maguya Almasi (MA) at Site 2. The width of the DTM section is approximately 400 m. (d) Difference model: $KK - MA$; (e) Difference model: $PA - MA$.

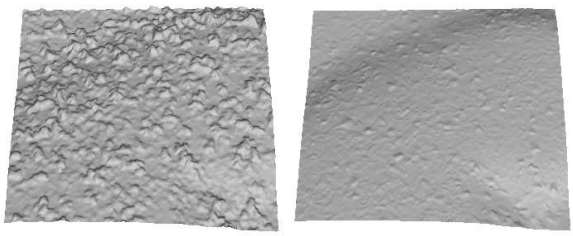

(**a**) (**b**)

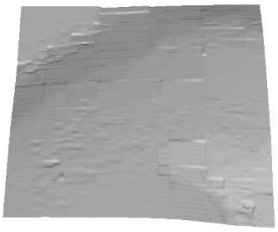

(**c**)

Figure 11. *Cont.*

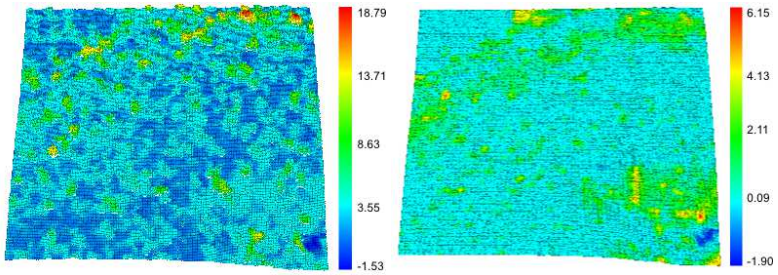

(**d**) (**e**)

Figure 12. Comparing DTMs produced by (a) Karl Kraus (KK), (b) Peter Axelsson (PA) and (c) Maguya Almasi (MA) at Site 3. The width of the DTM section is approximately 400 m. (d) Difference model: $KK - MA$; (e) Difference model: $PA - MA$.

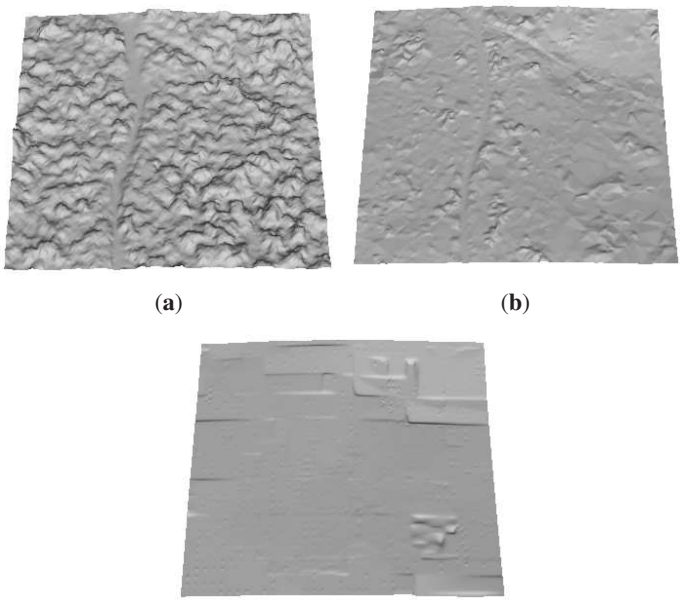

(**a**) (**b**)

(**c**)

Figure 12. *Cont.*

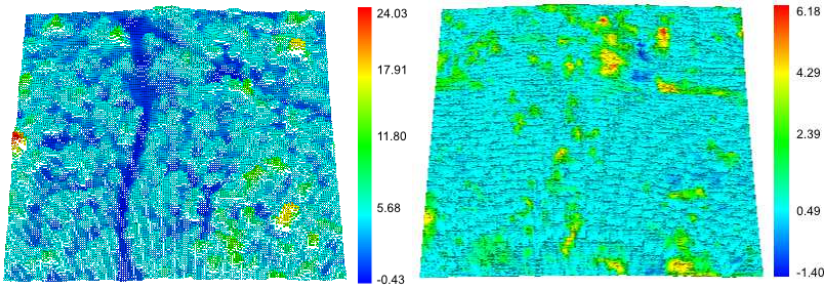

(**d**) (**e**)

Figure 10 shows that the biggest differences in elevation among the three algorithms occur in Site 1. This observation can be attributed to the fact that, of the three test sites, Site 1 encompasses the most challenging combination of terrain and data for ground filtering algorithms, *i.e.*, it has terrain with steep slopes and low data density. Here, KK seems to perform poorly, whereas PA and MA seem to agree for the most part, with a consistent difference of about 1 m, except for a few places where there is a difference of more than 5 m. These places are the ones in which KK seems to suffer the most (see Figure 10a). The big difference in elevation at these places is due to the closed canopy, which blocks most of the LiDAR pulses. This fools algorithms into misclassifying LiDAR returns from tree branches as ground returns.

In Site 2 PA and MA agree significantly, while KK still presents a significant discrepancy, although not as significant as that observed in Site 1. These differences between the two sites can be attributed to the fact that Site 2 is predominantly flat, less complex terrain. Similar results are observed in Site 3 for PA and MA, while KK continues to deviate.

4. Conclusions

This paper has presented an algorithm for extracting DTMs from LiDAR data in challenging forested terrain. The algorithm overcomes the challenge of low data density under forest canopies by iteratively generating a series of coarse DTMs, which are then combined to form the final DTM.

A comparison with traditional DTM extraction algorithms showed that the performance of the algorithm presented in this paper remained consistent with decreasing data density, while the performance of the traditional DTM extraction algorithms deteriorated with decreasing point density. The main limitation of the proposed algorithm is its inability to reproduce small artifacts in the terrain (e.g., small hills). This is especially true with extremely low data densities, where the sizes of the patches used for local interpolation have to be large enough to get the right amount of ground points for interpolation. Under the challenging circumstances of our three test sites, the quality of the DTM produced clearly outweighs the loss of small features in the terrain. Overall, comparing the ground hit percentages of the three test sites and the challenge they pose to DTM extraction algorithms, it appears that terrain complexity is more detrimental to DTM quality than point density: the Nepalese test site has

the most complex terrain, but almost ten times the number of ground hits of the other two test sites, yet it produced the biggest absolute differences between the DTMs.

The proposed algorithm will therefore serve as a base for a new generation of algorithms for DTM extraction in challenging forested terrain. Further work needs to be done to improve the gap-filling method, to find a more robust way to combine the sample DTMs and to conduct further tests on the algorithm.

Acknowledgments

We would like to thank Arbonaut Ltd. and the International Center for Integrated Mountain Development (ICIMOD) (Nepal) for providing the data used in this study. We also thank Katri Tegel and Risto Rautiainen of Arbonaut for their support during the entire course of this study. Finally, many thanks to authors of the FUSION software package. Most of the illustrations in this article were generated in FUSION.

Author Contributions

Almasi Maguya conducted this study under the supervision of Tuomo Kauranne and Virpi Junttila. Tuomo Kauranne also handled all of the administrative issues during the course of the study.

Conflicts of Interest

The authors declare no conflict of interest.

References

1. Wehr, A.; Lohr, U. Airborne laser scanning—An introduction and overview. *ISPRS J. Photogramm. Remote Sens.* **1999**, *54*, 68–82.
2. Næsset, E. Determination of mean tree height of forest stands using airborne laser sanner data. *ISPRS J. Photogramm. Remote Sens.* **1997**, *52*, 49–56.
3. Kraus, K.; Pfeifer, N. Determination of terrain models in wooded areas with airborne laser scanner data. *ISPRS J. Photogramm. Remote Sens.* **1998**, *53*, 193–203.
4. Axelsson, P. Processing of laser scanner data—Algorithms and applications. *ISPRS J. Photogramm. Remote Sens.* **1999**, *54*, 138–147.
5. Pfeifer, N.; Reiter, T.; Briese, C.; Rieger, W. Interpolation of high quality ground models from laser scanner data in forested areas. *Int. Arch. Photogramm. Remote Sens. Spat. Inf. Sci.* **1999**, *32*, 31–36.
6. Reutebuch, S.E.; Andersen, H.E.; McGaughey, R.J. Light Detection and Ranging(LiDAR): An emerging tool for multiple resource inventory. *J. For.* **2005**, *103*, 286–292.
7. Clark, M.L.; Roberts, D.A.; Ewel, J.J.; Clark, D.B. Estimation of tropical rain forest aboveground biomass with small-footprint LiDAR and hyperspectral sensors. *Remote Sens. Environ.* **2011**, *115*, 2931–2942.
8. Lemmens, M. Airborne LiDAR. In *Geo-information*; Gatrell, J.D., Jensen, R.R., Eds.; Springer Netherlands: Dordrecht, The Netherlands, 2011; Volume 5, pp. 153–170.

9. Full-Waveform Airborne Laser Scanning as a Tool for Archaeological Reconnaissance. Available online: http://w3.riegl.com/uploads/tx_pxpriegldownloads/Doneus_ROME_01.pdf (accessed on 15 July 2014).
10. Ullrich, A.; Studnicka, N.; Hollaus, M.; Briese, C.; Wagner, W.; Doneus, M.; Mücke, W. Improvements in DTM generation by using full-waveform airborne laser scanning data. In Proceedings of the 7th International Conference on Laser Scanning and Digital Aerial Photography, Today and Tomorrow, Moscow, Russia, 6–7 December 2007; Volume 6.
11. Jakubowski, M.K.; Guo, Q.; Kelly, M. Tradeoffs between LiDAR pulse density and forest measurement accuracy. *Remote Sens. Environ.* **2013**, *130*, 245–253.
12. Junttila, V.; Finley, A.O.; Bradford, J.B.; Kauranne, T. Strategies for minimizing sample size for use in airborne LiDAR-based forest inventory. *For. Ecol. Manag.* **2013**, *292*, 75–85.
13. Akay, A.; Oguz, H.; Karas, I.; Aruga, K. Using LiDAR technology in forestry activities. *Environ. Monit. Assess.* **2009**, *151*, 117–125.
14. Wang, C.; Glenn, N.F. A linear regression method for tree canopy height estimation using airborne LiDAR data. *Can. J. Remote Sens.* **2008**, *34*, S217–S227.
15. Takahashi, T.; Yamamoto, K.; Senda, Y.; Tsuzuku, M. Estimating individual tree heights of sugi (*Cryptomeria japonica* D. Don) plantations in mountainous areas using small-footprint airborne LiDAR. *J. For. Res.* **2005**, *10*, 135–142.
16. Van Leeuwen, M.; Nieuwenhuis, M. Retrieval of forest structural parameters using LiDAR remote sensing. *Eur. J. For. Res.* **2010**, *129*, 749–770.
17. Clark, M.L.; Clark, D.B.; Roberts, D.A. Small-footprint LiDAR estimation of sub-canopy elevation and tree height in a tropical rain forest landscape. *Remote Sens. Environ.* **2004**, *91*, 68–89.
18. Yamamoto, K.; Takahashi, T.; Miyachi, Y.; Kondo, N.; Morita, S.; Nakao, M.; Shibayama, T.; Takaichi, Y.; Tsuzuku, M.; Murate, N. Estimation of mean tree height using small-footprint airborne LiDAR without a digital terrain model. *J. For. Res.* **2011**, *16*, 425–431.
19. Nilsson, M. Estimation of tree heights and stand volume using an airborne LiDAR system. *Remote Sens. Environ.* **1996**, *56*, 1–7.
20. Guo, Z.; Fang, J.; Pan, Y.; Birdsey, R. Inventory-based estimates of forest biomass carbon stocks in China. *For. Ecol. Manag.* **2010**, *259*, 1225–1231.
21. Herold, M.; Román-Cuesta, R.; Mollicone, D.; Hirata, Y.; van Laake, P.; Asner, G.; Souza, C.; Skutsch, M.; Avitabile, V.; MacDicken, K. Options for monitoring and estimating historical carbon emissions from forest degradation in the context of REDD+. *Carbon Balance Manag.* **2011**, *6*, 1–7.
22. Avtar, R.; Sawada, H. Use of DEM data to monitor height changes due to deforestation. *Arab. J. Geosci.* **2012**, *6*, 4859–4871.
23. Liu, X. Airborne LiDAR for DEM generation: Some critical issues. *Progress Phys. Geogr.* **2008**, *32*, 31–49.
24. Kraus, K.; Pfeifer, N. Advanced DTM generation from LiDAR data. *Int. Arch. Photogramm. Remote Sens.* **2001**, *XXXIV-3/W4*, 23–30.
25. Vosselman, G. Slope based filtering of laser altimetry data. *Int. Arch. Photogramm. Remote Sens. Spat. Inf. Sci.* **2000**, *XXXIII*, 935–942.

26. Sithole, G. Filtering of laser altimetry data using a slope adaptive filter. *Int. Arch. Photogramm. Remote Sens.* **2001**, *XXXIV-3/W4*, 203–210.
27. Chen, Q.; Gong, P.; Baldocchi, D.; Xie, G. Filtering airborne laser scanning data with morphological methods. *Photogramm. Eng. Remote Sens.* **2007**, *73*, 175–185.
28. Kobler, A.; Pfeifer, N.; Ogrinc, P.; Todorovski, L.; Oštir, K.; Džeroski, S. Repetitive interpolation: A robust algorithm for DTM generation from Aerial Laser Scanner Data in forested terrain. *Remote Sens. Environ.* **2006**, *108*, 9–23.
29. Bao, Y.; LiïijŇ G.; Cao, C.; Li, X.; Zhang, H.; He, Q.; Bai, L.; Chang, C. Classification of LiDAR point cloud and generation of DTM from LiDAR height and intensity data in forested area. *Int. Arch. Photogramm. Remote Sens. Spat. Inf. Sci.* **2008**, *XXXVII*, 313–318.
30. Mongus, D.; Žalik, B. Parameter-free ground filtering of LiDAR data for automatic DTM generation. *ISPRS J. Photogramm. Remote Sens.* **2012**, *67*, 1–12.
31. Sithole, G.; Vosselman, G. Experimental comparison of filter algorithms for bare-earth extraction from airborne laser scanning point clouds. *ISPRS J. Photogramm. Remote Sens.* **2004**, *59*, 85–101.
32. Hyyppä, H.; Yu, X.; Hyyppä, J.; Kaasalainen, H.; Honkavaara, E.; Rönnholm, P. Factors affecting the quality of DTM generation in forested areas. *Int. Arch. Photogramm. Remote Sens. Spat. Inf. Sci.* **2005**, *36*, 85–90.
33. Holmgren, J.; Nilsson, M.; Olsson, H. Simulating the effects of LiDAR scanning angle for estimation of mean tree height and canopy closure. *Can. J. Remote Sens.* **2003**, *29*, 623–632.
34. Hopkinson, C. The influence of flying altitude, beam divergence, and pulse repetition frequency on laser pulse return intensity and canopy frequency distribution. *Can. J. Remote Sens.* **2007**, *33*, 312–324.
35. Hopkinson, D.; Chasmer, L.E.; Zsigovics, G.; Creed, I.F.; Sitar, M.; Treitz, P.; Maher, R.V. Errors in LiDAR ground elevation and wetland vegetation height estimates. *Int. Arch. Photogramm. Remote Sens. Spat. Inf. Sci.* **2004**, *36*, 108–113.
36. Takahashi, T.; Yamamoto, K.; Miyachi, Y.; Senda, Y.; Tsuzuku, M. The penetration rate of laser pulses transmitted from a small-footprint airborne LiDAR: A case study in closed canopy, middle-aged pure sugi (*Cryptomeria japonica* D. Don) and hinoki cypress (*Chamaecyparis obtusa* Sieb. et Zucc.) stands in Japan. *J. For. Res.* **2006**, *11*, 117–123.
37. Fisher, P.F.; Tate, N.J. Causes and consequences of error in digital elevation models. *Prog. Phys. Geogr.* **2006**, *30*, 467–489.
38. Meng, X.; Currit, N.; Zhao, K. Ground filtering algorithms for airborne LiDAR data: A review of critical issues. *Remote Sens.* **2010**, *2*, 833–860.
39. Maguya, A.; Junttila, V.; Kauranne, T. Adaptive algorithm for large scale dtm interpolation from LiDAR data for forestry applications in steep forested terrain. *ISPRS J. Photogramm. Remote Sens.* **2013**, *85*, 74–83.
40. Sah, B.P.; Hämäläinen, J.M.; Sah, A.K.; Honji, K.; Foli, E.G.; Awudi, C. The use of satellite imagery to guide field plot sampling scheme for biomass estimation in Ghanaian forest. *ISPRS Ann. Photogramm. Remote Sens. Spat. Inf. Sci.* **2012**, *I-4*, 221–226.

41. Gautam, B.; Peuhkurinen, J.; Kauranne, T.; Gunia, K.; Tegel, K.; Latva-Käyrä, P.; Rana, P.; Eivazi, A.; Kolesnikov, A.; Hämäläinen, J.; *et al*. Estimation of forest carbon using LiDAR-Assisted Multi-Resource Programme (LAMP) in Nepal. Presented at International Conference on Advanced Geospatial Technologies for Sustainable Environment and Culture, Pokhara, Nepal, 12–13 September 2013.
42. McGaughey, R.J.; Carson, W.W. Fusing LiDAR data, photographs, and other data using 2D and 3D visualization techniques. In Proceedings of Terrain Data: Applications and Visualization—Making the Connection, Charleston, SC, USA, 28–30 October 2003; pp. 16–24.
43. Terrascan. Terrasolid's Software for LiDAR Data Processing and 3D Vector Data Creation, 2012. Available online: http://www.terrasolid.com/products/terrascanpage.html (accesed on 28 January 2014).

Appendix

A. Parameters Used to Generate Test DTMs in Terrascan

The following parameters were used to generate the test DTMs used for comparison in this study:

Class:	2 (ground)
Value:	triangulated model
Export:	whole area
Grid spacing:	1 m
Maximum triangle length:	700 m
Model buffer:	100 m
Outside points:	skip
Z decimals:	0.123

B. Parameters Used to Generate Test DTMs in FUSION

The following command was used to generate the test DTMs used in this study from FUSION:

Ground filtering:
groundfilter/gparam:−1/wparam:2/tolerance:0.1/iterations:10 <output laser data (LDA) file> 2 <input LAS file>

DTM generation:
gridsurfacecreate/median:8/spike:20 <output DTM file> 2 M M 1 12 2 2 <input LDA file>

PUBL. III

Maguya, A. S., Tegel, K., Junttila, V., Kauranne, T., Korhonen, M., Burns, J., Leppanen, V. and Sanz, B., Moving Voxel Method For Estimating Canopy Base Height From Airborne LiDAR Data, *Remote Sensing*, 7(7), 8950–8972, 2015

Remote Sens. **2015**, *7*, 8950-8972; doi:10.3390/rs7078950

OPEN ACCESS

remote sensing

ISSN 2072-4292

www.mdpi.com/journal/remotesensing

Article

Moving Voxel Method for Estimating Canopy Base Height from Airborne Laser Scanner Data

Almasi S. Maguya [1,2,*], Katri Tegel [3], Virpi Junttila [1], Tuomo Kauranne [1,3], Markus Korhonen [3], Janice Burns [3], Vesa Leppanen [3] and Blanca Sanz [3]

[1] Lappeenranta University of Technology, P. O. Box 20, Lappeenranta 53851, Finland;
E-Mails: virpi.junttila@lut.fi (V.J.); tuomo.kauranne@lut.fi (T.K.);

[2] Faculty of Science and Technology, Mzumbe University, P. O. Box 1, Mzumbe, Tanzania

[3] Arbonaut Ltd., Kaislakatu 2, Joensuu 80130, Finland;
E-Mails: katri.tegel@arbonaut.com (K.T.); markus.korhonen@arbonaut.com (M.K.);
janice.burns@arbonaut.com (J.B.); vesa.leppanen@arbonaut.com (V.L.);
blanca.sanz@arbonaut.com (B.S.)

* Author to whom correspondence should be addressed; E-Mail: almasi.maguya@lut.fi;
Tel.: +358-294-462-111; Fax: +358-5-621-2350.

Academic Editors: Nicolas Baghdadi and Prasad S. Thenkabail

Received: 9 March 2015 / Accepted: 17 June 2015 / Published: xx

---

Abstract: Canopy base height (CBH) is a key parameter used in forest-fire modeling, particularly crown fires. However, estimating CBH is a challenging task, because normally, it is difficult to measure it in the field. This has led to the use of simple estimators (e.g., the average of individual trees in a plot) for modeling CBH. In this paper, we propose a method for estimating CBH from airborne light detection and ranging (LiDAR) data. We also compare the performance of several estimators (Lorey's mean, the arithmetic mean and the 40th and 50th percentiles) used to estimate CBH at the plot level. The method we propose uses a moving voxel to estimate the height of the gaps (in the LiDAR point cloud) below tree crowns and uses this information for modeling CBH. The advantage of this approach is that it is more tolerant to variations in LiDAR data (e.g., due to season) and tree species, because it works directly with the height information in the data. Our approach gave better results when compared to standard percentile-based LiDAR metrics commonly used in modeling CBH. Using Lorey's mean, the arithmetic mean and the 40th and 50th percentiles as CBH estimators at the plot level, the highest and lowest values for root mean square error (RMSE) and root mean square error for cross-validation ($RMSE_{cv}$) and R^2

for our method were 1.74/2.40, 2.69/3.90 and 0.46/0.71, respectively, while with traditional LiDAR-based metrics, the results were 1.92/2.48, 3.34/5.51 and 0.44/0.65. Moreover, the use of Lorey's mean as a CBH estimator at the plot level resulted in models with better predictive value based on the leave-one-out cross-validation (LOOCV) results used to compute the $RMSE_{cv}$ values.

Keywords: canopy base height; CBH; forest fire; LiDAR; moving voxel

1. Introduction

The last two decades have seen an increasing trend in forest fire frequency and the amount of land burned [1]. Extreme drought and the accumulation of fuels are the two major factors responsible for this increase [2–5]. For example, in the European region alone, the number of forest fires taking place annually is estimated to be 65,000, burning approximately half a million ha of forest [3]. Most of these fires (about 85%) take place in the Mediterranean region alone (mostly Portugal, Spain and Greece) [3–7]. Similarly, forest fires burn an average of 3.7 million ha of forest in the U.S. each year [1].

Forest fires can have a number of catastrophic consequences, including human casualties, destruction of property and forest assets, financial implications (fire suppression and post-fire rehabilitation costs), as well as ecological impacts. For example, in 2003, large forest fires in the districts of Castelo Branco, Portalegre and Santerm in Portugal led to the death of 21 people and damages estimated at over one billion euros [6,7], with more than one thousand people wounded. In another example, large forest fires in Greece led to the deaths of 80 people in 2007 and burned 1710 buildings. The estimated damage caused by these fires was 1.5 billion euros [8]. Forest fires also ravage boreal forests. Recently (summer 2014), large forest fires (the largest witnessed in four decades) raged in central Sweden, leaving at least one person dead and burning around 37,000 ha of forest [9,10].

Forest fires also play an important role in global carbon dynamics [11–13] by releasing a large amount of carbon dioxide (CO_2) gas into the atmosphere. Accumulation of CO_2 gas in the Earth's atmosphere contributes significantly to climate change [14,15]. As forest fires can cause serious damage and have other undesirable consequences, it is important that proper proactive measures be taken in order to: (1) minimize the risk of such disasters happening; and (2) be able to predict the behavior of fires when they break out.

Minimizing the risk of forest fire disasters is commonly done through fuel treatment practices, such as thinning or prescribed fires, so as to reduce the amount of fuel accumulated over time [16]. Since less fuel will be available to burn when fire breaks out, the intensity of the fire, as well as its rate of spread will be greatly minimized [17,18]. This will not only make the task of containing the fire less challenging, but it will also make the fire less destructive. In addition, being able to predict the behavior of fire (e.g., intensity and rate of spread) is important for fire managers, because it will enable them to make informed decisions in fire suppression (e.g., mobilization and allocation of resources). To this end, fire behavior and growth simulation models, such as FARSITE(see [19]), are indispensable for fire

managers. These models combine spatial and temporal information on topography, fuels and weather with existing models for surface fire, crown fire, spotting, post-frontal combustion and fire acceleration into a two-dimensional fire growth model [19].

To successfully model the behavior of forest fires or minimize their risk, however, good knowledge of the spatial distribution of fuels in a particular area is required [20]. On the one hand, fire managers need to know areas with excessive fuel loads, so that they can arrange resources for thinning and prescribed fires; on the other hand, to benefit from fire behavior simulation tools, such as FARSITE, several data layers pertaining to the fuel characteristics (metrics) in a particular area are needed [19]. Examples of these metrics include canopy bulk density (CBD), canopy height (CH) and canopy base height (CBH) [21–23]. CBD refers to the amount of fuel per unit volume (measured in kg/m^3). CH is the highest height at which the canopy fuel density is greater than a critical threshold (normally 0.011 kg/m^3), and CBH refers to the lowest height at which canopy bulk density exceeds a threshold of 0.011 kg/m^3 [21].

CBH describes the minimum amount of fuel required to propagate the fire from the surface fuel layer to the canopy fuel layer and therefore plays a role as the most important factor in crown fire initiation [23,24]. Crown fires are special in that they spread several times faster than surface fires, and they burn more severely and with larger flames, making them more destructive and difficult to control. Additionally, they can occur in a variety of forest types [25,26]. As a consequence, there has been an increasing amount of literature on modeling CBH in recent years. Much of this literature is based on current state-of-the-art remote sensing technologies, particularly light detection and ranging (LiDAR) [27,28]. Unlike passive remote sensing technologies, such as aerial photographs, LiDAR is an active remote sensing technology capable of penetrating forest canopies and providing 3D information about the canopy structure [29].

In a study conducted by [23], for example, CBH was estimated for loblolly pine forests at the plot level using both allometric equations and a software package known as CrownMass/FMAPlus. Unlike many studies, this study used Lorey's mean to estimate CBH at the plot level for a total of 50 sample plots. Lorey's mean is a weighted mean, which uses tree basal area as a weighting factor; thus, bigger trees contribute more to the mean [30]. In this study, the difference in CBH estimated using the two methods was relatively small (1.5 m), with Lorey's mean giving a higher CBH estimate. In another study, [31] used a data fusion (LiDAR and imagery) approach for estimating CBH and other canopy fuel parameters. This study investigated which remote sensing dataset (LiDAR or imagery) could estimate CBH more accurately and whether the fusion of the two could produce more accurate CBH estimates. The results of this study showed that LiDAR alone provides more accurate CBH estimates ($R^2 = 0.78$, RMSE = 1.63 m) compared to imagery ($R^2 = 0.31$, RMSE= 3.60 m), whereas fusion of the two led to a small improvement in performance ($R^2 = 0.84$, RMSE = 1.44 m).

LiDAR was also successfully used to estimate CBH in the studies by [21,22]. In the former study, LiDAR metrics and field-measured fuel metrics were used to build regression models for predicting CBH to develop maps for critical canopy fuel parameters, including CBH. The regression model for predicting CBH developed in this study had R^2 and RMSE values of 0.77 and 3.9 m, respectively. In the latter study, LiDAR data were partitioned into cells, and cluster analysis was performed on each classified vegetation cell to discriminate between understory and overstorey layers. CBH was taken to be the first percentile of the overstorey layer.

Although LiDAR has been used in many studies to estimate CBH and other critical canopy fuel parameters, two major limitations are consistently reported by these studies. One, most of the models proposed in these studies are species specific (e.g., [21,23,31]), and two, many studies report challenges in measuring canopy fuel parameters in the field. The consequence of the former is that regression models built in those studies cannot be applied directly to forests with different species, *i.e.*, they are limited to the area sampled in the respective studies and are likely to give unreliable results when used outside the sampled area. The consequence of the latter, on the other hand, is that there has not been a standard way for measuring canopy fuel parameters in the field, and hence, different studies adopt different approaches for measuring canopy parameters in the field, particularly CBH. Since measuring CBH accurately in the field is quite a difficult task [32], common practice has been to use the arithmetic mean or weighted (Lorey's) mean of tree crown base heights (C_rBH) in a plot (e.g., [23,31,33]), due to the fact that these two quantities are easy to measure or calculate.

Despite these challenges, previous studies have shown that LiDAR has a high potential to estimate crown fuel parameters with a high degree of accuracy. To this end, standardization of field measurement practices is of great importance. This importance is due to role of field measurements in calibrating regression models used to estimate CBH from LiDAR data. This paper seeks to address this challenge by proposing new LiDAR metrics for estimating CBH. The proposed metrics are derived (measured) directly from LiDAR height information. Unlike the common practice of using LiDAR height percentile information, the proposed metrics are not percentile-based. In particular, this paper aims to: (1) develop and test new LiDAR metrics for estimating CBH; and (2) use the developed metric as an independent variable in regression models to compare the different independent variables used to estimate CBH in the field, namely the arithmetic mean, Lorey's mean and percentile scores.

2. Material and Methods

2.1. Study Area

The study area is located about 340 m above sea level in Eastern Finland at the Koli Forest, which belongs to the Lieksa municipality (about 63°05′40″N, 29°48′31″E) (see Figure 1). The area is known for its white quartzite cliffs, steep topography and traditional landscapes. Over 70% of the region's surface area is forest land, and 20% is water. The forest is dominated by conifers (65% pine, 25% spruce, 7% birch and 3% other species). The main tree species are Scots pine (*Pinus sylvestris* L.), and Norway spruce (*Picea abies (L.) Karst*). The area is sparsely populated with a total area of 21,585 km^2 and a population of 175,000, which results in a population density of 9.8 inhabitants per square kilometer. Figure 1 shows a map of Finland and the location of the study site. The forests in the study site feature both natural and managed forests, with varying degrees of intensity. Conservation in the area is relatively young and was imposed less than twenty years ago. Both forest classes contain undergrowth.

Forest fires in Finland are mostly caught early on, because the country is still populated densely enough, and monitoring flights are frequent in the short hot season. However, as an example of neighboring Sweden from 2014 shows, strong winds and canopy fires can still be a devastating condition also in Finland.

Figure 1. Map of Finland showing the location of the study area.

2.2. Experimental Data

Two kinds of experimental data were used in this study, namely LiDAR data and field data. The following is a description of the data.

2.2.1. LiDAR Data

The LiDAR data used in this study were obtained free of charge from the National Land Survey (NLS) of Finland (www.maanmittauslaitos.fi). The data were acquired in 2014 using an average flight altitude of 2 km with a scan angle of ± 20 degrees. The resulting average LiDAR pulse density was 0.5 pulses per square meter, with an offset of approximately 1.4 m between the measurements. The mean

error for height was 15 cm at most, while the horizontal accuracy was 60 cm. The beam footprint at ground level was 50 cm in diameter.

Information recorded for each LiDAR pulse includes the class of the pulse (ground or vegetation), flight line number, time stamp of the outgoing pulse, X-, Y- and Z-coordinates, intensity and the back-scattering order of the pulse. An automatic classification of the pulses into ground and vegetation returns was performed, and the results were checked against a stereo model from aerial imagery by the NLS.

LiDAR data used in the current article are of the same kind as the operational laser scanning of the forests in Finland. In 2010, Finland decided to scan the entire country by airborne laser in ten year cycles. The density chosen for this is roughly 0.5 returns per square meter. In the past, the scanners have mostly used single pulse mode, but currently, multiple pulse mode is widely adopted. As the goal of the current research is to calculate forest fire potential maps for the whole country, it has not been possible to adjust scanning parameters, such as pulse density.

2.2.2. Field Data

Field measurements for crown fuels were collected in April 2014 for 26 circular plots equally representing the dominant fuel types in the study area. Each plot covered an area of 256 m^2 (radius = 9.03 m). A survey-grade Trimble GPS receiver was used to navigate to the plots and to georeference plot centers, acquiring data for plot centers from an average of at least 100 Global Navigation Satellite System (GNSS) locations.

Plot boundaries were measured using the Haglöff Vertex Laser Range Finder. The same instrument was used to measure the height of each tree. The diameter at breast height (DBH) was measured for all trees using a diameter tape. For each tree with a diameter at breast height (DBH) $\geq$ 8 cm in a plot, the following properties were recorded: tree class, species, DBH, height, crown base height (CBH) and crown class (dominant, co-dominant, intermediate and suppressed).

CBH was considered to be the distance between the ground and the lowest live branch in the crown of a tree. Small isolated branches with leaves, separated from the main crown, were not considered as indicating crown base height. The Haglöff vertex was used to measure CBH. The crown class of each tree was recorded as described above. Table 1 presents a summary of the field plots used as ground data.

In addition to CBH measurements for individual trees in each plot, five pictures were taken from the plot center facing in the four cardinal directions (N, S, E, W) and the sky. These photos were taken to help as a visual aid later when analyzing and interpreting the experimental data. Figure 2 shows examples of plot photos.

2.3. Methods

The method for estimating CBH from LiDAR data proposed in this paper is based on the idea of a moving voxel. A voxel, or volumetric pixel, is an analogy of a pixel in 3D. The use of the voxel in estimating CBH and other forest properties from LiDAR data has been reported in several past studies. In these studies, the emphasis had been to use the voxel to characterize the vertical structure of the canopy by dividing the LiDAR data into vertical bins (voxels) and counting the number of LiDAR hits in each

bin (e.g., [34,35]). This paper takes a different approach and uses a moving voxel to locate gaps in the LiDAR point cloud (and hence, in the respective forest) and then estimates the height of these gaps from the ground. This information is then used to derive LiDAR metrics, which are used to estimate CBH as independent variables in a linear regression. The main assumption behind the method is that tree crowns tend to block most of the LiDAR pulses falling on them, thus creating a partial gap underneath the crown (see Figure 3). The idea is to use a moving voxel to locate gaps and estimate their height relative to the ground. It turns out that, as will be shown in the next section, the heights of these gaps strongly correlate with field-measured CBH values and are the basis for the LiDAR metrics used in estimating CBH in this paper.

To estimate CBH from LiDAR data, three main steps are performed: (1) initialization and data pre-processing; (2) searching for gaps and estimating their height (gap mapping); and (3) LiDAR metric generation and CBH estimation.

Table 1. Summary of field plots used in this study. The mean value for canopy base height (CBH) is based on live trees in each plot.

		DBH			Height			CBH		
Plot ID	**No. of Trees**	**Min**	**Max**	**Mean**	**Min**	**Max**	**Mean**	**Min**	**Max**	**Mean**
1	17	9.9	33.7	19.4	2.0	28.8	15.0	0.0	11.7	6.3
3	1	17.5	17.5	17.5	16.0	16.0	16.0	3.1	3.1	3.1
4	21	8.5	42.6	13.7	6.9	26.2	13.0	2.8	9.2	6.1
5	3	10.9	23.8	19.4	11.4	18.8	16.3	0.0	1.0	0.3
6	32	8.0	20.0	12.1	6.0	16.0	11.4	0.4	5.7	3.3
8	4	9.8	29.1	23.5	6.6	21.8	14.6	0.5	18.5	8.8
10	19	9.0	37.3	19.9	9.4	23.6	17.2	4.7	12.5	8.9
11	29	8.3	59.3	18.4	6.1	24.4	15.7	0.5	14.7	7.5
12	16	8.4	34.3	21.6	6.6	25.8	17.8	5.7	15.3	11.0
13	16	6.8	46.0	21.4	8.4	26.5	19.4	0.2	16.9	8.5
14	16	8.2	37.5	20.8	3.3	27.1	10.8	0.3	11.9	3.2
15	24	9.0	32.8	17.9	1.7	22.8	13.1	1.0	10.8	6.5
16	14	8.3	36.5	17.2	5.8	19.8	11.3	0.8	6.6	3.6
17	24	8.0	28.9	11.4	5.5	16.5	9.3	0.0	3.2	2.2
18	6	19.0	31.4	26.8	22.2	29.1	25.7	8.7	16.9	14.3
19	19	8.6	42.0	26.0	5.8	26.1	19.7	1.2	16.2	9.6
20	26	7.5	27.0	16.0	7.7	22.6	14.9	3.6	10.8	7.9
21	35	8.8	39.4	19.3	3.2	26.7	16.7	0.9	14.4	6.2
22	43	8.8	22.8	13.3	7.1	16.4	11.5	0.5	8.9	5.2
23	16	13.9	39.7	24.9	12.3	28.2	21.9	1.5	12.1	5.2
24	24	9.3	37.0	22.2	6.1	24.8	17.3	1.4	14.2	4.0
26	28	8.0	27.2	16.0	5.9	21.8	13.3	0.7	11.0	3.7
27	28	8.7	35.0	16.9	7.0	23.8	14.6	1.7	12.8	4.9
32	22	8.0	17.1	10.0	1.8	13.9	9.0	0.9	5.1	2.6
33	14	8.0	11.8	9.3	5.9	8.8	7.4	0.4	4.5	2.3
44	20	9.7	30.8	18.6	5.1	21.2	13.4	0.9	10.3	3.3

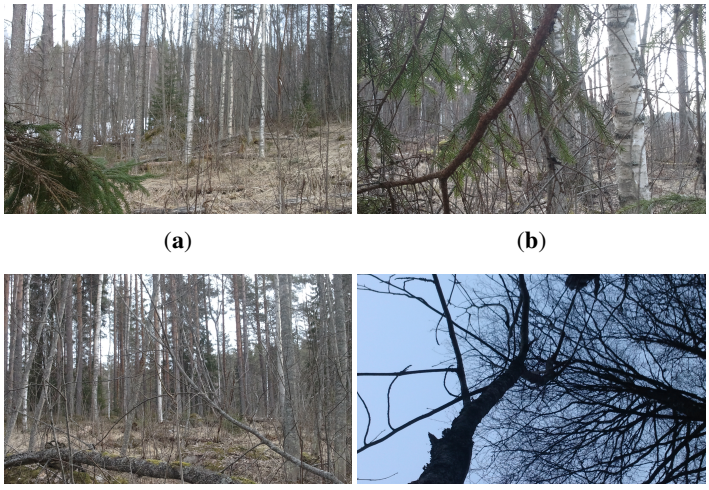

(**a**) (**b**)

(**c**) (**d**)

Figure 2. Examples of photos from one of the sample plots: (**a**) north facing; (**b**) south facing; (**c**) east facing; (**d**) sky facing.

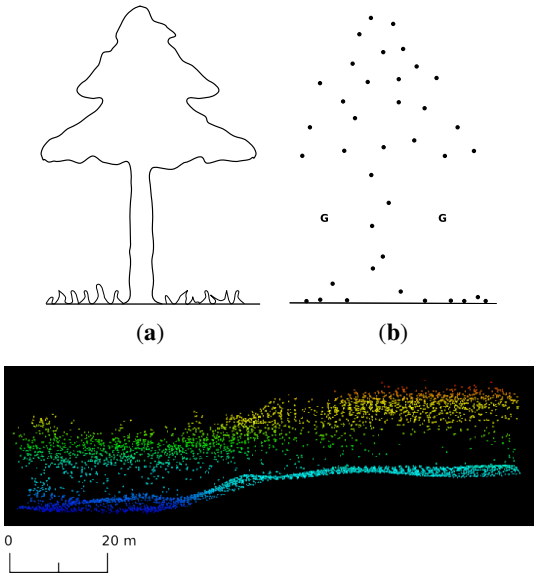

(**a**) (**b**)

(**c**)

Figure 3. Illustration of how a partial gap is formed (marked with a G) below a tree crown (**a**) in a LiDAR point cloud (**b**) due to most of LiDAR pulses being blocked by the crown and the absence of reflecting objects between the crown and the ground; (**c**) shows a partial gap formed below the canopy in a real LiDAR point cloud.

2.3.1. Initialization and Data Pre-Processing

The initialization and data pre-processing step sets the stage for subsequent steps. In this step, the LiDAR data are normalized, *i.e.*, the elevation of every point is subtracted from the DTM of the area, so that each point represents height (from the ground), and then, all points with a height of less than 0.5 m (considered ground points) are discarded. Next, parameters governing the operation of the method are determined and initialized. These parameters include: voxel width, voxel height, step size and point threshold. Voxel width specifies the width and length of the voxel (*i.e.*, the base), while voxel height specifies the height of the voxel. Step size specifies the distance (in meters) that the voxel moves horizontally (in the x-y plane), while point threshold specifies the maximum allowed number of points in a voxel to be considered a gap. Suitable values for these parameters for a given LiDAR point cloud are determined by experimenting on the field and LiDAR data. Values of these parameters used in this study were 8 m, 2 m, 1 m and 3 points for voxel width, voxel height, step size and point threshold, respectively. The choice of voxel width is influenced by point spacing in the LiDAR point cloud. If the width is too small relative to the point spacing, there will be too many false gaps, and if the width is too big, small gaps will be missed. Similarly, voxel height and step size are chosen, such that both small and large gaps are detected. Finally, if the point threshold is too small, very few gaps will be detected; if it is too high, there will be a large number of false gaps.

2.3.2. Gap Mapping

In this step, gaps in the LiDAR point cloud are located, and their heights relative to the ground are estimated. This is achieved by the use of a moving voxel in the search space. The search space is taken to be the box enclosing the pre-processed LiDAR point cloud with its origin at the point (Easting$_{min}$, Northing$_{min}$, 0), where Easting$_{min}$ and Northing$_{min}$ refer to the smallest easting and the smallest northing values in the point cloud, respectively (marked as P_1 and P_2, respectively, in Figure 4). Two kinds of movement are employed in the search space: (1) horizontal movement; and (2) vertical movement. Horizontal voxel movement is used to detect gaps, while vertical voxel movement is used to estimate the heights of the detected gaps.

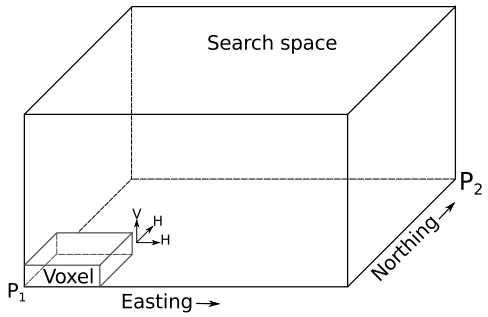

Figure 4. Illustration of the search space and the horizontal (marked with a H) and vertical (marked with a V) voxel movements.

Horizontal Voxel Movement

The goal of the horizontal voxel movement is to locate gaps in the search space. Starting at the origin of the search space, the voxel is first repeatedly moved along the x-axis (easting) using steps equal to the step size. At each step, points enclosed in the voxel are counted. A gap is detected when two conditions are met (see Figure 5): first, if the number of points in the voxel is less than or equal to the point threshold and, second, when the number of all of the points above the voxel is greater than the point threshold (see Figure 5a). The latter condition ensures that the gaps detected are not due to the absence of vegetation in the corresponding locations (see Figure 5c). After a gap has been detected, the next step is to estimate its height. This is achieved by using vertical voxel movement.

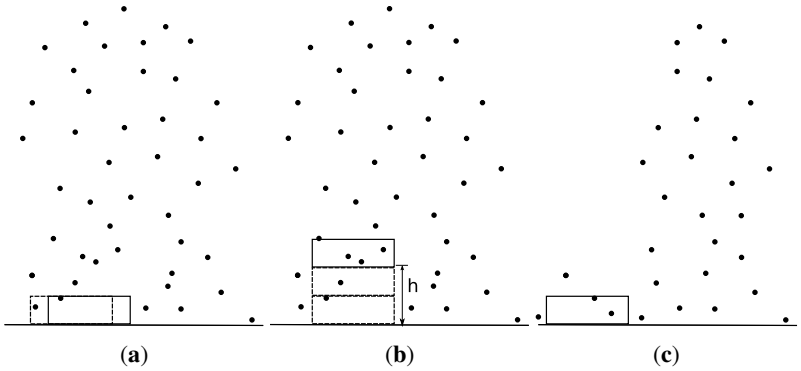

Figure 5. Detecting and estimating the height of a gap (side view): (**a**) a gap has been located (the number of points in the voxel is less than or equal to the point threshold, which was 2 in this example); (**b**) the height of the gap (marked as h) is estimated by using vertical voxel movement; (**c**) an example of a gap formed due to the absence of vegetation at a location. The dashed boxes represent the position of the voxel before movement.

Vertical Voxel Movement

The aim of the vertical voxel movement is to estimate the heights of the gaps that have been detected. To estimate the height of a gap, the voxel is repeatedly moved upwards in steps equal to the voxel height until the number of points in the voxel exceeds the point threshold (see Figure 5). The height of the gap is then given by $voxel\ height \times N$.

The outcome of the gap mapping step is a gap height raster with cell size equal to the step size and origin (top left corner) at ($Easting_{min} + \frac{voxel\ width}{2}$, $Northing_{max} - \frac{voxel\ width}{2}$); note the starting point of the voxel in Figure 4. Figure 6 shows a portion of the gap height raster. Note that to speed up processing, searching for gaps can be confined to the space extending a few meters from the plot boundary, as shown in Figure 7.

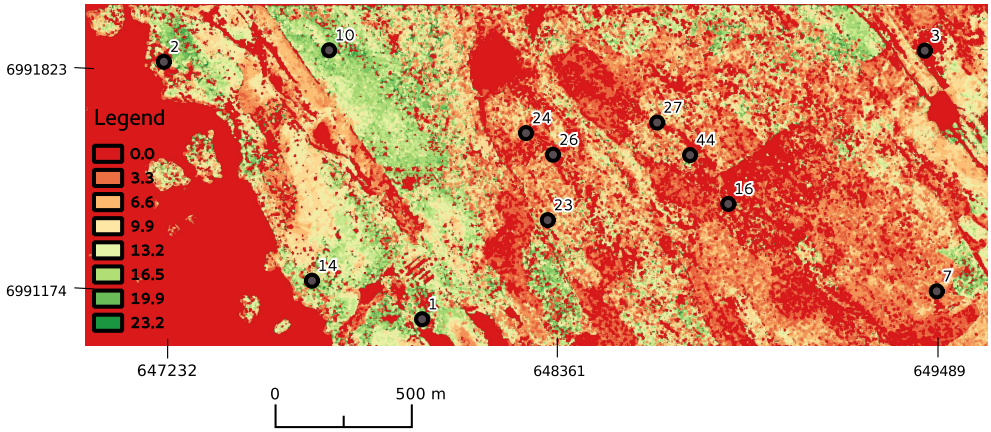

Figure 6. A portion of the gap height raster with some of the sample plots superimposed. The gap heights are in meters.

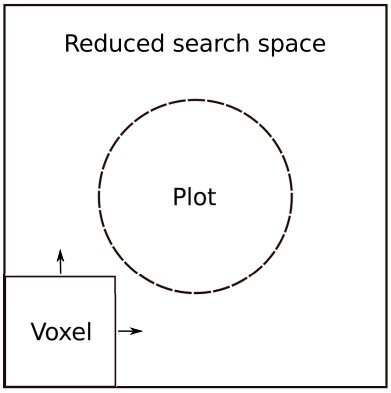

Figure 7. Speeding up processing by confining the search space (plan view). The arrows indicate horizontal voxel movement.

Figure 8 shows the degree of correlation between the estimated gap heights and the field-measured CBH values in 24 of the field plots. The plotted values for gap heights in each plot were obtained by taking the highest gap height values corresponding to the number of plots and matching them to the field-measured individual tree CBH values based on their magnitude (such that the highest goes with the highest, *etc.*). Plots with ID numbers 3 and 5 do not appear in the figure, because no information could be extracted from the LiDAR data corresponding to these plots. A possible reason for this anomaly is the fewer number of trees present in the plots (see Table 1 and Figure 9) and consequently fewer LiDAR points. Following this anomaly, subsequent analysis and results reported in the following sections are based on only the 24 plots shown in Figure 8.

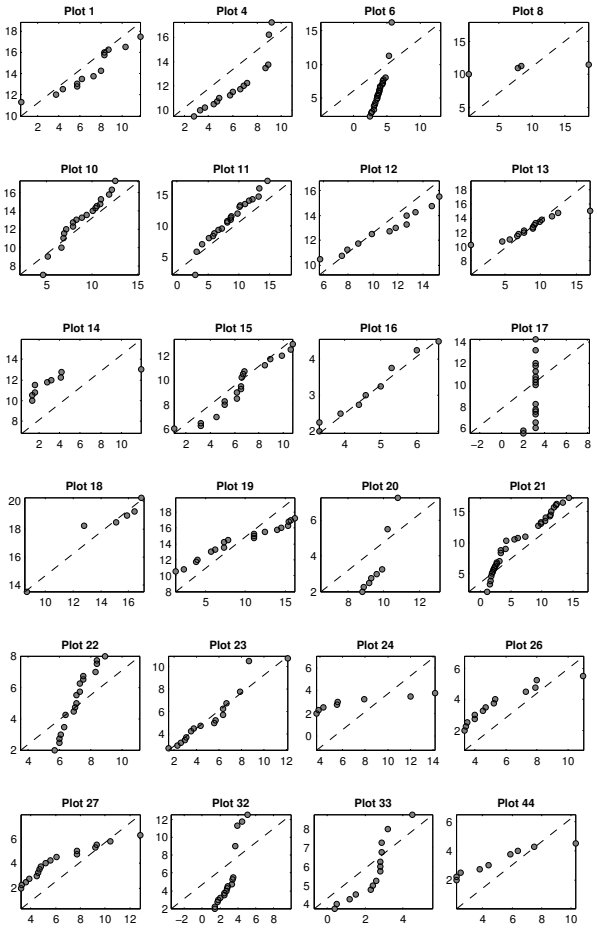

Figure 8. Correlation between calculated gap heights (y-axis) and field-measured CBH values (x-axis) for individual trees in 24 sample plots.

(**a**) (**b**)

Figure 9. *Cont*

(**c**) (**d**)

Figure 9. Examples of plots with anomalies: (**a**) Plot 3 east facing; (**b**) Plot 5 east facing; (**c**) Plot 17 south facing; (**d**) Plot 6 sky facing. The low number of trees in these plots or the lack of thereof led to very few LiDAR points in those plots.

2.3.3. LiDAR Metrics Generation and CBH Estimation

In this step, LiDAR metrics for use in CBH estimation (independent variables) are generated. These metrics are then combined with field-measured CBH values to form a dataset used for estimating CBH through linear regression.

LiDAR Metric Generation

To generate LiDAR metrics, the gap heights raster produced in the previous step is used. Points corresponding to each field-measured plot are extracted from the raster by taking all of the points that satisfy the equation:

$$R^2 \leq (X - r)^2 + (Y - s)^2$$

where R is the radius of each plot (9.03 m); r and s are the x- and y-coordinates of the center of the plot, respectively; and X and Y are the easting and northing values of the points in the gap heights raster. This is similar to placing a hypothetical cylinder of the same radius as the plots on the plot, such that the axis of the cylinder passes through the plot center, and taking all of the points in the cylinder.

Because of a small value for the step size used while generating the gap heights raster, there will be a high degree of duplication in the values extracted for each plot. Therefore, the next step is to remove duplicates from the values. To remove duplicates, the values are sorted (in either descending or ascending order) to bring equal values together into groups and picking one value from each group (see Figure 10). After duplicates have been removed, the following metrics (percentiles) are computed from the remaining values in each plot: g_{25}, g_{50}, g_{75} and g_{90}. These metrics serve as independent variables for estimating CBH.

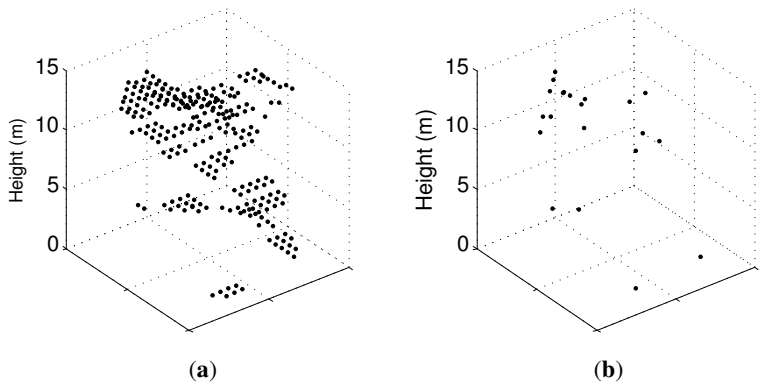

(**a**) (**b**)

Figure 10. Removing duplicates from gap height values: (**a**) before duplicates are removed; (**b**) after removing duplicates. Horizontal axes represent easting and northing.

CBH Estimation

To estimate CBH, several regression models were fitted. For the purpose of model fitting, several variables representing CBH at the plot level were derived from the field data. These variables served as dependent variables in regression models and include: (1) Lorey's mean (LOR); (2) the arithmetic mean (AVG); (3) the 40th percentile (P40); and (4) the 50th percentile (P50).

For comparison reasons, we fitted models using both the metrics introduced in this paper and traditional percentile LiDAR metrics (the coefficient of variation (CV), percentage of first returns, maximum height, mean height and the 25th, 50th, 75th and 90th percentiles) as independent variables.

Model fitting was done in the MATLAB^{TM}computing environment [36], whereby forward stepwise regression was used to automatically select variables for each model. Variable selection was based on the F-test. The minimum p-value for a variable to be removed was 0.1, while the maximum p-value for a variable to be added was set to 0.05. Leave-one-out cross-validation (LOOCV) was used to assess the predictive value of each regression model. For this purpose, the root mean squared error for cross-validation ($RMSE_{cv}$) was used.

3. Results

CBH estimation results obtained by using the LiDAR metrics introduced in this paper as independent variables are shown in Table 2 and in Figure 11. Results obtained using traditional percentile LiDAR metrics as independent variables are shown in Figure 12 and in Table 3. The CBH estimation results using traditional percentile LiDAR metrics are based on [21]. In each case, the best model for each dependent variable (*i.e.*, LOR, AVG, P40 and P50) obtained using stepwise regression is shown. The results shown in Table 3 were computed based on [21].

Table 2. Regression models obtained using different dependent variables against the proposed LiDAR metrics. LOR, Lorey's mean; AVG, arithmetic mean; P40, 40th percentile.

Variable	CBH	RMSE (m)	RMSE_{cv} (m)	R^2	*p*-value
LOR	$(0.60)g_{75} + 0.79$	2.40	2.69	0.46	0.0003
AVG	$(1.05)g_{25} - (1.47)g_{50} + (1.06)g_{75} + 0.40$	2.04	3.66	0.61	0.0003
P40	$(1.28)g_{25} - (1.97)g_{50} + (1.98)g_{75} - (0.69)g_{90} + 1.20$	1.74	3.36	0.75	0.00002
P50	$(1.16)g_{25} - (1.82)g_{50} + (2.09)g_{75} - (0.75)g_{90} + 1.16$	2.01	3.90	0.71	0.00006

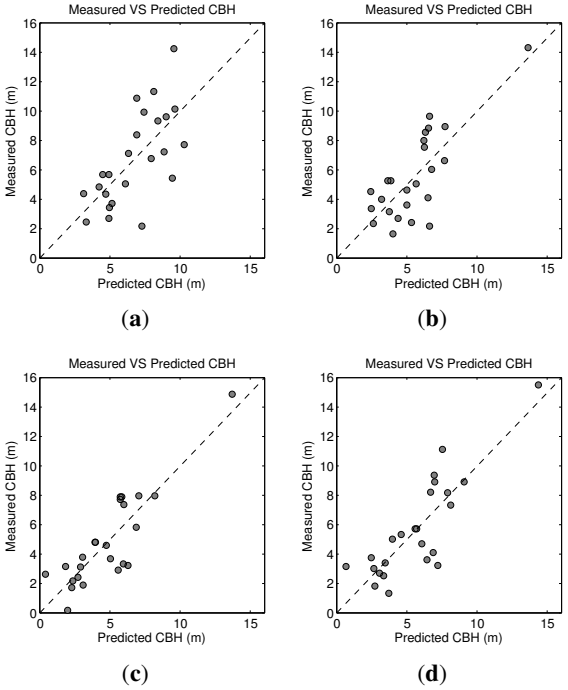

Figure 11. Plots showing a comparison between measured and estimated CBH for the proposed LiDAR metrics: (**a**) LOR; (**b**) AVG; (**c**) P40; (**d**) P50. The diagonal line shows a 1:1 relationship.

Table 3. Regression models obtained using different dependent variables against traditional percentile LiDAR metrics.

Variable	CBH	RMSE (m)	RMSE_{cv} (m)	R^2	*p*-value
LOR	$(0.56)h_{50} - 0.31$	1.92	3.34	0.65	0.002
AVG	$(0.44)h_{50} - 0.07$	2.31	3.51	0.44	0.0004
P40	$(1.62)h_{50} - (1.19)h_{75} + 2.56$	2.48	5.15	0.44	0.002
P50	$(1.80)h_{50} - (1.26)h_{75} + 2.29$	2.38	4.98	0.55	0.0002

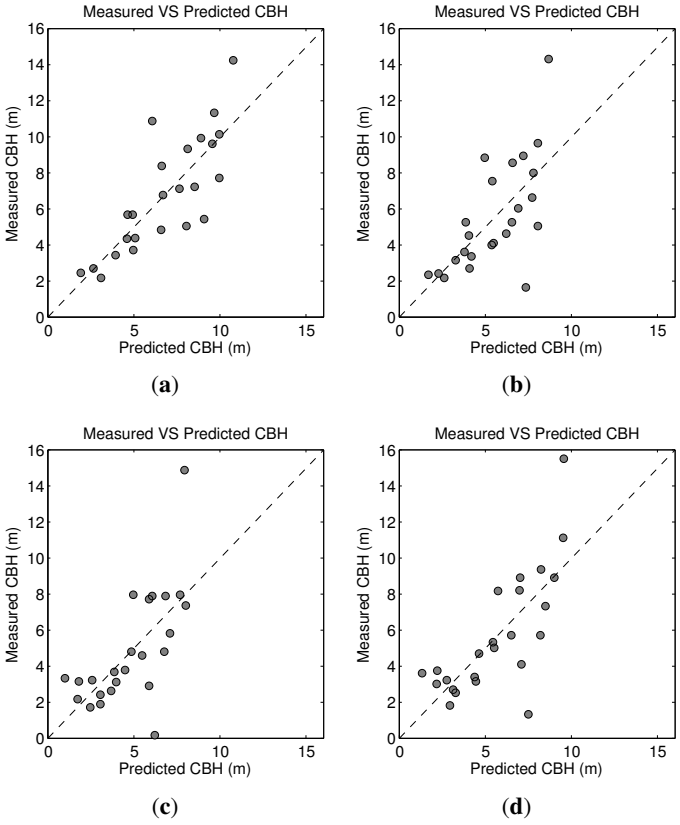

Figure 12. Plots showing a comparison between measured and estimated CBH for traditional percentile LiDAR metrics: (**a**) LOR; (**b**) AVG; (**c**) P40; (**d**) P50. The diagonal line shows a 1:1 relationship.

3.1. Effect of Voxel Width and Point Threshold

To study how the different dependent variables perform under various voxel dimensions and point thresholds, the effect of voxel dimensions was studied by varying the value of voxel width from 1 to 10 m, while keeping the point threshold and voxel height constant at three points and 2 m, respectively, and observing how the model RMSE for each dependent variable was affected. Similarly, The effect of point threshold was studied by varying the value of point threshold from 1–10 points. Figure 13 shows the effect of voxel width and point threshold on the model RMSE on the four dependent variables.

Results in Figure 13 show that LOR outperformed the other variables in both cases with lower and more consistent RMSE values in both cases. In the case of voxel width (Figure 13a), the best (more consistent) values for RMSE are obtained in the 5–8-m range. Outside this range, the RMSE values vary greatly among the variables. This behavior can be explained by the effect very large/very small voxels have. The effect of a large voxel for a given point threshold is that legitimate gaps will not be

detected (false negatives), while the effect of a small voxel is that illegitimate gaps will be detected (false positives). For the LiDAR data used in this study, suitable values of voxel width are in the range 5–10 m. On the other hand, all four variable are affected in a similar manner with changes in point threshold (Figure 13b). Suitable values for point threshold in this case are those in the range of 3–6 points. These results further demonstrate the suitability of LOR for representing CBH at the plot level.

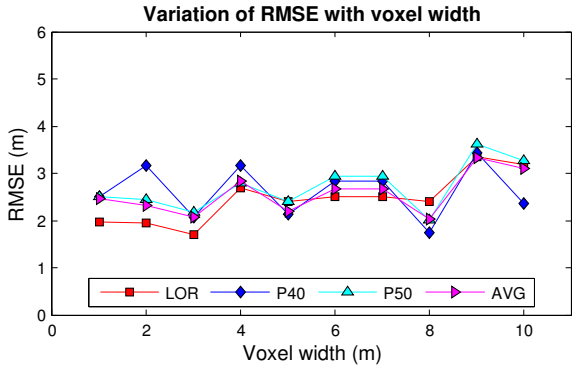

(**a**)

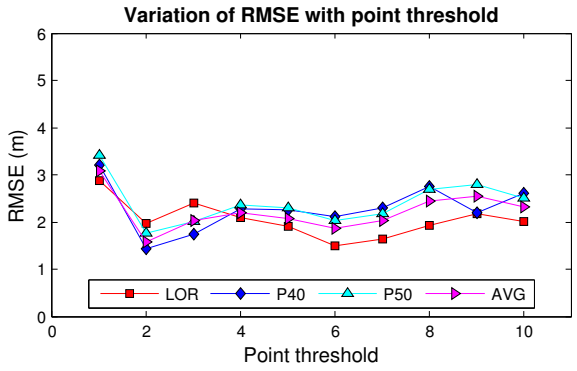

(**b**)

Figure 13. The effect of voxel width (**a**) and point threshold (**b**) on the model RMSE on the four dependent variables.

4. Discussion

Comparison of the four dependent variables (LOR, AVG, P40 and P50) showed that LOR gave the simplest model in either case (using traditional percentile LiDAR metrics and the proposed metrics) (see Tables 2 and 3). Furthermore, in both cases, the LOR-based model had the smallest $RMSE_{cv}$, which was very close to the corresponding RMSE value. This implies that, in both cases, the LOR-based models have better predictive value over models based on the other dependent variables. This observation is in agreement with results reported in previous studies (e.g., [23]). This observation further supports the

robustness of Lorey's mean in CBH estimation over the commonly-used arithmetic mean. However, Lorey's mean should be used with caution due to its tendency to be affected by big trees. This fact implies that in some cases, the CBH estimates obtained using Lorey's mean may be higher than the actual CBH, that is the minimum canopy bulk density required for the propagation of a surface fire to the crown could be reached at a lower height than that estimated using Lorey's mean.

With the exception of LOR, the remaining dependent variables gave more or less similar results in both cases, with higher RMSE and less consistent $RMSE_{cv}$ values being evident with models based on the traditional percentile LiDAR metrics. This similarity can be explained by the high degree of correlation among the variables, as shown in Figure 14. This observation implies that the use of different field estimates for CBH due to the lack of standardized field methods for estimating CBH does not have a profound effect on the final CBH estimation results. Despite this fact, LOR and AVG should be used with caution, because the former tends to be biased towards big trees, while the latter is susceptible to outliers. Point-cloud based voxels can also be seen as another way of defining CBH in a relatively objective way.

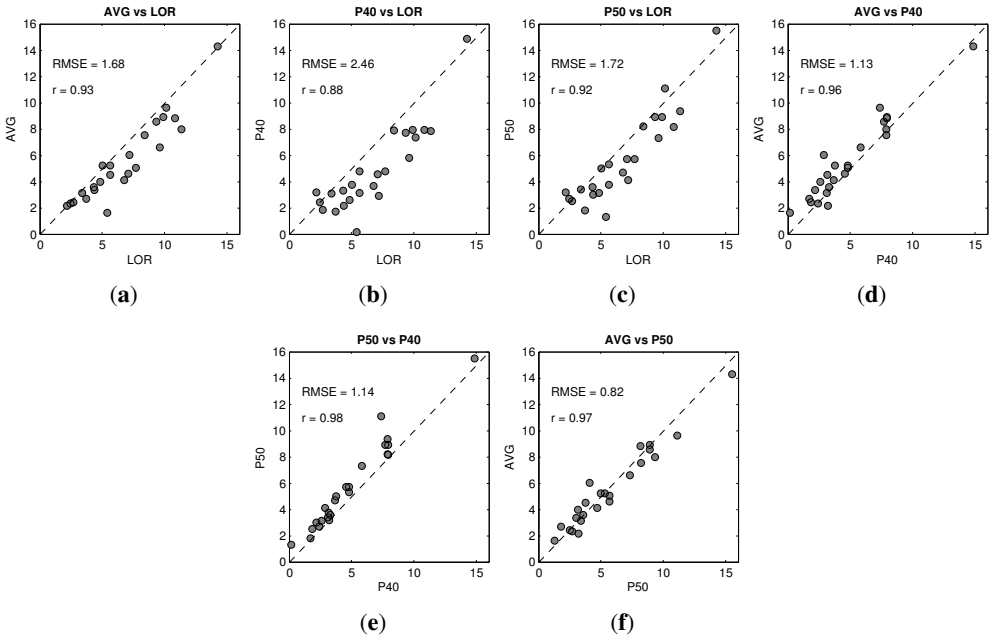

Figure 14. Comparison of the four dependent variables used in estimating CBH: (**a**) LOR *vs.* AVG; (**b**) LOR *vs.* P40; (**c**) LOR *vs.* P50; (**d**) P40 *vs.* AVG; (**e**) P40 *vs.* P50; (**f**) P50 *vs.* AVG. r represents the coefficient of correlation between the variables.

The lowest degree of correlation is seen between P40 and LOR (0.88) (Figure 14b), while the rest of the variable pairs exhibit higher correlation values of over 0.9. With this high level of correlation, it is expected that models based on either of these pairs of variables exhibit a high degree of similarity. In this respect, the two models based on the proposed metrics that used AVG and P50 as independent variables

(Table 2) exhibited a higher degree of agreement compared to similar models using traditional percentile LiDAR metrics (see Table 3).

Performance of the models based on the traditional percentile LiDAR metrics (see Table 3) compares well with results obtained in previous studies (e.g., [21,34]), although there are significant differences in the number and type of independent variables in the models. For example, [21] used the same percentile LiDAR metrics for estimating CBH and obtained similar results ($R^2 = 0.77$, RMSE $= 3.9$ and $\text{RMSE}_{cv} = 4.1$), but some of the variables (coefficient of variation (CV) and percentage of first returns (D)) did not appear in the regression models reported in this paper. A possible explanation for this difference could be differences in the distribution (characteristics) of the LiDAR data used in the two studies, which, in turn, is affected by tree species and the season of data collection, among other factors. Conversely, models based on the proposed metric (see Table 2) gave better results based on all four criteria (RMSE, RMSE_{cv}, R^2 and p-value). These models had smaller RMSEs, higher R^2 and smaller and more consistent RMSE_{cv} values.

Although our results compare well with previous similar studies, the main limitation of this study is the small number of field sample plots used (24 plots), which is one possible source of model error. In contrast, previous studies have used significantly larger numbers of field sample plots (e.g., [21] (101 plots); [34] (62 plots); [23] (50 plots)). In another example, [37] used the Sparse Bayesian regression implemented in ArboLiDARTools [38] to build a linear model to estimate CBH from cumulative percentile variables of the LiDAR point cloud and validated the results with laser range-finding and a hypsometer on the ground in 250 sample plots. The RMSE of CBH estimated from LiDAR was 1.03 m.

With more sample plots, and therefore more redundancy in the training data, we anticipate better results also for the current method. Other possible sources of error include measurement error and instrument error.

5. Conclusions

This paper has proposed new LiDAR-based metrics for estimating CBH. Several field-based plot-level tree CBH variables, namely Lorey's mean, arithmetic mean, the 40th and 50th percentiles, have been compared in order to find if there are any significant differences in using one variable over another.

Results obtained in this paper showed that the use of Lorey's mean to estimate CBH leads to a slight improvement in accuracy compared to the other variables; no significant differences, however, were found among the rest of the variables. The use of Lorey's mean over the other variables, however, will depend on the availability of the information required to compute Lorey's mean, namely diameter at breast height (DBH). This is because Lorey's mean is a weighted average with the basal area of individual trees as the weighting factor; therefore, bigger trees contribute more to the mean. However, since CBH is the minimum amount of fuel required to propagate the fire from the surface fuel layer to the canopy fuel layer, the use of Lorey's mean has the potential to overestimate CBH due to the influence of bigger trees. This means the minimum canopy bulk density required to propagate surface fires into the crown can be reached at a lower height than the CBH obtained using Lorey's mean. Therefore, based on this fact, Lorey's mean should be used with caution.

The method for estimating CBH proposed in this paper gave better results (lower and more consistent RMSE and $RMSE_{cv}$ values and higher R^2 values) compared to the use of traditional percentile LiDAR metrics, which have been widely used in previous studies. The main advantage of this method is that the metrics used for estimating CBH are derived from the estimated heights of gaps below trees as directly calculated from LiDAR data. The gap heights give an estimate of the distance of the lowest tree branches from the ground and correlate strongly with field-measured CBH values of individual trees. Moreover, a by-product of processing, which is a raster of gap heights, gives valuable information about the vertical structure of the forest stand below the canopy, *i.e.*, which areas are closed (contain ladder fuels) and, hence, may need immediate attention (e.g., thinning), or identifying areas with low fuel volumes that could be modified to create a fuel break with relatively little manual labor and cost. On the other hand, the main limitation of the proposed method is that it is not suited for areas with pronounced understory layers (e.g., tropical rainforests). This is because the method is suited for detecting fuel breaks, which originate from the ground.

The method for estimating CBH from LiDAR data proposed in this paper gave better results over the use of traditional percentile LiDAR metrics; therefore, the method can potentially be applied to other fire-prone areas provided that suitable parameters are determined from the LiDAR data. The main limitation of the study was that the number of sample plots used (24) was relatively small compared to similar previous studies. Therefore, it would be interesting to conduct further tests on the method using larger numbers of sample plots in different kinds of forests and different seasons.

Acknowledgments

We would like to thank Arbonaut Finland Ltd. for the financial support it provided during the course of this study, which covered data collection, travel expenses and logistics.

Author Contributions

Almasi S. Maguya did the coding, data processing and wrote most of the article. Katri Tegel wrote Sections 2.1 and 2.2.1. Virpi Junttila and Tuomo Kauranne handled administrative issues, as well as proofreading the article. Markus Korhonen, Janice Burns, Vesa Leppanen and Blanca Sanz collected and pre-processed field data.

Conflicts of Interest

The authors declare no conflict of interest.

References

1. Riebau, A.R.; Qu, J.J. Application of remote sensing and GIS for analysis of forest fire risk and assessment of forest degradation. In *Natural Disasters and Extreme Events in Agriculture*; Sivakumar, M., Motha, R., Das, H., Eds.; Springer: Berlin/Heidelberg, Germany; 2005; pp. 335–350.

2. Montealegre, A.L.; Lamelas, M.T.; Tanase, M.A.; de la Riva, J. Forest fire severity assessment using ALS data in a mediterranean environment. *Remote Sens.* **2014**, *6*, 4240–4265.
3. San-Miguel-Ayanz, J.; Moreno, J.M.; Camia, A. Analysis of large fires in European Mediterranean landscapes: Lessons learned and perspectives. *For. Ecol. Manag.* **2013**, *294*, 11–22.
4. Pausas, J.G.; Llovet, J.; Rodrigo, A.; Vallejo, R. Are wildfires a disaster in the Mediterranean basin? A review. *Int. J. Wildl. Fire* **2008**, *17*, 713–723.
5. Collins, R.D.; de Neufville, R.; Claro, J.; Oliveira, T.; Pacheco, A.P. Forest fire management to avoid unintended consequences: A case study of Portugal using system dynamics. *J. Environ. Manag.* **2013**, *130*, 1–9.
6. European Communities. *Forest Fires in Europe 2003*; Technical Report SPI.04.124 EN, Institute for Environment and Sustainability, Official Publication of the European Communities: Brussels, Belgium, 2004.
7. European Communities. *Forest Fires in Europe 2005*; Technical Report EUR 22 312 EN, Institute for Environment and Sustainability, Official Publication of the European Communities: Brussels, Belgium, 2006.
8. European Communities. *Forest Fires in Europe 2007*; Technical Report EUR 2349 EN; Institute for Environment and Sustainability, Official Publication of the European Communities: Brussels, Belgium, 2008.
9. NASA. Wildfire in Sweden: Image of the Day. Available online: http://earthobservatory.nasa.gov/IOTD/view.php?%20id=84155 (accesed on 3 October 2014).
10. Accuweather. Largest Wildfire in Over 40 Years Out of Control in Sweden. Available online: http://www.accuweather.com/en/weather-blogs/international/largest-wild-fire-in-over-40-years-out-of-control-in-sweden/31662445 (accesed on 3 October 2014).
11. Cui, X.; Gao, F.; Song, J.; Sang, Y.; Sun, J.; Di, X. Changes in soil total organic carbon after an experimental fire in a cold temperate coniferous forest: A sequenced monitoring approach. *Geoderma* **2014**, *226–227*, 260–269.
12. Loehman, R.A.; Reinhardt, E.; Riley, K.L. Wildland fire emissions, carbon, and climate: Seeing the forest and the trees—A cross-scale assessment of wildfire and carbon dynamics in fire-prone, forested ecosystems. *For. Ecol. Manag.* **2014**, *317*, 9–19.
13. Flannigan, M.; Amiro, B.; Logan, K.; Stocks, B.; Wotton, B. Forest fires and climate change in the 21st century. *Mitig. Adapt. Strateg. Glob. Chang.* **2006**, *11*, 847–859.
14. Amiro, B.D.; Todd, J.B.; Wotton, B.M.; Logan, K.A.; Flannigan, M.D.; Stocks, B.J.; Mason, J.A.; Martell, D.L.; Hirsch, K.G. Direct carbon emissions from Canadian forest fires, 1959–1999. *Can. J. For. Res.* **2001**, *31*, 512–525.
15. Oris, F.; Asselin, H.; Ali, A.A.; Finsinger, W.; Bergeron, Y. Effect of increased fire activity on global warming in the boreal forest. *Environ. Rev.* **2014**, *22*, 206–219.
16. Agee, J.K.; Skinner, C.N. Basic principles of forest fuel reduction treatments. *For. Ecol. Manag.* **2005**, *211*, 83–96.

17. Graham, R.T.; McCaffrey, S.; Jain, T.B. *Science Basis for Changing Forest Structure to Modify Wildfire Behavior and Severity*; Technical Report; USDA Forest Service, Rocky Mountain Research Station: Washington, DC, USA, 2004.
18. Peterson, D.L.; Johnson, M.C.; Agee, J.K.; Jain, T.B.; Mckenzie, D.; Reinhardt, E.D. Fuels planning: Managing forest structure to reduce fire hazard. In Proceedings of the 2nd International Wildland Fire Ecology and Fire Management Congress, Orlando, FL, USA, 16–20 November 2003; American Meteorological Society: Washington, DC, USA, 2003.
19. Finney, M.A. *FARSITE, Fire Area Simulator—Model Development and Evaluation*; USDA: Washington, DC, USA, 2004.
20. Arroyo, L.A.; Pascual, C.; Manzanera, J.A. Fire models and methods to map fuel types: The role of remote sensing. *For. Ecol. Manag.* **2008**, *256*, 1239–1252.
21. Andersen, H.; McGaughey, R.J.; Reutebuch, S.E. Estimating forest canopy fuel parameters using LIDAR data. *Remote Sens. Environ.* **2005**, *94*, 441–449.
22. Riaño, D.; Meier, E.; Allgöwer, B.; Chuvieco, E.; Ustin, S.L. Modeling airborne laser scanning data for the spatial generation of critical forest parameters in fire behavior modeling. *Remote Sens. Environ.* **2003**, *86*, 177–186.
23. Agca, M.; Popescu, S.; Harper, C.W. Deriving forest canopy fuel parameters for loblolly pine forests in eastern Texas. *Can. J. For. Res.* **2011**, *41*, 1618–1625.
24. Jain, T.B.; Graham, R.T. The relation between tree burn severity and forest structure in the Rocky Mountains. In *Restoring Fire-Adapted Ecosystems: Proceedings of the 2005 National Silviculture Workshop*; USDA Forest Service General Technical Report PSW-GTR-203; USDA: Washington, DC, USA, 2007; pp. 213–250.
25. Cohen, J.D.; Butler, B.W. Modeling potential structure ignitions from flame radiation exposure with implications for wildland/urban interface fire management. In Proceedings of the 13th Fire and Forest Meteorology Conference, International Association of Wildland Fire, Victoria, Australia, 27–31 October 1998; pp. 81–86.
26. Rothermel, R.C. *How to Predict the Spread and Intensity of Forest and Range Fires*; In Technical Report General Technical Report INT-143; Ogden, U.S. Department of Agriculture, Forest Service, Intermountain Forest and Range Experiment Station: Washington, DC, USA, 1983.
27. Lemmens, M. Airborne LIDAR. In *Geo-Information*, *Geotechnologies and the Environment*; Gatrell, J.D., Jensen, R.R., Eds.; Springer Netherlands: Dordrecht, The Netherlands, 2011; Volume 5, pp. 153–170.
28. Hudak, A.T.; Evans, J.S.; Stuart Smith, A.M. LiDAR utility for natural resource managers. *Remote Sens.* **2009**, *1*, 934–951.
29. Keane, R.E.; Burgan, R.; van Wagtendonk, J. Mapping wildland fuels for fire management across multiple scales: Integrating remote sensing, GIS, and biophysical modeling. *Int. J. Wildl. Fire* **2001**, *10*, 301–319.
30. Philip, M. *Measuring Trees and Forests*; CABI Publishing Series; CAB International: Wallingford, UK, 1994.

31. Erdody, T.L.; Moskal, L.M. Fusion of LiDAR and imagery for estimating forest canopy fuels. *Remote Sens. Environ.* **2010**, *114*, 725–737.
32. Van Wagner, C.E. Prediction of crown fire behavior in two stands of jack pine. *Can. J. For. Res.* **1993**, *23*, 442–449.
33. González-Olabarria, J.; Rodríguez, F.; Fernández-Landa, A.; Mola-Yudego, B. Mapping fire risk in the Model Forest of Urbión (Spain) based on airborne LiDAR measurements. *For. Ecol. Manag.* **2012**, *282*, 149–156.
34. Popescu, S.C.; Zhao, K. A voxel-based lidar method for estimating crown base height for deciduous and pine trees. *Remote Sens. Environ.* **2008**, *112*, 767–781.
35. Chasmer, L.; Hopkinson, C.; Treitz, P. Assessing the three-dimensional frequency distribution of airborne and ground-based lidar data for red pine and mixed deciduous forest plots. In Proceedings of the ISPRS Working Group VIII/2 "Laser-Scanners for Forest and Landscape Assessment", Freiburg, Germany , 3–6 October 2004; Volume XXXVI, pp. 66–70.
36. MATLAB. The Matlab Computing Environment. Available online: http://www.mathworks.com/products/matlab (accessed on 8 October 2014).
37. Korhonen, M. Predicting Canopy Base Height (CBH) from Sparse Airborne LiDAR in a Scots Pine Dominated Forest and Enhancing the Efficiency of Field Measurements of CBH (in Finnish). Master's Thesis, University of Eastern Finland, Savonlinna, Eastern Finland, Finland, 2012.
38. Arbonaut Ltd. ArboLiDAR Forest Inventory–Automatic Stand Segmentation Manual, 2012. In Proceedings of the ArboLiDAR User Days 2012 workshop, Joensuu, Finland, 2–4 October 2012.

PUBL. IV

Junttila, V., Gautam, B., Karky, B. S., Maguya, A. S., Tegel, K., Kauranne, T., Gunia, K., Hämäläinen, J., Latva-Käyrä, P., Nikolaeva, E., and Peuhkurinen, J., Robustness of model-based high-resolution prediction of forest biomass against different field plot designs, Accepted for publication in *Carbon Balance and Management*, 2015

Junttila *et al. Carbon Balance Manage (2015) 10:29*
DOI 10.1186/s13021-015-0038-1

Carbon Balance and Management
a SpringerOpen Journal

RESEARCH Open Access

Robustness of model-based high-resolution prediction of forest biomass against different field plot designs

Virpi Junttila[1], Basanta Gautam[2], Bhaskar Singh Karky[3], Almasi Maguya[1,4*], Katri Tegel[2], Tuomo Kauranne[1,2], Katja Gunia[2], Jarno Hämäläinen[2], Petri Latva-Käyrä[2], Ekaterina Nikolaeva[1] and Jussi Peuhkurinen[2]

Abstract

Background: Participatory forest monitoring has been promoted as a means to engage local forest-dependent communities in concrete climate mitigation activities as it brings a sense of ownership to the communities and hence increases the likelihood of success of forest preservation measures. However, sceptics of this approach argue that local community forest members will not easily attain the level of technical proficiency that accurate monitoring needs. Thus it is interesting to establish if local communities can attain such a level of technical proficiency. This paper addresses this issue by assessing the robustness of biomass estimation models based on air-borne laser data using models calibrated with two different field sample designs namely, field data gathered by professional forester teams and field data collected by local communities trained by professional foresters in two study sites in Nepal. The aim is to find if the two field sample data sets can give similar results (LiDAR models) and whether the data can be combined and used together in estimating biomass.

Results: Results show that even though the sampling designs and principles of both field campaigns were different, they produced equivalent regression models based on LiDAR data. This was successful in one of the sites (Gorkha). At the other site (Chitwan), however, major discrepancies remained in model-based estimates that used different field sample data sets. This discrepancy can be attributed to the complex terrain and dense forest in the site which makes it difficult to obtain an accurate digital elevation model (DTM) from LiDAR data, and neither set of data produced satisfactory results.

Conclusions: Field sample data produced by professional foresters and field sample data produced by professionally trained communities can be used together without affecting prediction performance provided that the correlation between LiDAR predictors and biomass estimates is good enough.

Keywords: Above-ground biomass, LiDAR, REDD+, Participatory forest monitoring

Background

Greenhouse gas (GHG) emissions from tropical deforestation and forest degradation contribute about 15–20 % of total annual global GHG emissions, making them the second largest source of greenhouse gases globally [1]. To reduce especially CO_2 (carbon dioxide) emissions from the forestry sector, the United Nations has established a program that would provide payments for the reduction of emissions from deforestation and forest degradation (REDD+). REDD+ is a performance-based policy instrument aimed at reducing anthropogenic emissions of GHG [2, 3].

Nepal is one of the countries participating in REDD+. After successful implementation of a Community Forestry programme, Nepal has taken another leap by piloting innovative REDD+ projects. The International Centre for Integrated Mountain Development (ICIMOD) is one of the first organizations to implement a

*Correspondence: almasi.maguya@gmail.com
[4] Mzumbe University, P.O. Box 1, Mzumbe, Morogoro, Tanzania
Full list of author information is available at the end of the article

community-based REDD+ pilot at micro-watershed level. ICIMOD and its partners, the Federation of Community Forestry Users, Nepal (FECOFUN) and the Asia Network for Sustainable Agriculture and Bioresources (ANSAB) implemented a pilot project from 2009–2013, with support from the Norwegian Agency for Development Cooperation (NORAD) climate and forest Initiative [4]. The major focus of the project was to develop and demonstrate an innovative benefit-sharing mechanism for REDD+ incentives using institutionally and socially inclusive approaches to address the drivers of deforestation and forest degradation and improve forest governance [5] in three micro-watersheds, namely Kayarkhola in Chitwan, Ludikhola in Gorkha and Charanawati in Dolakha districts. The pilot project focused on sequestering carbon through community-based forest management. It is one of the first carbon offset demonstration projects in the world that involves local communities in monitoring the carbon in their forests and providing the necessary training for them to do so. Training on assessing forest carbon pools was provided to the local communities that manage the forest [6]. The trained local communities collected field plot data from 2010 to 2012. The results of this effort are summarized in [7].

In a joint effort, the Forest Resource Assessment Nepal project, Arbonaut Ltd. and ICIMOD carried out a wall-to-wall airborne discrete-return light detection and ranging (LiDAR) data and subsequent field plot collection in two watersheds in Chitwan and Gorkha. The main aim of the work was to estimate accurately and with a high spatial resolution the forest above ground biomass (AGB)/carbon in the watersheds. The field data was collected by professional foresters and technicians.

In measuring biomass for calculating REDD+ compensation the measurements should be conducted in a biennial manner, as has been recently agreed at a UNFCCC meeting in Bonn [8]. As national measurements are required at such a high frequency, traditional sampling-based methods become prohibitively expensive. We therefore propose to use a model-based strategy for biomass prediction, where field plots are only used for model calibration, i.e. model parameter estimation, and biomass prediction models are based on remotely sensed data, such as LiDAR, which is used in this study, or satellite imagery.

In this study, plot-level AGB values estimated from field measurements (labelled as "AGB field estimates" in this article) in given inventory areas are predicted ("predictions") in new validation plot locations ("validation set") using linear model which is calibrated using field measurements obtained from the respective areas ("training set"). The field measurements are collected by two types of forest inventory teams: a professional measurement team ("Prof") and measurement teams trained from the local community members ("Comm"). The local community members were trained to do forest inventory work by professionals from ICIMOD and its project partners that operated independently of the professional measurement team. Inventory work, i.e., field sample plot selection and actual measurement work, is thus performed by two separate groups, which may lead to data sets with different characteristics, even when the measurements are conducted in the same area.

To justify the use of participatory forest monitoring and inventory work of local communities, it is important that there are no significant differences in AGB predictions based on field measurements of both teams. Thus, it is needed to verify if different data sets from the same area lead to similar model based predictions, and if the datasets can be combined and used together in predicting AGB for the areas in the future. In this study, we first analyse the field estimates measured by both teams and validate the correlation between the model auxiliary data, LiDAR predictors, and the corresponding field estimates. We then validate the robustness of high-resolution model-based biomass estimation against different sampling designs from the same area. Models using different sources of training set data but resulting in the same predictions with the same validation data are considered robust against the training set source.

Results

The model-based predictions and corresponding error analyses were performed using data collected from two inventory study sites located in Nepal, namely Gorkha (labelled as "Go") and Chitwan ("Ch"), see Fig. 1 for the location of the sites. The scope in forest inventory by the different inventory teams was different. The professional team measured only closed canopy forest owned by both the state and by the forest communities. The local field teams measured both open and closed canopy forests but only those owned by communities. Only the field plots of similar forest types, plots from closed canopy forest owned by communities, were used in this study. The number of plots measured by the community teams located in closed type forests that are owned by the communities is 151 in study site Gorkha and 151 in study site Chitwan, while the number of plots measured by the professional teams located in closed type forests owned by the communities is 41 in Gorkha and 26 in Chitwan. See Fig. 1 for plot locations and Fig. 2 for the distribution of field estimates.

Examples of the combined distributions of LiDAR predictor values and AGB field estimates of each sample are shown in Fig. 3. The LiDAR predictor—AGB field estimate correlation of both sample in Gorkha, the plots

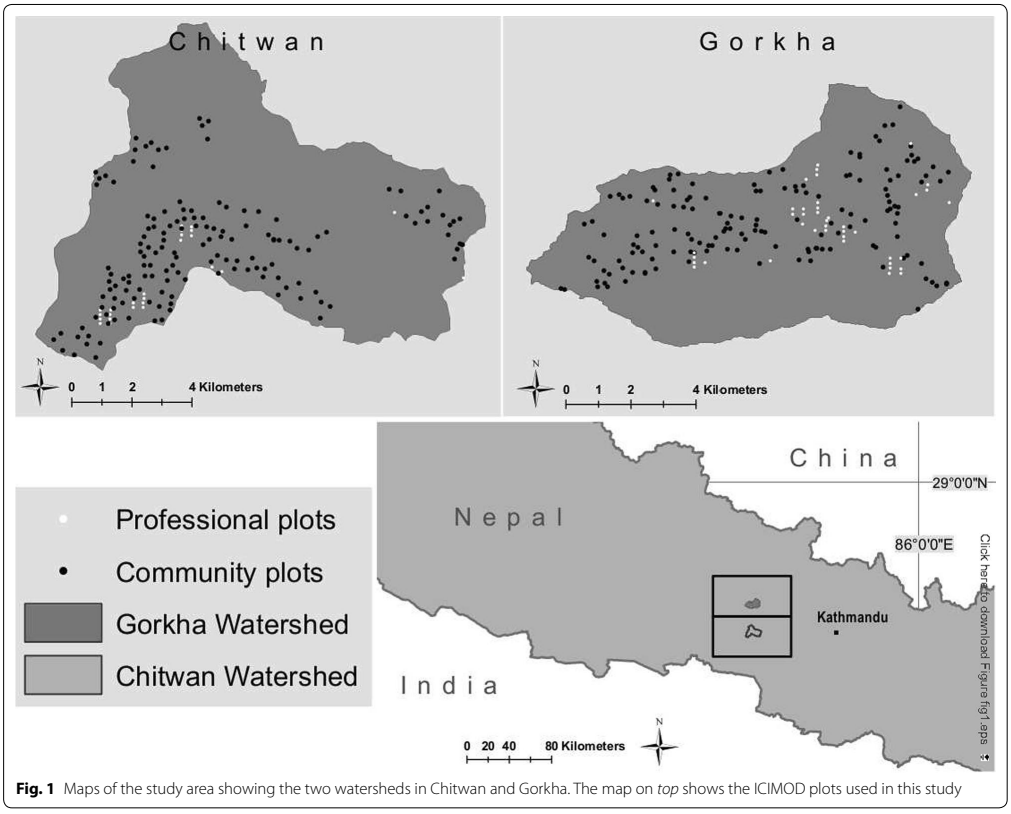

Fig. 1 Maps of the study area showing the two watersheds in Chitwan and Gorkha. The map on *top* shows the ICIMOD plots used in this study

measured by professional teams and the plots measured by the members of local communities, is higher than in Chitwan. The correlation of AGB and the LiDAR example predictor in Gorkha is 0.66 for sample ProfGo, 0.59 for CommGo, and in Chitwan it is 0.52 for ProfCh and 0.45 for CommCh. With visual analysis, the LiDAR predictor—AGB distributions of different inventor teams are similar in both study sites. Similar properties hold for each predictor used in this study.

Results of study site Gorkha

The results for predictions in study site Gorkha are shown in Table 1 and Figs. 4 and 5. In the table, model prediction precision and accuracy are evaluated by relative root mean square error (RMSE %) and relative mean difference (D %). The prediction error distributions in two validation sets (Comm and Prof) resulting from three different model training set data (Comm, Prof and the combined set of these plots, Comm + Prof) are verified. The differences of the mean values (D %) between the self-validation (validation set and training set are the same) and the cross-validation cases (training set is different than validation set) are tested by a two-sample t test with a 5 % significance level against the case where the validation set and training set are the same. Similarly, the difference of the RMSE % values are tested with a two-sample F test for equal variances with a 5 % significance level. The tests show that distributions of prediction error among different models in the validation set Comm are similar. The mean of the errors are the same as that for training set Comm (t test p values > 0.79 for training sets Prof and Comm + Prof) and also the variance of the error distributions are similar (variance test p values > 0.89). Similar results are shown for the AGB predictions in the plots measured by the professional teams. The statistical tests for the prediction error show no significant difference in error mean or error variance compared to the predictions estimated with training set Prof (t test p values are > 0.84

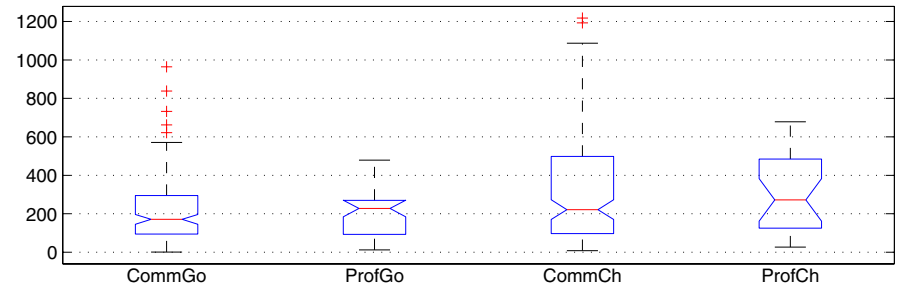

Fig. 2 Boxplots of AGB field estimates in plots located in closed type community owned forests. Median, 25th and 75th percentiles and outliers are shown

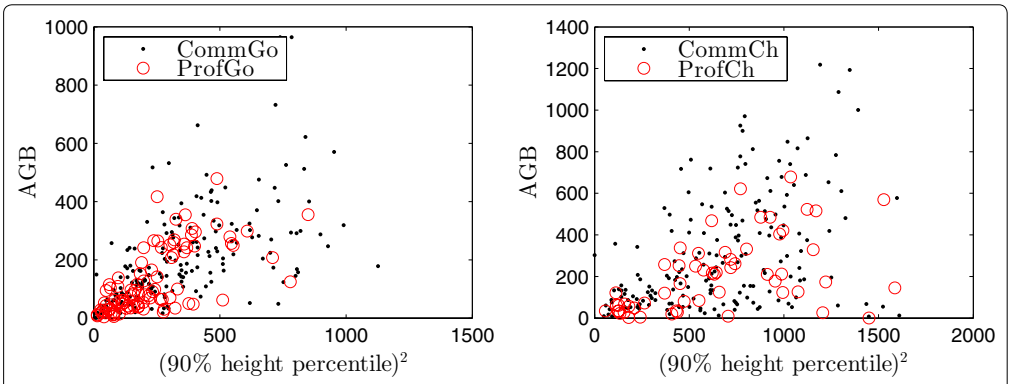

Fig. 3 An example of LiDAR predictor—AGB field estimate scatterogram

Table 1 Results with different combinations of training set–validation set in study site Gorkha

Training set	Error stat.		Test against baseline, p values	
	RMSE %	BIAS %	Variance test	t test for mean
Validation set: Comm				
Comm (baseline)	59.2	0.0		
Prof	59.3	−1.8	0.994	0.794
Comm + Prof	58.6	−0.2	0.888	0.977
Validation set: Prof				
Prof (baseline)	37.5	0.2		
Comm	34.4	1.9	0.586	0.839
Comm + Prof	34.8	1.5	0.644	0.872

and variance test p values are > 0.59 for training sets Comm and Comm + Prof). Figure 4 shows that independent of the training and validation set used, a relatively good model fit is obtained for validation set Comm ($r^2 \geq 0.46$ for all training sets) and for validation set Prof ($r^2 \geq 0.58$ for all training sets).

Also the distributions of the AGB predictions shown in Fig. 5 are close to each other. The lack of ability to predict accurately the largest AGB values in plots measured by the Community teams is similar when using any of the training sets (see the left sub-figure). Up to about 300 Mg/ha, the AGB distributions of all predictions are very close to the distribution AGB field estimates of Community teams, the larger AGB values tend to be underestimated. In case of the AGB field estimates of the

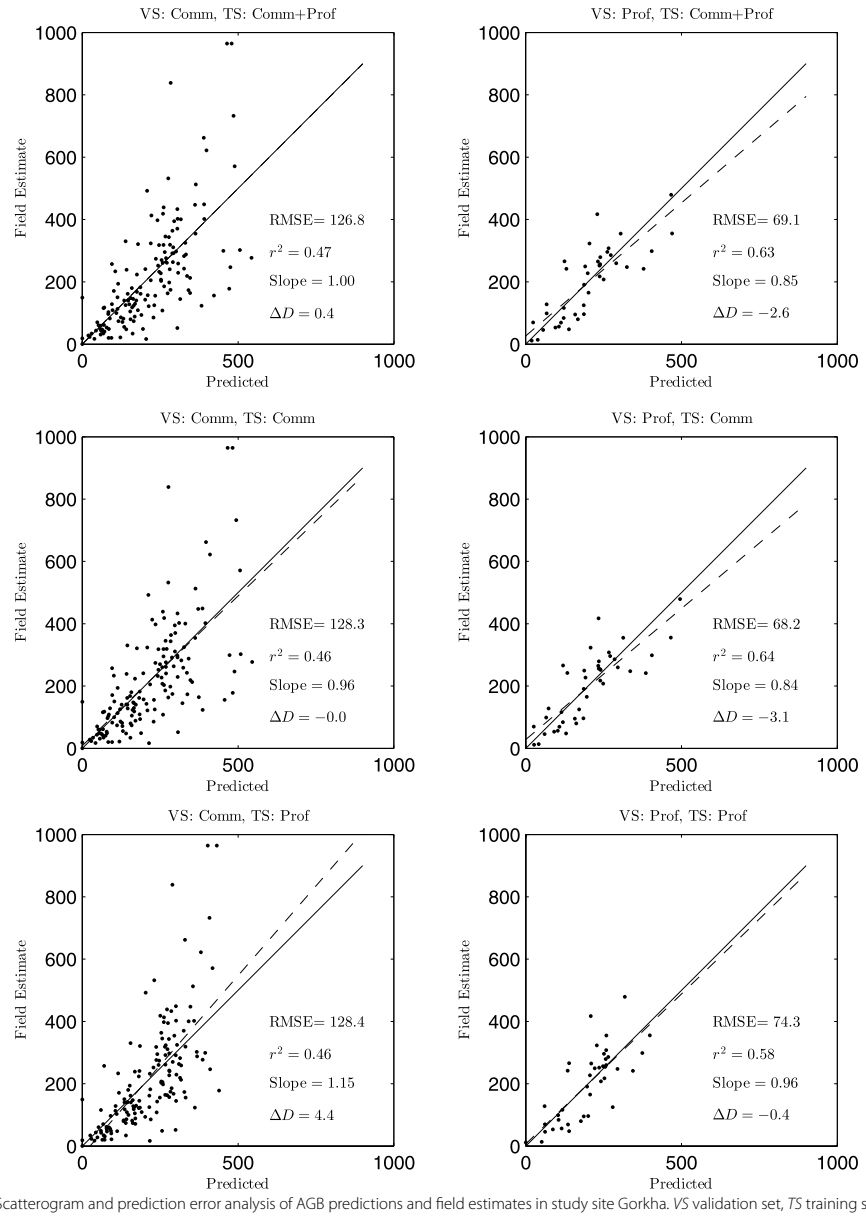

Fig. 4 Scatterogram and prediction error analysis of AGB predictions and field estimates in study site Gorkha. *VS* validation set, *TS* training set

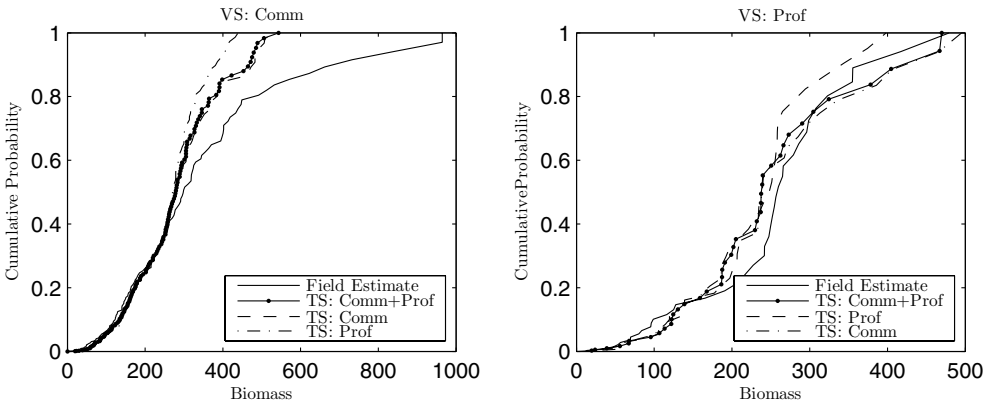

Fig. 5 Cumulative distribution of plot-level AGB field estimates and plot-level AGB predictions estimated with models based on different training subsets in study site Gorkha

Professional teams, predictions estimated by different training sets of either of the teams result in quite correct AGB distributions. No big deviations can be seen up to 400–500 Mg/ha.

Results of study site Chitwan

Results of AGB predictions in study site Chitwan are shown in Table 2 and Figs. 6 and 7. The variance test in Table 2 shows no significant difference between the prediction precision (RMSE %) between the predictions obtained with different training sets for either validation sets (p values > 0.81 for validations set Comm, > 0.43 for Prof). However, the t test for the average values of the average relative differences, D %, shows significant difference (p value $0.008 < 0.05$) for prediction of community team plots using model calibrated with field estimates of professional teams. Similarly, predictions for professional team measured plots predicted with model calibrated using the community team plots, the p value is close to 0.05 although not less than it. Thus, there is significant average error in predictions when the training set and validation set are different. Similar doesn't hold when the training set consists also data from the validation set (Training set Comm + Prof).

Table 2 Results with different combinations of training set–validation set in study site Chitwan

Training set	Error stat.		Test against baseline, pvalues	
	RMSE %	BIAS %	Variance test	t test for mean
Validation set: Comm				
Comm (baseline)	72.1	−0.5		
Prof	74.2	−22.6	0.806	0.008
Comm + Prof	71.7	−3.5	0.931	0.720
Validation set: Prof				
Prof (baseline)	55.5	−2.5		
Comm	52.9	23.6	0.433	0.079
Comm + Prof	51.3	19.0	0.452	0.146

The one-to-one scatterograms in Fig. 6 shows that the correlation between AGB field estimates and model based predictions is poor in each cross-validation set. Even the predictions estimated using the same training set and validation set (self-validation: validation set Comm estimated with training set Comm and validation set Prof estimated with training set Prof) fail. The RMSE of the predictions is large compared to the variation of the AGB values and the model fit is poor ($r^2 \leq 0.33$) in each case.

In Fig. 7 it can be seen that the models severely underestimate the cumulative probability distribution of AGB for values for AGB greater than 200 Mg/ha in validation set Comm (left sub-figure). This happens regardless of the training set used to train the model, also when the training set is the same as validation set. For validation set Prof, the model over-estimates the cumulative probability distribution of AGB for values of AGB less than 400 Mg/ha regardless of the training set used to train the model (right sub-figure) and for values of AGB greater than 400 Mg/ha the model under-estimates the cumulative probability distribution for each training set.

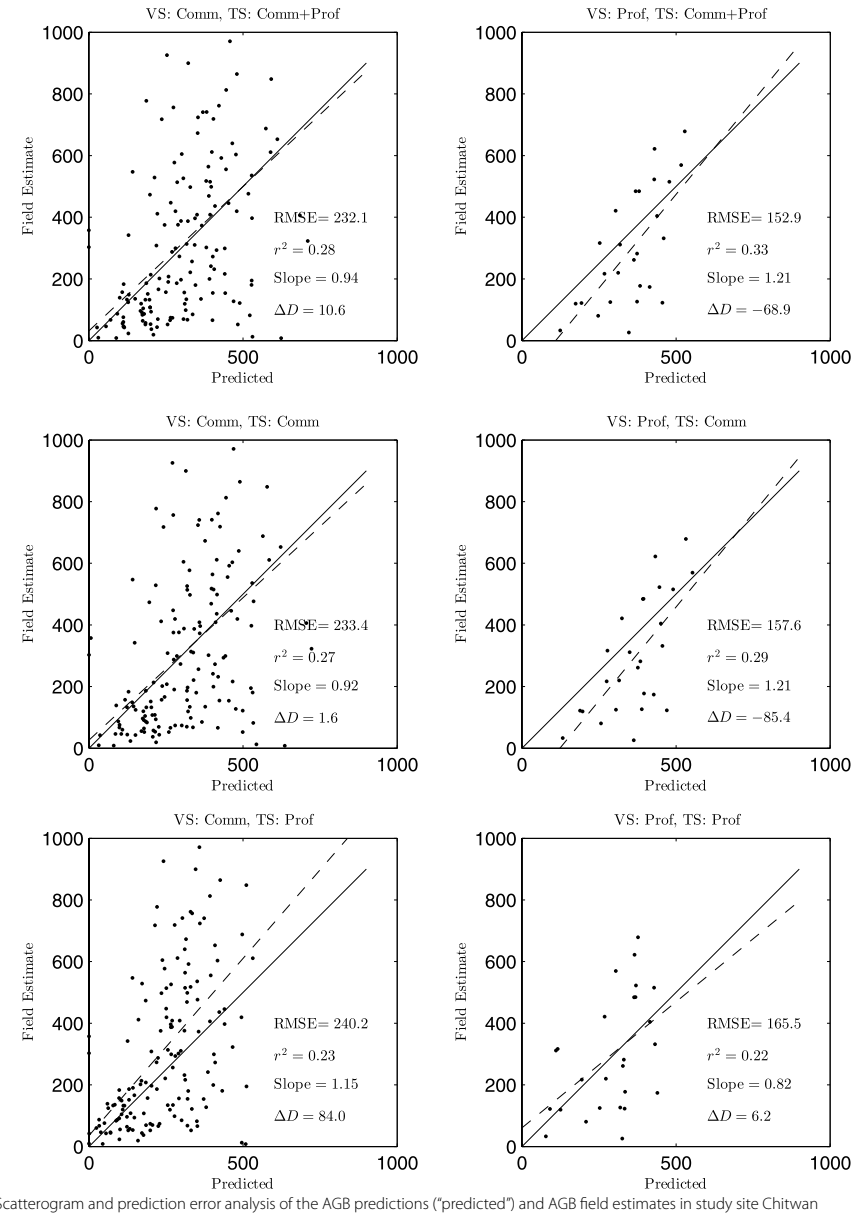

Fig. 6 Scatterogram and prediction error analysis of the AGB predictions ("predicted") and AGB field estimates in study site Chitwan

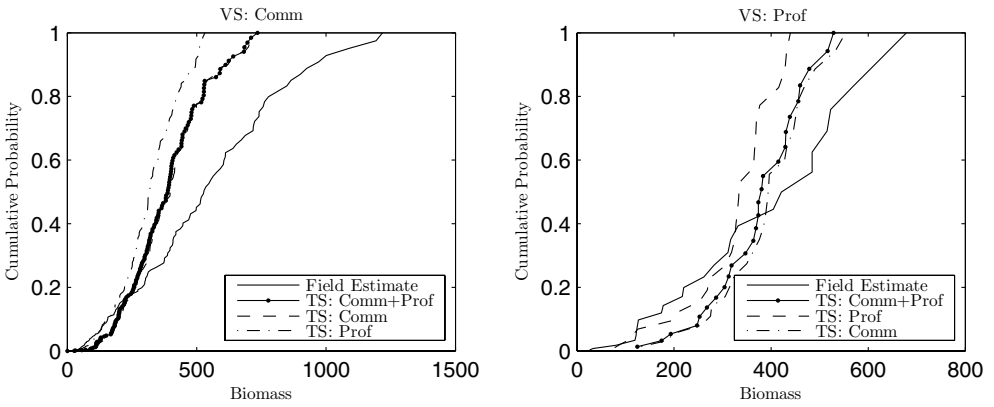

Fig. 7 Cumulative distribution of plot-level AGB field estimates and plot-level AGB predictions estimated with models based on different training subsets in study site Chitwan

Discussion

The results above show that the predictions in study site Gorkha are quite accurate and precise in each case in the cross-validation procedure and no significant difference occurs when different sources of training set data are used. However, there are severe problems in the predictions of AGB in study site Chitwan. The cross-validation procedure shows that there is significant difference in the mean of prediction error when the training set and validation set are different. However, in this study site, the prediction precision overall is weak, the RMSE is large and model fit poor.

In model-based prediction, the correlation between the response, AGB field estimates, and the auxiliary data, LiDAR predictors, define whether the auxiliary data can be used to accurately predict the response over the whole spatial area. In this study, the plot-level prediction map in Fig. 6 and the LiDAR predictor—AGB field estimate correlation in Fig. 3 (right sub-figure) show the basic problem in Chitwan data—the signal (or correlation) between the LiDAR predictors and AGB field estimates is not good enough for precise prediction, and total lack of fit ensues independently of the training set source. Even the predictions of community team plots obtained using community team plots as the training set of the model show no correlation with the field estimates, as seen in the middle left sub-figure in Fig. 6. Even though the error mean is nearly zero, the model fit is poor ($r^2 = 0.27$). Similar results can be seen for the predictions for professional team plots that are obtained using professional team field measurements as the training set (bottom right sub-figure).

With the lack of LiDAR predictor—AGB field estimate correlation, the predictions in study site Chitwan are dominated by the average values of the field estimates in the training sets. In community team measurements the average of the field estimates is larger than in the professional team measurements. The community plot AGB field estimates are thus heavily under-estimated (22.6 % of the average AGB field estimates) when using the training set of professional team measurements as training set, and overestimated in the opposite case.

It is plausible that the lack of fit of model predictions between different training sets in Chitwan is due to different forest populations used in their sampling. The samples generated separately for each population are not necessarily probabilistic samples on the intersection of the populations, i.e. on closed canopy community forests and bias may ensue. However, the prediction analysis of the various models do not support such an interpretation. In both Gorkha and Chitwan model fit is similar, acceptable in Gorkha and very poor in Chitwan, with all combinations of teaching set and validation set, whether these are cross-validated or self-validated. It seems therefore that the reason to the lack-of-fit in Chitwan is caused by some other effect and not inappropriate sampling.

Model-based prediction of biomass uses field plots for model calibration but they can also be used for model validation. When plot collection is conducted by randomly sampling individual plots or plot clusters, such field campaigns can also be used to test model-based predictions for possible lack of fit.

In the current tests between 50 and 200 plots were measured for two areas of roughly 10,000 hectares each.

In heterogeneous forests it is plausible that not every forest type gets an adequate statistical coverage with such a sample. However, even this sampling density far exceeds the cost per area of any foreseeable field sample for nationwide estimates, and is much higher than common sampling densities in national forest inventories. We therefore have to try and use the randomness of sampling as a guarantee against bias at least over sufficiently large forest areas. Once lack of bias has been attained for a model-based estimation method, it becomes much more feasible to provide even high-resolution biomass updates using remote sensing data alone.

Conclusions

The lessons from this study are positive towards using participatory field measurements. The analyses above show that the LiDAR-data based models calibrated with in situ field estimates conducted by professional foresters or by trained community forest members that use different field sample selection methods, different field sample plot sizes and different methods at the field work itself can be used together without degrading model prediction performance, if the correlation between LiDAR predictors and field estimates is good enough. This was evident in study site Gorkha. In Chitwan, the correlation was poor independent of the source of field measurements leading to imprecise predictions. The combined distributions of AGB field estimates with respect to LiDAR predictors were visually assessed to come from the same distribution in both study sites with both field data, Comm and Prof, see Fig. 3. Thus, there is no evidence that the error in Chitwan predictions is caused by the use of different samples, but from the lack of correlation between LiDAR predictors and AGB field estimates. Thus in both study sites, the prediction results were equally good or bad for both participatory and professional field plot measurements.

Previous studies, e.g. [9], concluded that it is possible to utilize data collected with participatory approaches for traditional forest inventories. The authors of [9] studied the feasibility of participatory REDD+ MRV processes in Tanzania. Their study compared the field estimates from the community forest user groups and professional teams and showed that the mean of AGB field estimates differed by no more than 7 % and mostly by 5 %. The variance was higher in the community measurements, therefore indicating that even though the accuracy was as good as professional measurements the precision was weaker.

These types of participatory inventories are limited in the geographic representativeness [10], especially when the aim is the estimation of carbon resources for the remuneration of local communities, since the Community Forests are relatively small compared to the landscape scale.

The present study is the first attempt of its kind to utilize field data collected by community people in LiDAR-based biomass inventories within the REDD+ context. The implementation of participatory methods for the monitoring & measuring, reporting and verification (M&MRV) of forest carbon credits with high accuracy and resolution is a fundamental step for the implementation of REDD+ projects in community forestry level.

The results of this study support the conclusions of a side event on evolving requirements and solutions for REDD+ monitoring, with community focus, at the UN climate change conference in Warsaw in 2013 (COP19) [11]. The side event concluded with the agreement that community monitored data can be scientifically accurate and support also new technology, such as LiDAR. But concerns were raised on whether community monitoring of carbon performance can form the basis for broader financial rewards for REDD+ and whether the data can be integrated into a broader national forest monitoring systems.

This study agrees with the study by [12]. They reported that the overall aboveground biomass estimated by community members differed only slightly from the estimates by the professional foresters. The results of this study therefore show that it is possible to use calibration plots measured by community people in model-based predictions of above-ground biomass. They also show that a model-based analysis can be used to validate the accuracy of field plots by calculating predictions with a model based on different subsets of the plots. If the model predictions thus obtained are compatible and consistent, the field estimates can be regarded as reliable. This approach gives ownership of verified data to different stakeholders which is key to implementing performance based financing mechanism.

The approach described here will hopefully be helpful for unbiased monitoring, reporting, and verification under a result-based payment mechanism in which plot data collected by local communities are integrated with advanced remote sensing-based measurements.

Methods

Study area

The study area consists of two separate sites, Kayarkhola watershed in Chitwan (labeled as Ch) and Ludikhola watershed in Gorkha (Go) located in Nepal, see Fig. 1 for the site locations. The sites are located quite near each other, the distance from northernmost part of Chitwan area is about 20 km to the southernmost part of Gorkha area. The study area in Chitwan is about 12.2 km from west to east, 8.0 km from south to north. The distances in Gorkha are about 10.6 km from east to west, 6.5 km from south to north.

The Kayarkhola watershed is located in Chitwan district, which is a part of the Central Development Region of Nepal. Its total area is 8,002 hectares (ha) and it consists of tropical to sub-tropical forests, covering an altitudinal range of 245–1944 m [5] with 16 Community Forest User Groups (CFUGs) managing this forest. The watershed consists of three different types of forest namely Sal forest, mixed hardwood forest and Riverine forest [13]. The watershed is inhabited by socially and ethnically diverse forest-dependent indigenous communities such as the Chepang and Tamang [14]. These ethnic groups are some of the most marginalized ethnic groups in the country. Chepang and Tamang communities practice shifting cultivation which puts severe pressure on forest resources. The REDD+ pilot project implemented in the area plays a major role to address the issues of forest degradation and deforestation by promoting sustainable forest management practices and linking it with the REDD+ incentive mechanism [13].

The Ludikhola watershed in Gorkha district is located in the southern part of Gorkha. The watershed is located in the Hill region characterized by sub-tropical broad leaved forests, ranging from 318 to 1714 m above sea level. The total area of the watershed is 5750 ha, out of which 4869 ha is forest area, 632 ha is agricultural land and the rest is barren, grassland and natural water bodies. There are 31 CFUGs managing an area of 1888 ha of forests as Community Forests (CFs). The forest in Gorkha represents sub-tropical forests. The watershed was heavily deforested in the past and this has been controlled through sustainable community forest management and conservation through REDD+.

Dominant forest types in the study area are hill sal (*Shorea robusta*) forest, and Schima-Castanopsis forest. Even though Shorea robusta mixed subtropical hill deciduous forest forms the major forest type in Kayarkhola (Chitwan) and Ludikhola (Gorkha), associated species varies between these two watersheds. *Lagerestroemia parviflora*, *Mallatus phillipinensi* and *Terminelia tomentosa* are dominant associates in Kayarkhola (Chitwan) whereas *Schima wallichii* and *Castanopsis indica* are the most common associates in Ludikhola (Gorkha). According to broader climatalogical categorization of forests, forests in Kayarkhola fall under tropical broadleaved forests and in Ludikhola the forests are of sub-tropical broadleaved forest mostly, with *Shorea robusta* and *Schima wallichi* (sal and chilaune) as principal dominant species.

LiDAR data

Airborne discrete-return LiDAR data was acquired in February/March 2011 from the two watersheds. The two watersheds were scanned in full coverage from 2200 m average height above ground using a local helicopter equipped with a Leica ALS50-II lidar-scanner device. The helicopter flight path was east-west strips at 1 km distance. The scanning parameters are presented in Table 3. The collected LiDAR data were evaluated after each flight, and supporting scans were conducted if data gaps or other problems occurred.

Raw LiDAR data were classified by the vendor into three categories: ground, vegetation and error returns. Further pre-processing included calculation of a digital terrain model (DTM) from the ground returns, removal of overlaps from the raw data, and conversion of height coordinates (zvalues) of the vegetation returns from absolute elevation into distance-to-ground using the DTM [15]. Overlap removal is a procedure to ensure uniform density of points for estimation by the area-based approach (ABA). ABA methods use quantized vertical histograms as the regression variables and it is seen as desirable that their sampling noise, i.e. density of LiDAR points per square meter, is uniformly distributed. From the pre-processed LiDAR data, several LiDAR features were estimated in order to serve as the LiDAR-predictors in the AGB prediction model. The features have been taken from [16] and are an extended and modified version of those published by [17]. They include: (1) different height percentiles for the first-pulse and last-pulse returns, (2) mean height of first-pulse returns above 5 m (high-vegetation returns), (3) standard deviation for first-pulse returns, (4) ratio between first-pulse returns from below 1 m and all first-pulse returns, and (5) ratio between last-pulse returns from below 1 m and all last-pulse returns. These features were estimated from LiDAR points within the plot footprints described below.

Field samples

Field sample plots were selected with two different methods, depending on the inventory team. The professional

Table 3 Specifications for the LiDAR scanning data

Parameter	Value
Average flying altitude above ground level	2200 m
Flying speed	80 knots
Sensor pulse rate	52.9 khz
Sensor scan speed	20.4 lines per second
Nominal outgoing pulse density at ground level	0.8 points per square meter
Scanning field of view (FOW) half angle	20°
Swath width at ground level	1601.47 m
Point spacing on the ground (across-track / along-track)	max. 1.88/2.02 m
Geometric accuracy (horizontal and vertical)	max. 1 m

forest measurement teams and forest measurement teams coming from the local communities collected the field data during the year 2011. The selection criteria for the field plots were different among the two groups of forest measurement teams.

Field plot center coordinates were recorded using Differential GPS (DGPS) with ProMark 3 and MobileMapper CX devices, and corrected in post-processing mode (GNSS Solutions software and MobileMapper Office software). Plots were located with a family of GPS devices where one device is left stationary for all day and it provides differential correction to all other GPS devices used in positioning the plots within a cluster of plots. Subsequent off-line DGPS post-processing was also used and plot geo-location error was estimated to be less than 1 m.

The professionally collected plots were collected as a part of a much larger campaign addressing the REDD+ program in Nepal. This larger program requires sampling from a national, officially accepted forest mask. Since that nationally accepted forest mask does not admit auxiliary information, such as vegetation index, elevation or aspect, clustered random sampling with uniform probability on the area of interest covered with LiDAR was used.

Sampling design and field plot design used by community teams

A stratification was done where forests with more than 70 % of canopy cover were considered as dense strata (i.e. closed canopy) and less than 70 % as sparse strata (i.e. open canopy). In a post-processing step the classification between open and closed canopy was revisited based on LiDAR pulse density so as to obtain a uniform classification of closed canopy for both sets of field plots. Plots deemed not to fall on closed canopy forest were eliminated from the sample by a 70 % canopy cover criterion. The 70 % canopy cover was used as a surrogate variable for selecting as similar a sample of community plots as possible to the professional plot exclusion policy. This 70 % canopy cover was computed as the proportion of vegetation points of all LiDAR points. Since plot sampling was clustered or simple random sampling for professional and community plots, respectively, it was assumed that the plots satisfying the canopy cover criterion reflect different AGB classes in their respective statistical proportions and the estimates are therefore unbiased.

Forest stratification was carried out using high resolution remote sensing imagery (GeoEye image) in ERDAS and ArcGIS software. The random permanent plots that were established during baseline survey were measured for the purpose of monitoring. A total of 365 permanent plots were measured in the field. There were 298 plots in closed canopy forests and 67 plots in open canopy forests.

The size of the plot was fixed to a circle of 8.92 m radius. A sub-plot of 5.64 m radius was established for saplings and a sub-plot with 1 m radius was established for counting regeneration.

Sampling design and field plot design used by professional teams

Before the field campaign, the location of sample plots was designed using a systematic clustered random sampling method. Each cluster contained eight sample plots. Within the clusters, the sample plots were aligned in two parallel columns in North-South direction, with four plots per column. The distance between plots was 300 m, both between columns and rows. The original sampling design generated 16 clusters for the Kayarkhola watershed with a total number of 112 plots while it included 15 clusters for a total of 115 plots for the Ludikhola watershed. The actual number of plots available for the purpose of the study is less than that because some plots were either placed outside the area of study or in non forested areas (water, agricultural and bare soil areas). The total number of plots available for the study was therefore 57 for Kayarkhola and 92 for Ludikhola. The plots were of fixed circular shape with a 12.62 m radius, equivalent to an area of 500 m^2.

The field data were collected in April/May 2011. All the sample plots that were located in forest with at least 10 % canopy cover were measured in the field. The measurements at tree-level included all living trees and shrubs above 5 cm diameter within the plot area.

Above ground biomass measurement estimates

Within each plot, individual tree diameter at breast height measurements for both live and dead trees were taken and used in allometric equations given in [18] to estimate above ground biomass, AGB (stem, branch and foliage biomass). The individual tree AGB field estimates were totaled for each subplot and converted to AGB Mg/ha.

Large AGB field estimate values (over 1500 Mg/ha) are assumed to be outliers, caused by e.g., plot-level AGB estimation errors or measurement errors. At plot level, with relatively small plots, it sometimes occurs that one or a few very thick trees cause the polynomial formula for plot level volume computation to become unstable because of extrapolation. This extrapolation error may cause the volume of a single exceptional tree to be estimated so high that a timber volume of more than 2000 m^3 per hectare is attained, which is not realistic. There is no adequate statistical data available to quantify this phenomenon and revisiting the plots for validation is not feasible either. We therefore resorted to manual removal of probable outliers that are detected as statistical outliers

of AGB field estimate distribution and also by visual interpretation from LiDAR predictor—AGB field estimate scatterograms.

In field measurements of the local teams, there were two plots in which the estimated AGB was very high, 2202.6 Mg/ha and 3257.6 Mg/ha, respectively, and could be assumed as outliers. Visual assessment of the LiDAR predictor—AGB field estimate distribution supported this decision. Thus these two plots were discarded as outliers. Otherwise, the estimated AGB values of the plots are treated as the ground truth. After deletion of outliers, a total of 372 field plots measured by local forest measurement teams (182 in the study site Chitwan, 190 in the study site Gorkha), and a total of 149 field plots by the professional measurement teams (57 in Chitwan, 92 in Gorkha) were available for this analysis.

Figure 8 shows the variability of AGB field estimates in each dataset without outliers. Especially data collected by the local forest inventory teams in the study site Chitwan (CommCh) contain a significantly larger range of values than the other subsets. Also, the averages of the ABG field estimates in the field plots measured by local measurement teams were larger than those estimates by the professional inventory teams in both study sites, Gorkha and Chitwan.

Differences between field estimates due to different sampling designs

Different sampling designs affect the distribution of AGB field estimates due to different characteristics of the forest in which the sample plots are located. In particular, the ownership of the forest affects the distribution average and median values, see Table 4 and Fig. 2. The sample collected by local community teams contain fewer plots from privately owned forests compared to samples collected by professional teams. After discarding those plots from the sample of local community teams, i.e., considering only plots within community owned forests, the average and median values of AGB are larger compared to AGB values obtained by considering all the plots in the professional teams' sample. This effect does not happen in the sample of local community teams. Also, in the case where only plots within closed canopy forests are considered, the average AGB values are slightly larger than in the case where all the measured plots are included.

When only the plots in dense community owned forests are considered, the average AGB values obtained are the largest. The sizes of these subsets are relatively small (only 26–41 field plots). This small sample size may cause problems in the model-based prediction of AGB.

Validation procedure

In this study, a method based on a linear model to predict the AGB values, namely a Bayesian linear model with orthogonal predictors resulting from truncated singular value decomposition is used [19]. This model is designed to give accurate and precise predictions when using a small training set size compared to the number of possibly correlated predictors. It utilizes the singular value decomposition of the normalized predictors, and allows bigger deviation from zero to the regression parameters of the orthonormalized predictors which are known to explain the original predictor variability most, i.e., have biggest singular values. With this method, the effective number of predictors is cut down according to the given data and predictor explanation ratio, and thus it performs better especially with small training sets.

The characteristics and distributions of the AGB field estimates vary among the subsets, e.g., subset CommCh contains data with highest values of AGB, subset ProfGo the lowest values. Variation can be seen also in the LiDAR predictor values among different subsets. If the data can be considered as samples from the same distribution, i.e., there are no significant differences in the forest characteristics nor in the field sample measurement routines, a common model based on all these data should

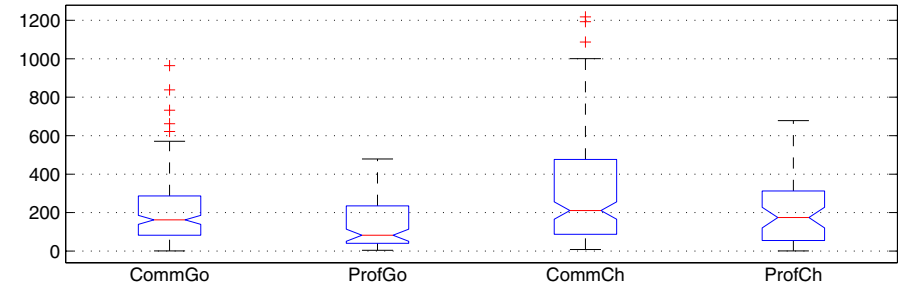

Fig. 8 Boxplots of the AGB field estimates

Table 4 Sizes and average AGB values (Mg/ha) of different measurement team dependent subsets in Chitwan and Gorkha areas

Subset	Comm		Prof	
	N	$\overline{\text{AGB}}$	*N*	$\overline{\text{AGB}}$
Gorkha				
All	190	203.3	92	127.3
Community owned	184	202.9	45	190.4
Closed canopy	157	216.5	82	133.5
Community owned and closed canopy	151	216.5	41	198.3
Chitwan				
All	182	308.4	57	205.8
Community owned	178	313.8	31	290.3
Closed canopy	154	318.8	48	207.0
Community owned and closed canopy	151	323.7	26	298.0

perform well. That is, the prediction model where model parameters are estimated with all the data (in this study Comm + Prof), or with some subset of data (Comm or Prof), should give equally accurate estimates, both in the data belonging to the teaching set subset, or to the other subsets [20]. Thus, to validate whether the data come from the same distribution and if data from one subset can be used to predict the AGB field estimates of another, cross-validation procedure is used. Each subset (Comm and Prof) at time serve as the validation set and the predictions estimated with different subsets (Comm, Prof and Comm + Prof) are validated.

To verify the prediction performance of different data validation subset of size N_v on different models, root mean square error,

$$\text{RMSE} = \sqrt{\frac{\sum_{i=1}^{N_v} \left(\tilde{y}_{v,i} - y_{v,i}\right)^2}{N_v}}, \quad (1)$$

mean difference,

$$\text{D} = \frac{\sum_{i=1}^{N_v} \left(\tilde{y}_{v,i} - y_{v,i}\right)}{N_v}, \quad (2)$$

relative RMSE ($\text{RMSE}\,\% = \text{RMSE} \times 100\,\% / \bar{y}_v$) and relative mean difference ($\text{D}\,\% = \text{D} \times 100\,\% / \bar{y}_v$) are used. Here $\tilde{y}_{v,i}$ is the the predicted AGB value for plot i, $y_{v,i}$ is the corresponding field estimate ("truth"), and $\bar{y}_v = \sum_{i=1}^{N_v} y_{v,i}/N_v$.

The error statistics are calculated using both leave-one-out cross-validation (LOOCV) procedure and straight cross-validation, depending on the case. In a case, where the training set contains the same plots as the validation set, for example in the full dataset case (Comm + Prof) and self-validation cases (training and validation sets are the same), LOOCV is used. In LOOCV, one plot of the training set, i, at a time is used as the validation plot, and the rest of the training set is used to estimate the model parameters which are then used to predict the validation plot AGB. With the predicted values $\tilde{y}_{v,i}$, $i = 1, 2, \ldots, N_v$ the error statistics are calculated using formulas (1) and (2). In case where the AGB field estimates of one subset are predicted using a model calibrated with another subset (e.g. validation set Comm plots are predicted using training set Prof), the calibrated model is used as such to predict all the values of the other subset and the error statistics are calculated in a straightforward manner using the given formulas.

Authors' contributions

VJ conducted all lidar modeling work and wrote most of the text. BG lead the professional field teams and served as the liaison between ICIMOD, Arbonaut and LUT teams as well as reviewed the manuscript. BK lead the training of the community forest teams and managed their field collection. AM wrote the final version of the article. KT, KG and PL computed, screened and recomputed several times plot level estimates and LiDAR model features at different stages of the project. JH managed the work of the Arbonaut team. EN classified and compared the field plot designs and identified the field sample designs used. JP supervised the Lidar processing and model building efforts. TK contributed to the mathematical analysis of the results and lead the overall effort at LUT and Arbonaut. All authors read and approved the final manuscript.

Author details

[1] Department of Mathematics and Physics, Lappeenranta University of Technology, P.O.Box 20, 53851 Lappeenranta, Finland. [2] Arbonaut Ltd, Kaislakatu 2, 80130 Joensuu, Finland. [3] International Centre for Integrated Mountain Development (ICIMOD), G.P.O. Box 3226, Khumaltar, Lalitpur, Kathmandu, Nepal. [4] Mzumbe University, P.O. Box 1, Mzumbe, Morogoro, Tanzania.

Acknowledgements

This work has been carried out with the financial and institutional supports from the Governments of Finland and Nepal under the Forest Resource Assessment (FRA) Nepal project and ICIMOD. We would like to thank Finnmap International for successful completion of the airborne laser scanning. Our special thanks go to our field teams and community forest user group members for timely and accurate field data collection.

Competing interests

The authors declare that they have no competing interests.

Received: 23 March 2015 Accepted: 19 October 2015
Published online: 02 December 2015

References

1. IPCC. Climate change 2013: the physical science basis. Contribution of working group 1 to the Fifth Assesment Report: Chapter 6: carbon and other biogeochemical cycles. 2013. Retrieved from http://www.ipcc.ch/report/ar5/wg1/.
2. Angelsen A., Brown S, Loisel C, Peskett L, Streck C, Zarin D. Reducing emissions from deforestation and forest degradation (REDD): an options assessment report. Technical report, Prepared for the Government of Norway by the Meridian Institute. 2009. Retrieved from http://www.REDD-OAR.org.
3. UN FCCC. Guidance for modalities relating to forest reference levels and forest reference emissions levels—a contribution in response to SBSTA's invitation to submit views (see FCCC/SBSTA/2011/L.14, para.4 & annex 1, para.2). 2011. Retrieved from http://unfccc.int/resource/docs/2011/smsn/ngo/332.

4. ICIMOD, ANSAB and FECOFUN. Pilot project: Design and setting up of a governance and payment system for Nepal's Community Forest Management under Reducing Emissions from Deforestation and Forest Degradation. 2011. Retrieved from http://theredddesk.org/countries/initiatives/design-and-setting-governance-and-payment-system-nepal's-community-forest.
5. Karky B, Vadiya R, Karki S, Tulachan B. What is REDD+ additionality in community managed forest for Nepal? J Forest Livelihood. 2013;11(2):37–45.
6. Skutsch MM, Karky BS, Rana EB, Kotru R, Karki S, Joshi L, Pradhan N, Gilani H, Joshi G. Options for Payment Mechanisms Under National REDD+ Programmes. Working Paper 2012/6. Kathmandu: ICIMOD; 2012.
7. Shrestha S, Karky BS, Karki S. Case study report: Redd+ pilot project in community forests in three watersheds of nepal. Forests. 2014;5(10):2425–39.
8. UN FCCC: Bonn climate change conference, the 42nd session of the subsidiary body for scientific and technological advice (SBSTA). 2015. Presentations retrieved from http://www.unfccc.int/meetings/bonn_jun2015/session/8855.php.
9. Skutch MM, Van Laake PE, Zahabu E, Karky BS, Phartiyal P. The value and feasibility of community monitoring of biomass under REDD+. 2009. Retrieved from http://www.communitycarbonforestry.org/NewPublications/CIFOR%20paper%20Nov%205%20version.
10. Asner GP, Hughes RF, Varga TA, Knapp DE, Kennedy-Bowdoin T. Environmental and biotic controls over aboveground biomass throughout a tropical rain forest. Ecosystems. 2009;12:261–78.
11. UN FCCC. Warsaw climate change conference, the nineteenth session of the conference of the parties (COP 19). 2013. Presentations retrieved from https://www.seors.unfccc.int/seors/reports/archive.html.
12. Danielsen F, Adrian T, Brofeldt S, van Noordwijk M, Poulsen MK, Rahayu S, Rutishauser E, Theilade I, Widayati A, The An N, Nguyen Bang T, Budiman A., Enghoff M, Jensen AE, Kurniawan Y, Li Q, Mingxu Z, Schmidt-Vogt D, Prixa S, Thoumtone V, Warta Z, Burgess N. Community monitoring for REDD+: international promises and field realities. Ecology Soc. 2013;18(3):41. Retrieved from http://www.dx.doi.org/10.5751/ES-05464-180341.
13. Karna YK. Mapping above ground carbon using worldview satellite image and lidar data in relationship with tree diversity of forests. The Netherlands: Master's thesis, Faculty of Geoinformation Science and Earth Observation, University of Twente; 2012.
14. ICIMOD, ANSAB, FECOFUN. A monitoring report on forest carbon stocks changes in REDD project sites (Ludikhola, Kayarkhola and Charnawati). 2011. http://theredddesk.org/sites/default/files/icimod-ansab-fecofun-redd-carbon-monitoring-report-22-oct-2011.pdf.
15. Gautam B, Peuhkurinen J, Kauranne T, Gunia K, Tegel K, Latva-Käyrä P, Rana P, Eivazi A, Kolesnikov A, Hämäläinen J, Shrestha SM, Gautam SK, Hawkes M, Nocker U, Joshi A, Suihkonen T, Kandel P, Lohani S, Powell G, Dinerstein E, Hall D, Niles J, Joshi A, Nepal S, Manandhar Kandel UY, Joshi C. Estimation of forest carbon using lidar-assisted multi-source programme (LAMP) in nepal. In: International Conference on Advanced Geospatial Technologies for Sustainable Environment and Culture, Pokhara, Nepal; 2013. An event of ISPRS, Technical Commission VI, Education and Outreach, Working Group 6. Retrieved from http://report.arbonaut.com/arbo_site_uploaded_files/pdf/pdf/Estimation of Forest Carbon Using LiDAR-Assisted Multi-source Programme (LAMP) in Nepal.pdf.
16. Junttila V, Kauranne T, Leppänen V. Estimation of forest stand parameters from LiDAR using calibrated plot databases. Forest Science. 2010;56(3):257–70.
17. Næsset E. Predicting forest stand characteristics with airborne scanning laser using a practical two-stage procedure and field data. Remote Sens Environ. 2002;80:88–99.
18. Chave J, Andalo C, Brown S, Cairns MA, Chambers JQ, Eamus D, Folster H, Fromard F, Higuchi N, Kira T, Lescure J-P, Nelson BW, Ogawa H, Puig H, Riera B, Yamakura T. Tree allometry and improved estimation of carbon stocks and balance in tropical forests. Oceologia. 2005;145:87–99.
19. Junttila V, Kauranne T, Finley AO, Bradford JB. Linear models for airborne laser scanning based operational forest inventory with small field sample size and highly correlated LiDAR data. IEEE Trans Geosci Remote Sens. 2015;53(10):1–13.
20. Nikolaeva E. Comparison of model-based above ground biomass predictions from LiDAR. Master's Thesis, Finland: Lappeenranta University of Technology ; 2014.

ACTA UNIVERSITATIS LAPPEENRANTAENSIS

646. HAN, BING. Influence of multi-phase phenomena on semibatch crystallization processes of aqueous solutions. 2015. Diss.

647. PTAK, PIOTR. Aircraft tracking and classification with VHF passive bistatic radar. 2015. Diss.

648. MAKKONEN, MARI. Cross-border transmission capacity development – Experiences from the Nordic electricity markets. 2015. Diss.

649. UUSITALO, ULLA-MAIJA. Show me your brain! Stories of interdisciplinary knowledge creation in practice. Experiences and observations from Aalto Design Factory, Finland. 2015. Diss.

650. ROOZBAHANI, HAMID. Novel control, haptic and calibration methods for teleoperated electrohydraulic servo systems. 2015. Diss.

651. SMIRNOVA, LIUDMILA. Electromagnetic and thermal design of a multilevel converter with high power density and reliability. 2015. Diss.

652. TALVITIE, JOONAS. Development of measurement systems in scientific research: Case study. 2015. Diss.

653. ZUBEDA, MUSSA. Variational ensemble kalman filtering in hydrology. 2015. Diss.

654. STEPANOV, ALEXANDER. Feasibility of industrial implementation of laser cutting into paper making machines. 2015. Diss.

655. SOKOLOV, MIKHAIL. Thick section laser beam welding of structural steels: methods for improving welding efficiency. 2015. Diss.

656. GORE, OLGA. Impacts of capacity remunerative mechanisms on cross-border trade. 2015. Diss.

657. AURINKO, HANNU. Risk assessment of modern landfill structures in Finland. 2015. Diss.

658. KAIJANEN, LAURA. Capillary electrophoresis: Applicability and method validation for biorefinery analytics. 2015. Diss.

659. KOLHINEN, JOHANNA. Yliopiston yrittäjämäisyyden sosiaalinen rakentuminen. Case: Aalto-yliopisto. 2015. Diss.

660. ANNALA, SALLA. Households' willingness to engage in demand response in the Finnish retail electricity market: an empirical study. 2015. Diss.

661. RIABCHENKO, EKATERINA. Generative part-based Gabor object detector. 2015. Diss.

662. ALKKIOMÄKI, VILLE. Role of service and data reuse in enterprises. 2015. Diss.

663. VÄNTSI, OLLI. Utilization of recycled mineral wool as filler in wood plastic composites. 2015. Diss.

664. KLEMOLA, KATJA. Tuottavuuden, vaikuttavuuden ja kustannusvaikuttavuuden arviointi alueellisesti integroiduissa sosiaali- ja terveyspalveluissa – palvelujen käyttöön perustuva malli ja esimerkkejä. 2015. Diss.

665. HEROLD, KRISTIINA. Impact of Word-of-Mouth on consumer decision-making: An information processing perspective in the context of a high-involvement service. 2015. Diss.

666. OLABODE, MUYIWA. Weldability of high strength aluminium alloys. 2015. Diss.

667. VANHALA, ERNO. The role of business model in computer game development organizations. 2015. Diss.

668. SALAMPASIS, DIMITRIOS. Trust-embedded open innovation: Towards a human-centric approach in the financial industry. 2015. Diss.

669. DE SMET, DIETER. Innovation ecosystem perspectives on financial services innovation. 2015. Diss.

670. PORRAS, PÄIVI. Utilising student profiles in mathematics course arrangements. 2015. Diss.

671. SALMINEN, JUHO. The role of collective intelligence in crowdsourcing innovations. 2015. Diss.

672. ROSAS, SAILA. Co-operative acquisitions – the contextual factors and challenges for co-operatives when acquiring an investor-owned firm. 2015. Diss.

673. SINKKONEN, TIINA. Item-level life-cycle model for maintenance networks – from cost to additional value. 2015. Diss.

674. TUUNANEN, JUSSI. Modelling of changes in electricity end-use and their impacts on electricity distribution. 2015. Diss.

675. MIELONEN, KATRIINA. The effect of cationic-anionic polyelectrolyte multilayer surface treatment on inkjet ink spreading and print quality. 2015. Diss.

676. OMAJENE, JOSHUA. Underwater remote welding technology for offshore structures. 2015. Diss.

677. NUUTINEN, PASI. Power electronic converters in low-voltage direct current distribution – analysis and implementation. 2015. Diss.

678. RUSATSI, DENIS. Bayesian analysis of SEIR epidemic models. 2015. Diss.

679. STRAND, ELSI. Enhancement of ultrafiltration process by pretreatment in recovery of hemicelluloses from wood extracts. 2015. Diss.

680. TANNINEN, PANU. Press forming of paperboard – converting tool optimization and process control. 2015. Diss.

681. VALTONEN, PETRI. Distributed energy resources in an electricity retailer’s short-term profit optimization. 2015. Diss.

682. FORSSTRÖM-TUOMINEN, HEIDI. Collectiveness within start up-teams – leading the way to initiating and managing collective pursuit of opportunities in organizational contexts. 2015. Diss.